Doctoral Dissertations   Graduate School

8-2009

Structure-Function Studies of the Large Subunit of Ribonucleotide Reductase from Homo sapiens and Saccharomyces cerevisiae

James Wesley Fairman
University of Tennessee - Knoxville

To the Graduate Council:

I am submitting herewith a dissertation written by James Wesley Fairman entitled "Structure-Function Studies of the Large Subunit of Ribonucleotide Reductase from Homo sapiens and Saccharomyces cerevisiae." I have examined the final electronic copy of this dissertation for form and content and recommend that it be accepted in partial fulfillment of the requirements for the degree of Doctor of Philosophy, with a major in Biochemistry and Cellular and Molecular Biology.

Chris G. Dealwis, Major Professor

We have read this dissertation and recommend its acceptance:

David A. Brian, Elias J. Fernandez, Elizabeth E. Howell, Ana A. Kitazono

Accepted for the Council:

Carolyn R. Hodges

Vice Provost and Dean of the Graduate School

(Original signatures are on file with official student records.)

To the Graduate Council:

I am submitting herewith a dissertation written by James Wesley Fairman entitled "Structure-Function Studies of the Large Subunit of Ribonucleotide Reductase from *Homo sapiens* and *Saccharomyces cerevisiae*." I have examined the final electronic copy of this dissertation for form and content and recommend that it be accepted in partial fulfillment of the requirements for the degree of Doctor of Philosophy, with a major in Biochemistry, Cellular, and Molecular Biology.

Chris G. Dealwis, Major Professor_____

We have read this dissertation
and recommend its acceptance:

David A. Brian_____

Elias J. Fernandez_____

Elizabeth E. Howell _____

Ana A. Kitazono_____

Accepted for the Council:

_____
Carolyn R. Hodges
    Vice Provost and Dean of the Graduate School

Structure-Function Studies of the Large Subunit of Ribonucleotide Reductase from *Homo sapiens* and *Saccharomyces cerevisiae*

A Dissertation
Presented for the
Doctor of Philosophy
Degree
The University of Tennessee, Knoxville

James Wesley Fairman
August 2009

ACKNOWLEDGEMENTS

I would like to start by thanking my mentor Chris Dealwis for allowing me to join his laboratory and for his guidance during my graduate studies at the University of Tennessee. He is always willing to push my boundaries, both mentally and as a scientist, and I commend him for that. Second, I would like to thank all the remaining members of my committee: Elias Fernandez, Elizabeth Howell, Ana Kitazono, and David Brian. Their input and advice has been critical to the completion of my research, the yeast Rnr project in particular. In addition, I would like to acknowledge our collaborator Julian Simon at the Fred Hutchinson Cancer Research Center, as he provided the basis for half of my dissertation research project. I would also like to thank Yun Yen at the City of Hope for providing me with plasmid containing the cDNA of human Rnr1.

All the members of the Dealwis lab have contributed either directly or indirectly to the work presented here, and it would not have been possible without both their friendship and dedication. Tomoaki Uchiki was involved in both my training and the initial stages of my research projects. He also developed the purification scheme for yeast Rnr, a protocol I have performed more times than I can possibly remember. Anna Gardberg, Brad Bennet, and Hai Xu were all heavily involved in my training as an X-ray crystallographer, teaching me the intricacies of various crystallographic refinement and analysis software. Sanath Wijerathna, a fellow graduate student in the Dealwis lab, has been instrumental in providing critical analysis, data, and moral support throughout the years. Structure factor data for the yeast hexamer and size exclusion data provided by Sanath will be instrumental in publishing of the research in Chapter 4 of this dissertation into the scientific literature. Beth Helmbrecht and John Lamaccia are two

ABSTRACT

Sufficient pools of deoxyribonucleotide triphophates (dNTPs) are essential for the high fidelity replication and repair of DNA, the hereditary material for a majority of living organisms. Ribonucleotide reductase (Rnr) catalyzes the rate-limiting step of de-novo DNA synthesis, the reduction of ribonucleosides to deoxyribonucleosides. Since the cell relies primarily upon ribonucleotide reductase for its dNTPs, both the cellular levels and activity of Rnr are heavily regulated, especially when DNA damage occurs or during replication blocks in the cell cycle. If dNTP pools become too high, too low, or imbalanced, genomic instability results, leading to either the formation of cancerous cells or cell death. High levels of dNTPs are required by actively propagating cells for the replication of new DNA molecules. Therefore, Rnr makes an excellent target for anti-cancer, anti-microbial, and anti-fungal chemotherapeutic agents.

Deficiencies in the cellular mismatch repair (MMR) machinery have been linked to genetic instability and carcinogenesis. Two alleles of *Rnr1* were recently discovered, $Rnr1^{S269P}$ and $Rnr1^{S610F}$, which have a mismatch repair synthetic lethal (*msl*) phenotype in *Saccharomyces cerevisiae* cells with missing or defective MMR genes. To uncover the molecular mechanism of the *msl* phenotype in these two mutants, recombinant Rnr1p-S269P and Rnr1p-S610F were subjected to *in vitro* activity assays, X-ray crystallography, and *in vitro* nucleoside-binding assays (**Chapter 3**). The $Rnr1^{S269P}$ allele was shown to dysregulate specificity cross talk by X-ray crystallography experiments, leading to reduced levels of dATP in the cell. A 2-fold reduction in binding of ADP substrate was observed in the $Rnr1^{S610F}$ allele, however reduction of the k_{cat} is believed to cause the observed *msl* phenotype in this mutant.

The first X-ray crystal structures of the large subunit of ribonucleotide reductase from *Homo sapiens* (hRRM1) are also presented here (**Chapter 4**). The hRRM1●TTP and hRRM1●TTP●GDP structures describe the binding of effector and substrate to the specificity and catalytic sites. In addition, the two structures hRRM1●TTP●ATP and hRRM1●TTP●dATP are the first X-ray crystal structures of Rnr from any species with the allosteric activity site occupied with the natural ligands ATP and dATP. Size exclusion chromatography data and a low resolution X-ray crystal structure of hexameric *S. cerevisiae* Rnr provide a model for dATP-dependent oligomerization.

TABLE OF CONTENTS

LIST OF TABLES

LIST OF FIGURES

LIST OF ABBREVIATIONS AND SYMBOLS

ABBREVIATIONS

ADP   Adenosine 5'-diphosphate or atomic displacement factor
Ala   Alanine
AMPPNP   5'-adenylyl-β-γ-imidodiphosphate
Arg   Arginine
Asn   Asparagine
ATP   Adenosine triphosphate
CDP   Cytidine 5'-diphosphate
Ci   Curies
CPM   Counts per minute
Cys   Cysteine
Da   Dalton; measurement of molecular weight equal to one
                       hydrogen atom
DEAE   Diethylaminoethyl
DHF   Dihydrofolate
DHFR   Dihydrofolate reductase
DPM   Disintegrations per minute
DTT   Dithiothreitol
dATP   2'-deoxyadenosine 5'-triphosphate
dCTP   2'-deoxycytidine 5'-triphosphate
dGTP   2'-deoxyguanosine 5'-triphosphate
dTTP   2'-deoxythymidine 5'-triphosphate
EcRR1   Large subunit of ribonucleotide reductase from *E. coli*
EDTA   Ethylenediaminetetraacetic acid
EMS   Ethylmethanesulfonate
EPR   Electron paramagnetic resonance
E. coli   *Escherichia coli*
FFT   Fast Fourier Transform
GDP   Guanosine 5'-diphosphate
Gln   Glutamine
Glu   Glutamate
Gly   Glycine
HEPES   4-(2-hydroxyethyl)-1-piperazineethanesulfonic acid
His   Histidine
hRRM1   Large subunit of ribonucleotide reductase from *H. sapiens*
H. sapiens   *Homo sapiens*
IDL   Insertion/deletion loop
Ile   Isoluecine
IMAC   Immobilized metal affinity chromatography
IPTG   Isopropyl β-D-1-thiogalactopyranoside
LB   Luria-Bertani media

Leu	Leucine
LSC	Liquid Scintillation Counter
Lys	Lysine
KCl	Potassium chloride
K_d	Dissociation constant
kDa	Kilodalton; measurement of molecular weight equal to one thousand Daltons
Met	Methionine
mg/ml	Milligrams per milliliter
$MgCl_2$	Magnesium chloride
MIN	Microsatellite instability
MIR	Multiple Isomorphous Replacement
MLH	MutL homologue
MMR	Mismatch repair
MR	Molecular Replacement
mRRM1	Large subunit of ribonucleotide reductase from *M. musculus*
MSH	MutS homologue
msl	Mismatch repair synthetic lethal
NaCl	Sodium chloride
NDK	Nucleoside phosphate kinase
NPK	Nucleoside diphosphate kinase
OD_{280}	Optical density at 280 nanometers
OD_{600}	Optical density at 600 nanometers
PCR	Polymerase Chain Reaction
PDB	Protein Data Bank
PEG	Polyethylene glycol
Phe	Phenylalanine
PMSF	Phenylmethylsulphonyl fluoride
Pro	Proline
psi	Pounds per square inch; unit of pressure
RCSB	Reasearch Collaboratory for Structural Bioinformatics
RMSD	Root mean square deviation
Rnr	Ribonucleotide Reductase
Rnr1	Large subunit of ribonucleotide reductase
Rnr2	Small subunit of ribonucleotide reductase
Rnr3	Isoform of the large subunit of ribonucleotide reductase found in *Saccharomyces cerevisiae*
Rnr4	Isoform of the small subunit of ribonucleotide reductase found in *Saccharomyces cerevisiae*
RR1	Large subunit of ribonucleotide reductase
RR2	Small subunit of Ribonucleotide reductase
ScRR1	Large subunit of ribonucleotide reductase from *S. cerevisiae*
S. cerevisiae	*Saccharomyces cerevisiae*
SEC	Size exclusion chromatography

Ser	Serine
StRR1	Large subunit of ribonucleotide reductase from *S. typhimurium*
TB	Terrific Broth media
THF	Tetrahydrofolate
Thr	Threonine
TLS	Translation, libration, and screw
TmRR1	Large subunit of ribonucleotide reductase from *T. maritima*
TRIS	Tris(hydroxymethyl)aminomethane
Trp	Tryptophan
TS	Thymidylate synthase
Tyr	Tyrosine
UDP	Uridine 5'-diphosphate
Val	Valine
v/v	Volume per volume
w/v	Weight per volume
x g	Gravity

SYMBOLS

˚C	Degrees celcius; unit of temperature
α	Alpha; type of three-dimensional protein helical structure or crystallographic unit cell constant or large subunit of ribonucleotide reductase
β	Beta; type of three-dimensional protein sheet structure or crystallographic unit cell constant or small subunit of ribonucleotide reductase
γ	Gamma; crystallographic unit cell constant
Å	Angstrom; equal to 10^{-10} meters
σ	Sigma; contour level of an electron density map
λ	Lambda; wavelength of electromagnetic radiation

1. BACKGROUND AND INTRODUCTION

1.1 INTRODUCTION AND OVERVIEW

The enzyme ribonucleotide reductase (Rnr) is a conserved and absolutely required enzyme in all living organisms that use DNA as their hereditary material, from viruses to humans (Stubbe *et al.* 2001; Lembo *et al.* 2009). It catalyzes the rate-limiting step of *de novo* DNA synthesis in these organisms via the conversion of all four ribonucleotides, the building blocks of RNA, to 2'-deoxyribonucleotides, the building blocks of DNA, by abstracting the 2'-OH group and replacing it with a hydrogen using the power of free- radical chemistry (Andersson 2008). Crucial for both the synthesis and repair of DNA, Rnr maintains balanced pools of deoxyribonucleoside triphosphates (dNTPs) in the cell. Levels of dNTPs are tightly regulated in the cell as an excess can cause misincorporation of nucleotides into newly synthesized DNA, and a deficiency will not allow for the repair of damaged DNA or synthesis of new DNA, eventually leading to genomic instability which can result in either cancer formation or cell death (Chabes *et al.* 2003; Chabes *et al.* 2003). Therefore, Rnr makes an excellent target for the treatment of pathologies where rapid proliferation takes place, such as anti-cancer, anti-microbial, anti-fungal, and anti-viral chemotherapeutic agents (Johns *et al.* 1998; Ingram *et al.* 1999; Romanelli *et al.* 1999; Balzarini 2000; Tripathy 2002; Manegold 2004; Boukovinas *et al.* 2008; Taira *et al.* 2008; Xu *et al.* 2008; Danesi *et al.* 2009).

The lab of Dr. Peter Reichard at the Karolinska Institute in Sweden performed the pioneering purifications and biochemical characterizations in the field of Rnr research during the 1960s (Moore *et al.* 1964; Blakley *et al.* 1965; Holmgren *et al.* 1965; Berglund *et al.* 1969; Brown *et al.* 1969; Brown *et al.* 1969; Brown *et al.* 1969). During this time, his group was able

to provide the scientific community with a basic understanding of how the enzyme worked: the allosteric selection rules and need for free-radicals to function, which will be discussed further in other sections of this dissertation. Since then, a panacea of knowledge about Rnr has been added to the field by research groups around the globe, most notably by Dr. Joanne Stubbe at the Massachusetts Institute of Technology.

In the remainder of this chapter, the reader will be provided with a solid understanding of many aspects of Rnr. First, the reader will be introduced to the classification of Rnrs from various organisms into different categories based on the method of free-radical generation. A brief description of each class of Rnr will follow. Second, the *de novo* synthesis of dNTPs and catalytic mechanism of Rnr will be discussed, along with a brief description of catalytic inhibitors of Rnr. Third, the regulation of Class I Rnrs will be discussed. Since the regulation of Rnrs is so diverse depending on the organism, and the research in this dissertation is focused on the Rnr from *Saccharomyces cerevisiae* and *Homo sapiens*, the regulation of Rnr in these two species will be covered in greater detail. Fourth, a discussion of the currently available structural information on Rnrs will be covered. Finally, the objectives and impact of the research performed for this dissertation will be reviewed.

1.2 CLASSIFICATION OF RIBONUCLEOTIDE REDUCTASES

Ribonucleotide reductases from various organisms are divided into three distinct groups, referred to as classes in the literature: (1) Class I, (2) Class II, and (3) Class III (Nordlund *et al.* 2006). This classification is based upon the method used by Rnr to generate the conserved cysteinyl free-radical in the active site required for catalytic turnover (Torrents *et al.* 2008) (**Figure 1.1**). Class I Rnrs depend upon the formation of a stable tyrosyl radical on an additional

non-identical protein subunit and require the presence of oxygen. Class II Rnrs require the vitamin B_{12} cofactor 5'-deoxyadenosyl cobalamin and are able to function either in the presence or absence of oxygen. Class III Rnrs require S-adenosylmethionine (SAM) and an iron-sulfur cluster present in an additional protein subunit for the generation of a glycyl free-radical, which is extremely oxygen sensitive. These Rnr classes are distributed widely across species in nature. Eukaryotes and viruses which infect eukaryotic organisms encode only Class I Rnrs. Bacterial and Eubacterial species can encode any of the three classes; many bacterial species even have the ability to encode multiple classes of Rnr genes depending on environmental queues. Members of archaebacteria which thrive in strictly anaerobic environments encode only Class III Rnrs. Thanks to the recent and rapid genomic sequencing of organisms, a comprehensive catalog of all Rnr sequences currently available is compiled into a database called the Ribonucleotide Reductase Database (Rnrdb), which can be found at http://rnrdb.molbio.su.se. We will now consider each class of Rnr in greater detail.

1.2.1 Class I Ribonucleotide Reductases

Members of the Class I Rnr family require the presence of oxygen to function and are found in virtually all eukaryotic organisms that have had their genomes sequenced thus far (Torrents *et al.* 2008). Class I Rnrs require the presence of at least two distinct subunits for their activity: (1) the α or large subunit and (2) the β or small subunit (Jordan *et al.* 1998). The larger α subunit contains the catalytic site of the enzyme where
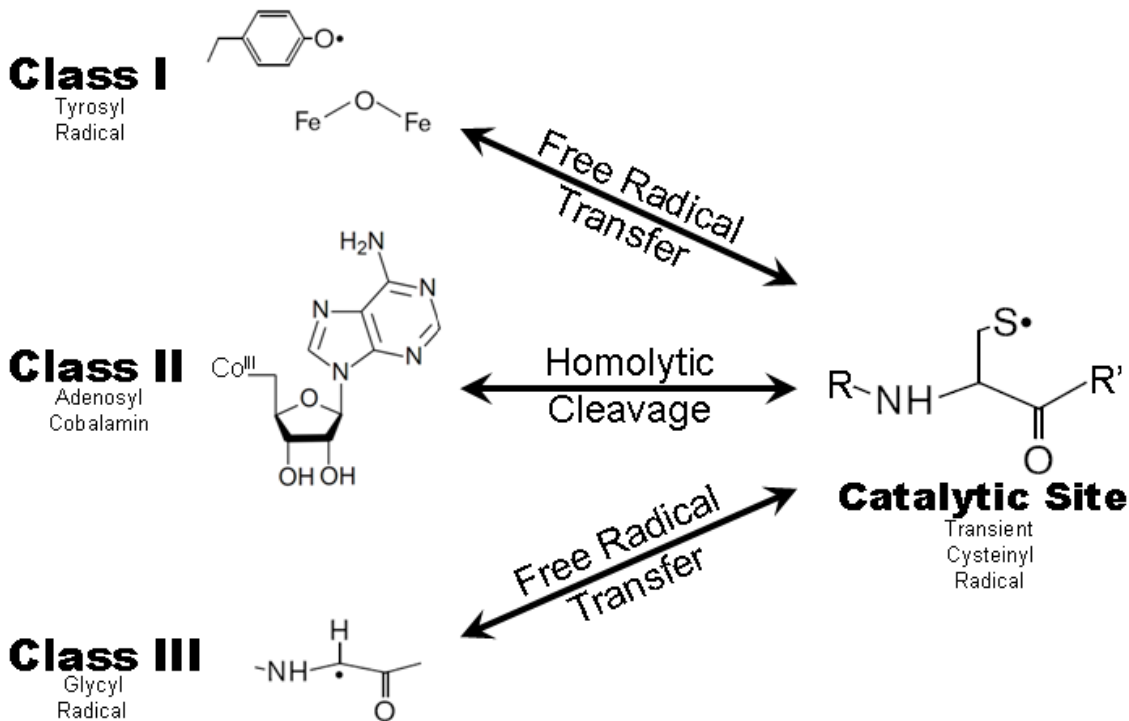
Figure 1.1: Generation of the cysteinyl radical in all three classes of Rnr.
Each class of Rnr uses a different method to generate the transient cysteinyl free-radical in the catalytic site. Class I Rnrs generate a stable tyrosyl radical in the small subunit that is transferred over a distance of 30 Å to the catalytic site on the large subunit. Class II Rnrs use the hemolytic cleavage of 5'-deoxyadenosyl cobalamin to generate a free-radical which is transferred onto the catalytic cysteine. Class III Rnrs generate a stable glycyl radical using S-adenosylmethionine. The glycyl radical is transferred 5 Å to the catalytic cysteine during catalysis.

substrate is converted to product (see **Section 1.3**) and binding site(s) for allosteric effector molecules (see **Section 1.4.1**). In addition, this subunit contains five conserved cysteine residues, three in the catalytic site and two on the flexible C-terminal tail, which are required for enzymatic activity (Aberg *et al.* 1989; Mao *et al.* 1992). The smaller β subunit houses a di-iron oxo binding site which is required for the generation of a stable tyrosyl radical (Petersson *et al.* 1980; Larsson *et al.* 1986) (**Figure 1.1**). During each catalytic turnover event, the free-radical is transferred a distance of over 30 Å, from the tyrosine in the small subunit to the catalytic cysteine in the large subunit, via a set of conserved aromatic residues in both the small and large subunits (Nordlund *et al.* 1990; Seyedsayamdost *et al.* 2007). The free-radical in the small subunit is regenerated after each catalytic event where it is protected from decay by storage as a stable tyrosyl radical. A single free-radical, once formed inside the small subunit, can perform multiple turnovers in the absence of oxygen, assuming the tyrosyl radical does not decay (Petersson *et al.* 1980).

The oligomeric state of the active enzyme both *in vivo* and *in vitro* remains unclear as there are conflicting reports present in the literature of tetramers, hexamers, and octamers containing varying combinations of α and β subunits (Kashlan *et al.* 2002; Rofougaran *et al.* 2006; Wang *et al.* 2007; Radivoyevitch 2008), and is a subject addressed further in **Section 1.4.1** and **Chapter 4** of this dissertation. However, it is believed that the minimal configuration for activity in Class I Rnrs is an $\alpha_2\beta_2$ heterotetramer (Nordlund *et al.* 2006). Class I Rnrs only have the ability to catalyze ribonucleoside diphosphates to 2'-deoxyribonucleoside diphosphates.

Class I Rnrs are further divided into two sub-categories based upon their genetic profiles, structural topology, and source of reducing equivalents: (1) Class Ia and (2) Class Ib. Class Ia

enzymes are found in both eukaryotic, which includes *S. cerevisiae* and *H. sapiens*, and prokaryotic organisms. On the other hand, Class Ib enzymes are found only in prokaryotes. In Class Ia Rnrs the α subunit is encoded by the *nrdA* locus and the β subunit is encoded by the *nrdB* locus, while in Class Ib Rnrs the α subunit is encoded by the *nrdE* locus and the β subunit is encoded by the *nrdF* locus (**Figure 1.2**). Reducing equivalents are shuttled onto Class Ia Rnrs via either glutathione/glutaredoxin or thioredoxin, which ultimately receive their reducing power from NADPH (Gon *et al.* 2006; Koc *et al.* 2006; Camier *et al.* 2007; Avval *et al.* 2009) (**Figure 1.3**). On the other hand, all organisms that encode a Class Ib Rnr also carry a copy of the *nrdH* gene (**Figure 1.2**), which encodes an Rnr-specific glutaredoxin-like protein that serves the same purpose as glutathione and thioredoxin in Class Ia Rnrs (Jordan *et al.* 1997). In addition, species which carry Class Ib Rnrs harbor the *nrdI* gene (**Figure 1.2**), a flavodoxin protein which has recently been observed to be involved in the maintenance of the free-radical in the NrdF subunit (Cotruvo *et al.* 2008; Roca *et al.* 2008). A free-radical maintenance function has also been observed for the *E. coli* Class Ia Rnr by a protein known as YfaE (Wu *et al.* 2007; Hristova *et al.* 2008). An additional distinction between the two Class I Rnrs subclasses is the presence (Class Ia) or absence (Class Ib) of the ATP-binding cone domain (Aravind *et al.* 2000) at the N-terminus. The ATP-binding cone serves as an allosteric switch, which is able to turn the enzyme on or off by binding either ATP or dATP, respectively (see **Section 1.4.1** and **Chapter 4**).
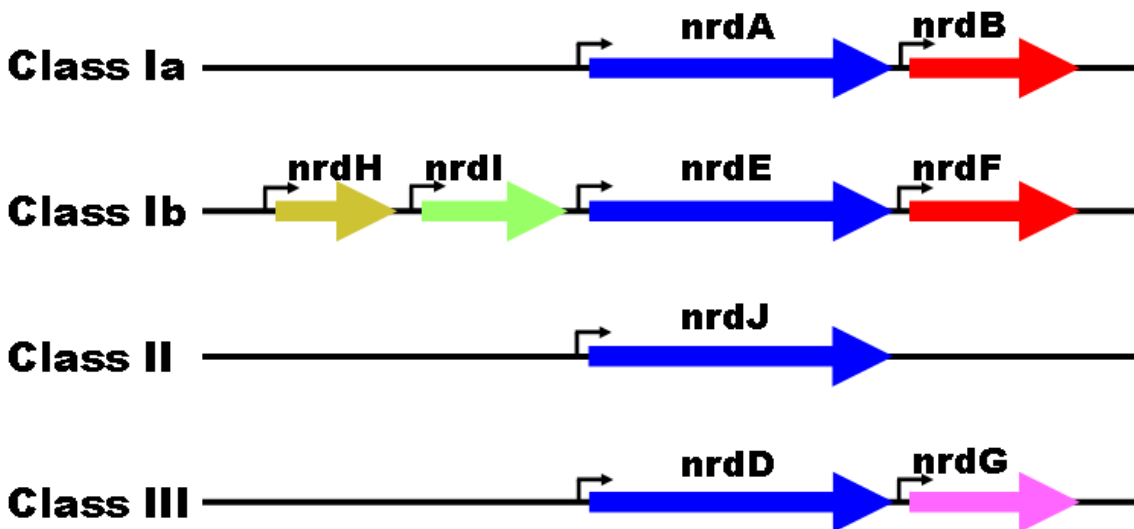
Figure 1.2: The organization of genes in the three classes of Rnrs.
Loci that encode large subunits are colored blue and loci that encode small subunits are colored red. nrdH encodes a glutaredoxin-like protein which specifically reduces nrdE after catalytic turnovers occur and nrdI is involved in the maintenance of the stable free-radical on the nrdF subunit. The nrdG gene contains an iron-sulfur center and is required for the formation of glycyl free-radicals on the nrdD subunit of Class III Rnrs. This figure was adapted from (Torrents *et al.* 2008).
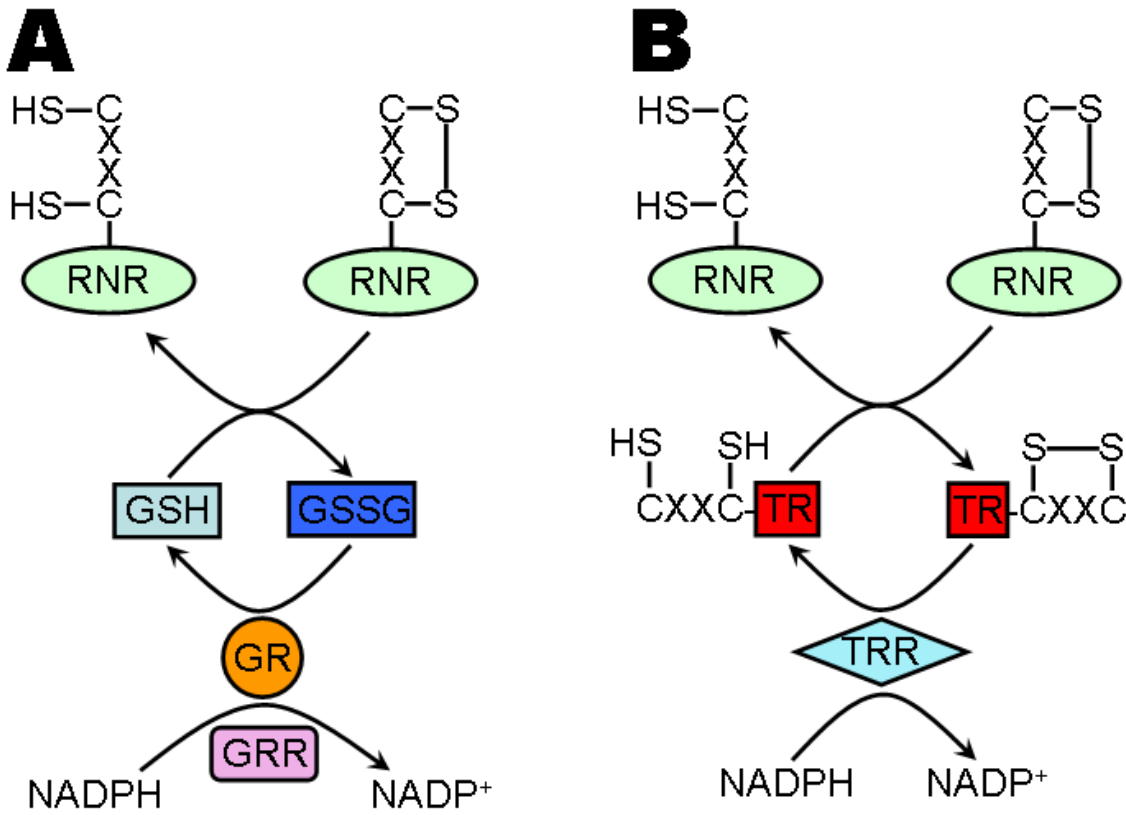
Figure 1.3: Cellular reduction of Class Ia and Class II Rnrs
Class Ia Rnrs form a disulfide bond on their C-terminus after reducing the catalytic site after each turnover. The C-terminal disulfide is then reduced either by glutathione or thioredoxin. **(A)** Glutathione (GSH) reduces Rnr to form oxidized glutathione (GSSG). GSSG is then reduced by glutaredoxin (GR). Glutaredoxin is supplied with reducing equivalents by glutaredoxin reductase (GRR), which receives its reducing power from NADPH. **(B)** Thioredoxin provides reducing equivalents to Rnr. Disulfides on thioredoxin are then reduced by thioredoxin reductase, which also receives reducing power from NADPH.

1.2.2 Class II Ribonucleotide Reductases

Members of the Class II Rnr family are indifferent to the presence of oxygen and are only carried in the genomes of prokaryotic organisms. Unlike Class I Rnrs, the activity of Class II Rnrs requires only the large α subunit, which is encoded by the *nrdJ* locus (**Figure 1.2**) (Licht *et al.* 1996). The *nrdJ* gene product contains the catalytic site and a specificity site, which is used by the enzyme to select for binding of substrates to the catalytic site (Sintchak *et al.* 2002; Larsson *et al.* 2004). Free-radicals are provided to the catalytic site via homolytic cleavage of the vitamin B_{12} cofactor 5'-deoxyadenosyl cobalamin, which neither requires nor is inhibited by the presence of oxygen (Chen *et al.* 2003) (**Figure 1.1**). After homolytic cleavage occurs, the free-radical is transferred from the adenosyl co-factor to the free-radical-bearing cysteine in the catalytic site over a distance of 6 Å (Gerfen *et al.* 1996; Licht *et al.* 1999). Transfer of and catalysis by the free-radical of Class II Rnrs is extremely fast, and one cobalamin cofactor has been shown to be able to service multiple large subunits by dissociating from one and re-associating with another (Licht *et al.* 1999). Five conserved cysteine residues, three in the catalytic site and two on the C-terminal tail, are present on the large subunit (Booker *et al.* 1994), and serve the same function as those present in the Class I family large subunits. As in Class Ia Rnrs, reducing equivalents are provided to Class II family members by either glutathione or thioredoxin (Borovok *et al.* 2002) (**Figure 1.3**).

Members of the Class II family have been observed to be functional as α monomers (Panagou *et al.* 1972; Sintchak *et al.* 2002) or as α_2 dimers (Tsai *et al.* 1980; Larsson *et al.* 2004) depending upon the bacterial species from which they are isolated from. The monomeric nrdJ from *Lactobacillus leichmannii* contains a small insert which mimics the portion of the protein

that would normally be provided by its dimeric partner. Class II Rnrs from some bacterial species are able to catalyze nucleoside diphosphates, while Rnrs from other species catalyze nucleoside triphosphates (Panagou *et al.* 1972; Jordan *et al.* 1997; Riera *et al.* 1997; Tauer *et al.* 1997). A majority of Class II Rnrs do not carry the ATP-binding cone at their N-termini as in Class Ib members, and therefore lack the ability to be allosterically activated or inhibited by ATP and dATP (Jordan *et al.* 1997).

1.2.3 Class III Ribonucleotide Reductases

Members of the Class III family of Rnrs are extremely sensitive to the presence of oxygen and are only carried in the genomes of strict anaerobic archaebacteria or by facultative anaerobes when oxygen is not available (Torrents *et al.* 2008). Class III Rnrs require the presence of two non-identical subunits for their activity: (1) an α, or large, subunit encoded by the *nrdD* locus and (2) a small subunit encoded by the *nrdG* locus (Torrents *et al.* 2001) (**Figure 1.2**). The α subunit is structurally similar to the large subunits from Class I and Class II family members and contains a catalytic site and two allosteric effector binding sites (Logan *et al.* 1999). A stable free-radical is created on a glycine residue on the α subunit, which is then transferred a distance of 5 Å to the catalytic cysteine residue where substrate turnovers take place (Sun *et al.* 1996; Young *et al.* 1996). This glycyl free-radical is extremely sensitive to oxygen, and exposure of Class III Rnrs containing the free-radical results in cleavage of the peptide bond at the N-terminus of the free-radical-bearing glycine residue, destroying the protein (King *et al.* 1995). The NrdG protein is a member of the radical S-adenosyl methionine super-family (Sofia *et al.* 2001), and contains an iron-sulfur center that is required for the generation and maintenance of the glycyl radical on the large subunit (Young *et al.* 1994; Sun *et al.* 1995;

Ollagnier *et al.* 1996; Tamarit *et al.* 2000; Torrents *et al.* 2001). Unlike members of both Class I and Class II Rnrs, Class III Rnrs receive their reducing equivalents from the small organic molecule formate (Mulliez *et al.* 1995). However, the mechanism by which formate is able to serve as a reductant for the large subunit still remains poorly understood (Nordlund *et al.* 2006).

Active Class III Rnrs are believed to be in an $\alpha_2\beta_2$ oligomeric configuration when they are active, where α is the gene product of the *nrdD* locus and β is the gene product of the *nrdG* locus (Ollagnier *et al.* 1996; Torrents *et al.* 2001). However, dimers of α that were first activated by β_2 and then separated from one another were also shown to be active. All Class III Rnrs that have currently been investigated utilize ribonucleoside triphosphates as their substrates (Fontecave *et al.* 1989; Young *et al.* 1994). In addition, all of the Class III Rnrs sequenced to date contain an ATP-binding cone at their N-terminus, which has been shown to successfully stimulate and inhibit catalytic activity of Class III Rnrs (Eliasson *et al.* 1994; Torrents *et al.* 2000).

1.3 CATALYSIS IN CLASS Ia RIBONUCLEOTIDE REDUCTASES

1.3.1 Ribonucleosides to Deoxyribonucleosides

The conversion of the four ribonucleoside diphosphates to their corresponding deoxyribonucleoside diphosphates by Rnr is the rate-limiting step of *de novo* DNA synthesis. The ribonucleoside diphosphates uridine 5'-diphosphate (UDP), cytidine 5'-diphosphate (CDP), guanosine 5'-diphosphate (GDP), and adenosine 5'-diphosphate (ADP) can all serve as substrates for Class Ia Rnrs (**Figure 1.4**). The enzyme can select for the binding and catalysis of a particular ribonucleoside diphosphate at the catalytic
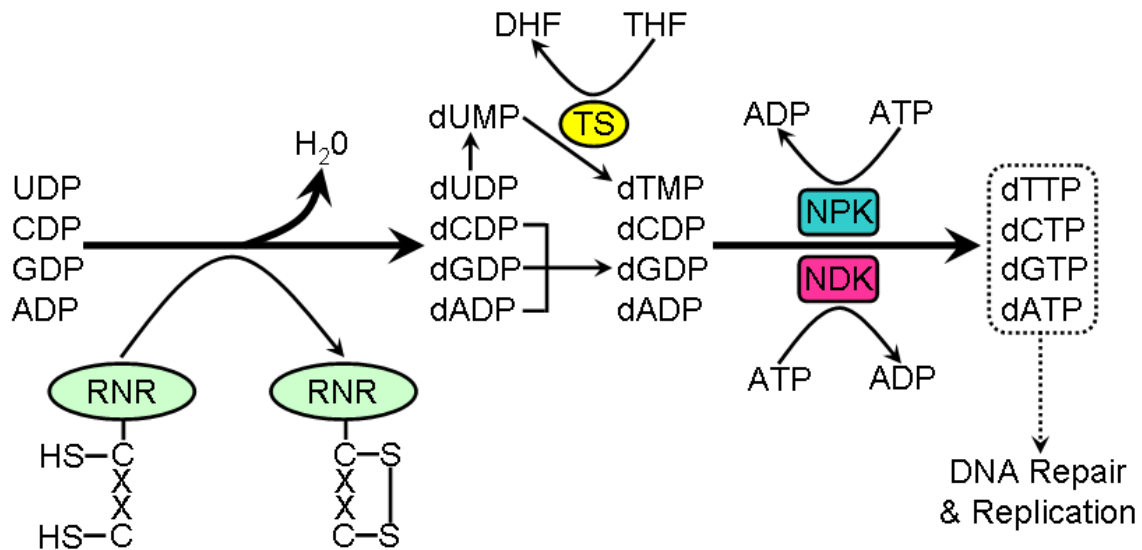
Figure 1.4: *De novo* deoxyribonucleotide synthesis pathway in Class Ia Rnrs.
Ribonucleoside diphosphates are reduced to deoxyribonucleoside diphosphates by ribonucleotide reductase. After each turnover of Rnr, a disulfide bond is formed which must in turn be reduced so that catalytic turnovers can continue. dUMP is then converted to dTMP via thymidylate synthetase (TS). dTMP, dCDP, dGDP, and dADP are then converted into deoxyribonucleoside triphosphates by nucleoside phosphate kinase (NPK) and nucleoside diphosphate kinase (NDK).

site (C-site) via the binding of effector molecules to a separate allosteric site on the enzyme, which is referred to as the specificity site (S-site) in the literature (Eriksson *et al.* 1997; Uppsten *et al.* 2003; Larsson *et al.* 2004; Xu *et al.* 2006). A detailed description of allosteric control by the S-site is discussed in **Section 1.4.1**.

Catalysis is accomplished via free-radical chemistry using a transient cysteinyl radical residue in the catalytic site (Thelander 1974; Lin *et al.* 1987) (**Figure 1.1**). Following catalysis, a disulfide bond is formed between two cysteine residues in the catalytic site, which must be reduced before binding of new substrates and further catalytic turnovers can occur (Eriksson *et al.* 1997) (**Figure 1.4**). Two conserved cysteines on the C-terminal tail of Class Ia Rnrs, with the consensus sequence CXXC, provide reducing equivalents to the catalytic site. The disulfide bond formed by CXXC on the C-terminal tail after C-site reduction is then reduced either by glutathione or thioredoxin (**Figure 1.3**). 2'-deoxyuridine diphosphate (dUDP) is phosphorylated by nucleoside diphosphate kinase (NDK) and then has two of the phosphates removed by dUTP diphosphohydrolase, forming dUMP. The enzyme thymidylate synthetase (TS) then catalyzes the methylation of dUMP to form dTMP, converting tetrahydrofolate (THF) to dihydrofolate (DHF) during the reaction, which is later recycled by the enzyme dihydrofolate reductase (DHFR) (Kraut 1987) (**Figure 1.4**). The kinases nucleoside phosphate kinase (NPK) and NDK then fully phosphorylate all four deoxynucleoside diposphates and monophosphates to dNTPs, which can be used by the cell to either repair existing or synthesize new DNA strands (**Figure 1.4**).

1.3.2 Catalytic Mechanism of Ribonucleotide Reductases

Although they may have differences in their free-radical generation, Rnrs from all three classes share a common catalytic core: a conserved 10-stranded α-β barrel which surrounds a loop containing the catalytic cysteinyl free-radical (Nordlund *et al.* 2006). Class I and Class II Rnrs, which are both reduced by glutathione or thioredoxin, share a similar catalytic mechanism (**Figure 1.5**). It is believed that Class III enzymes share the first steps of the catalytic process with Class I and Class II members, but the mechanism by which formate acts as a reductant for the catalytic cysteines currently remains unknown.

The catalytic mechanism for Class I Rnrs is presented in **Figure 1.5**. Although more complicated catalytic schemes with many more small steps are present in the literature (Ge *et al.* 2003; Nordlund *et al.* 2006), this scheme was chosen for both brevity and simplicity (Zipse *et al.* 2009). The reader will now be presented with an introduction to the catalytic site and the amino acids which are important for catalysis of substrates to products: three cysteine residues, one glutamic acid, and one asparagine residue (**Figure 1.5**). Two of the conserved cysteines provide reducing equivalents for reduction of the ribonucleoside diphosphate substrates, while the third receives the free-radical from the small subunit and transfers it to the substrate during catalysis (Thelander 1974; Lin *et al.* 1987). The glutamate acts as a general acid-base during catalysis, accepting and donating a hydrogen atom from the 3'-OH (Lenz *et al.* 1997). Although the asparagine does not directly participate in any of the chemistry steps, it has been shown by site-directed mutagenesis to be essential for catalysis in Class I Rnrs (Kasrayan *et al.* 2002). The current hypothesis is that it stabilizes the other catalytic residues in the proper position
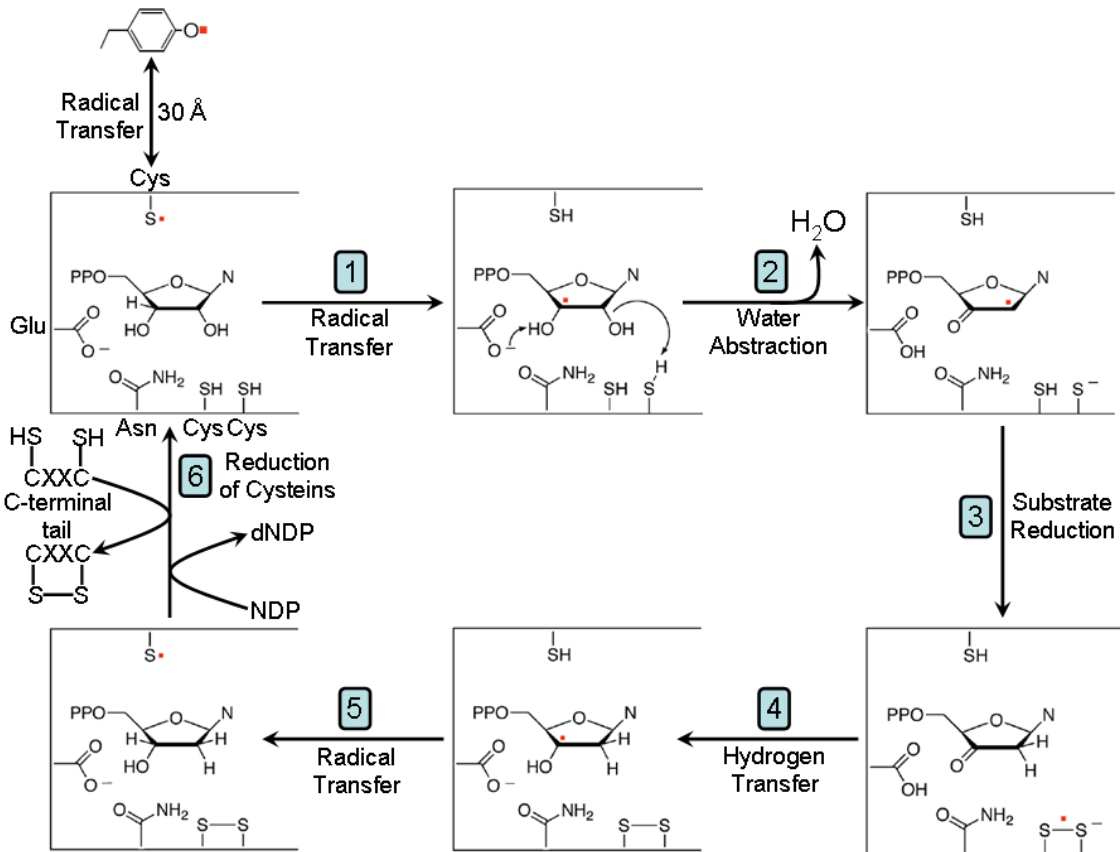
Figure 1.5: Catalytic mechanism for Class Ia Rnrs.
Five residues of the catalytic site are required for catalsis: three cysteines, one asparagine, and one glutamate. Free-radical is transferred from the small subunit on to one of the conserved cysteines in the catalytic site. The radical is transferred to the substrate and abstraction of water takes place. Following water abstraction, the substrate is further reduced by the remaining two catalytic cysteines, forming a disulfide bond. Hydrogren is transferred back onto the 3'-OH from glutamic acid and the free-radical is transferred back onto the original catalytic cysteine. Product is released, free-radical is transferred back to the small subunit for storage as a tyrosyl radical, and the disulfide bond is reduced by the C-terminal tail of the large subunit. PPO attached to the 5'-carbon of the sugar represents a diphosphate. N attached to the 1'-carbon of the sugar represents one of the four nitrogenous bases. The red dot indicates the position of the free-radical at during each step. This figure is adapted with permission from (Zipse *et al.* 2009). © 2009 American Chemical Society.

and orientation for catalysis to occur.

The substrate, which can be any of the four ribonucleoside diphosphates, must first bind to the catalytic site of the large subunit. After substrate binding occurs, the free-radical is transferred from the small subunit over a distance of 30 Å to the catalytic cysteine residue of the large subunit (**Figure 1.5**). Subtle conformational re-arrangements gate this step, which has been previously shown to be rate-limiting under pre-steady-state conditions (Ge *et al.* 2003). In Step 1, the free-radical is transferred from the cysteine residue onto the 3'-carbon of the substrate, extracting a hydrogen atom in the process (**Figure 1.5**). During Step 2, two processes occur: (1) the covalent bond between the 2'-OH and the 2'-carbon is cleaved and (2) a hydrogen atom from the 3'-OH is transferred onto the conserved glutamate residue (**Figure 1.5**). As the 2'-OH is abstracted from the substrate; it removes one hydrogen atom from one of the disulfide-forming cysteines, forms a water molecule, and joins the bulk solvent. Another consequence of the 2'-OH abstraction is the transfer of the free-radical from the 3'-carbon to the 2'-carbon. Step 3 results in the reduction of the 2'-carbon by one of the catalytic cysteines and formation of a free-radical containing disulfide bond (**Figure 1.5**). During Step 4, the catalytic glutamate releases its proton onto the 3'-OH group of the substrate and the free-radical is transferred onto the 3'-carbon atom (**Figure 1.5**). The free-radical is then transferred back to the original free-radical-bearing cysteine during Step 5, transferring the hydrogen it removed during Step 1 back on to the 3'-carbon. This forms the product, a 2'-deoxyribonucleoside diphosphate (**Figure 1.5**). To ensure that the free-radical does not decay, it is transferred back to the small subunit and stored as a stable tyrosyl radical. During Step 6, product dissociates from the catalytic site and the disulfide bond formed during Step 3 is reduced by the C-terminal tail of the large subunit

containing the consensus sequence CXXC, which has been shown rate-limiting under steady state conditions (Ge *et al.* 2003) (**Figure 1.5**). Chemical steps 2 through 5 take place so rapidly that electron paramagnetic resonance (EPR) experiments are unable to detect any change in the concentration of tyrosyl radicals on the small subunit, even under steady state conditions (Ge *et al.* 2003).

1.3.3 Catalytic Inhibitors of Class Ia Ribonucleotide Reductases

The catalytic cycle of ribonucleotide reductase is an ideal drug target for the treatment of cancers, viral, and bacterial infections. Sufficient levels of dNTPs are required for the rapid proliferation of both cancer cells and pathogenic bacteria/viruses. Creating imbalances in the dNTP pools or lowering the overall production of dNTPs so that the concentrations of dNTPs fall can halt replication or result in cell/viral/bacterial death. Here the reader will be presented with a description and discussion of Rnr inhibitors targeted at the catalytic activity of Rnr: (1) substrate analogues and (2) free-radical scavengers.

Substrate analogues of Rnr are ribonucleosides that are similar in molecular structure to the natural substrates and are usually modified at the 2' position where catalytic activity is centered (Thelander *et al.* 1976; Gallicchio 2005) (**Figure 1.6**). Modification of the 2' position is normally performed by substitution with halogen groups such as fluorine or chlorine. Inhibitors targeting the catalytic site of Rnr function either by causing the decay of the essential free-radical, by covalent modification of the catalytic cysteine residues, or by a combination of both (Pereira *et al.* 2004; Pereira *et al.* 2004; Pereira *et al.* 2006). Although many more substrate analogues exist,
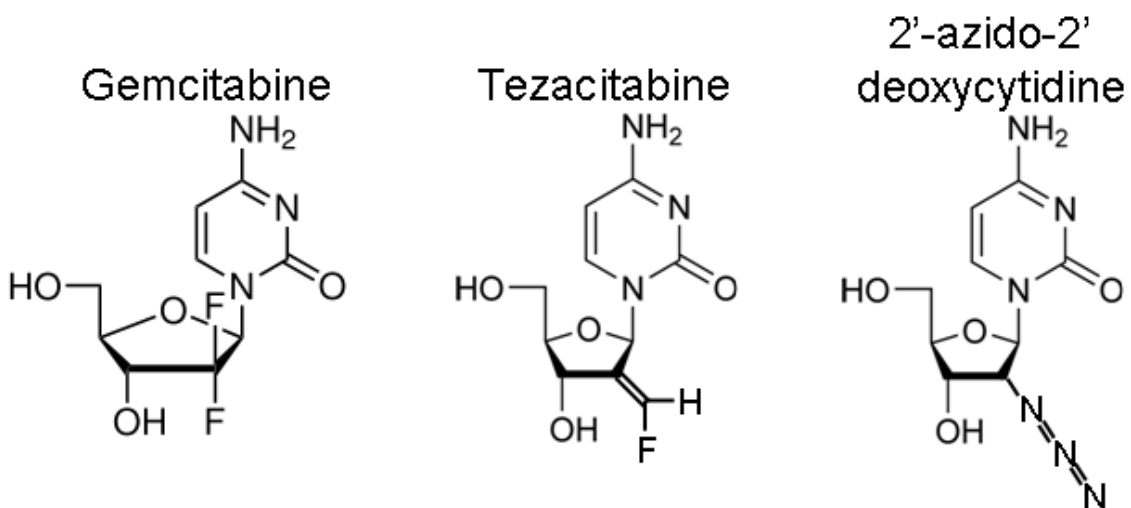
Figure 1.6: The chemical structures of three substrate analogues.
Three substrate analogues for Rnr are shown: gemcitabine, tezacitabine, and 2'-azido-2'-deoxycytidine. A majority of substrate analogues are substituted on their 2' position with halogens or other good leaving groups.

for brevity only a brief description of three will be presented here: (1) gemcitabine, (2) tezacitabine, and (3) 2'-azido-2'-deoxyribonucleosides.

Gemcitabine, 2',2'-difluorodeoxycytidine, is a cytidine-based substrate analogue with two fluorines substituted at the 2' position (**Figure 1.6**). It has been FDA approved for the treatment of ovarian, breast, pancreatic, and lung cancers (http://www.fda.gov/cder/foi/label/2006/020509s039lbl.pdf). The inhibition of Rnr activity by gemcitabine is caused by the decay of the tyrosyl radical on the small subunit and has been observed to alkylate the catalytic cysteine residues of the large subunit (Silva *et al.* 1998; van der Donk *et al.* 1998; Pereira *et al.* 2004). The free-radical becomes trapped on the drug molecule, and gemcitabine-based free-radical appears concurrent with the loss of tyrosyl radical on the small subunit (van der Donk *et al.* 1998). A crystal structure of the large subunit of Rnr from *S. cerevisiae* bound to gemcitabine shows that the orientation of gemcitabine in the catalytic site is altered from that of the natural substrate (Xu *et al.* 2006).

Tezacitabine, (E)-2'-fluoromethylene-2'-doxycitidine-5'-diphosphate, is another cytidine-based substrate analogue that has strong anti-proliferative properties against multiple cancer types which is currently undergoing clinical trails (Pereira *et al.* 2006) (**Figure 1.6**). Inactivation of Rnr is accomplished by accelerated free-radical decay and alkylation of catalytic site residues by the ribose analogue (van der Donk *et al.* 1996). Like gemcitabine, the appearance of a substrate-based free-radical is observed concurrent with the decay of the tyrosyl free-radical of the small subunit.

Substrate analogues with azido groups (R-N=N=N) substituted at the 2' position have also been observed to be mechanistic inhibitors of Rnr activity (Pereira *et al.* 2004). A 2'-azido-

2'-deoxycytidine is shown in **Figure 1.6**. Much like the previously described substrate analogues, 2'-azido modified substrates results in the decay of the tyrosyl free-radical on the small subunit and the covalent attachment of the substrate to one of the catalytic cysteine residues through a nitrogen atom (Fritscher *et al.* 2005).

Unlike the substrate analogues described above, free-radical scavengers act directly on the small subunit. They attack and cause the decay of the stable tyrosyl radical of the small subunit of Class Ia and Class Ib Rnrs. Hydroxyurea, a potent free-radical scavenger, was the first drug ever used against Rnr for the treatment of cancers, and is still used today (Stearns *et al.* 1963; Thurman *et al.* 1963; Saban *et al.* 2009). However, the high levels of hydroxyurea required for cancer chemotherapuetic treatment can cause undesired toxicities in the body (Woo *et al.* 2004; Randi *et al.* 2005; Strouse *et al.* 2008).

Free-radical scavengers are not only applicable to cancer treatment but also for combating infectious microbes. The free-radical scavenger N-methylhydroxylamine was recently found to be several hundred-fold more efficient than hydroxyurea at inhibiting the Rnr of *Bacillus anthracis* (Torrents *et al.* 2005). N-methylhydroxylamine was also a much more potent free-radical scavenger against the *B. anthracis* NrdF than it was against *H. sapiens* NrdB, providing selectivity against the small subunits of *B. anthracis*. Selectivity of free-radical scavenging agents against the small subunit of various pathogenic organisms and microbes provides an excellent path for designing less toxic antibiotic drugs targeted at their Rnr small subunits.

1.4 REGULATION OF CLASS Ia RIBONUCLEOTIDE REDUCTASES

Pools of dNTPs are tightly regulated in the cell, as an excess can cause misincorporation of nucleotides into newly synthesized DNA, and a deficiency will not allow for the repair of damaged DNA or synthesis of new DNA (Chabes *et al.* 2003). Either one of these results can lead to genomic instability and eventually to cancer or cell death (Chabes *et al.* 2003). Since Rnr is the primary source of dNTPs in cells, it is highly regulated by multiple mechanisms which include: (1) allosteric regulation by effector nucleotide binding (Beck *et al.* 1966; Eriksson *et al.* 1997; Uppsten *et al.* 2003; Larsson *et al.* 2004; Xu *et al.* 2006), (2) by oligomeric state (Kashlan *et al.* 2003; Wang *et al.* 2007; Rofougaran *et al.* 2008), (3) transcriptional regulation by repressors and activators (Huang *et al.* 1998; Zaim *et al.* 2005; Grinberg *et al.* 2009), (4) spatial regulation by cell compartmentalization (Yao *et al.* 2003; Lee *et al.* 2008; Pontarin *et al.* 2008; Wu *et al.* 2008), and (5) by small protein inhibitors (Zhao *et al.* 1998; Bondar *et al.* 2004; Uchiki *et al.* 2004; Hakansson *et al.* 2006). In the remainder of **Section 1.4**, the reader will be presented with a review of Rnr regulation by each of these mechanisms. First, allosteric and oligomeric regulation of Class Ia Rnrs via the binding of effectors to the specificity and activity sites will be presented, followed by short reviews on the regulation of Rnr in *S. cerevisiae* and *H. sapiens*.

1.4.1 Allosteric and Oligomeric Regulation

Ribonucleotide reductase must not only produce sufficient pools of the four dNTPs for replication and repair of DNA, but must keep those pools in balance. Class Ia Rnrs accomplish this unique balancing act through a very complex allosteric regulation scheme consisting of two separate effector-binding sites on the large subunit of Rnr. The α subunit of Class Ia Rnr houses three nucleoside-binding sites: (1) the catalytic site (C-site), (2) the specificity site (S-site), and

(3) the activity site (A-site) (**Figure 1.7**). The C-site binds the ribonucleoside diphosphates UDP, CDP, GDP, and ADP, which are catalyzed to their 2'-deoxyribonucleoside diphosphate counterparts by the enzyme (**Figure 1.8**). The S-site binds to the ribonucleoside triphosphate ATP and the 2'-deoxyribonucleoside triphosphates dATP, TTP, and dGTP, each of which causes unique structural rearrangements in the protein to select for binding of substrates at the C-site. The A-site binds to either ATP or dATP and serves as an overall activity regulator of Rnr; binding of dATP inhibits the activity of Rnr and binding of ATP stimulates activity.

First, allosteric regulation of substrate binding to the C-site via the S-site will be discussed. The selection rules for the catalysis of substrates in the C-site based on the binding of allosteric effector nucleosides to the S-site were first observed in the 1960s by the research group of Dr. Peter Reichard, and are conserved across all three classes of Rnrs (Larsson *et al.* 1966). The binding of ATP at the S-site selects for the binding and reduction of the pyrimidines CDP and UDP (**Figure 1.8**). The product dUDP is then processed to dUMP by dUTP diphosphohydrolase and further catalyzed by thymidylate synthetase and nucleoside kinase enzymes to produce TTP (**Figure 1.4**). Binding of TTP to the S-site selects for the binding and reduction of the purine GDP in the C-site (**Figure 1.8**). Nucleoside diphosphate kinases convert dGDP to dGTP. dGTP then binds to S-site to select for the binding and catalysis of the purine ADP at the C-site (**Figure 1.8**). Conversion of dADP to dATP is accomplished via NDKs, followed by inhibition of Rnr activity by binding of dATP to the A-site (**Figure 1.8**).
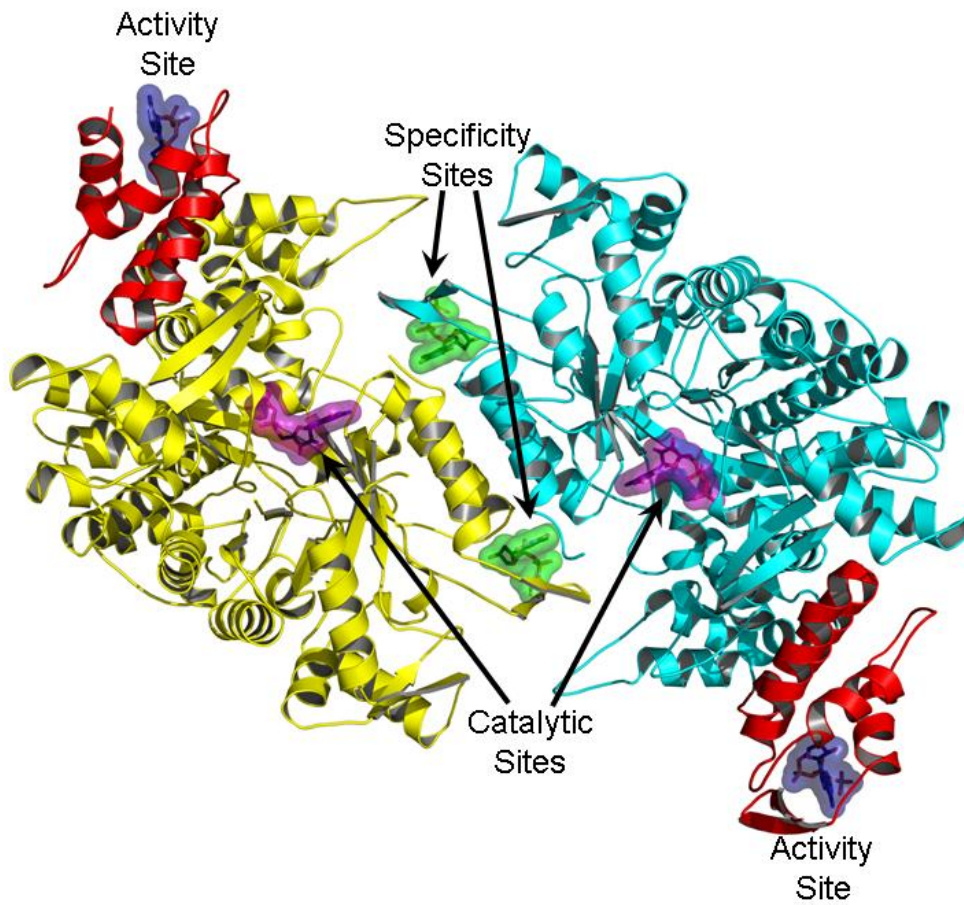
Figure 1.7: X-ray crystal structure of a Class Ia Rnr large subunit dimer.
The X-ray crystal structure of the large subunit of the Class Ia Rnr from *H. sapiens* is shown in ribbon format. One monomer of the dimer is colored yellow and the other monomer is colored cyan. The location of the catalytic site is indicated with a magenta surface, the location of the specificity site is indicated with a green surface, and the location of the activity site is indicated with a blue surface. The ATP-binding cone domain, present in Class Ia Rnrs but absent in Class Ib Rnrs, is shown in red.
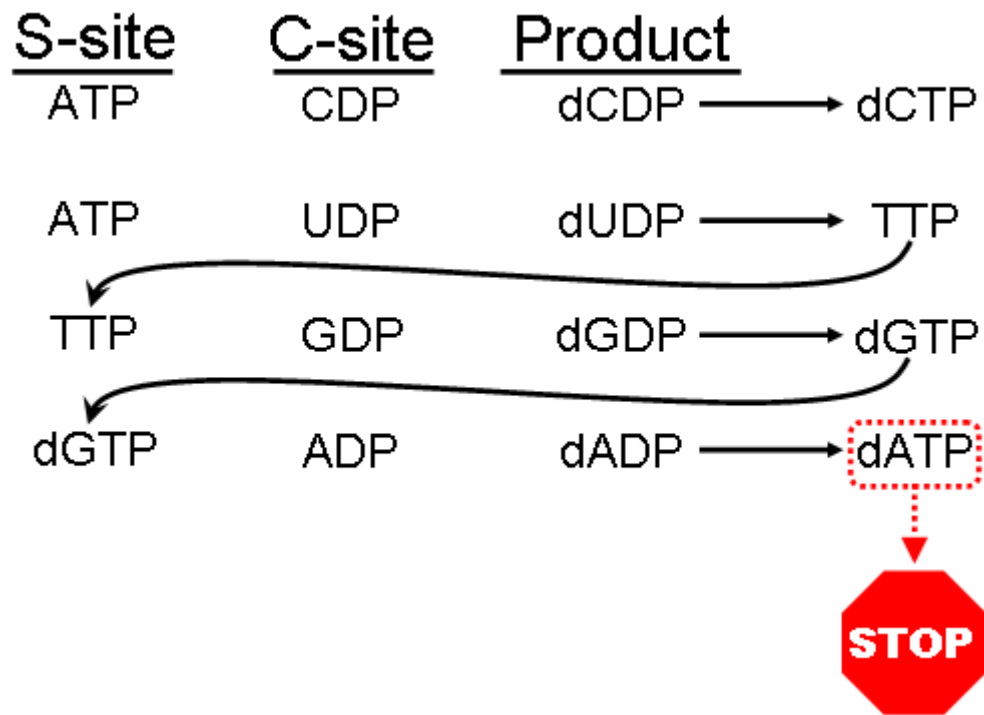
Figure 1.8: Allosteric regulation pathway for Class Ia Rnr.
Binding of ATP or dATP to the S-site leads to the reduction of CDP and UDP substrates. TTP binding to the S-site leads to the selection of GDP. dGTP binding at the S-site then selects for ADP at the C-site, leading to elevated levels of dATP. dATP eventually reaches a critical level, binds to the overall activity site, and inhibits the activity of Rnr.

Recently, a series of X-ray crystal structures of the large subunit of members of Class Ia, Class Ib, Class II, and Class III Rnrs with the S-site occupied by each of the four effector nucleoside triphosphates confirms the selection rules that were observed with biochemical experiments (Eriksson *et al.* 1997; Larsson *et al.* 2001; Uppsten *et al.* 2003; Larsson *et al.* 2004; Xu *et al.* 2006). However, only the allosteric regulation in Class Ia enzymes will be considered here. Allosteric control of the C-site by the S-site is accomplished through two regulatory loop regions of the protein, named loop 1 and loop 2 (**Figure 1.9A**). Loop 1 is involved solely in the binding of effector nucleoside triphosphates to the S-site, with specificity cross-talk between the two sites taking place on loop 2. Depending upon the effector bound to the S-site, residues that make up loop 2 undergo a series of distinct structural conformations which select for the binding of substrate in the C-site (**Figure 1.9B**). The conformation of loop 2 for each effector-substrate pair is completely unique. The binding of substrates in the C-site is also able to alter the conformation of loop 2, a phenomenon which has been termed "specificity cross-talk" (Xu *et al.* 2006).

The overall activity of Class Ia and Class III Rnrs is further controlled by the presence of an ATP-binding cone at their N-termini, referred to as the A-site (**Figure 1.7**). This allosteric site serves as an on-off switch for the enzyme and allows for feed-back inhibition (**Figure 1.8**). Binding of ATP to this four-helical bundle results in an increase in the activity of the enzyme, and binding of dATP results in inhibition of the activity of the enzyme. Mutations of residues in the ATP-binding cone from multiple species have been observed which lack the ability to be inhibited by dATP, but are still activated by ATP
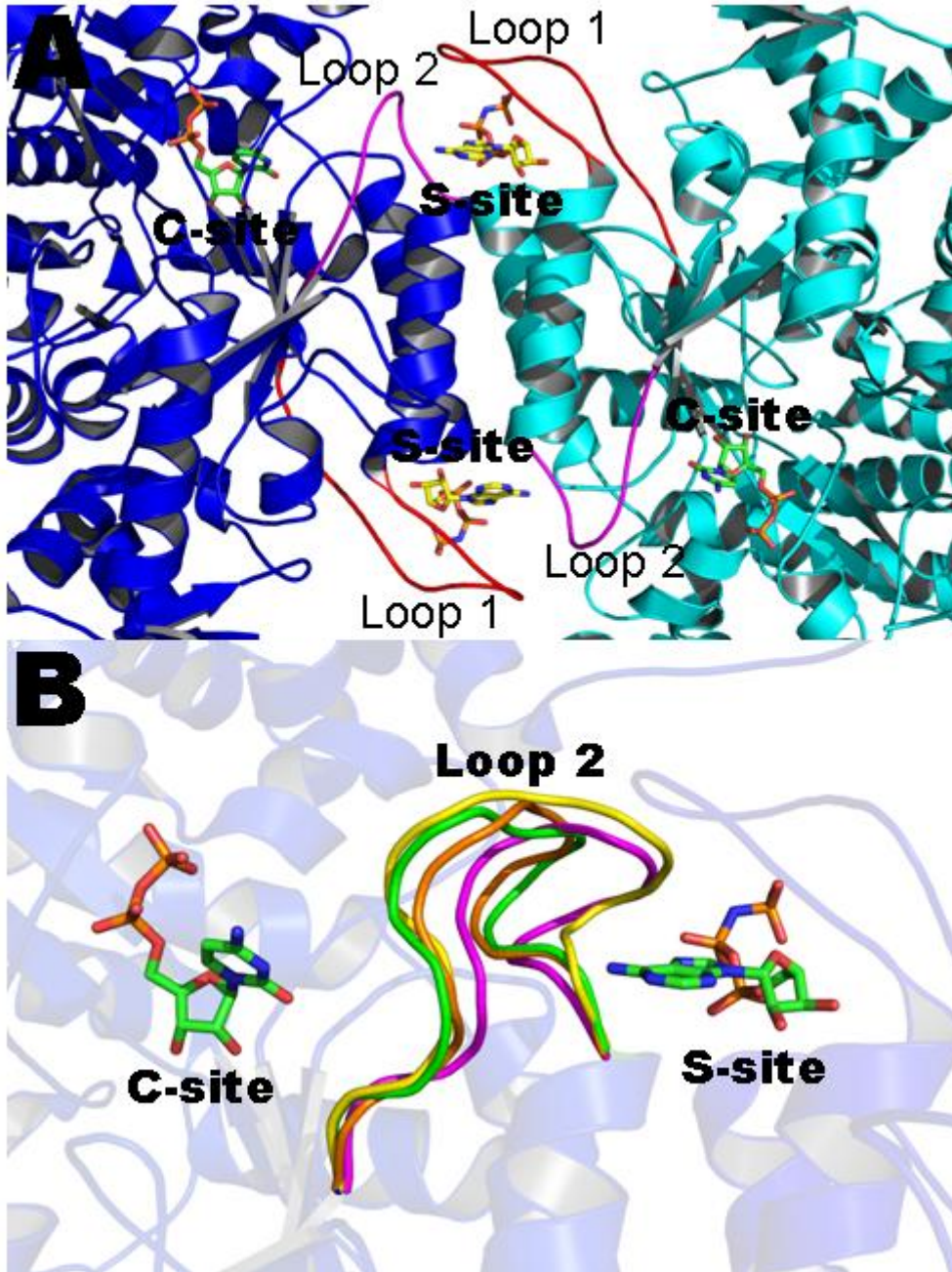
Figure 1.9: Allosteric regulation of the C-site by the S-site.
(A) A dimer of *S. cerevisiae* Rnr1p bound to AMPPNP (yellow carbons) and CDP (green carbons). Loop 1 is colored in red and loop 2 is colored in magenta. One dimer is cyan and the other is blue. **(B)** Unique structural conformations of loop 2 in *S. cerevisiae* Rnr1p when bound to AMPPNP-CDP (green), ANPPNP-UDP (orange), TTP-GDP (yellow), and dGTP-ADP (magenta). CDP is shown in the C-site and AMPPNP is shown in the S-site, both with green carbon atoms, blue nitrogen atoms, red oxygen atoms, and orange phosphorous atoms.

26

(Reichard *et al.* 2000; Roshick *et al.* 2000; Birgander *et al.* 2004; Torrents *et al.* 2006). The binding of the ATP analogue 5'-adenylyl-β-γ-imidodiphosphate (AMPPNP) to the A-site of *E. coli* Rnr1 has been characterized by X-ray crystallography (Eriksson *et al.* 1997). However, the natural ligands ATP and dATP have never been described binding to the A-site of any Class Ia or Class III Rnr. The large subunit of Rnr from *H. sapiens* was crystallized and X-ray crystal structures of the A-site occupied by both ATP and dATP were obtained, which is one of the subjects of **Chapter 4**.

Recently, the regulation of Rnr by the oligomerization of the large subunit has become apparent in Class Ia family members. In the absence of any allosteric effector nucleosides, the large subunit of Class Ia Rnrs exists as an inactive monomeric species. Binding of ATP, dATP, TTP, or dGTP to the S-site induces dimerization and formation of catalytically active heterotetramers ($\alpha_2\beta_2$) with a dimer of the small subunit. Formation of higher order oligmers have been observed when the A-site is occupied by either ATP or dATP (Kashlan *et al.* 2003; Rofougaran *et al.* 2006; Rofougaran *et al.* 2008).

The active form of the *E. coli* Class Ia Rnr has been shown to be an $\alpha_2\beta_2$ heterotetramer in the presence of ATP and other effectors that bind to the S-site. However, in the presence of dATP, formation of inactive $\alpha_4\beta_4$ hetero-octamers was induced by the binding of dATP to the α subunit (Rofougaran *et al.* 2008). The outcome of experiments with mouse Rnrs has also shown oligomerization-based regulation upon binding of either ATP or dATP to the A-site (Kashlan *et al.* 2002). Cooperman's group has shown that binding of ATP and dATP to the A-site induced the formation of both active and inactive α_4 oligomers. In addition, he hypothesizes that the formation of hexamers of the large subunit requires the binding of ATP, but not dATP, to an

27

additional allosteric site referred to as the H-site (Kashlan *et al.* 2003). However, no biochemical evidence for such a site exists, and the formation of dATP-induced hexameric species has been observed by several groups, including ours, which would not be possible according to his model (see **Chapter 4**) (Rofougaran *et al.* 2006).

In contrast to the results of Cooperman, (Rofougaran *et al.* 2006) were able to observe the formation of both ATP and dATP-induced hexamers (α_6) of mouse Rnr at concentrations of effectors that were significantly lower than those reported in (Kashlan *et al.* 2002; Kashlan *et al.* 2003). Both the ATP and dATP-induced hexamers were also observed binding to dimers of the small subunit, forming $\alpha_6\beta_2$ octamers. The anti-cancer drug gemcitabine, a substrate analogue (see **Section 1.3.3**), has also been shown to induce the formation of α_6 oligomers of the large subunit of human Rnr (Wang *et al.* 2007). In **Chapter 4**, nucleotide-dependent oligomerization will be further explored, and a comprehensive model for oligomerization of the large subunit of human Rnr will be provided.

1.4.2 Ribonucleotide Reductase and its Regulation in S. cerevisiae

In the budding yeast *S. cerevisiae*, there are two loci that encode large subunits, known as *Rnr1p* and *Rnr3* (Elledge *et al.* 1990), and two genetic loci that encode the small subunit, known as *Rnr2* and *Rnr4* (Elledge *et al.* 1987; Hurd *et al.* 1987; Huang *et al.* 1997). The two proteins Rnr1p and Rnr2p share the most homology with large and small subunits from other organisms, while Rnr3p and Rnr4p are yeast-specific homologues of the α and β subunits, respectively. In other eukaryotic organisms, the simplest active oligomeric configuration is an $\alpha_2\beta_2$ heterotetramer, but in *S. cerevisiae* the active configuration consists of an $\alpha_2\beta\beta'$ heterotetramer where α is Rnr1p, β is Rnr2p, and β' is Rnr4p.

Deletion of the *Rnr4* gene is lethal to many strains of yeast and is essential for the formation and transfer of free radicals from Rnr2p to the large subunit (Elledge *et al.* 1987; Huang *et al.* 1997; Wang *et al.* 1997). Purified Rnr2p has no enzymatic activity when combined together with purified Rnr1p *in vitro* and contained no detectable tyrosyl radical (Torrents *et al.* 2008). Rnr4p lacks several of the conserved amino acids which are required for the binding of iron and can not form tyrosyl free-radicals on its own (Wang *et al.* 1997). The formation of stable tyrosyl radicals on Rnr2p requires the presence of Rnr4p, however the mechanism by which Rnr4p assists Rnr2p in radical formation is still unclear (Chabes *et al.* 2000; Voegtli *et al.* 2001). Current hypotheses suggest that Rnr4p assists in the proper folding of Rnr2p or that Rnr4p assists in the loading of iron onto Rnr2p. Rnr2p and Rnr4p have the ability to form both homodimers (β'_2 and β_2) and heterodimers ($\beta\beta'$) both *in vivo* and *in vitro*, and X-ray crystal structures are available for all three of these oligomeric states (Voegtli *et al.* 2001; Sommerhalter *et al.* 2004).

The role Rnr3p plays in the yeast cell is not clear as Rnr1p is the major active large subunit in *S. cerevisiae*. Rnr3p is expressed at extremely low levels during normal cell growth, but under conditions where DNA damage occurs or when cells experience stress, its expression is up-regulated 50-100 fold (Domkin *et al.* 2002). Null mutations of Rnr3p in *S. cerevisiae* cells result in no phenotypic effects, even after DNA damage when it is being expressed at the highest levels. However, over-expression of Rnr3p is able to rescue yeast cells which have a null mutation for Rnr1p (Domkin *et al.* 2002).

Yet another caveat of Rnr from *S. cerevisiae* is the presence of the small protein inhibitor Sml1p. It binds to and inhibits the large subunit of Rnr by an as yet to be described mechanism

(**Figure 1.10**). However, recent work using yeast two hybrid experiments suggests that Sml1p may compete with the C-terminus of Rnr1p for access to the catalytic site (Zhang *et al.* 2007). In response to DNA damage or replication blocks, Sml1p is phosphorylated by Dun1 kinase and degraded to relieve the inhibition of Rnr, which then allows for the production of dNTPs for DNA repair or replication (Zhao *et al.* 1998; Chabes *et al.* 1999; Zhao *et al.* 2002; Uchiki *et al.* 2004) (**Figure 1.10**). Sml1p has no known homologues in any other organism, although a small protein called Spd1 from *Schizosacchromyces pombe* has been recently discovered to have a similar inhibitory effect on the large subunit of Rnr (Hakansson *et al.* 2006).

The transcription of Rnr genes is also heavily regulated in *S. cerevisiae*. The transcriptional repressor Crt1 binds to the upstream regions of Rnr genes, called X-boxes, where it recruits the general transcriptional repressors Tup1 and Ssn6 (Huang *et al.* 1998) (**Figure 1.10**). Transcriptional inhibition of Rnr genes is relieved by the hyper-phosphorylation of Crt1 in a Dun1 dependent manner. Phosphorylated Crt1 no longer binds DNA and transcriptional activators can access the Rnr genes, leading to up-regulation of the transcription of Rnr genes (Huang *et al.* 1998) (**Figure 1.10**). Another protein named Crt10 has also recently been discovered to be involved in the transcriptional regulation of Rnr genes, although the mechanism by which it functions is not as well understood as Crt1 (Fu *et al.* 2006). However, it is known that Crt10 is also downstream of Dun1 kinase of the Mec1/Rad53/Dun1 pathway.
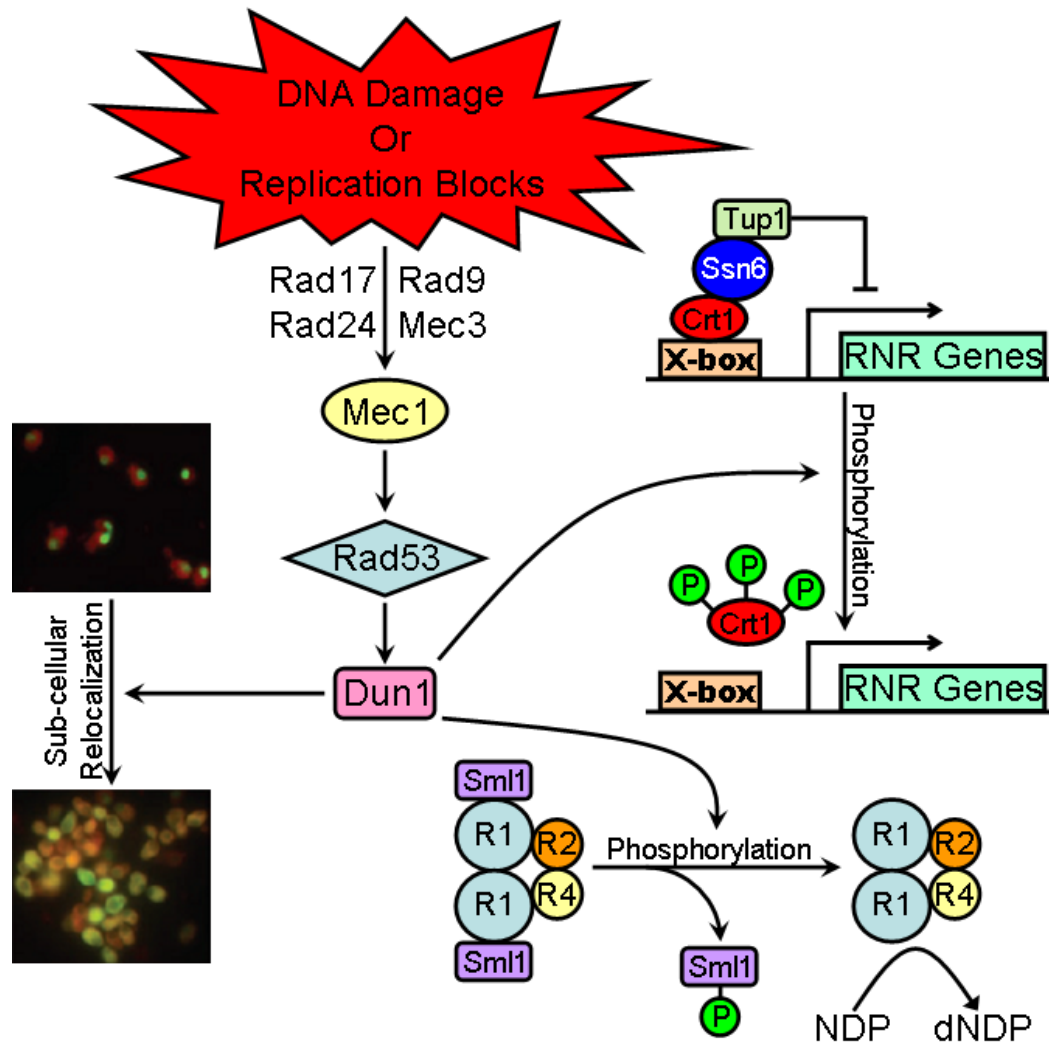
Figure 1.10: Regulation of *S. cerevisiae* Rnr by the Mec1/Rad53/Dun1 pathway.
The Mec1/Rad53/Dun1 pathway regulates Rnr via multiple methods. Dun1 directly phosphorylates the small protein Sml1p leading do its degradation by the proteasome. Degradation of Sml1p relieves inhibition of Rnr, activating the catalysis of NDPs to dNDPs. Crt1 recruits the general inhibitors Ssn6 and Tup1 to inhibit the transcription of Rnr genes. Crt1 is hyper-phosphorylated in a Dun1 dependent manner, relieving transcriptional inhibition of Rnr genes. The small subunits (shown in green) are relocated from the nucleus to the cytoplasm in a Dun1 dependent manner, forming active Rnr complexes with the large subunits (shown in red) in the cytoplasm. Fluorescence microscopy figures were adapted with permission from (Yao *et al.* 2003). © 2003 National Academy of Sciences.

Yet another regulatory pathway for Rnr in *S. cerevisiae* is the compartmentalization of

the large and small subunits (Yao *et al.* 2003). When cells are not in S-phase, Rnr1p is localized

to the cytoplasm and heterodimers of the small subunit are targeted for import into the nucleus

by the protein Wtm1, a beta propeller protein which is also a transcriptional regulator in yeast. Nuclear localization is accomplished via the nuclear envelope importin protein Kap122 (Pemberton *et al.* 1997; Lee *et al.* 2006; Zhang *et al.* 2006). After import into the nucleus via Wtm1 and Kap122, the small subunits are anchored inside the nucleus by the protein Dif1 (Wu *et al.* 2008). After DNA damage or when dNTP levels are too low, Dun1 directly phosphorylates Dif1, leading to its degradation (Lee *et al.* 2008). The small subunits are then relocalized to the cytoplasm to form active holoenzymes with the large subunit so that production of dNTPs can occur (**Figure 1.10**).

1.4.3 Ribonucleotide Reductase and its Regulation in Mammalian Species

In humans and other mammalian species such as mice, there is one known genetic locus that encodes the large subunit *Rnr1*, and two known genetic loci that encode the small subunit *Rnr2* and *p53R2* (Liu *et al.* 2008). Rnr1 and Rnr2 are the normal functional α and β that are the most homologous to the large and small subunits of other species.

The small subunit p53R2, which is 80% similar to Rnr2, is unique to humans and other mammalian species and was first discovered and described by (Tanaka *et al.* 2000). As its name suggests, expression of p53R2 is controlled downstream of the tumor suppressor p53 in response to DNA damage and oxidative stress (Yamaguchi *et al.* 2001). It is also expressed at low levels in quiescent cells that have not undergone DNA damage (Hakansson *et al.* 2006). Mice with null mutations for p53R2 grow normally for 6 weeks but then die shortly after from renal failure (Kimura *et al.* 2003; Powell *et al.* 2005), and mutations of p53R2 in the human population result in severe mitochondrial DNA depletion (Bourdon *et al.* 2007). Studies of p53R2 *in vitro* have shown that it has the ability to substitute for Rnr2, forming functional hetero-oligomers with

Rnr1 that reduce ribonucleoside diphosphate substrates (Guittet *et al.* 2001; Shao *et al.* 2004). Recently published data suggest that the main function of p53R2 is to provide low levels of dNTPs to quiescent non-proliferating cells for both the repair of genomic DNA and the replication of mitochondrial DNA (Liu *et al.* 2008; Pontarin *et al.* 2008). In addition, several groups have suggested that p53R2 is also involved in free-radical scavenging and oxidative stress response (Guittet *et al.* 2008; Liu *et al.* 2008).

Early studies on the compartmentalization of Rnr subunits in mammalian cells concluded that in response to DNA damage or during S-phase, the Rnr subunits were all sequestered into the nucleus (Xue *et al.* 2003; Liu *et al.* 2005). However, a recently published study has established unequivocally by several independent methods, that Rnr1, Rnr2, and p53R2 are all localized to the cytoplasm and never undergo relocalization, even after DNA damage or during S-phase (Pontarin *et al.* 2008). Instead, ribonucleotide reduction is under tight control by cell cycle-dependent degradation and transcription of the Rnr2 subunit (Johansson *et al.* 1998; Chabes *et al.* 2000; Chabes *et al.* 2004). During S-phase, the Rnr2 is expressed at high levels, allowing the production of a large amount dNTPs for replication of genomic DNA. A KEN-box on the N-terminus of the Rnr2 subunit is recognized by the Cdh1-anaphase-promoting complex during the M-phase. After recognition, Rnr2 becomes poly-ubiquitinated, targeting it for degradation by the proteasome (Chabes *et al.* 2003). On the other hand, p53R2 lacks the KEN box and is not degraded during M-phase. Cells in G_0/G_1 contain only p53R2; cells in S-phase and G_2-phase contain both Rnr2 and p53R2; and cells in M-phase target Rnr2 for degradation, leaving only p53R2.

1.5 CURRENT RNR STRUCTURAL INFORMATION

In this section, the focus will be on the X-ray crystal structural information currently available in the Rnr research field. The Research Collaboratory for Structural Bioinformatics (RCSB) Protein Data Bank (PDB) database was polled for X-ray crystal structures of both large and small subunits of Rnr. All currently available structures are compiled in **Table 1.1**. This list is truncated in that many structures of both the large and small subunits have been solved with either site-directed mutants or in different oxidation states. Although information about the small subunit is provided in **Table 1.1**, the discussion will stay focused on structures of the large subunit.

The first structure of the large subunit of Rnr from any organism to be solved by X-ray crystallography was that of the Class Ia *E. coli* enzyme in 1994 (Uhlin *et al.* 1994). Co-crystallization of *E. coli* NrdA with the C-terminal 20-mer peptide of *E. coli* NrdB was required to obtain well ordered crystals at reasonable resolutions. This initial structure did not contain any allosteric effectors or substrates bound to it. However, the location of the catalytic site was identifiable using previous biochemical and mutagenesis data as a guide. The location of effector binding sites and detailed information about the binding of allosteric effectors and substrates would remain a mystery until 1997 when the structure of *E. coli* NrdA was solved with the allosteric effector TTP bound to the S-site, AMPPNP in the A-site, and the substrate GDP in the C-site (Eriksson *et al.* 1997). This structure revealed for the first time the role of the regulatory loops, Loop 1 and Loop 2, in

Table 1.1: Structures of α and β subunits currently deposited in the PDB database.

Species	Class	α PDB ID	β PDB ID	Publication Reference
E. coli	Ia	1RLR (R2-peptide)		(Uhlin *et al.* 1994)
		2R1R (TTP)		(Eriksson *et al.* 1997)
		3R1R (AMPPNP)		
		4R1R (TTP-GDP)		
			1RIB	(Nordlund *et al.* 1993)
S. cerevisiae	Ia	1ZZD (apo)		(Xu *et al.* 2006)
		2CVT (AMPPNP)		
		2CVU (AMPPNP-CDP)		
		2CVV (AMPPNP-UDP)		
		2CVW (TTP-GDP)		
		2CVX (dGTP-ADP)		
		2CVY (R2-peptide)		
			1SMS (R4 dimer)	(Sommerhalter *et al.* 2004)
			1SMQ (R2 dimer)	
			1JK0 (R2-R4)	(Voegtli *et al.* 2001)
M. musculus	Ia		1XSM	(Kauppi *et al.* 1996)
H. sapiens	Ia	**TTP**		**This Study**
		TTP-GDP		
		TTP-ATP		
		TTP-dATP		
			2UW2 (R2)	Structural Genomics Group
			2VUX (p53R2)	
S. typhimurium	Ib	1PEM (apo)		(Uppsten *et al.* 2003)
		1PEO (dCTP)		
		1PEQ (TTP)		
		1PEU (dATP)		
		2BQ1 (dGTP)		
		2BQ1 (Holo Complex)	1R2F	(Uppsten *et al.* 2006)
P. vivax	Ia		2O1Z	Currently Unpublished
M. tuberculosis	Ib		1UZR	(Uppsten *et al.* 2004)
B. halodurans	Ia	2RCC (apo)		Structural Genomics Group
C. ammoniagenes	Ib		3DHZ	(Andersson *et al.* 2004)
T. maritima	II	1XJF (dATP)		(Larsson *et al.* 2004)
		1XJM (TTP)		
		1XJJ (dGTP)		

Table 1.1 continued.

Species	Class	α PDB ID	β PDB ID	Publication Reference
T. maritima	II	1XJE (TTP-GDP)		(Larsson *et al.* 2004)
		1XJG (dATP-UDP)		
		1XJK (dGTP-ADP)		
		1XJN (dATP-CDP)		
L leichmannii	II	1L1L (apo)		(Sintchak *et al.* 2002)
Bacteriophage T4	III	1H7B (apo)		(Larsson *et al.* 2001)
		1H78 (dCTP)		
		1HK8 (dGTP)		
		1H79 (TTP)		
		1H7A (dATP)		
B. subtilis	III		1RLJ (nrdI)	Currently Unpublished

PDB is the protein data bank, which can be found at http://www.pdb.org

substrate selection at the C-site. However, many questions remained unanswered. How did the binding of different nucleotides at the S-site cause the protein to bind different substrates as the C-site? How do the natural substrates ATP and dATP bind to the A-site?

The next large subunit to have its X-ray crystal structure solved was the Class III NrdD from the bacteriophage T4 (Larsson *et al.* 2001). This structure showcased the binding of all four nucleotide effectors to an S-site that was distinctly different from that of the Class Ia enzyme. The dimer of Class III enzymes was oriented quite differently from that of Class Ia enzymes. These structures were also able to show the binding of substrates to Class III Rnrs. Class Ib NrdE from *S. typhimurium* was the next large subunit to have its structure solved (Uppsten *et al.* 2003). X-ray crystal structures of the large subunit from *S. typhimurium* bound to all four of the allosteric effectors at the S-site provided a much-improved picture of the allosteric mechanisms taking place between the S-site and the C-site in Class I Rnrs, but the structure of a

Class I or Class II large subunit bound to both substrates and effectors simultaneously still remained elusive.

The first Class II NrdJ to have its X-ray crystal structure solved was that of the bacteria *L. leichmannii* (Sintchak *et al.* 2002). NrdJ from this species contains a large amino acid insert that mimics the presence of a dimer and allows for the selection and catalytic turnovers to occur in monomeric form. In addition, the binding site of B_{12} was identified via the binding of the analogue adeninylpentyl cobalamin. In 2004, the structure of the large subunit from the Class II NrdJ from *T. maritima* bound to the substrate-effector pairs dATP-CDP, dATP-UDP, TTP-GDP, and dGTP-ADP was solved (Larsson *et al.* 2004). Finally, the mechanism by which the S-site and C-site communicate with one another was elucidated; Loop 2 adopts a unique conformation depending on the substrate and effector bound at the C- and S-sites. Yet another question was initiated with the publishing of these structures: did allosteric regulation in Class Ia enzymes follow the same mechanism of Class II Rnrs?

This question was answered two years later with the publishing of the Class Ia NrdA from *S. cerevisiae* bound to all four effector-substrate pairs (Xu *et al.* 2006). Effector-substrate communication was found to be similar to that of the Class II NrdJ; however the binding of the C-terminal peptide of small subunits from mammalian Rnrs was revealed to be quite different from that of bacterial Rnrs (Xu *et al.* 2006). The holo complex of the Class Ib NrdE-NrdF from *S. typhimurium* was also solved in 2006 (Uppsten *et al.* 2006). However, the information from this structure does not agree with biophysical data in the literature. For example, the distance between the stable tyrosyl radical and the catalytic cysteine has been measured to be between 30 and 35 Å by EPR experiments, but the distance from the tyrosine to the catalytic cysteine is

greater than 40 Å in the holo complex crystal structure. Rather, this structure is believed to be an intermediate on the pathway to the holo-complex.

Structures of the large subunits from all three classes of Rnrs share a common catalytic core: a 10 stranded α/β barrel. The location of the catalytic and allosteric sites are also conserved across classes. This suggests that all three classes of Rnrs have evolved from a common ancestral Rnr (Stubbe *et al.* 2001). Class III family members are probably the most ancient. Organisms harboring Class III Rnrs could thrive in the early-earth environment where oxygen was absent. They also require the system with the least-complicated chemistry for generation of the free-radical and reduction of the catalytic cysteines. Class II was most likely second: the presence of oxygen in the atmosphere destroys Class III Rnrs, requiring a new method for the production of dNTPs that was tolerant to presence of oxygen. Eventually, Class I enzymes would evolve late in the evolutionary time-period which require the presence of oxygen. This theory is further confirmed by the distribution of the classes of Rnrs throughout species. More complex eukaryotic mammalian organisms all carry Class I Rnrs, bacteria can carry any of the three classes, and a majority of archaebacteria carry only class III Rnrs.

1.6 OBJECTIVES AND IMPACT OF THIS DISSERTATION RESEARCH

Perturbations of cellular dNTP pools have been shown to be mutagenic in many cell types across multiple organisms (Chan *et al.* 1981; Weinberg *et al.* 1981; Ayusawa *et al.* 1983; Roguska *et al.* 1984; Chabes *et al.* 2003). Over-abundance of dNTPs leads to misincorporation of nucleotides into newly synthesized DNA, and inadequate levels of dNTPs will not allow for the repair or synthesis of DNA. As the sole source of deoxynucleosides produced from *de novo* sources, Rnr is one of the most heavily regulated proteins in the cell. Dysregulation of Rnr can

lead to over-production, underproduction, or imbalanced production of deoxyribonucleosides, all of which can lead to genomic instability or even cell death. Due to its central role in the cellular replication of all organisms, Rnr is an ideal drug target in diseases where rapid proliferation is required, such as cancer.

Another source of genomic instability in the cell is the presence of deficient mismatch repair (MMR) machinery genes, which can lead to carcinogenesis. In fact, many cancer types are known to harbor defective or missing MMR genes including leukemias, lymphomas, myelomas, brain, breast, prostate, testis, lung, ovary, stomach, colon, skin, liver, and pancreatic cancers (DeWeese *et al.* 1998; Abuin *et al.* 2000; Whiteside *et al.* 2002; Vaish *et al.* 2005; Vaish 2007). In addition, defective MMR machinery can result in resistance to commonly used anti-cancer chemotherapeutic drugs, and relapses can occur even after long treatment regimes (Branch *et al.* 2000; Vaish 2007). Julian Simon's group at the Fred Hutchinson Cancer Research Center recently discovered several alleles of the large subunit of Rnr in *S. cerevisiae* which result in a lethal phenotype when expressed in genetic backgrounds where MMR is also deficient. The main objective of this dissertation research presented in **Chapter 3** is the elucidation of the molecular mechanisms that govern the mismatch repair synthetic lethal (*msl*) phenotype in *S. cerevisiae* cells harboring the mutant *Rnr1p* alleles *rnr1*^{S269P} and *Rnr1*^{S610F}. Combined with data from Dr. Simon's study, this dissertation research suggests a new therapeutic approach involving dysregulation rather than inhibition of Rnr activity as a treatment strategy for MMR-deficient cancer types.

The focus of this dissertation research in **Chapter 4** is on the X-ray crystal structures of the large subunit of Rnr from *H. sapiens*, the first mammalian Rnr1 to have its X-ray crystal

structure solved, bound to TTP, TTP●GDP, TTP●ATP, and TTP●dATP. The crystal structures of hRRM1●TTP●ATP and hRRM1●TTP●dATP provide a structural basis for the difference in ATP and dATP binding at the A-site and insight into the oligomeric regulation of Rnr. Finally, a low-resolution X-ray crystal structure of the large subunit of Rnr from *S. cerevisiae* as a dATP-induced hexamer combined with size exclusion chromatography data provides a model for regulation of the large subunit of Rnr by dATP-induced oligomerization.

2. MATERIALS AND METHODS

2.1 SITE-DIRECTED MUTAGENESIS

Point mutations were made using the Quick-Change Site-Directed Mutagenesis Kit (Stratagene, La Jolla, CA). Each mutagenesis PCR was 50 μL in volume and consisted of the following: 4 μL dNTP mix containing 100 mM of each nucleotide, 2.5 μL of each mutagenesis primer (5 μL total) at a concentration of 10 μM, 5 μL of 10X reaction buffer, 1 μL of cloned Pfu polymerase (Stratagene, La Jolla, CA), 100 ng of template DNA, and then molecular biology grade water was added until the total volume reached 50 μL. Primers used for each mutagenesis reaction can be found in **Table 2.1**.

For all mutagenesis PCRs, a PCR program with gradient annealing temperatures on an MJ Mini Personal Thermal Cycler (Biorad, Hercules, CA) was used. The first step was incubation at 95°C for 2 minutes followed by 30 cycles of 95°C for 30 seconds, 52-65°C annealing for 30 seconds, and 72°C for 8 minutes. After the 30 cycles were over, the reactions were allowed to incubate at 72°C for 5 minutes and then were stored at 4°C. Following the PCR reaction, a Dpn I (New England Biolabs, Ipswich, MA) digest was performed to destroy the parental DNA and ensure that only mutated plasmids remained. Digested samples were then transformed into Max Efficiency DH5α (Invitrogen, Carlsbad, CA) *E. coli* competent cells, plated onto LB with the proper antibiotic, and incubated overnight at 37°C. The following morning, colonies were picked and scaled up into 10 mL cultures of LB containing the proper antibiotic and plasmid DNA was purified using the Wizard SV Miniprep kit (Promega, Madison, WI). Purified plasmid DNA was sequenced at the Molecular Biology Research Facility (MBRF) on the University of Tennessee campus to confirm the presence of the site-directed mutations.

Table 2.1: Forward and reverse PCR primers used for site-directed mutagenesis

	Mutation	Primer Sequence
Forward Primer	S269P	5'-GGTACAAACGGTACT**CCT**AACGGTTTAATTCC-3'
Reverse Primer		5'-GGAATTAAACCGTT**AGG**AGTACCGTTTGTACC-3'
Forward Primer	S610F	5'-CCAATGCCCTACTGCA**TTC**ACATCCCAAATATTGGG-3'
Reverse Primer		5'-CCCAATATTTGGGATGT**GAA**TGCAGTAGGCATTGG-3'

The location of mutations in the primers are marked with a bold red font.

2.2 PROTEIN CONCENTRATION DETERMINATIONS

Protein concentrations were determined via the Bradford Assay (Bradford 1976), using the Bio-Rad Protein Assay Kit (BioRad, Hercules, CA) or the Coomassie Plus Protein Assay Reagent Kit (Pierce Biochemicals, Rockford, IL). Bovine serum albumin (BSA) of a known concentration was used as the protein to create the standard curve for these assays. For *S. cerevisiae* Rnr1p and hRRM1, the concentrations were determined by measuring their absorbance at a wavelength of 280 nm as described in (Pace *et al.* 1995). Concentration determinations via the (Pace *et al.* 1995) method provide more reproducible and more accurate results than the standard Bradford assay. The final concentration of Rnr1 was determined using the Beer-Lambert Law:

$$A_\lambda = \varepsilon_\lambda c l \hspace{4cm} (\textbf{Equation 2.1})$$

Where A_λ is the absorbance of a compound at a particular wavelength λ, ε_λ is the extinction coefficient of a compound at a particular wavelength λ in M^{-1}/cm, c is the concentration of the sample in mol/L, and l is the path-length of the cuvette being used in centimeters. The extinction coefficients of the yeast and human Rnr1 proteins were determined to be 119070 M^{-1}/cm and

124110 M^{-1}/cm respectively using the Expasy ProtParam server (http://ca.expasy.org/tools/protparam.html) (Gasteiger *et al.* 2005). The extinction coefficients provided by ProtParam are calculated as if the protein is completely unfolded into a linear chain. Therefore, the chaotropic agent urea was used at a concentration of 8 moles per liter to ensure complete unfolding of all samples that had their concentrations determined by the (Pace *et al.* 1995) method.

2.3 PRODUCTION OF PEPTIDE AFFINITY RESINS

The C-terminal peptide of small subunit has been previously used for the purification of the large subunit (Yang *et al.* 1990). This property was used to create affinity resins to purify the large subunit of *S. cerevisiae* and hRRM1. Peptide affinity columns were produced using NHS-Activated Sepharose 4-Fast Flow resin (GE Life Sciences, Piscataway, NJ) and peptides synthesized at the W.M. Keck Facility (Yale). The C-terminal 9 amino acids of *H. sapiens* Rnr2 and *S. cerevisiae* Rnr4p were used for the affinity tag with the sequences **NH$_2$-NSFTLDADF-COOH** and **NH$_2$-KEINFDDDF-COOH**, respectively. The protocol provided by GE Life Sciences was followed for covalent attachment of the peptide to the resin with one alteration: 20 mM peptide was used in the coupling reaction rather than the low concentrations suggested by the product manual. At this concentration, coupling efficiency was increased and greater amounts of large subunit could be purified from resins produced using higher concentrations of peptide during the coupling step.

2.4 EXPRESSION AND PURIFICATION OF *S. CEREVISIAE* RNR1p

S. cerevisiae Rnr1p proteins were expressed recombinantly in *E. coli* BL21(DE3) pLysS (Invitrogen, Carlsbad, CA) cell lines as in (Nguyen *et al.* 1999; Xu *et al.* 2006; Xu *et al.* 2008). Plasmid pWJ751-3, conferring ampicillin resistance, was transformed into BL21(DE3) pLysS

(Invitrogen, Carlsbad, CA) cells. A single colony was picked from the transformation plate and an overnight culture of cells was grown. The overnight culture was scaled up into large culture flasks containing liquid Terrific Broth (TB) media, 100 mg/L ampicillin, and 34 mg/L chloramphenicol. A 1% innoculum was used (ie: if the flask contained 1 L of TB media, 10 mL of overnight culture was added). The large flasks were then incubated at 37˚C while shaking at 200 RPM until OD_{600} reached a value of 0.6. Cells were then chilled to 15˚C for 30 minutes and protein expression was induced with 0.5 mM IPTG for 16-20 hours at 15˚C while shaking at 200 RPM. Harvesting of cells was performed by centrifugation at 5000 x g for 30 minutes. Following centrifugation, cells were flash-frozen in liquid nitrogen and stored at -80˚C.

Cells were removed from the -80˚C and allowed to thaw on ice. After thawing, the cells were resuspended in lysis buffer (50 mM HEPES pH 7.0, 5 mM $MgCl_2$, 5% glycerol v/v, 5 mM DTT, 1 mM PMSF, 1x COMPLETE EDTA Free Protease Inhibitor (Roche Biochemicals, Indianapolis, IN)) and then lysed using French pressure at 15,000 pounds per square inch (psi). Lysate was then centrifuged at 30,000 x g for 40 minutes to remove cellular debris. Following centrifugation, the supernatant was collected and then streptomycin sulfate added to a final concentration of 1.5% w/v. The streptomycin sulfate-cell lysate mixture was incubated at 4˚C for 30 minutes and then centrifuged at 30,000 x g for 40 minutes to remove precipitated ribonucleoproteins. Supernatant was collected and ammonium sulfate was added to a final concentration of 40% w/v and allowed to incubate at 4˚C for 30 minutes. Precipitated proteins were then collected by centrifugation at 30,000 x g for 30 minutes. Supernatant was discarded and the protein pellet containing Rnr1p was stored at -80˚C.

Ammonium sulfate pellets were thawed on ice and resuspended in the cell lysis buffer. Resuspended ammonium sulfate pellets were then de-salted using PD10 disposable de-salting

columns (GE Lifesciences, Piscataway, NJ). De-salted protein sample was incubated with Rnr4p

9-mer peptide-affinity resin (see **Section 2.3**) for one hour at 4˚C on a rocker inside a 1 cm inner

diameter Econo-column (Biorad, Hercules, CA). After incubation, the column was washed with

5 column volumes of Buffer A (50 mM HEPES pH 7.0, 5 mM $MgCl_2$, 5% glycerol, 5 mM DTT).

The affinity column was then placed onto a Biorad Biologic FPLC Workstation (Biorad,

Hercules, CA) or an AKTA Purifier (GE Lifesciences, Piscataway, NJ).   The column was

washed with Buffer A until OD_{280} reached 0, followed by another wash of 80% Buffer A + 20%

Buffer B (Buffer A + 1 M KCl) to remove weakly and non-specifically bound proteins. *S.*

cerevisiae Rnr1p was then eluted from the column with 15 column volumes Buffer B (**Figure**

2.1A). Purity was assessed by 12% SDS-PAGE (**Figure 2.1B**). Pure fractions were pooled and

concentrated using CentriPlus, Centricon, and Microcon centrifugal concentrators (Millipore,

Bedford, MA) with a molecular weight cutoff of 50 kDa. The protein sample was diluted 1:10

with Buffer A to bring the concentration of KCl down to 0.1 M and the diluted sample was then

re-concentrated for either crystallization or flash-frozen in liquid nitrogen for storage at -80 ˚C.

2.5 EXPRESSION AND PURIFICATION OF *hRRM1*

H. sapiens Rnr1 proteins were expressed recombinantly in *E. coli* BL21 (DE3)

CodonPlus-RIL (Stratagene, La Jolla, CA) cell lines. Plasmid containing the wild-type hRRM1,

which confers ampicillin resistance, was transformed into BL21(DE3) CodonPlus-RIL

(Stratagene, La Jolla, CA) cells. A single colony was picked from the transformation plate and

an overnight culture of cells was grown. The overnight culture of cells was scaled up into large

culture flasks containing liquid Terrific Broth (TB) media, 100 mg/L ampicillin, and 34 mg/L

chloramphenicol. A 1% innoculum was used
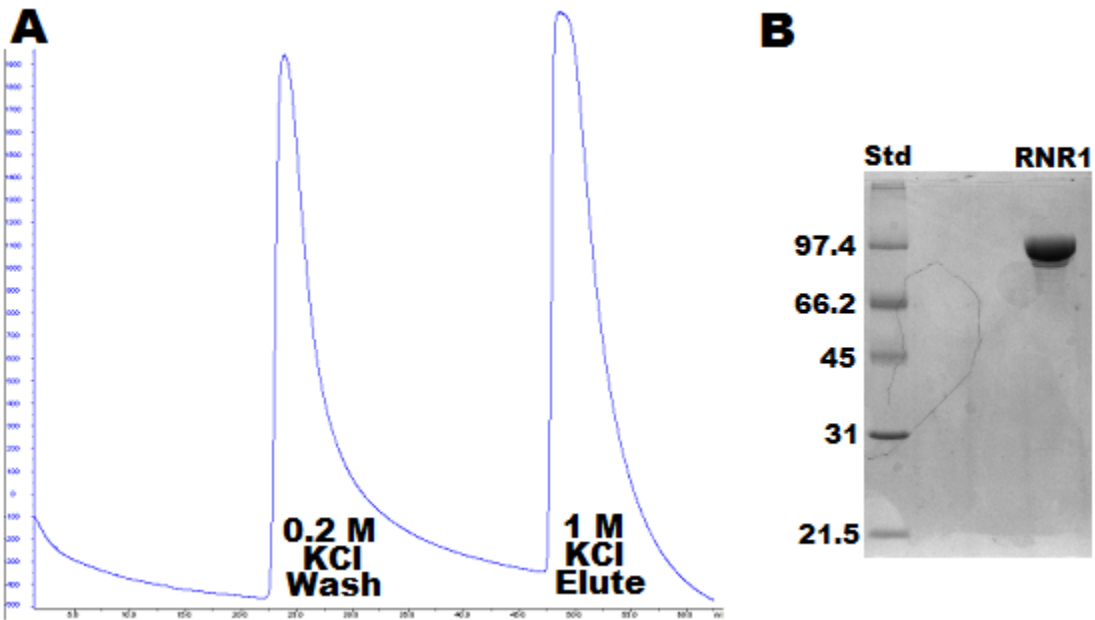
Figure 2.1: Purification of *S. cerevisiae* Rnr1 expressed recombinantly in *E. coli*.
A) Typical chromatogram for the purification of *S. cerevisiae* Rnr1 from Y4 9-mer peptide-affinity resin. The blue line indicates the A_{280}. Impurities and weakly-binding proteins are washed off in the 0.2 M KCl wash and pure Rnr1 is then eluted with 1.0 M KCl. **B)** Reducing 12% SDS-PAGE after pooling and concentrating the fractions from the elution peak. Numbers on the left side of the gel indicate the molecular weight of standard proteins in kDa.

(ie: if the flask contained 1 L of TB media, 10 mL of overnight culture was added). The large flasks were then incubated at 37˚C while shaking at 200 RPM until OD_{600} reached 0.6. Cells were then chilled to 15˚C for 30 minutes and protein expression was induced with 0.5 mM IPTG for 16-20 hours at 15˚C while shaking at 200 RPM. Harvesting of cells was performed by centrifugation at 5000 x g for 30 minutes. Following centrifugation, cells were flash-frozen in liquid nitrogen and stored at -80˚C.

Cells were thawed on ice and then resuspended in lysis buffer (50 mM TRIS pH 8.0, 5% glycerol, 5 mM $MgCl_2$, 10 mM DTT, 1 mM PMSF, 1x COMPLETE EDTA Free Protease Inhibitor (Roche Biochemicals, Indianapolis, IN), 1:10000 dilution Benzonase DNase (EMD Biosciences, San Diego, CA)). Lysis of cells was performed by French pressure at 15,000 psi, followed by centrifugation at 30,000 x g for 60 minutes to remove cellular debris. After centrifugation, the supernatant was collected, had ammonium sulfate added to a final concentration of 50% w/v, and was then incubated at 4˚C for 30 minutes. Precipitated protein was then collected by centrifugation at 30,000 x g for 30 minutes. The ammonium sulfate pellet containing Rnr1 was stored at -80 C˚.

Ammonium sulfate pellets were thawed on ice and then resuspended in lysis buffer which did not contain Benzonase DNase. The resuspended ammonium sulfate pellet was then de-salted using PD10 disposable de-salting columns. Human Rnr2 9-mer peptide affinity resin with a bed volume of 1 ml was packed into a 1 cm inner diameter Econo-column (Biorad, Hercules, CA). De-salted protein sample was then passed through the packed resin twice by gravity flow. Passing sample through the resin twice resulted in increased yield over a single pass. After incubation, the column was loaded onto the Biorad Biologic FPLC Workstation (Biorad, Hercules, CA) or an AKTA Purifier (GE Lifesciences, Piscataway, NJ). Protein was eluted

using a gradient from 100% Buffer C (50 mM TRIS pH 8.0, 5% glycerol, 5 mM $MgCl_2$, 10 mM DTT) to 100% Buffer D (Buffer A + 2 M NaCl) over a volume of 192 mL (**Figure 2.2A**). Fractions were analyzed for purity by 12% SDS-PAGE and fractions containing human Rnr1 were pooled and concentrated using an Amicon Ultrafiltration (Millipore, Bedford, MA) device with a molecular weight cutoff of 30 kDa (**Figure 2.2B - 2.2C**). After concentration, the sample was diluted with Buffer A to bring the concentration of NaCl down to 0.1 M and re-concentrated for either crystallization or frozen in liquid nitrogen and stored at -80˚C.

2.6 CO-EXPRESSION AND PURIFICATION OF *S. CEREVISIAE* RNR2P AND RNR4P

S. cerevisiae Rnr2p and Rnr4p were co-expressed recombinantly in *E. coli* BL21(DE3)-CodonPlus-RIL cells (Stratagene, La Jolla, CA) as in (Chabes *et al.* 2000). Plasmids p(His)6-Y2 and pY4J, conferring kanamycin and ampicillin resistance respectively, were co-transformed into BL21(DE3)-CodonPlus-RIL cells. A single colony was picked from the transformation plate and an overnight culture of cells was grown. The overnight culture was scaled up into large culture flasks containing liquid Terrific Broth (TB) media, 100 mg/L ampicillin, 50 mg/L kanamycin, and 34 mg/L chloramphenicol. A 1% innoculum was used (ie: if the flask contained 1 L of TB media, 10 mL of overnight culture was added). The large flasks were then incubated at 37˚C while shaking at 200 RPM until OD_{600} reached 0.6. Cells were then chilled to 15˚C for 30 minutes and protein expression was induced with 0.5 mM IPTG for 16-20 hours at 15˚C while shaking at 200 RPM. Harvesting of cells was performed by centrifugation at 5000 x g, which were then flash-frozen in liquid nitrogen and stored at -80˚C.
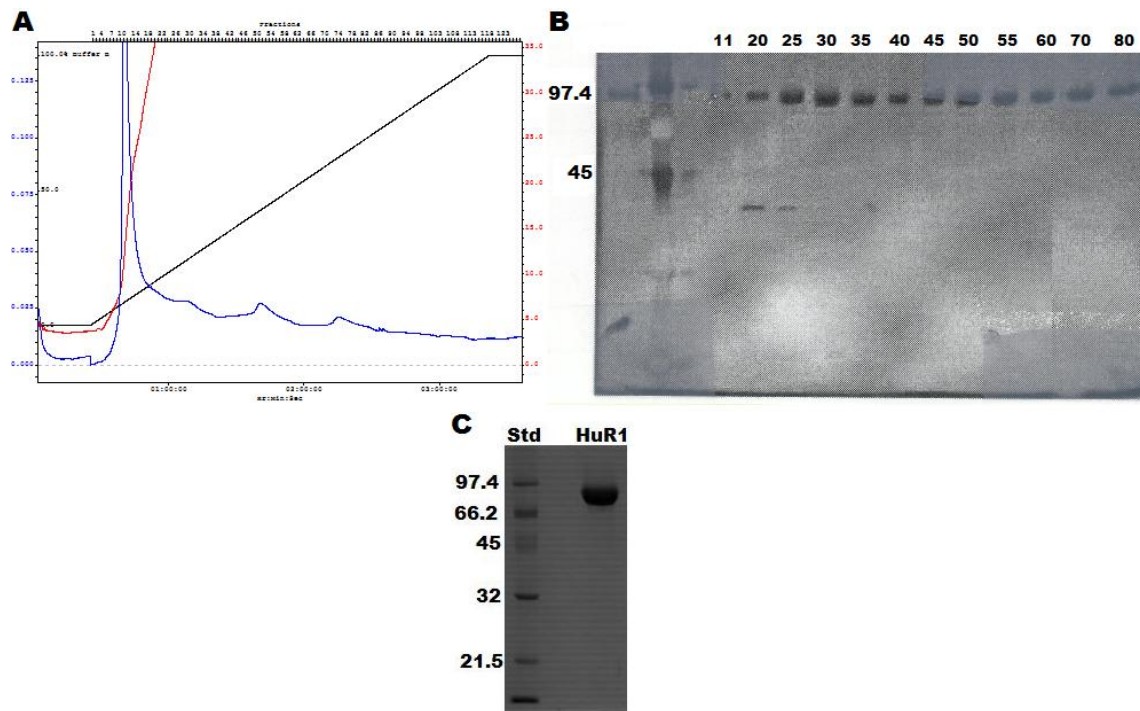
Figure 2.2: Purification of hRRM1 expressed recombinantly in *E. coli*.
A) Typical chromatogram for the purification of hRRM1 from the HR2 9-mer peptide affinity resin. The blue, red, and black lines represent A_{280}, conductivity, and % buffer B respectively. **B)** Silver stain of a reducing 12% SDS-PAGE run on individual fractions from the chromatogram in part A. Numbers across the top represent fraction number and numbers on the left side represent the molecular weight of standard proteins in kDa. **C)** Reducing 12% SDS-PAGE of pooled fractions after concentration to 20 mg/ml. Numbers on the left indicate the molecular weight of standard proteins in kDa.

Cell pellets were removed from -80˚C, thawed on ice, and resuspended in lysis buffer (50 mM HEPES pH 7.4, 5% glycerol, 10 mM Imidazole, 150 mM KCl, 1 mM PMSF, 1x COMPLETE EDTA Free Protease Inhibitor (Roche Biochemicals, Indianapolis, IN)). Cells were lysed via use of a French pressure cell at 15,000 psi and then centrifuged at 30,000 x g for 30 minutes to obtain cleared lysate. Powdered ammonium iron (II) sulfate was then added to a concentration of 1 mM and allowed to incubate for 15 minutes to load Rnr2p with iron. Proteins were purified via immobilized metal affinity chromatography (IMAC) using TALON Cobalt Affinity resin (Clontech, Mountain View, CA) or High Yield PrepEase® His-Tagged Protein Purification Resin (USB, Cleveland, OH). Cleared lysate was batch-bound to the affinity resin for one hour at 4˚C while rocking and then loaded into a 1 cm inner diameter Econo-column (Biorad, Hercules, CA) and loaded onto a Biorad Biologic FPLC Workstation (Biorad, Hercules, CA) or an AKTA Purifier (GE Lifesciences, Piscataway, NJ). The resin was washed with Buffer E (50 mM HEPES pH 7.4, 5% glycerol, 10 mM imidazole, 150 mM KCl) until OD_{280} reached 0 (**Figure 2.3A**). Protein was then eluted with Buffer F (Buffer A + 100 mM imidazole) and fractions were analyzed for purity by 12% SDS-PAGE (**Figure 2.3B**). Pure fractions were pooled and concentrated by ultrafiltration with a YM-30 Centricon (Millipore, Bedford, MA). The imidazole concentration was reduced to less than 1 mM by either dialysis against 2 liters of Buffer A or by repeated dilution and concentration using the centricon. Concentrated protein was then flash-frozen in liquid nitrogen and stored at -80 C˚.
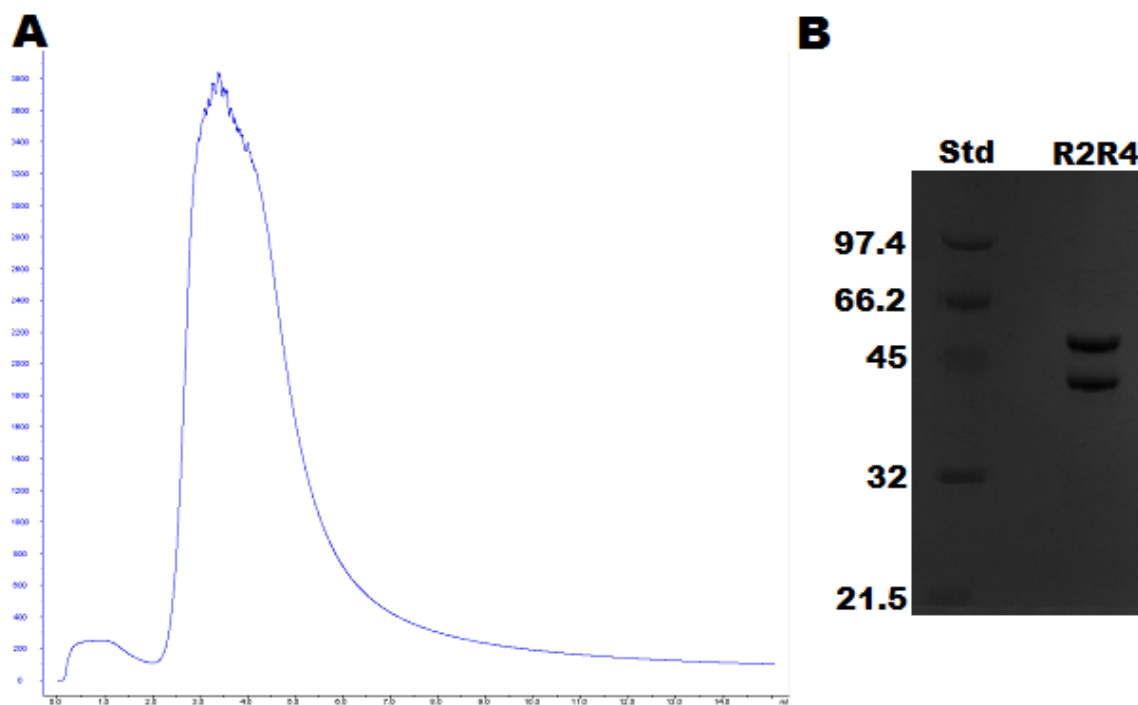
Figure 2.3: Co-purification of *S. cerevisiae* Rnr2p and Rnr4p expressed recombinantly in *E. coli*.

A) Typical chromatogram for the purification of *S. cerevisiae* Rnr2p and Rnr4p over High Yield PrepEase His-Tagged Protein Purification Resin. The blue line represents the A_{280}. The Y-axis represents the A_{280} and the X-axis represents the elution volume. **B)** Reducing 12% SDS-PAGE gel of pooled fractions after concentration. Numbers on the left indicate the molecular weight of standard proteins in kDa.

2.7 EXPRESSION AND PURIFICATION OF *S. CEREVISIAE* SML1p

Yeast Sml1p was expressed recombinantly in BL21(DE3)-CodonPlus-RIL *E. coli* cells (Stratagene, La Jolla, CA) as in (Uchiki *et al.* 2002; Gupta *et al.* 2004; Uchiki *et al.* 2004). Plasmid pWJ-750-2, carrying *Sml1* and conferring ampicillin resistance, was transformed into BL21(DE3)-CodonPlus-RIL-pLys (Stratagene, La Jolla, CA) cells. A single colony was picked from the transformation plate and an overnight culture of cells was grown. The overnight culture was scaled up into large culture flasks containing liquid Terrific Broth (TB) media, 100 mg/L ampicillin, and 34 mg/L chloramphenicol. Cells were grown in liquid TB media at 37˚C until OD_{600} reached 0.6. Cells were then induced with 0.5 mM IPTG for 3 hours at 37˚C and harvested by centrifugation at 5000 x g for 30 minutes. Harvested cells were resuspended in lysis buffer (50 mM TRIS pH 7.4, 10% glycerol, 5 mM DTT, 1 mM PMSF, 1 mM EDTA, 1x COMPLETE EDTA Free Protease Inhibitor (Roche Biochemicals, Indianapolis, IN), and 1:10000 dilution of Benzonase DNase (EMD Biosciences, San Diego, CA)). Resuspended samples were flash-frozen in liquid nitrogen and stored at -80˚C.

Cells were thawed on ice and then underwent ultra-centrifugation at 150,000 x g for 1 hour in an Ultima Max ultracentrifuge (Beckman, Fullerton, CA). The supernatant was collected, and ammonium sulfate was then added to a final concentration of 25% w/v, which was then incubated while stirring at 4˚C for 30 minutes. Precipitated protein was separated from the supernatant by centrifugation at 30,000 x g for 30 minutes. The ammonium sulfate pellet was then resuspended in 2.5 ml Buffer G (50 mM TRIS pH 7.4, 5% glycerol, 100 mM KCl, 5 mM DTT, 1 mM PMSF, 1x COMPLETE EDTA Free Protease Inhibitor (Roche Biochemicals, Indianapolis, IN)) and loaded onto a HiLoad 16/60 Superdex 75 (GE Lifesciences, Piscataway, NJ) size exclusion column (**Figure 2.4A**). Protein peaks were analyzed by 15% SDS-PAGE and

the fractions containing Sml1p were pooled (**Figure 2.4B**). Following purification of Sml1p from the size exclusion column, the ratio of the A_{260} to the A_{280} was determined to test for the presence of DNA in the purified protein. If DNA was determined to be present, it was removed by performing anion exchange chromatography using DEAE Sepharose (GE Lifesciences, Piscataway, NJ) on the pooled Sml1p fractions using Buffer G. After anion exchange, the Sml1p solution was concentrated using a Centricon (Millipore, Bedford, MA) ultrafiltration device with a molecular weight cut-off of 10 kDa, flash-frozen in liquid nitrogen, and then stored at -80˚C.

2.8 CRYSTALLIZATION OF PROTEINS

2.8.1 Initial Crystallization Screening

The rate-limiting step in the process of structure determination of any protein by macromolecular X-ray crystallography is the production of high-quality well-diffracting protein crystals. Currently, there is no method to predict the crystallizability of a protein based on either its sequence or predicted structural homology to other proteins which may contain similar folds (Chayen *et al.* 2008). Even when large milligram quantities of exceptionally pure protein sample are available, finding the correct conditions under which the protein forms highly-ordered diffracting crystals can be quite an arduous task. Since discovering the correct conditions for the formation protein crystals is equivalent to searching for a needle in a haystack, the first step is usually the screening of a large number of crystallization conditions, which are composed of various salts, buffers, organics, PEGs, and other protein precipitating agents.
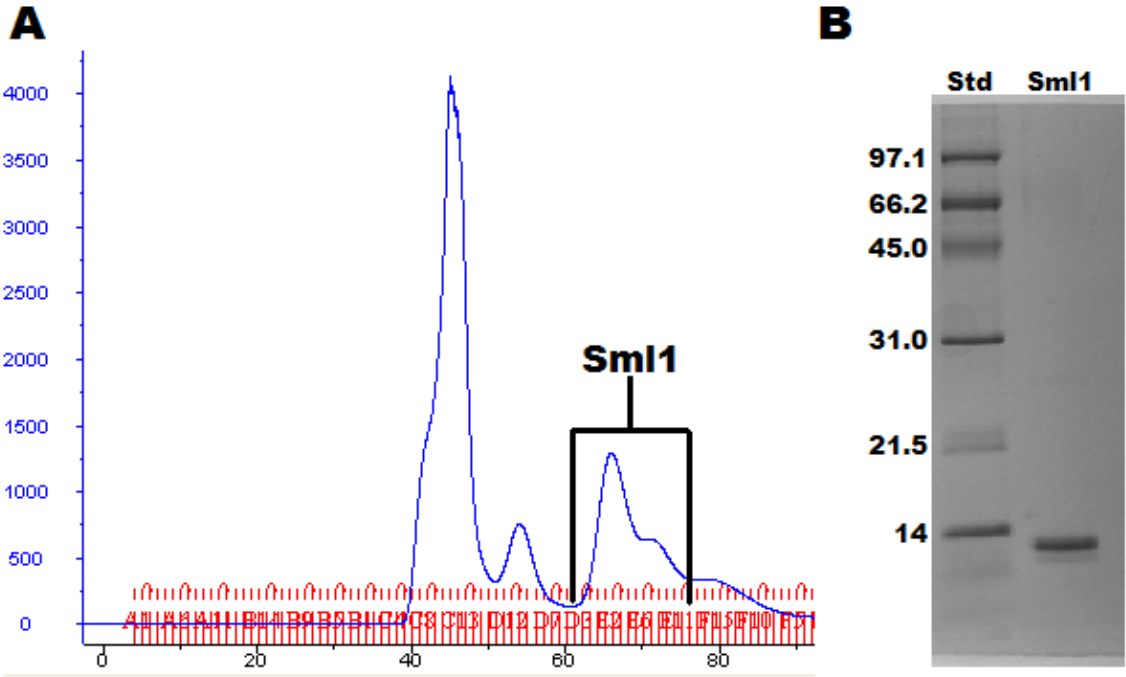
Figure 2.4: Purification of *S. cerevisiae* Sml1p expressed recombinantly in *E. coli*.
A) Chromatogram of ammonium sulfate cut after being injected onto a Sephadex HiLoad 16/60 Superdex 75 size exclusion column. Sml1p elutes in the third peak as a mixture of dimers and monomers. The X-axis represents the elution volume and the Y-axis represents the A_{280}. The red lines represent fractionation separations of the size-exclusion run. **B)** Reducing 15% SDS-PAGE gel of the pooled fractions after concentration to 20 mg/ml. Numbers on the left indicate the molecular weight of standard proteins in kDa.

Classically, setting up a single screen containing ninety-six conditions can consume several milligrams of precious protein sample. However, recent advances in automation and extremely low volume dispensing robotics allow completion of an entire screen with as little as 0.3 milligrams of protein (Luft *et al.* 2003; Bard *et al.* 2004). The most common type of screen which is conducted is known as a sparse-matrix screen (Jancarik *et al.* 1991). Sparse-matrix screens are usually composed of a compilation of conditions which have been previously observed to result in the successful crystallization of target proteins. Examples of sparse-matrix screens currently available and in use are Crystal Screen I and the Index Screen from Hampton Research. These screens generally consist of anywhere from fifty to one-hundred different conditions. In addition to sparse-matrix screens, systematic screens provide another tool to probe for conditions that will result in the crystallization of a target protein. These screens are designed to sample precipitant conditions in a balanced and rational manner (Bergfors 1999; Delucas *et al.* 2005). Some examples of systematic screens currently available are the PEG-Ion Screens from Hampton Research and the JBScreen PEG/Salt screen from Jena Biosciences. Although thousands of conditions are available via sparse and systematic matrix screens from various vendors and companies, it has been suggested by the Joint Center for Structural Genomics at the Scripps Research Institute that a minimal screen consisting of approximately one-hundred different conditions has been sufficient to crystallize 98% of target proteins (Page *et al.* 2004).

Performing crystallization screens on a protein has one of several results: (1) all of the protein remains in solution, (2) amorphous precipitate, (3) phase separation, (4) crystalline precipitate, or (5) crystals. Any condition which results in the formation of phase separation,

55

crystalline precipitate, or crystals can be considered to be a hit or a lead. Leads which are identified in initial screens can then be optimized to form larger or better-ordered crystals by varying solubility parameters of the conditions such as protein concentration, temperature, precipitant concentration, or ionic strength (Chayen 2004; Chayen *et al.* 2008).

2.8.2 The Vapor Diffusion Method

Vapor diffusion crystallization experiments are the most common and popular within the realm of protein crystallography and was the method used to co-crystallize both mutant *S. cerevisiae* Rnr1p and hRRM1 in the presence of the effector TTP (**Figure 2.5**). There are two configurations under which vapor diffusion experiments usually occur: (1) hanging drop and (2) sitting drop. In both experimental setups, a small volume of concentrated protein solution is mixed together with an equal volume of precipitant solution and then sealed off from the outside environment in a reservoir containing the precipitant solution, often referred to as the "well buffer" (**Figure 2.5**). The final volume for both hanging and sitting drops usually ranges between 0.2 µL and 10 µL and the volume of the well buffer can range between 50 µL and 1 mL, depending on the type of crystallization plate being used. Initially, the conditions in the hanging or sitting drop are in the unsaturated portion of the phase diagram (**Figure 2.5**). Over the course of the experiment, water will evaporate from the protein drop until the concentration of precipitant in the protein drop reaches equilibrium with the concentration of precipitant in the well buffer. As evaporation occurs, the volume of the protein drop continuously shrinks, increasing the protein concentration.
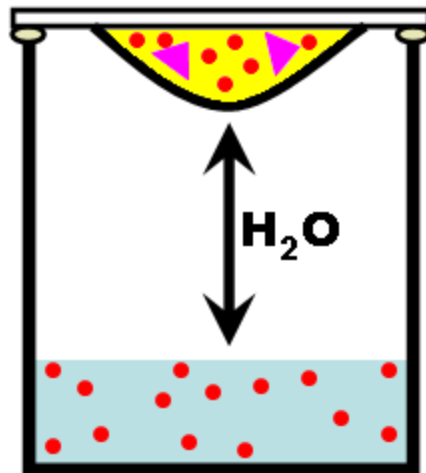
Figure 2.5: Schematic diagram showing a vapor diffusion crystallization setup.
In all figure parts, protein molecules are represented as purple triangles, precipitant molecules are represented at red spheres, buffer containing protein is represented as yellow, and buffer containing precipitant is represented as light blue. Protein and precipitant solution are mixed into a small drop, which then undergoes vapor diffusion with the well buffer until equilibrium is reached. The hanging drop method is shown.

The drop eventually becomes supersaturated with protein and spontaneous nucleation events will occur, allowing the process of crystal growth to begin. In addition to optimizing the usual precipitation parameters such as pH, temperature, and precipitant concentration, crystallization conditions in vapor diffusion can be further optimized by altering the volume ratio of protein to precipitant solution in the hanging or sitting drop. For example, a drop which contains 1 µL protein solution and 1 µL of precipitant solution may never reach supersaturation, while a drop which contains 1.5 µL of protein solution and 0.5 µL of precipitant solution does.

2.8.3 Seeding and Crystal Growth

A major dilemma for the growth of large well-ordered protein crystals is that the conditions under which nucleation events occur is not ideal for crystal growth and vice versa. The spontaneous formation of nuclei occurs at high levels of supersaturation while, on the other hand, the slow ordered growth of large protein crystals requires saturation levels in the metastable zone of the phase diagram (Weber 1997; Bergfors 2003). Seeding is a commonly used method which avoids the problem of excess nucleation in a crystallization experiment by separating these two processes (Weber 1997; Bergfors 2003; Chayen *et al.* 2008). In a seeding experiment, ready-made nuclei from a previous crystallization experiment are placed directly into protein solutions which are prepared in the metastable state. Seeding experiments are divided into two categories depending upon the size of the seed to be used: (1) microseeding and (2) macroseeding. The size of the seeds in a microseeding experiment are sub-microscopic and are not visually resolvable (Bergfors 2003). On the other hand, macroseeding experiments consist of single crystals, usually in the size range of 5-50 µm (Bergfors 2003).

Microseeding experiments are the simpler of the two seeding methods to perform. The production of microseeds can be accomplished by crushing crystals via vortexing, sonication,

seed beads, or with other tools (Luft *et al.* 1999). Crystal nuclei are then transferred to a new crystallization solution which is in the metastable zone by pipetting, streaking, touching the surface, or mixing. The optimum number of nuclei for the formation of crystals in the new drop must be determined experimentally and is usually done by performing seeding experiments with serial dilutions of the original seed stock. An alternative to crushing pre-formed crystals is the streak-seeding method, where animal hair, most commonly horse hair or cat whiskers, are used as seeding wands (Bergfors 2003). The seeding wand is touched to the surface of a crystal where it is able to commandeer crystal nuclei. After the hair or whisker is loaded with nuclei, it is serially streaked through a series of new drops that are prepared in the metastable zone.

Macroseeding experiments are slightly more complicated than microseeding experiments. A small crystal is removed from its original crystallization condition and placed into a new unsaturated solution, referred to as the etching solution. Under the unsaturating conditions of the etching solution, misoriented protein molecules and any other molecules which may have poisoned the growth of the crystal should be removed. Following a short exposure in the etching solution, the macroseed is then transferred to a new metastable solution. With the removal of crystal poisoning agents in the etching solution, the macroseed can now incorporate more protein and increase its size significantly.

2.8.4 Crystallization of S. cerevisiae Rnr1p

S. cerevisiae Rnr1p was crystallized in the orthorhombic $P2_12_12$ space group by the hanging drop method at room temperature as in (Xu *et al.* 2006; Xu *et al.* 2008) (**Figure 2.6**). Well buffer for crystallizations contained 500 μL of 50 mM HEPES pH 7.5, 200 or 250 mM NaCl, and 15-25% w/v PEG-3350. Hanging drops contained 1 μL protein solution at 20 mg/mL Rnr1p and 2.4 mg/mL Sml1p in 50 mM HEPES pH 7.0, 5 mM $MgCl_2$, 5% glycerol v/v, 5 mM

DTT, 0.1 M KCl, 20 mM dTTP and 1 μL of well buffer. To obtain data for Rnr1p complexed to effectors and substrates, crystals were soaked in the well buffer containing 20 mM nucleotides, 10 mM DTT, and 10 mM MgCl$_2$. After soaking for between 3 and 9 hours, crystals were transferred to the cryoprotectant buffer (50 mM HEPES pH 7.5, 200 or 250 mM NaCl, 15-25% w/v PEG-3350, and 20% w/v glycerol) and then flash-frozen in liquid nitrogen for data collection.

2.8.5 Crystallization of hRRM1

H. sapiens Rnr1 was crystallized in the orthorhombic P2$_1$2$_1$2$_1$ space group by the hanging drop method at room temperature. Well solution for crystallizations contained 0.1 M TRIS pH 7.9, 0.2 M Li$_2$SO$_4$, and 19-25% w/v PEG-3350. Hanging drops contained 1 μL of protein solution at 20 mg/ml in 50 mM TRIS pH 8.0, 5% glycerol, 5 mM MgCl$_2$, 10 mM DTT, 20 mM dTTP and 1 μL of the well solution. The well buffer used for obtaining the original crystals of hRRM1 consisted of concentrations of PEG-3350 that were between 20 and 25% w/v. Crystals which formed under these conditions generally only reached between 100 and 150 μm in size and the diffraction quality of these crystals was poor, with reflections recorded at a resolution of up to 4.8 Å (**Figure 2.7A**). To obtain both higher quality and higher resolution reflections in the X-
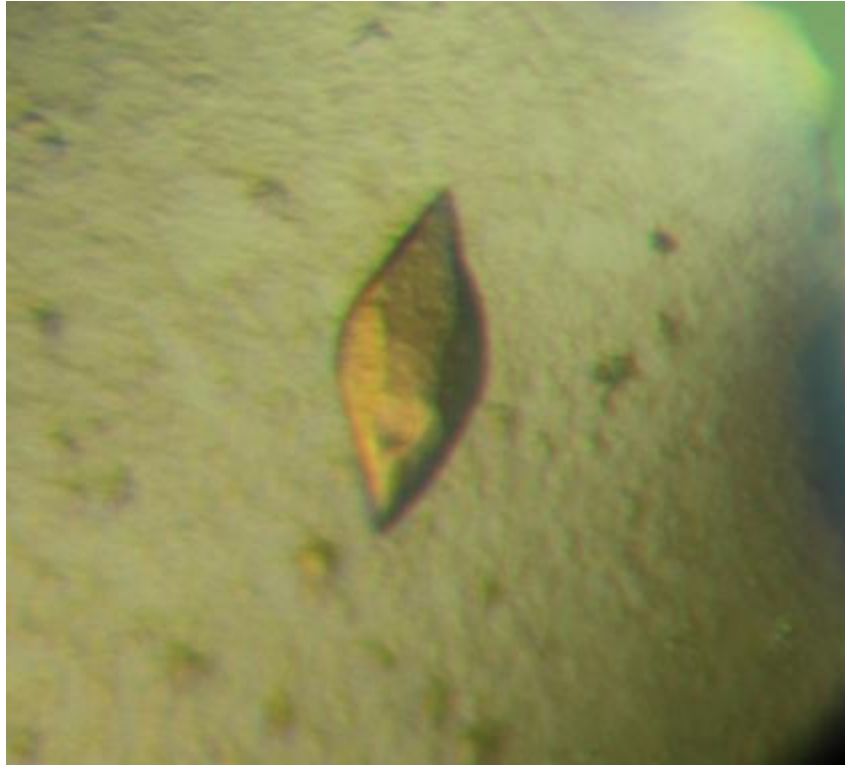
Figure 2.6: Protein crystal of *S. cerevisiae* Rnr1.
A single crystal of *S. cerevisiae* Rnr1 which belongs to the orthorhombic P2$_1$2$_1$2 space group.
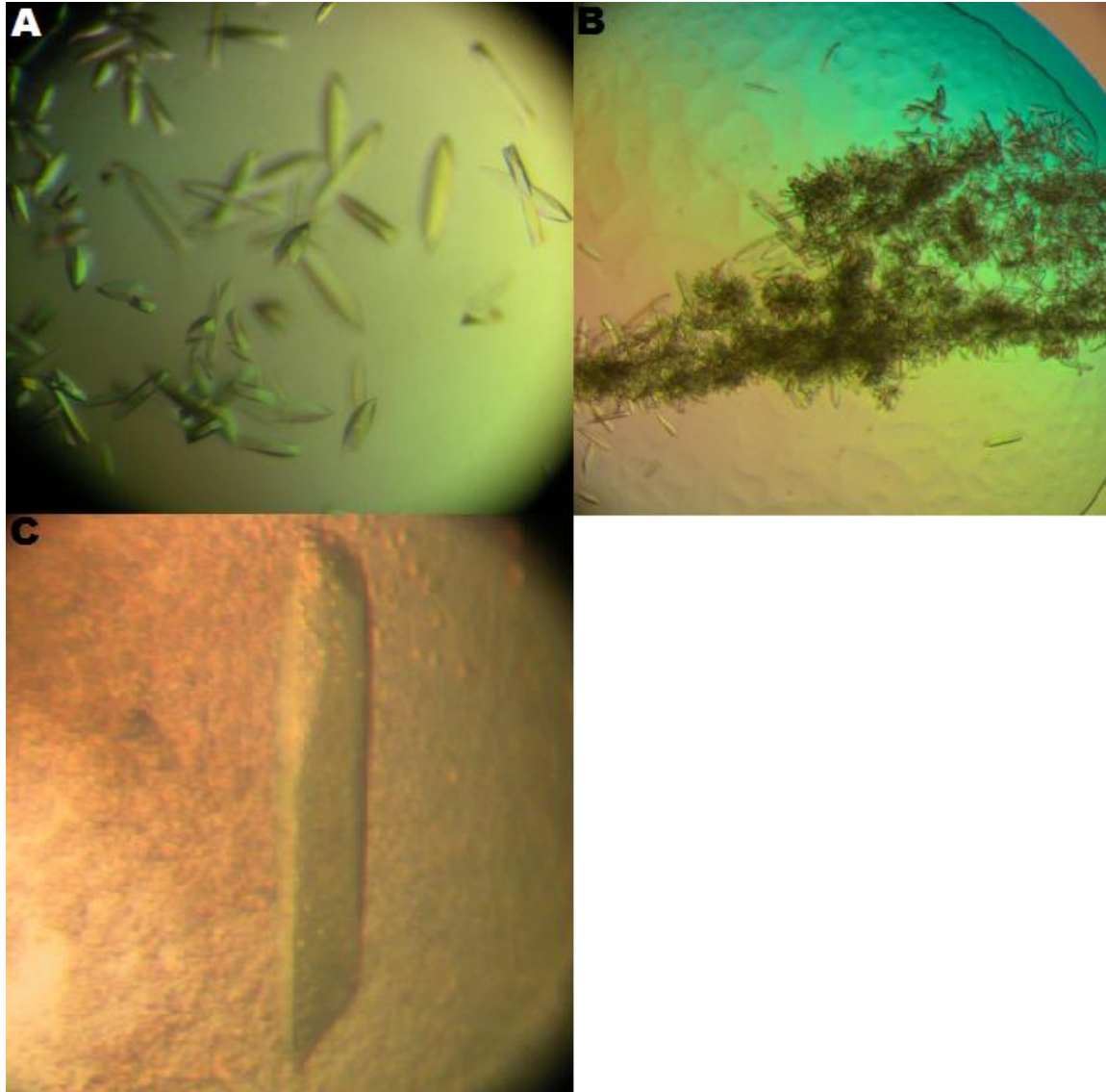
Figure 2.7: Orthorhombic crystals of hRRM1 belonging to the P2₁2₁2₁ space group.
A) Crystals measuring between 100 and 150 μm in a hanging drop with 21% w/v PEG-3350. **B)** Microcrystals of hRRM1 used for microseeding experiments. **C)** A single crystal measuring 450 μm (from top to bottoms) from a microseeding experiment in a hanging drop containing 19% w/v PEG-3350.

ray diffraction experiments, the size of the crystals was increased to between 300 and 500 μm using the streak-seeding microseeding method (**Figure 2.7C**). First, screening for conditions under which hRRM1 was in the metastable zone was performed by lowering the concentration of PEG-3350. If the concentration of PEG-3350 in the well buffer was decreased below 20% w/v, crystals did not form in the hanging drops (ie: a drop containing 19% w/v PEG-3350 did not produce any crystals but a drop with 20% w/v PEG-3350 did). To obtain as few crystals as possible during microseeding experiments and to make them as large as possible, 19% w/v PEG-3350 was utilized for the well buffer and, using a cat's whisker, crystal seeds were serially diluted into a series of hanging drops. The number of hanging drops used for serial dilution of seeds for the microseeding of hRRM1 crystals was twelve. Drops at the beginning of the serial dilution series grew multiple small crystals, while drops near the end of the series tended to produce one or two single large crystals. Streak-seeding experiments in hanging drops where 19% w/v PEG-3350 was used as the well buffer grew both fewer and larger protein crystals as compared to the conditions that contained greater than or equal to 20% w/v PEG-3350 (compare **Figure 2.7A** to **Figure 2.7C**). The larger crystals from the streak-seeding experiments also yielded much improvement in the resolution of the diffraction data as compared to the smaller crystals (2.4 Å vs. 4.8 Å). Crystals from the microseeding hanging drops were transferred to cryoprotectant buffer (0.1 M TRIS pH 7.9, 0.2 M Li$_2$SO$_4$, 19% w/v PEG-3350, and 20% glycerol) and then flash-frozen in liquid nitrogen for data collection.

To obtain structures of hRRM1 in which the activity site and the catalytic site were occupied, several sets of soaking experiments were performed. For the structure in which ATP is bound to the activity site, a quick soaking method was used. Crystals were transferred from the hanging drops in which they formed to a newly prepared hanging drop with a volume of 2 μL

63

in a well that was equilibrated for 5 minutes with the buffer composition 0.1 M TRIS pH 7.9, 0.2 M Li_2SO_4, 19% w/v PEG-3350, and 10 mM ATP. Crystals were soaked in the ATP-containing drop for 15 seconds, transferred to a drop containing cryoprotectant buffer, and then immediately flash-frozen in liquid nitrogen. A very short soaking time was required to obtain data for this complex, as soaking the crystals in the ATP solution for any longer than 30 seconds produced no diffraction pattern when exposed to X-rays, indicating that the binding of ATP deforms the crystalline lattice.

For the Rnr1●TTP●GDP ternary complex crystal structure, the soaking experiments were performed for longer periods of time (the crystal used for solving the Rnr1●TTP●GDP structure was soaked for 9 hours). Soaking drops for this complex contained 0.1 M TRIS pH 7.9, 0.2 M Li_2SO_4, 19% w/v PEG-3350, 50 mM DTT, 1 mM TTP, and 40 mM GDP. After soaking was completed, crystals were transferred to a drop containing cryoprotectant buffer, and then flash-frozen in liquid nitrogen. The inclusion of at least 50 mM DTT was necessary to reduce the disulfide bond between cysteine residues 218 and 444 in the catalytic site and obtain high occupation by the GDP substrate. When soaking experiments were performed with concentrations of DTT lower than 50 mM, no difference density was observed in the F_o-F_c or $2F_o$-F_c Fourier electron density maps for the GDP substrate.

For the Rnr1●TTP●dATP complex, crystals of hRRM1 were soaked for 5 hours in a freshly prepared hanging drop containing 0.1 M TRIS pH 7.9, 0.2 M Li_2SO_4, 10 mM DTT, 1 mM dATP, and 19% PEG-3350. After soaking experiments were completed, crystals were transferred to a drop containing cryoprotectant buffer, and then flash-frozen in liquid nitrogen. Crystals were viable in this solution even after 14 hours of soaking. However, raising the concentration to 4 mM or higher resulted in the complete loss of the ability of the soaked crystals

to diffract X-rays. The crystal used for the Rnr1•TTP•dATP structure reported in this dissertation was soaked for 5 hours. Crystals soaked for 4 hours or less produced no observable F_o-F_c or $2F_o$-F_c Fourier electron density for the dATP ligand in the activity-site.

2.9 X-RAY CRYSTALLOGRAPHY

2.9.1 Data Collection of S. cerevisiae Rnr1p S269P and S610F Mutants

Crystals of *S. cerevisiae* Rnr1p were prepared for data collection in liquid nitrogen as described in **Section 2.8.4**, and data collection was performed at a cryogenic temperature of 100 K using the oscillation method. Data collection strategy for crystals of *S. cerevisiae* Rnr1p was fairly straightforward. These crystals were generally highly ordered and usually had a mosaic spread of between 0.5 and 1.0 degrees. Since the mosaicity for these crystals was low and the maximum unit cell edge was ~120 Å, Δφ wedges were chosen be between 0.5 and 1.0 degree and the crystal to detector distances ranged between 150 and 250 millimeters, depending on both the beam-line and detector type, with no danger of overlaps. See **Section 2.9.4** for details on the treatment of *S. cerevisiae* Rnr1p X-ray diffraction data.

2.9.2 Data Collection of hRRM1

Crystals of hRRM1 were prepared for data collection in liquid nitrogen as described in **Section 2.8.5**, and data collection was performed at a cryogenic temperature of 100 K using the oscillation method. Collection of diffraction data from hRRM1 was slightly more complicated. The largest unit cell edge is ~ 220 Å, almost two times larger than that of *S. cerevisiae* Rnr1p. Mosaicity was a major concern with data collection from these crystals. One of the main problems with the hRRM1 crystals is that the mosaicity is anisotropic, meaning that wedges of data covering one portion of reciprocal space have a mosaicity as low as 1.0 degree, however other portions of the reciprocal space harbor reflections with mosaicities of up to 2.5 degrees.

Portions of the data containing high mosaicity also contained a large portion of overlapping reflections, which can be predicted with the simulated data collection strategy in HKL2000 (**Figure 2.8**). Since the frames at the beginning of a data collection always contain the highest resolution data because the crystal has not yet been damaged by radiation, the data collection was always started at a region directly after a region where a large percentage of overlaps were present (**Figure 2.8**).

With the combination of both the large unit cell edge and anisotropic mosaicities of the hRRM1 crystals, $\Delta\varphi$ was always required to be less than or equal to 0.5 degrees and the crystal to detector distance was usually set between 300 and 400 millimeters, depending on the beamline and detector used for the data collection. For most crystals, between 100 and 180 degrees of rotation resulted in a complete dataset. Even with very small $\Delta\varphi$ wedges (ie: <0.25 degrees) and large crystal to detector distances (ie: >400 millimeters), portions of *H. sapiens* reflection data that were highly mosaic contained large numbers of overlaps and were not useable (**Figure 2.8**). However, due to the symmetry of hRRM1 crystals, it was still possible to accurately determine the intensities of the reflections in these highly mosaic regions by
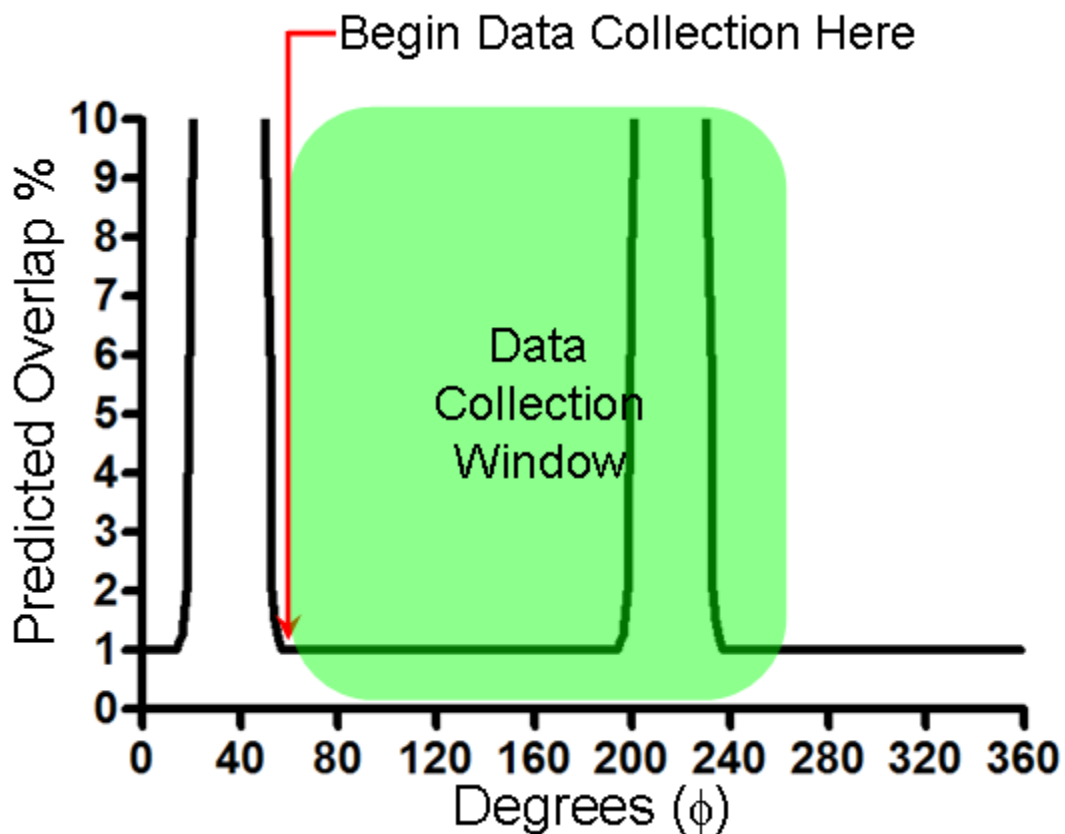
Figure 2.8: Data collection strategy for hRRM1.
Highly mosaic regions of the data correspond to regions with a high percentage of overlaps (shown here between 20 and 60 degrees and 200 and 240 degrees). Data collection was always started directly after a region with a high amount of overlaps to ensure maximum resolution and data completeness. This figure was generated with the data collection strategy tool in the program HKL2000.

measuring the intensities of their symmetry related reflections in the regions of the data where the mosaicity was lower. See **Section 2.9.5** for details on the treatment of hRRM1 X-ray diffraction data.

Crystals of hRRM1 were also quite sensitive to radiation damage. For example, the 2.4 Å dataset for the TTP-bound structure collected at the GMCA-CAT ID-B beamline had diffraction data to a resolution of 2.0 Å in the first 10 frames. However, as frames were collected and the crystal underwent radiation damage, the resolution of the reflections slowly degraded, resulting in a 2.4 Å dataset rather than the 2.0 Å which was expected. Attempting to lower the exposure time or increase the attenuation of the X-ray beam on this crystal during initial screening resulted in loss of several thenths of angstroms of resolution. We knew that at the attenuation level and exposure time selected, radiation damage was going to occur. Had we chosen a slightly lower exposure time and increased the attenuation of the X-ray beam, the initial resolution would have been slightly lower (~2.2 Å) but radiation damage may not have occurred as quickly. This may have resulted in a slightly higher overall resolution than that obtained, but in the end a compromise was made between radiation damage and data resolution.

At the time of the writing of this dissertation, the GMCA-CAT ID-B and BIOCARS ID-B beamlines were constantly being upgraded with new equipment, detectors, software, attenuators, etc. The settings used for data collection in this dissertation are provided, however caution should be used when attempting to use these settings in the future, as the same settings will most likely not provide the user with the same results due to equipment changes and upgrades. For data collected at the GMCA-CAT ID-B beamline, the attenuation was usually selected to be either 10 or 20-fold, the exposure times were usually between 1 and 2 seconds, and the beam size was selected to be as large as possible (200x50 μM at the time of the writing of

this dissertation). For data collected at the BIOCARS ID-B beamline, an attenuator with 50-fold attenuating power was placed in the path of the beam and exposure times were generally between 5 and 25 seconds. The attenuation values and exposure times were optimized for each crystal from which data was collected to obtain optimal resolution and data completeness.

2.9.3 Indexing, Integration, and Scaling of X-ray Reflection Intensities

Current data collection strategies for macromolecular crystallography involve the collection of large amounts of oscillation images where the orientation of the crystal to both the X-ray beam and the detector is not known at the time of data collection. In addition, the unit cell constants, unless previously determined, are also usually unknown. Indexing then, is the process of extracting this information from either a single or multiple sequential oscillation images (Gewirth *et al.* 2004). The computer program HKL2000 contains two modules, XDisp and Denzo, which are used to search for peaks on oscillation images and then index those peaks by assigning each peak a value of *hkl* (Otwinowski *et al.* 1997; Gewirth *et al.* 2004). Autoindexing of reflection data by Denzo is based on a proprietary algorithm that uses a Fast Fourier Transform (FFT) (Gewirth *et al.* 2004). Denzo provides the user with basic information about the crystal such as the unit cell constants and an estimation of mosaicity if multiple oscillation images were used in the analysis. Assignment of the crystal to a particular Bravais lattice requires intervention by the user. However Denzo does provide some assistance to users in the form of a value known as the distortion index. If the distortion index for a particular Bravais lattice is high, it requires a large amount of distortion of the unit cell to fit the lattice. Thus, the highest symmetry lattice with the lowest distortion index should be chosen by the user (Gewirth *et al.* 2004). Following the assignment of the unit cell and Bravais lattice, detector and crystal

parameters are refined by the least squares method to minimize the difference in position of the reflection centroids from the predicted positions, which is monitored by the χ^x and χ^y values.

After proper indexing has been performed, the next step is the integration of the reflection data from the oscillation images. During integration, the background from the detector is subtracted from the reflection intensities via a process known as profile fitting (Gewirth *et al.* 2004). The background-corrected intensities and *hkl* indices of all reflections from all of the oscillation images are measured and then recorded into text files by the program Denzo.

The scaling and merging of X-ray reflection data sets along with global refinement of crystal parameters is accomplished with the program Scalepack, which is included with the program HKL2000 (Gewirth *et al.* 2004). The algorithm used by the program Scalepack for the scaling of data is based on the method of Fox and Holmes (Fox *et al.* 1966). In addition, the output log files from Scalepack provide three values which are most commonly considered when deciding the resolution at which to cut the data off at: (1) I/σ, (2) R_{merge} also known as R_{symm}, and (3) completeness. The value I/σ is simply a measure of the ratio of the intensity of a reflection to the error of that intensity. As long as the value of I/σ is greater than or equal to 2, a reflection is generally considered useable. The value R_{merge} is the more traditional method for determination of the resolution cut-off and is the agreement between the intensities of symmetry related reflections which are usually measured multiple times during an oscillation data collection experiment:

$$R_{merge} = \Sigma_{hkl} \, \Sigma_i \, |I_{i(hkl)} - I_{hkl}| \, / \, \Sigma_{hkl}\Sigma_i \, I_{(hkl)}$$ **(Equation 2.2)**

Where *hkl* is index of a particular reflection, *i* is the observation number of a reflection *hkl*, $I_{i(hkl)}$ is the intensity of the *i*th observation of the reflection *hkl*, and I_{hkl} is the average intensity of all the observations of the reflection *hkl* (Otwinowski *et al.* 1997; Gewirth *et al.* 2004). If the intensities measured for a reflection *hkl* are identical, the value of R_{merge} approaches 0. However, if intensities measured for a particular reflection diverge from the average, the value of R_{merge} increases.

There is a large amount of disagreement in the crystallographic community over which value, I/σ or R_{merge}, is the superior judge of the resolution of a particular data set. More traditional crystallographers seem to prefer R_{merge} as a measure of the resolution cut-off where R_{merge} in the highest resolution shell is less than 50%, however I/σ is currently considered as a superior criterion for the judgment of resolution cut-off (Gewirth *et al.* 2004). This is because the value of R_{merge} can easily be manipulated by either inclusion or exclusion of reflections (ie: if the redundancy of a data set is decreased, R_{merge} will artificially be reduced because less reflections are being used to compute it) amongst other factors (Gewirth *et al.* 2004). The final criterion used to judge the resolution cut-off of a data set is the completeness. Generally, overall completeness should be greater than 90% and the completeness of the last resolution shell should be greater than 70%. There are cases where lower percentages of completeness are acceptable.

2.9.4 Treatment of S. cerevisiae Rnr1p X-ray Diffraction Data

Datasets for crystals of *S. cerevisiae* Rnr1p belong to the space group $P2_12_12$. However, during data collection the two screw axes are present on the b and c axes rather than the a and b axes, and hence when the data are collected the space group $P22_12_1$. In this space group, the 2-fold axis without the screw axis is the unique axis. Crystallographic convention tells us that the unique axis should be on the c-axis, and the data must therefore be re-indexed from abc to bca so

that the screw axes are present on the a and b axes and the unique axis corresponds to the c-axis.

Each reflection *hkl* is multiplied by a reindexing matrix as follows:

$$M = \begin{bmatrix} 0 & 1 & 0 \\ 0 & 0 & 1 \\ 1 & 0 & 0 \end{bmatrix}$$ **(Equation 2.3)**

2.9.5 Treatment of H. sapiens X-ray Diffraction Data

Data for crystals of hRRM1 were anisotropic with respect to the value of mosaicity (see **Section 2.9.2**). Wedges of reciprocal space where mosaicities were high (>1.5 degrees) contained a large amount of overlaps and linear R-factors for reflections recorded from these wedges often exceeded 0.2. Even when attempting to break the data into 15 degree wedges, scaling each wedge separately, and then combining each scaled wedge together, the R_{symm}, χ^2, and resolution cut-off values were very unreasonable. To alleviate these problems, frames which contained highly mosaic data with R-factors greater than 0.2 during the scaling step of data processing were excluded. This significantly improved the data statistics which allowed for much higher resolution cut-offs. Although a large chunk of data was discarded during this process, the symmetry of the orthorhombic space group $P2_12_12_1$ allowed processing of datasets where the completeness was still >90 %.

2.9.6 Molecular Replacement

Molecular replacement was the method used to solve the phase problem for both the original hRRM1 bound to TTP and the dATP-induced hexamers of *S. cerevisiae* Rnr1p. This method is based on the assumption that classes of proteins have homologous structural motifs

which are conserved evolutionarily. For example, the *S. cerevisiae* Rnr1p protein is very similar in structure to the hRRM1 protein even though they are separated by a large distance evolutionarily. In a molecular replacement experiment, a macromolecular X-ray crystal structure where the phases α_{hkl} are known can be used to provide the phases for a homologous structure where the phases remain unknown (Rossmann 1972). Phases for the unknown molecule may be determined by rotating and translating the structure of the protein with known phases into the same position of the homologous protein with unknown structure. This rotational and translational search can be expressed mathematically as follows:

A' = R[A] + T   **(Equation 2.4)**

Where A' is the position of the target macromolecule with unknown phases, A is the position of the homologous search macromolecule with known phases, [R] is the rotation matrix, and T is the translation vector (**Figure 2.9A**).

Molecular replacement is a six dimensional search: three angles for the rotation of the search molecule and three vectors for the x, y, and z translation. Rather than performing the search on all six variables simultaneously, it is split into two independent searches with three variables each: (1) the rotation function and (2) the translation function. This significantly reduces the amount of computing power needed to perform the molecular replacement experiments.

The rotation function was originally performed by the method of Rossmann and Blow (Rossmann *et al.* 1962):

73

$$f(R) = \int_u P_1(x)P_2(Rx)\,dV \qquad\qquad\qquad \textbf{(Equation 2.5)}$$

Where $f(R)$ is the rotation matrix that relates P_1 to P_2; P_1 and P_2 are the intramolecular Patterson functions of the target and search molecules respectively; and U is the volume over which the integration occurs. When the rotation function reaches a maximum, the search molecule is potentially in the same orientation as the target molecule. **Equation 2.5** can be rewritten in such a way that relates the structure factors of the search and the target molecules:

$$R(\alpha,\beta,\gamma) = (U/V^3)\,\Sigma_h\Sigma_p\,|F(h)|^2|F(p)|^2 G_{hh} \qquad\qquad \textbf{(Equation 2.6)}$$
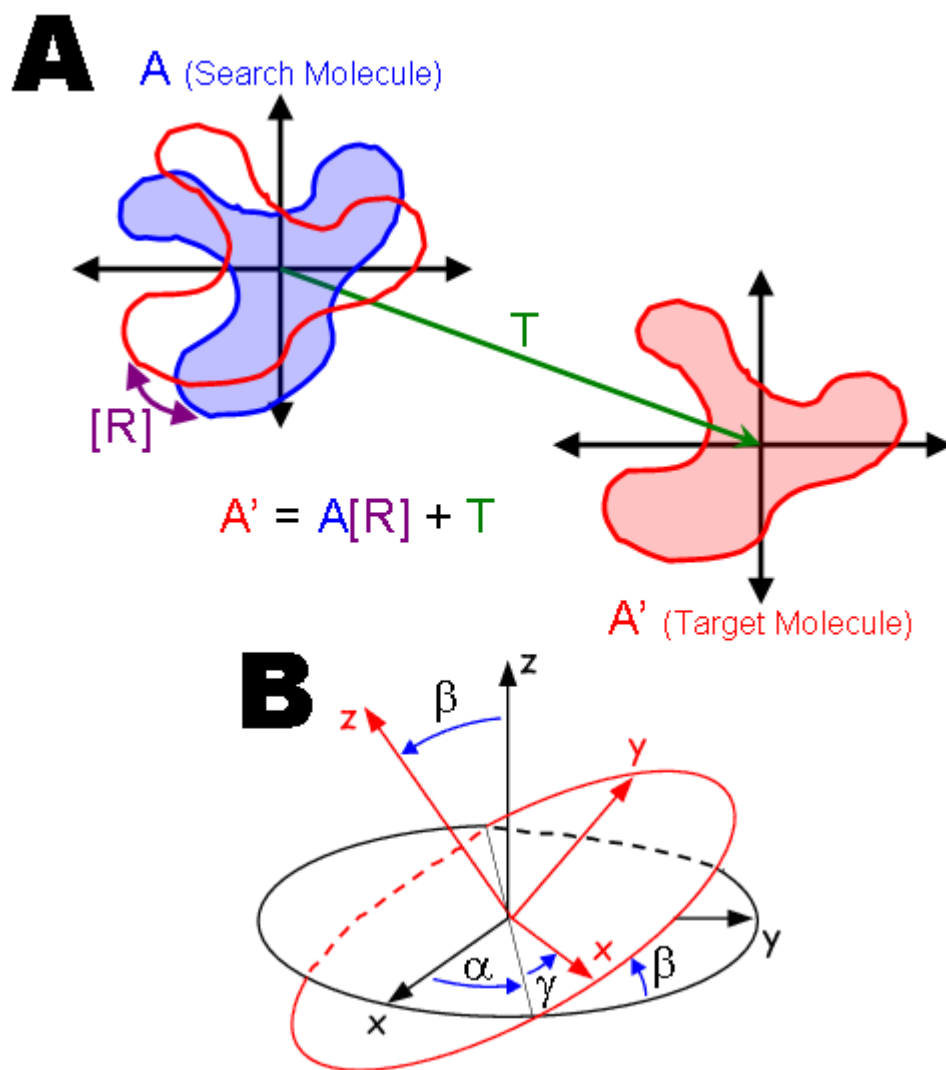
Figure 2.9: Visual representation of the molecular replacement method.
(A) The search molecule A undergoes rotation via a rotation matrix [R] and then translation by the translation vector T until it is in the same position of the target molecule A'. Molecular replacement is an iterative search through a multitude rotation matrices and translation vectors until the proper solution is found. **(B)** The Eulerian coordinate system showing the rotation angles α, β, and γ used during the rotation function shown in **Equation 2.4**. The black sphere represents the pre-rotation orientation and the red sphere represents the orientation after the rotation matrix R(α,β,γ) has been applied.

Where F(h) and F(p) are the structure factors of the target and search molecules, G_{hh} is the interference function which describes the volume U over which the function is integrated, and $R(\alpha,\beta,\gamma)$ is the rotation matrix depending upon the angles α, β, and γ (**Figure 2.9B**). The fast rotation function (Crowther 1972) is an update and modification of the rotation function published by Rossmann and Blow (Rossmann *et al.* 1962) which uses approximately 100 times less computational power to perform the search.

After the search molecule has been successfully oriented by the rotation function $R(\alpha,\beta,\gamma)$, a second search for the proper translation vector is undertaken (**Figure 2.9A**). The translation function moves the properly oriented search molecules about the unit cell and then compares the calculated structure factors from the search molecule to the observed structure factors from the target (Rossmann 1972):

$$T1(x) = \Sigma_h \ |F_{obs}(h)|^2 |F_{calc}(h,x)|^2 \qquad \textbf{(Equation 2.7)}$$

where $T1(x)$ is the T1 translation function, $F_{obs}(h)$ is the observed structure factor calculated from the intensities during the diffraction experiment, and $F_{calc}(h,x)$ is the calculated structure factor of the search molecule after the translation vector x has been applied. However, the T1 translation function only takes one of the symmetry related molecules into account, the T2 translation function is able to account for all of the symmetry operations which may occur in the unit cell and is the function most commonly used in modern molecular replacement programs:

$$T2(x) = \Sigma \ |F_{obs}(h)|^2_{cross} \ 2\Sigma_i\Sigma_j \ F_{Mi}F_{Mj} \ e^{-2\pi hx} \qquad \textbf{(Equation 2.8)}$$

where $|F_{obs}(h)|^2_{cross}$ is the corrected observed structure factors with the self Patterson contributions subtracted, and F_{Mi} and F_{Mj} are calculated structure factors for the molecule M at the positions i and j. When this function is maximized, the xyz position of the search molecule should be at the proper position to match the target molecule.

The accuracy of a molecular replacement model can be monitored via a value known as the correlation coefficient (CC). Molecular replacement solutions with larger CCs have a higher propensity for being correct. The solution with the highest CC is chosen and then subjected to rigid body refinement. The accuracy of a molecular replacement model can be monitored via the crystallographic residual or R-factor after rigid body refinement:

$$R = (\Sigma_{hkl} |\, |F_{obs}| - |F_{calc}|\, |) / \Sigma_{hkl} |F_{obs}| \qquad \textbf{(Equation 2.9)}$$

As the structure factors for the observed and calculated data become closer and closer together, the R-factor decreases. When the observed and calculated structure factors are identical, the R-factor has a value of 0. A molecular replacement solution with an R-factor value of 0.4 or lower after rigid body refinement usually results in successful determination of the phases for a structure. Molecular replacement experiments performed for hRRM1 and hexameric *S. cerevisiae* Rnr1p were performed using the program PHASER (McCoy *et al.* 2007) (see **Chapter 4**).

2.9.7 The Difference Fourier Method

For all of the *S. cerevisiae* Rnr1p mutant X-ray crystal structures and for hRRM1 X-ray crystal structures that were soaked with nucleotides, the difference Fourier method was used for structure determination. To use the difference Fourier method, the structure desired to be solved,

referred to as the "derivative" dataset, must be isomorphous to a previously determined X-ray crystal structure of the same protein, referred to as the "native" dataset. The "derivative" dataset is usually obtained from a crystal that has been soaked with some type of ligand, peptide, inhibitor, or allosteric effector which binds to the target protein at a specific location. In this dissertation research, co-crystals of Rnr1 and TTP were "derivatized" by soaking crystals with various nucleoside di- and tri-phosphates. Since the phases of the "native" dataset, α_{native}, should be approximately equal to the phases of the "derivative" dataset (ie: $\alpha_{native} \approx \alpha_{derivative}$), the atomic coordinates of the "native" structure are refined against the reflection data of the "derivative" dataset to produce a difference Fourier electron density map:

$$\Delta\rho_{xyz} = \frac{1}{V}\sum_{hkl}| F_{hkl_{derivative}} |-| F_{hkl_{native}} | e^{-2\pi i(hx+ky+lz+\alpha_{hkl_{native}})}$$

(Equation 2.10)

Where $F_{derivative}$ is the structure factor amplitude of the soaked "derivative", Fnative is the structure factor amplitude of the "native" protein structure, and α_{native} is the phase of the native protein structure. The structure factor amplitude $F_{derivative}$ is calculated directly from the intensities of the reflections output by the program Scalepack:

$I_{hkl} = |F_{hkl}|^2$

(Equation 2.11)

The structure factor amplitude F_{native} is calculated from the molecular model of the native structure as follows:

$$F_{hkl_{native}} = \sum_j n_j f_j e^{2\pi i (hx_j + ky_j + lz_j)} e^{\left[\frac{-B_j \sin^2 \theta}{\lambda^2}\right]}$$

(Equation 2.12)

Where n_j is the occupancy of each atom j, f_j is the scattering factor for each atom j, x_j,y_j,z_j are the x,y,z positions of each atom j, and B_j is the isotropic temperature factor for each atom j. The difference electron density maps produced by **Equation 2.10** are commonly referred to as "F_o-F_c" maps and will have three results: (1) areas in which there are no peaks, (2) areas where there are positive peaks, and (3) areas where there are negative peaks. Areas where the "native" and "derivative" structures match will have no difference electron density peaks. Negative electron density peaks indicate the position of atoms which are present in the "native" structure but absent in the "derivatized" structure. On the other hand, positive electron density peaks indicate the position of atoms not present in the "native" structure which are present in the newly "derivatized" structure. For example, soaking *S. cerevisiae* Rnr1p crystals with TTP and GDP results in the appearance of positive electron density peaks in the C-site and S-site, which correspond to the shape of GDP and TTP molecules. In addition, rearrangements in the "derivative" structure which took place as a result of soaking with an effector or inhibitor are easily observable. Negative F_o-F_c density will occupy the position of the misplaced atoms from the "native" structure and nearby positive F_o-F_c density indicates the position of these atoms in the "derivative" structure.

Another difference Fourier map commonly used during the modeling and refinement process is the "$2F_o$-F_c" map, which is calculated as follows:

$$\rho_{xyz} = \frac{1}{V} \sum_{hkl} (2 \,| F_{obs} | - | F_{calc} |) e^{-2\pi i(hx+ky+lz+\alpha_{hkl_{calc}})}$$ **(Equation 2.13)**

Where F_{obs} is the structure factor amplitude of the observed reflection data, F_{calc} is the structure factor amplitude calculated from the model structure, and $\alpha_{hklcalc}$ is the phase angle for the structure factor calculated from the model structure. While the F_o-F_c maps will display difference density peaks at half-height, $2F_o$-F_c maps have the advantage of displaying the differences between the model and the observed data at full height.

2.9.8 Model Building

During model building for this dissertation research, F_o-F_c difference maps were observed at a contour level of 3σ and $2F_o$-F_c difference maps were observed at a contour level of 1σ within the molecular graphics program Coot (Emsley *et al.* 2004). The model was fit into the $2F_o$-F_c density as much as possible. For regions where the $2F_o$-F_c map and model disagreed or where model had not yet been built, the F_o-F_c difference density maps were used for model building. Water molecules were added to the model either by using the automated water-picking tool within the program Coot, or manually into positive F_o-F_c difference density peaks contoured at 3σ.

2.9.9 Crystallographic Refinement

Each atom in a structural model is defined by a set of parameters: (1) the x, y, and z coordinates of each atom, (2) the B-factor of each atom defining the mobility of that atom, and (3) the occupancy of that atom. It is the job of the crystallographer to manipulate the parameters that define the molecular model such that the back-calculated structure factors F_{calc} from the

structural model are as close as possible to the observed structure factors F_{obs} from the diffraction experiment. F_{calc} can be calculated as follows (Rhodes 2000):

$$F_{calc} = G\sum_j n_j f_j e^{2\pi i(hxj+kyj+lzj)} e^{-Bj\left[\frac{\sin\theta}{\lambda}\right]2} \qquad \textbf{(Equation 2.14)}$$

Where G is a scaling factor, n_j is the occupancy of each atom j, f_j is the scattering factor for each atom j, x_j, y_j, z_j are the x,y,z positions of each atom j, and B_j is the isotropic temperature factor for each atom j. One method for monitoring the agreement between the F_{obs} and the F_{calc} was described in the previous section as the crystallographic residual or R-factor (**Equation 2.9**). The approach in crystallographic refinement is to perform a least squares minimization with the F_{obs} and F_{calc} values in between rounds of manual model building to minimize the R-factor with the function defined by Φ (Rhodes 2000):

$$\Phi = \Sigma_{hkl} \; w_{hkl}(|F_{obs}| - |F_{calc}|)^2_{hkl} \qquad \textbf{(Equation 2.15)}$$

Where w_{hkl} is a weighting term that can be used to up or down-weight a reflection hkl depending upon its reliability. For the least squares analysis, the F_{calc} for each reflection hkl is subtracted from the F_{obs} for each reflection hkl. Since F_{calc} is determined as in **Equation 2.14**, the value of F_{calc} can be altered to more closely resemble the F_{obs} by modifying the x,y,z position of each atom, the B-factor for each atom, and the occupancy of each atom of the molecular model. Modern crystallographic refinement programs also add restraints during the least squares minimization to ensure bond lengths and bond angles stay within a reasonable range:

$$\Sigma_i\, w_i(|d_{ideal}| - |d_{model}|)^2 + \Sigma_j\, w_j(|\varphi_{ideal}| - |\varphi_{model}|)^2 \qquad \textbf{(Equation 2.16)}$$

Where *w* is a weighting value, *d* is the bond length of each bond *i,* and φ is the bond angle of each bond *j*. These terms are added onto **Equation 2.15** to ensure adjustments made to the structure during least squares minimization do not violate ideal bond lengths and angles.

Each iterative cycles of refinement result in small changes to variables in **Equation 2.14**, either positive or negative. These cycles of least squares minimization are continued until the value of Φ converges to a single value, and no longer increases or decreases. One disadvantage of the least squares method is that the value of Φ will minimize to the local minimum nearest to the starting point of the refinement. It is then ideal to start the least squares minimization with the F_{calc} values as close to the F_{obs} as possible so that the value is minimized to the global minimum rather than a local minimum.

A typical step, usually performed early in the refinement process, is the application of simulated annealing (Kirkpatrick *et al.* 1983) in a program such as CNS (Brunger *et al.* 1987; Brunger *et al.* 1998) to allow the model to move out of any local minima in which it may be trapped towards the global minimum. Simulated annealing can also be used to remove any model bias if the phases of the structure were determined by molecular replacement. It is a computation process where the protein molecule is "heated" until it reaches a state where it can flow and act as a liquid. The temperature is then allowed to slowly cool such that the protein atoms will occupy the lowest energy state and approach the global minimum.

Another issue of the least squares minimization method appears because it is possible to create models in which the R-factor shows that the F_{calc} and F_{obs} match extremely well, but the

model contains obvious flaws; atoms may deviate from the ideal stereo chemical values or even worse, there may be other more serious errors in the model such as D-amino acids. To remedy this obvious problem, Brunger invented the free R-factor, which is commonly referred to as R_{free} (Brunger 1992). When calculating the R_{free} value, 5-10% of the structure factors are left out of the least squares refinement to minimize the R-factor. After the refinement takes place with the remaining 90-95% of the data, the R_{free} value is calculated using the 5-10% which were sequestered from the least squares minimization. The R_{free} value clarifies whether the differences between the F_{obs} and F_{calc} were really minimized by improving the molecular model, or whether the decrease in the R-factor was simply an artifact of the least squares minimization method. It serves as a more reliable guide for molecular modeling and refinement than the traditional R-factor.

There are a number of assumptions which must be made when performing least squares minimization (Tronrud 2004). For example, it must be assumed that all the observed F_{obs} were perfectly measured with an exact known amount of error and that the phase angles are determined with no uncertainty. Erroneous determination of phase angles and measurement of reflection intensities can lead to predicted models that are incorrect because of unpredictable errors that are present in the F_{obs} data. An alternative to the least squares method for the refinement of crystallographic parameters is the maximum likelihood method (Pannu *et al.* 1996; Murshudov *et al.* 1997). Refinement by maximum likelihood is superior to least squares because it can accommodate both F_{obs} and F_{calc} with varying amounts of uncertainty. The maximum likelihood function used in refinement programs is computed as follows (Tronrud 2004):

$$\Phi = \Sigma_{hkl} \; w_{hkl}(|F_{obs}| - <|F_{calc}|>)^2 \qquad \textbf{(Equation 2.17)}$$

where F_{obs} is the observed structure factor amplitude and $<|F_{calc}|>$ is the expectation of structure factor amplitude of the model. Unlike in the least squares method where the phase of the F_{obs} and F_{calc} are assumed to be identical, the value of $<|F_{calc}|>$ is determined by integrating over all phase angles to determine the most likely amplitude and phase angle (Tronrud 2004). The crystallographic refinement programs CNS (Brunger *et al.* 1998) and Refmac (Murshudov *et al.* 1997) used in this dissertation research both take advantage of the maximum likelihood method.

2.9.10 TLS Refinement

The position of each atom within the model of an X-ray crystal structure is approximated to be at a point xyz within the unit cell with an atomic displacement factor (ADP) that is either isotropic or anisotropic (Winn *et al.* 2003). Atomic displacement parameters are used during macromolecular refinements to provide a molecular model that more accurately describes the observed data. Isotropic ADPs, often referred to as B-factors, can be described as spherical in shape and require only a single parameter per atom to define, while anisotropic ADPs can be described as 'thermal ellipsoids' and require six parameters per atom to define (Trueblood *et al.* 1996). The six additional parameters required by modeling the ADPs as ansitropic are not justifiable unless the data is collected at almost atomic resolution (≤ 1.2 Å). Attempting to refine anisotropic ADPs at resolutions lower than 1.2 Å produces data to parameter ratios which can result in overfitting of the experimental data (Winn *et al.* 2001). Overfitting of the data can give an artificial agreement between the model and the experimental data, which may eventually lead to large errors in the model (Schomaker *et al.* 1998). For 'medium resolution data' (3.2-1.2 Å) ADPs are instead modeled as isotropic even though anisotropic motion could be present in the

model that would more accurately describe the data, because only one additional parameter is required.

Translation, libration, and screw axis (TLS) refinement provides crystallographers with a method to add anisotropic motion to their macromolecular models at medium resolutions while avoiding over-parameterization that would occur if ADPs were modeled as anisotropic (Schomaker *et al.* 1968). TLS refinement provides the description of anisotropic motion of a group of atoms using only 21 additional parameters (Winn *et al.* 2003). Therefore, the movement of a group 4 or more atoms by TLS refinement provides an overall reduction in the number of parameters required for describing anisotropic motion in the model (ie: the additional number of parameters required for individual anisotropic ADP refinement of 4 atoms is 24, 6 for each atom). The method of TLS refinement for the modeling of anisotropic motion in macromolecular models in X-ray crystallography was first reported by (Holbrook *et al.* 1984) and has been used for the refinement of many other X-ray crystal structures since then (Sali *et al.* 1992; Wilson *et al.* 2000). Refinement of structural models using TLS groups is accomplished using the computer program Refmac (Murshudov *et al.* 1997) which has recently been integrated by Martyn Winn (Winn *et al.* 2001).

To perform TLS refinement, the macromolecular model must be broken down into several rigid groups. The selection of rigid groups depends upon the protein and previous knowledge of dynamic movements in the protein. TLS groups can be as small as a single amino acid and as large as an entire polypeptide chain (Winn *et al.* 2001). For TLS refinements of structures in this dissertation, TLS groups were selected based on backbone chain breaks where parts of the model were separated by disordered regions (**Table 2.2**). This usually resulted in between three and six TLS rigid body groups being assigned per polypeptide chain. Adding a

large amount of TLS groups is not reasonable for the resolution range of any of these datasets as over parameterization would occur. Using these criterion for the assignment of TLS groups, there were typically improvements in R_{free} and R_{work} of between 1% and 4% over refinement of isotropic ADP alone, indicating that the choice of rigid groups for TLS refinement gives an improved agreement between the structural model and the observed data. Iterative cycles of

Table 2.2: TLS groups selected for refinements.

Species	Structure	Chain A TLS Groups	Chain B TLS Groups
H. sapiens	TTP	14-290, 293-316, 326-742	1-291, 294-742
H. sapiens	TTP●ATP	14-288, 295-319, 326-742	1-289, 295-318, 324-626, 634-742
H. sapiens	TTP●dATP	14-288, 295-316, 326-742	1-287, 294-629, 632-742
H. sapiens	TTP●GDP	14-289, 294-742	2-6, 9-48, 51-289, 294-628, 633-742
S. cerevisiae	S610F●dGTP●ADP	76-292, 294-459, 462-630, 638-746	N/A
S. cerevisiae	S610F●dATP●UDP	89-291, 294-459, 462-630, 369-746	N/A
S. cerevisiae	S610F●dATP●CDP	89-291, 294-319, 321-456, 463-628, 640-746	N/A

refinement in Refmac using TLS parameterization were allowed to continue until convergence was reached (ie: further cycles did not change the values of R_{free} and R_{work}).

2.10 PREPARATION OF RADIOLABELED NUCLEOTIDE STOCKS FOR ACTIVITY AND BINDING ASSAYS

Radio-labeled ^{14}C-CDP, ^{14}C-ADP, and ^{3}H-dGTP were purchased from Moravek Biochemicals, Perkin Elmer, and Amersham Biosciences, respectively. Nucleotides from these companies come in aqueous form in a 50% v/v ethanol solution. Between 50 and 100 µCi was aliquoted from the original stocks and liquid was removed from labeled nucleotides using a Savant SC110 Speed-Vac (Thermo Scientific, Waltham, MA) until the samples reached complete dryness. Radioactive stocks from these companies can vary in their concentration and specific activity from lot to lot. The amount of volume used should be carefully calculated each time, as even the same radionucleotide ordered from the same company may have a different specific activity if it is from a different lot. A 25 mM solution of unlabeled ADP or CDP or 5 mM dGTP was prepared in 50 mM HEPES pH 7.5. Approximately 200 µL of the non-radioactive ADP or CDP was then added to the tube containing the ^{14}C-labeled or ^{3}H-labeled nucleotides in lyophilized powdered form. Radio-labeled nucleotides were then re-suspended in the solution by pipetting up and down fourty to fifty times with a P-200 Micropipettor. The final concentration of CDP, ADP, or dGTP in the stock was determined spectrophotometrically using the Beer-Lambert Law (**Equation 2.1**). The extinction coefficients for ADP, CDP, and dGTP have been previously determined; ε_{270} for CDP is 9000 M^{-1}/cm, ε_{253} for GDP is 13700 M^{-1}/cm, and ε_{259} for ADP is 15400 M^{-1}/cm (Cavaluzzi *et al.* 2004). One µL of the radioactive stock was aliquoted for liquid scintillation counting and DPM/µL was determined (see **Appendix A.1**). To determine total specific activity of the radioactive stock, DPM/µL was divided by the

concentration of total ADP or CDP in nmol/µL to determine the amount of DPM/nmol total ADP or CDP. See **Appendix A.1** for a detailed example calculation.

2.11 PREPARATION OF BORATE-AFFINITY RESIN

Three hundred mL bed volume of AG-X8 anion exchange resin (Biorad, Hercules, CA) was packed into a large chromatography column (2.5 cm I.D. x 75 cm length) by gravity. Three liters of 1 M NaOH was then passed through the column to replace Cl^- ions already present on the resin with OH^-. Resin was then washed with three liters of H_2O and equilibrated with 0.6 L of 0.6 M potassium tetra-borate and allowed to incubate overnight. The following morning, loaded borate resin was washed with three more liters of H_2O and then stored in 20% (v/v) ethanol for future use. Affinity columns for the separation of substrates and products were produced by plugging the bottom of Pasteur pipettes with glass wool and then filling them with approximately 2.5 mL bed volume of loaded borate resin.

2.12 QUANTITATIVE ASSAY FOR DETERMINATION OF THE SPECIFIC ACTIVITY OF RNR1

Activity assays to determine specific activities under steady-state conditions were performed by altering the methods of Ge *et al*. (Ge *et al.* 2001; Ge *et al.* 2003). The protocol was modified to use DTT as the reductant rather than thioredoxin or glutaredoxin. This description is written for *S. cerevisiae* Rnr1p, however assays using hRRM1 were performed similarly (see below). The reaction mixture consisted of Rnr1p (1 µM), Rnr2p●Rnr4p (5 µM), effector nucleotides, and reaction buffer. Reaction buffer consisted of 20 mM HEPES pH 7.4, 200 mM potassium acetate, 20 mM magnesium acetate, 20 mM DTT, and 20 µM $FeCl_3$. When 1 mM CDP was used as substrate, the effector was 2 mM ATP. When 1 mM ADP was used as substrate, 2 mM ATP and 2mM dGTP were used as effectors. After preparing the reaction mixture described above, it was allowed to incubate at 30 ºC for three minutes. The reaction was

then initiated by the addition of either CDP or ADP with a ^{14}C-label at a specific activity between 2000 and 5000 DPM/nmol. Immediately after the addition of substrate, the reaction was mixed, a 50 μL aliquot was taken, and the reaction in the aliquot was quenched by immersing it into a boiling water bath. Additional 50 μL aliquots were removed at 4, 8, and 12 minute time points and quenched in the same boiling water bath. After boiling each reaction, precipitated proteins were removed by centrifugation at 20,000 x g for 5 minutes. Each time point was then treated with 950 μL of alkaline phosphatase (EMD Biosciences, San Diego, CA) at 42°C for 2 hours in the alkaline phosphatase buffer to remove the α- and β-phosphate groups. Removal of phosphate groups from the products and substrates is required to ensure that they do not non-specifically bind to the borate affinity resin. The alkaline phosphatase buffer consisted of 50 mM TRIS pH 9.3, 1 mM MgCl2, 0.1 mM ZnSO4, 10.5 units alkaline phosphatase/mL, and 400 μM deoxycytidine. The reaction mixture was then fed through AG 1-X8 resin (Biorad, Hercules, CA) loaded with borate to separate 2'-deoxycytidine and 2'-deoxyadenosine products from cytidine and adenosine substrates. The cis-diol of the ribose sugar on the substrates form a cyclic ester bond with the borate group on the resin (Kim *et al.* 2004) (**Figure 2.13**). Un-reacted substrate will remain bound to the column while products will flow through and be collected. Following the flow-through, an additional 8 mL of water was fed through the column. The total volume collected at
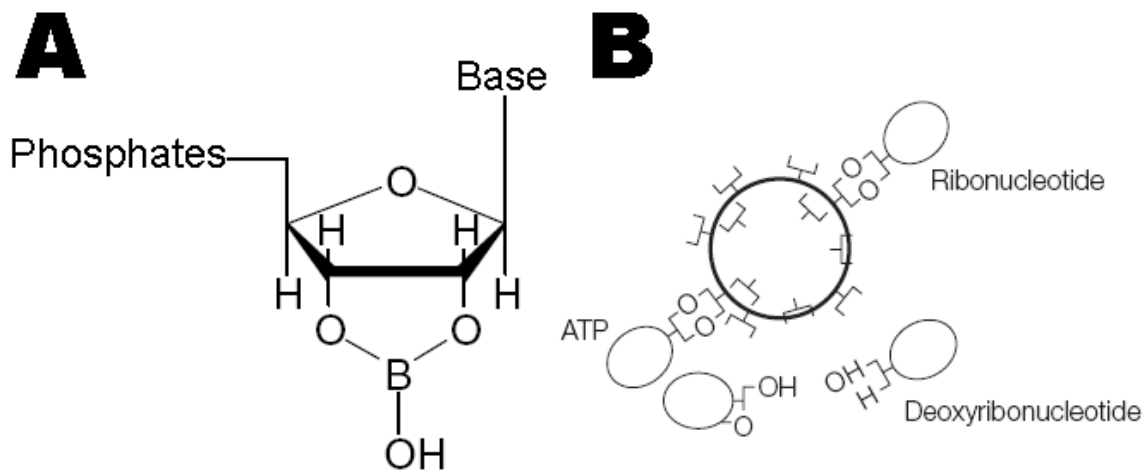
Figure 2.10: Borate binding to the cis-diol of ribonucleosides.
(A) Borate binding to a ribonucleoside base. For high-affinity binding, the –OH groups must be in the cis-diol conformation. **(B)** Schematic of a borate affinity bead. Ribonucleotides such as ATP will bind to the borate affinity resin, while deoxyribonucleosides will remain unbound and be collected in the flow-through. Figure B was adapted from the user's manual for Affi-Gel Boronate Gel (© by Bio-Rad Laboratories, Hercules, CA).

the bottom of the column should now be 8.95 mL. The amount of deoxycytidine or deoxyadenosine formed was then quantified by scintillation counting in a Beckman Coulter LS6500 Multi Purpose Scintillation Counter (Beckman, Fullerton, CA). Three milliliters out of the 8.95 was used for scintillation counting, which was corrected for mathematically during data analysis (see **Appendix A.2**). Activity assays for hRRM1 were performed under similar conditions as the *S. cerevisiae* Rnr1p assays with the following alterations: 1 μM hRRM1 and 5 μM *H. sapiens* Rnr2 were used and the temperature under which the assay was performed was changed to 37°C to match the

physiological temperature that hRRM1 is exposed to. See **Appendix A.2** for a detailed example of how to calculate the specific activity from some sample data.

Although the conditions of the *in vitro* activity assay provide the ability to determine specific actities, the concentration of the large subunit has a large effect on the k_{cat} in the *E. coli* Class Ia Rnr (Ge *et al.* 2003). When the concentration of Rnr1 monomer was between 0.05 and 0.5 μM, the k_{cat} was observed to be approximately 10 s^{-1}. However, if the concentration of Rnr1 was increased above 0.5 μM, the value of k_{cat} was observed to slowly decrease until it reached a plateau of approximately 2 s^{-1} at a concentration of 3 μM. According to this kinetic analysis, observation of the maximum value of k_{cat} will occur when the concentration of the large subunit is less than or equal to 0.5 μM (Ge *et al.* 2003).

2.13 QUANTITATIVE ASSAY FOR DETERMINATION OF THE DISSOCIATION CONSTANTS OF RNR1

The dissociation constants (K_d) of nucleotides for *S. cerevisiae* Rnr1p were determined using the experimental method developed by Dr. Sjoberg's group at the University of Stockholm (Ormo *et al.* 1990). Purified Rnr1p at a concentration of between 0.5 and 10 uM was mixed with varying concentrations of radio-labeled nucleotides in buffer containing 50 mM HEPES pH 7.6,

100 mM NaCl, 5 % glycerol (v/v), 50 mM DTT, 5 mM MgCl. Concentrations of nucleotides were chosen such that they ranged from 0.1 to 200 μM, depending on the K_d to be determined. Although the K_d values for the *S. cerevisiae* Rnr1p enzyme were unknown, the K_d values for *E. coli* Rnr1 have previously been determined (Ormo *et al.* 1990). Therefore, the concentration ranges used in the experiments were based on the previously determined values in *E. coli* (Ormo *et al.* 1990). Following incubation on ice for 5 minutes, the entire volume of the binding assay (150 μL) was loaded into the upper well of an Amicon Ultrafree-MC Ultrafiltration unit with polysulfone PTTK membranes (Millipore, Bedford, MA), with a molecular weight cut-off of 30 kDa. A 30 μL aliquot of the binding assay was removed from the upper well of the ultrafiltration device for scintillation counting and determination of the total nucleotide concentration. The ultrafiltration device then underwent centrifugation at 4000 x g for 4 minutes. After centrifugation, 30 μL of the flow-through was removed for scintillation counting and determination of the free nucleotide concentration. Concentration of bound nucleotide was calculated by subtracting the free nucleotide concentration from the total concentration before filtration. Dissociation constants were determined by fitting non-linear regressions with a one-site binding model to the data in the scientific graphing program Prism (Graphpad Software). See **Appendix A.3** for a set of detailed example calculations on some sample data.

3. STRUCTURAL AND MECHANISTIC BASIS FOR SYNTHETIC LETHALITY IN MISMATCH REPAIR-DEFICIENT YEAST HARBORING HYPOMORPHIC *RNR1* ALLELES

3.1 INTRODUCTION

This chapter will focus on two single amino acid mutants of *S. cerevisiae* Rnr1p, S269P and S610F. First the data from Dr. Julian Simon's group that led to the identification of the Rnr1 mutants causing the synthetic lethal phenotype, will be investigated in **Section 3.2**. Then, biochemical and X-ray crystallographic data generated for this dissertation research project will be presented to the reader in **Section 3.3**. The results and their implications will then be discussed in **Section 3.4**. The results of this dissertation work, along with that of Dr. Julian Simon's group, have been combined together into a manuscript which is currently submitted to the scientific journal PLoS One, entitled "Structural and Mechanistic Basis for Synthetic Lethality in Mismatch Repair-deficient Yeast Harboring Hypomorphic *Rnr1* Alleles". Experimental methods used in the dissertation research presented in this chapter have been outlined in **Chapter 2**.

Deficiencies in the mismatch repair (MMR) machinery have been linked to genetic instability and carcinogenesis. Cancers that are known to harbor defective MMR genes, such as hereditary non-polyposis colon cancer, are attractive targets for selectively-toxic chemotherapeutic agents. In an effort to identify anticancer drug targets in MMR-deficient cells, the research group headed by Dr. Julian Simon at the Fred Hutchinson Cancer Research Center carried out a genetic screen in *S. cerevisiae*. His group identified a single ribonucleotide reductase (*Rnr1p*) allele, A245V, and using directed mutagenesis, they generated additional

Rnr1p msl (for <u>m</u>ismatch repair <u>s</u>ynthetic <u>l</u>ethal) alleles. *Rnr1p^{S269P}* and *Rnr1p^{S610F} msl* alleles confer synthetic lethality in MMR-deficient haploid strains (ie: yeast cells harboring an *msl Rnr1* allele and wild-type MMR have no phenotype, but the combination of an *msl Rnr1* allele with defective MMR is lethal to the cells). Analysis of nucleotide pools in *msl* strains of *S. cerevisiae* revealed severe under-production of dATP. Crystal structures of Rnr1p-S269P and Rnr1p-S610F mutant proteins reveal deformations in the specificity site (S-site) and the catalytic site (C-site), respectively. Both mutations weaken allosteric specificity control over reduction of ribonucleotide diphosphates leading to a drastic decrease in ribonucleotide reductase catalytic proficiency and unbalanced dNTP pools. *In vitro* activity assays of these mutants also indicated severe impairment of catalytic activity as compared to the wild-type enzyme. Combined together, these studies suggest a new therapeutic strategy involving deregulation rather than inhibition of Rnr activity as a context-specific, synthetic lethal therapeutic strategy for MMR-deficient tumors.

3.2 BACKGROUND AND OBJECTIVES

Section 3.2 consists of background and preliminary data produced by Dr. Julian Simon's research group describing the generation of *msl Rnr1* alleles. Ribonucleotide reductases catalyze the reduction of ribonucleotide diphosphates to their corresponding deoxyribonucleoside diphosphates. As the only *de novo* source of dNTPs in mammalian cells, ribonucleotide reductase is an attractive anti-proliferative therapeutic drug target. Hydroxyurea, gemcitabine, and clofarabine are among the FDA-approved drugs for the treatment of various cancers that target ribonucleotide reductases (Shao et al. 2006).

The mismatch repair system plays a major role in genome stability during repeated replication (Kolodner *et al.* 1999; Marti *et al.* 2002; Surtees *et al.* 2004). The loss of MMR

function is mutagenic and has been shown to be a causative factor in cancers with microsatellite instability (MIN), such as hereditary non-polyposis colon cancer (Bronner *et al.* 1994; Papadopoulos *et al.* 1994). The MMR system is best characterized in *E. coli*, where *MutS*, *MutL*, *MutH*, and *UvrD* are the essential components (Welsh *et al.* 1987; Ban *et al.* 1998; Dao *et al.* 1998; Hall *et al.* 1998; Ban *et al.* 1999; Hall *et al.* 1999; Lamers *et al.* 2000; Mechanic *et al.* 2000; Obmolova *et al.* 2000). All eukaryotes have MutS homologues (MSHs) and MutL homologues (MLHs), but appear to lack MutH or UvrD homologues. Unlike prokaryotes, where MutS and MutL function as homodimers, eukaryotic MSHs and MLHs form heterodimers with multiple proteins. *S. cerevisiae* has six MSH genes (*MSH1-6*) and four MLH genes (*PMS1*, *MLH1-3*) (Kolodner *et al.* 1999; Marti *et al.* 2002). There are two major MutS heterodimeric complexes: Msh2p•Msh6p (MutSα) and Msh2p•Msh3p (MutSβ). MutSα functions in the repair of mismatches and a range of insertion/deletion loops (IDLs), and MutSβ primarily functions in the repair of IDLs (Alani 1996; Habraken *et al.* 1996; Marsischky *et al.* 1996). The major MutL heterodimeric complex in yeast is Mlh1p•Pms1p (MutLα), which is able to interact with both MutSα and MutSβ (Prolla *et al.* 1994). MMR strand recognition in eukaryotes is not as well understood as it is in prokaryotes, but it has been shown that the machinery preferentially excises mismatches from nicked DNA, such as those found on the lagging strand (Pavlov *et al.* 2003).

Since MIN tumors have an MMR-deficient background while somatic cells are MMR-proficient, Dr. Simon's group hypothesized that screening for mutations that are mismatch repair synthetic lethal (*msl*) in yeast may identify targets for selective drug toxicity in mammalian cells. His screen uncovered several strong *msl* alleles in the proofreading subunits of DNA polymerases δ (*POL3*), ε (*POL2*), and more importantly, a weak *msl* allele of *Rnr1p*, A245V.

To identify mutations that were synthetically lethal with defects in the mismatch repair pathway, Dr. Simon's group screened approximately 400,000 colonies of an ethylmethanesulfonate (EMS) mutagenized *mlh1Δ* strain of *S. cerevisiae*. One of the colonies isolated in the screen was rescued by a yeast genomic library plasmid that complemented the synthetic lethal phenotype. The library insert contained the open reading frames for four genes: (1) *YER071C*, (2) *VTC1*, (3) *ALD5*, and (4) *Rnr1p*. Of the four genes present on the rescuing plasmid, only a plasmid containing wild-type *Rnr1p* was able to rescue the synthetic lethality phenotype of the colony. Eventually, the genomic copy of *Rnr1p* from the colony displaying the *msl* phenotype was sequenced, revealing a single amino acid substitution, A245V.

With the sequencing of the A245V mutant, Dr. Simon's group showed that mutations in *Rnr1p* are capable of displaying synthetic lethality with a mismatch repair gene, in this case *MLH1*. To identify additional *msl* alleles, the coding region of *Rnr1p* underwent large-scale targeted mutagenesis using PCR amplification, which yielded approximately 1 nucleotide mis-incorporation event per PCR product. Mutagenized plasmids were then transformed into *Rnr1ΔRnr3Δ* haploid strains to test for viability of mutagenized *RNR1p* alleles. Approximately 10,000 functionally viable mutated *Rnr1p* alleles were observed. Each of the 10,000 viable mutant alleles of *Rnr1p* was then transformed into *MLH1* and *mlh1Δ* strains of *S. cerevisiae* to test each one for the *msl* phenotype. Several mutant *Rnr1p* alleles were observed to give the *msl* phenotype. However, only two retained the *msl* phenotype when expressed under the control of the native *Rnr1p* promoter: (1) $Rnr1^{S269P}$ and (2) $Rnr1^{S610F}$. The $Rnr1^{S269P}$ and $Rnr1^{S610F}$ alleles were also observed to be synthetically lethal in *pms1Δ* and *msh2Δ* strains, indicating that these alleles are synthetically lethal with MMR defects, not just the loss of the *MLH1* gene (**Figure A.6**).

Dr. Simon's group then measured the genomic instability induced by the $Rnr1^{S269P}$ and $rnr1^{S610F}$ alleles of $Rnr1p$ expressed in plasmids under control of the native $Rnr1p$ promoter in $Rnr1\Delta$ $Rnr3\Delta$ yeast. The mutation rates were measured to be 9-fold and 60-fold higher than the wild-type for $Rnr1^{S610F}$ and $Rnr1^{S269P}$, respectively. Not only that, but in both the $Rnr1^{S269P}$ and $Rnr1^{S610F}$ strains, the vast majority of substitutions occurred in AT base pairs (92% for $Rnr1^{S269P}$ and 87% for $Rnr1^{S610F}$), and the vast majority of frameshifts were deletions of an AT base pair (100% for $Rnr1^{S269P}$ and 93% for $Rnr1^{S610F}$). These results suggested that the msl phenotype observed in MMR-deficient yeast cells was due to skewed nucleotide pools, where either dATP or TTP levels were too low.

Dr. Simon's group then measured the nucleotide pools of yeast cells carrying the $Rnr1^{S269P}$ and $Rnr1^{S610F}$ alleles during mid S-phase. The dNTP pool measurements obtained for the $Rnr1^{S269P}$ and $Rnr1^{S610F}$ alleles were similar to one another. All of the dNTPs were within 1 to 2.4-fold of wild-type levels except for dATP. The concentration of dATP was measured to be 3.7-fold lower in the $Rnr1^{S269P}$ allele and 9.7-fold lower in the $Rnr1^{S610F}$ allele. Combined with the mutation data, the msl phenotype seemed to be caused by skewed nucleotide pools where the concentration of dATP was deficient during S-phase. To test this hypothesis, his group attempted to rescue the msl phenotype by supplementing the growth media with 8 mM dAMP, which can be directly imported into the cells and phosphorylated to obtain dATP. Inclusion of dAMP at this concentration was able to rescue the msl phenotype of $Rnr1^{S610F}$ but not $Rnr1^{S269P}$.

Potential cell death mechanisms due to the msl phenotype include random mutational catastrophe or damage to a subset of AT-rich essential genes, which may be vulnerable to a frameshift deletion or mutation in a low dATP environment. To determine which of these two possibilities was causing cell death, the msl $Rnr1p$ alleles were transferred into diploid yeast

cells. Diploid cells should be resistant to the random mutational catastrophe mechanism, as mutation of an essential gene must occur at two independent locations, and less resistant to the AT-rich gene deletion/mutation mechanism. An attenuated *msl* phenotype is still visible in $Rnr1^{S269P}$ strains in diploid yeast cells, suggesting that the mechanism of cell death yeast carrying the $Rnr1^{S269P}$ allele is not due to mutational catastrophe but rather through mutation of a limited subset of AT-rich genes since. However, the results for $Rnr1^{S610F}$ were inconclusive as the $Rnr1^{S610F}$ mutant allele does not support growth in either *mlh1*-/- or *MLH1*+/+ background in diploid cells.

The goal of the dissertation research presented in this chapter has been to characterize the two mutant proteins, Rnr1p-S269P and Rnr1p-S610F, *in vitro* in an attempt to understand the molecular mechanism(s) in Rnr1p causing the observed *msl* phenotype. To accomplish this, both biochemical characterizations and the technique X-ray crystallography were utilized. Each mutant was first subjected to an *in vitro* activity assay to measure the rate at which the substrates CDP and ADP were reduced. Rnr1p-S269P and Rnr1p-S610F were then crystallized and soaked with the effector-substrate pairs to observe changes that might occur in the C-site and S-site due to these mutations. Analysis of the X-ray crystal data suggests a mechanism for the Rnr1p-S269P mutant, but not for Rnr1p-S610F. To investigate the Rnr1p-S610F mutant further, *in vitro* nucleoside binding assays were performed.

3.3 EXPERIMENTAL RESULTS

3.3.1 *In vitro Ribonucleotide Reductase Activity Assays*

Since skewed pools of nucleotides were observed in yeast cells harboring the *msl* alleles $Rnr1^{S269P}$ and $Rnr1^{S610F}$ by Dr. Simon's group, the catalytic activities of both mutants for the substrates CDP and ADP were determined. Plasmid containing the wild-type Rnr1p was

mutagenized as detailed in **Section 2.1**. Mutant proteins were expressed and purified as in **Section 2.4**. The Rnr1p-S269P and Rnr1p-S610F mutant proteins had identical chromatographic profiles to that of the wild-type during purification (**Figure 2.1**). Using an *in vitro* activity assay (see **Section 2.12** and **Apendix A.2**), both the S269P and S610F Rnr1p point mutants were evaluated for their ability to reduce CDP and ADP substrate to dCDP and dADP, respectively. As shown, the CDP reductase activity of the Rnr1p-S269P and Rnr1p-S610F mutants is diminished to 7.6% and 4.6% specific activity of the wild-type respectively (**Figure 3.1A**). In addition, the Rnr1p-S269P and Rnr1p-S610F mutants also had diminished ADP reductase activity, 15.9% and 0.7% respectively, as compared to the wild-type (**Figure 3.1B**).

3.3.2 X-ray Crystal Structures of Rnr1p-S269P and Rnr1p-S610F

To investigate the structural consequences of the Rnr1p-S269P and Rnr1p-S610F mutations, X-ray crystal structures of the Rnr1p-S269P mutant were solved soaked with
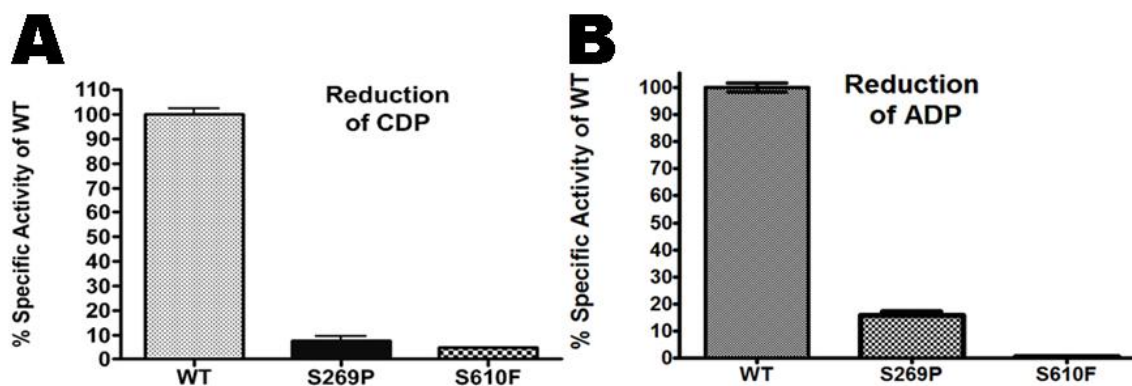
Figure 3.1: Comparison of wild-type, Rnr1p-S269P and Rnr1p-S610F mutant Rnr1p activities
Specific activities of Rnr1p were determined by ^{14}C-CDP and ^{14}C-ADP reduction. Activities of the mutant Rnrs were are normalized against the activity of the wild-type. (**A**) The specific activities of the Rnr1p-S269P and Rnr1p-S610F mutants are 7.6% and 4.6% of the wild-type activities for CDP reduction, respectively. (**D**) Rnr1p-S269P and Rnr1p-S610F mutants also had reduced specific activities for ADP as compared to the wild-type, 15.9% and 0.7% respectively.

dGTP●ADP and TTP●GDP, and the Rnr1p-S610F mutant in complex with dATP●CDP, dATP●UDP, and dGTP●ADP cognate effector-substrate combinations. The highest resolution structure was determined at 2.1 Å for the Rnr1-S269P mutant in complex with dGTP-ADP and the lowest resolution structures were determined at 2.8 Å for both of the Rnr1-S610F effector-substrate pairs. The Rnr1p-substrate-effector complexes reported were obtained via the soaking method as described in **Section 2.8.5**. Structures of both Rnr1p-S269P and Rnr1p-S610F complexes were solved using the difference Fourier method because the crystals were isomorphous with the wild-type crystals. Data collection and refinement statistics for all datasets are presented in **Table 3.1** and **Table 3.2**.

The Rnr1p-S269P point mutation is found within the Loop 1 region, which is responsible for binding nucleotide effectors to the S-site. Particularly, S269 interacts with the effector bound to the S-site via water-mediated hydrogen bonds. There are two major changes that take place when comparing the Rnr1p-S269P mutant structure to the wild-type structures. First, a large portion of Loop 1 is disordered in both of the Rnr1p-S269P structures as compared to the wild-type (**Figure 3.2** and **Figure 3.3**). There is no electron density present for any of the residues from positions 258-270 and 261-269 in the dGTP●ADP and TTP●GDP soaked structures, respectively. Since mutating serine 269 to proline destabilizes Loop 1, effector nucleotides can no longer bind to the S-site, and no electron density is visible for either dGTP or TTP in the Rnr1p-S269P structures (**Figure 3.2** and **Figure 3.3**). Furthermore, since there is no effector bound at the S-site, residues that make up Loop 2, which bridges the S-site and the C-site, are also disordered and no electron density is observable in the Rnr1p-S269P mutant X-ray crystal structures

Table 3.1: Data collection and refinement statistics for the Rnr1p-S269P mutant.

Name of Data	S269P●dGTP●ADP	S269P●dTTP●GDP
Space Group	P2$_1$2$_1$2	P2$_1$2$_1$2
Cell Dimensions		
a,b,c	108.7,117.1,63.4	106.1,116.4,63.2
α,β,γ	90,90,90	90,90,90
wavelength	0.9002	0.9002
resolution	50-2.15	27.3-2.60
unique reflections	43786	23884
R$_{sym}$	5 (45.6)	11 (35.3)
I/σ	26.8 (2.58)	14.4 (3.8)
completeness	98.7 (98.8)	96.6 (85.6)
redundancy	4.4	5.5
Refinement		
resolution	50-2.15	50-2.6
# reflections	39354	21415
R$_{work}$/R$_{free}$ ▲	22.01/26.47	21.39/28.44
# Atoms	5173	5322
protein	4915	5151
ligand/ion	32	27
water	226	144
Average B-factors		
protein	48.4	56.9
ligand/ion	74	61.5
water	48.7	49.3
RMS Deviations		
bond length	0.012	0.013
bond angle	1.463	1.563

▲ R$_{work}$ and R$_{free}$ = $\Sigma||F_o|-|F_c||/\Sigma|F_o|$, where F$_o$ and F$_c$ are the observed and calculated structure factor amplitudes. For the calculation of R$_{free}$, 10% of the data were selected and omitted from refinement.

Table 3.2: Data collection and refinement statistics for the Rnr1p-S610F mutant.

Name of Data	S610F●dATP●CDP	S610F●dATP●UDP	S610F●dGTP●ADP
Space Group	$P2_12_12$	$P2_12_12$	$P2_12_12$
Cell Dimensions			
a,b,c	107.9,117.5,64.9	107.9,117.1,64.4	107.8,117.4,64.6
α,β,γ	90,90,90	90,90,90	90,90,90
wavelength	0.9002	0.9002	0.9002
resolution	50-2.8	50-2.8	50-2.2
unique reflections	19901	19406	41089
R_{sym}	9.8 (31.8)	9.3 (46.4)	7.7 (46.3)
I/σ	10.14 (2.29)	13.62 (2.06)	19.88 (2.51)
completeness	95.1 (75.3)	93.2 (71)	96.2 (86.3)
redundancy	3.5	3.9	5.8
Refinement			
resolution	50-2.8	50-2.8	50-2.2
# reflections	17916	17417	36945
R_{work}/R_{free} ▲	22.75/27.99	21.76/27.7	21.19/26.83
# Atoms	5331	5298	5583
protein	5195	5202	5272
ligand/ion	55	55	58
water	81	41	253
Average B-factors			
protein	46.9	55.6	48.5
ligand/ion	55.7	67.5	45.2
water	38.9	46.7	48.1
RMS Deviations			
bond length	0.009	0.01	0.013
bond angle	1.402	1.308	1.506

▲R_{work} and $R_{free} = \Sigma||F_o|-|F_c||/\Sigma|F_o|$, where F_o and F_c are the observed and calculated structure factor amplitudes. For the calculation of R_{free}, 10% of the data were selected and omitted from refinement.
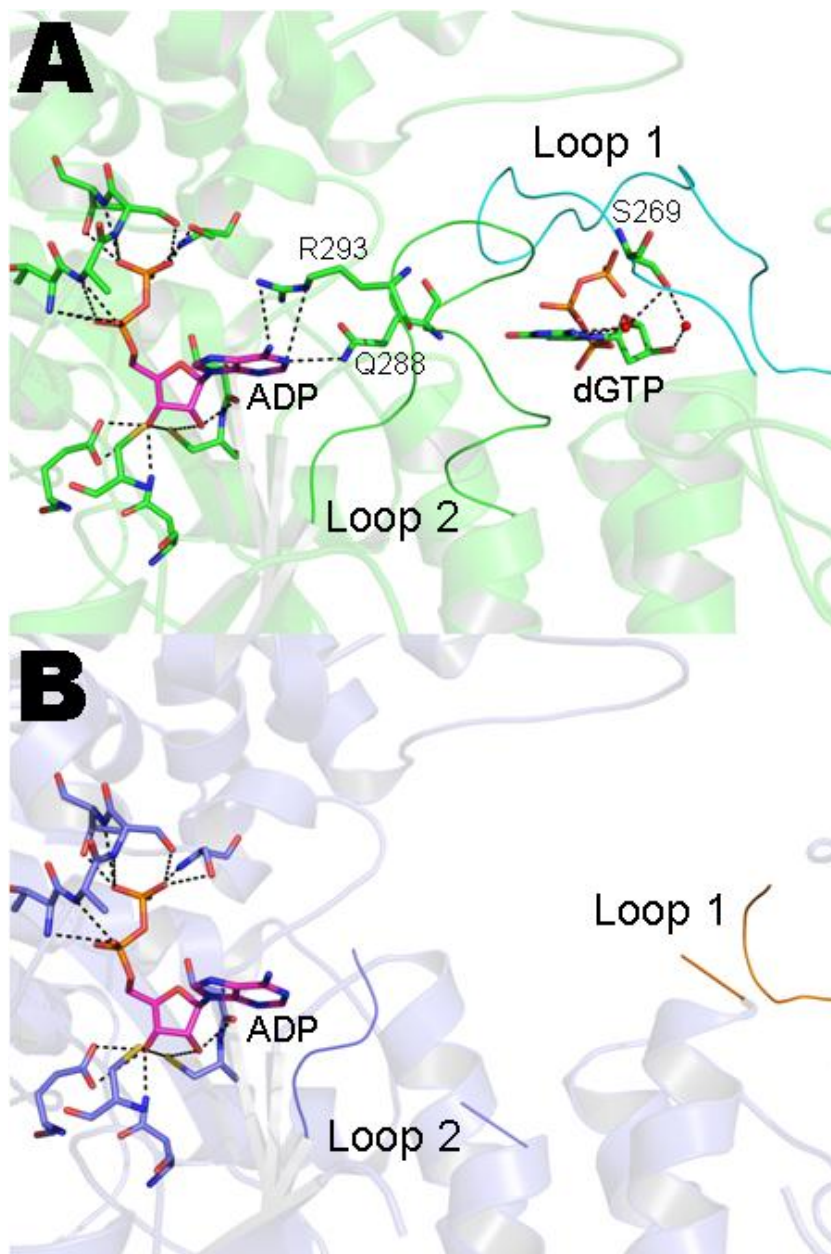
Figure 3.2: The C- and S-sites of WT and S269P Rnr1p complexed with dGTP and ADP.
(**A**) WT Rnr1p complexed with dGTP and ADP. Amino acids in the C-site plus residues S269 are shown as sticks with green carbons, blue nitrogens, and red oxygens. Loop 1 is shown in cyan and Loop 2 is shown in green. dGTP and ADP are shown in stick form with green carbons, blue nitrogens, red oxygens, and orange phosphorous atoms, while ADP is shown with magenta carbons. (**B**) Rnr1p-S269P complexed with dGTP and ADP. Amino acids in the C-site are shown as sticks with sky-blue carbons, blue nitrogens, and red oxygens. Loop 1 is shown in orange and Loop 2 is shown in sky-blue. ADP is shown in stick form with magenta carbons and orange phosphorous atoms.
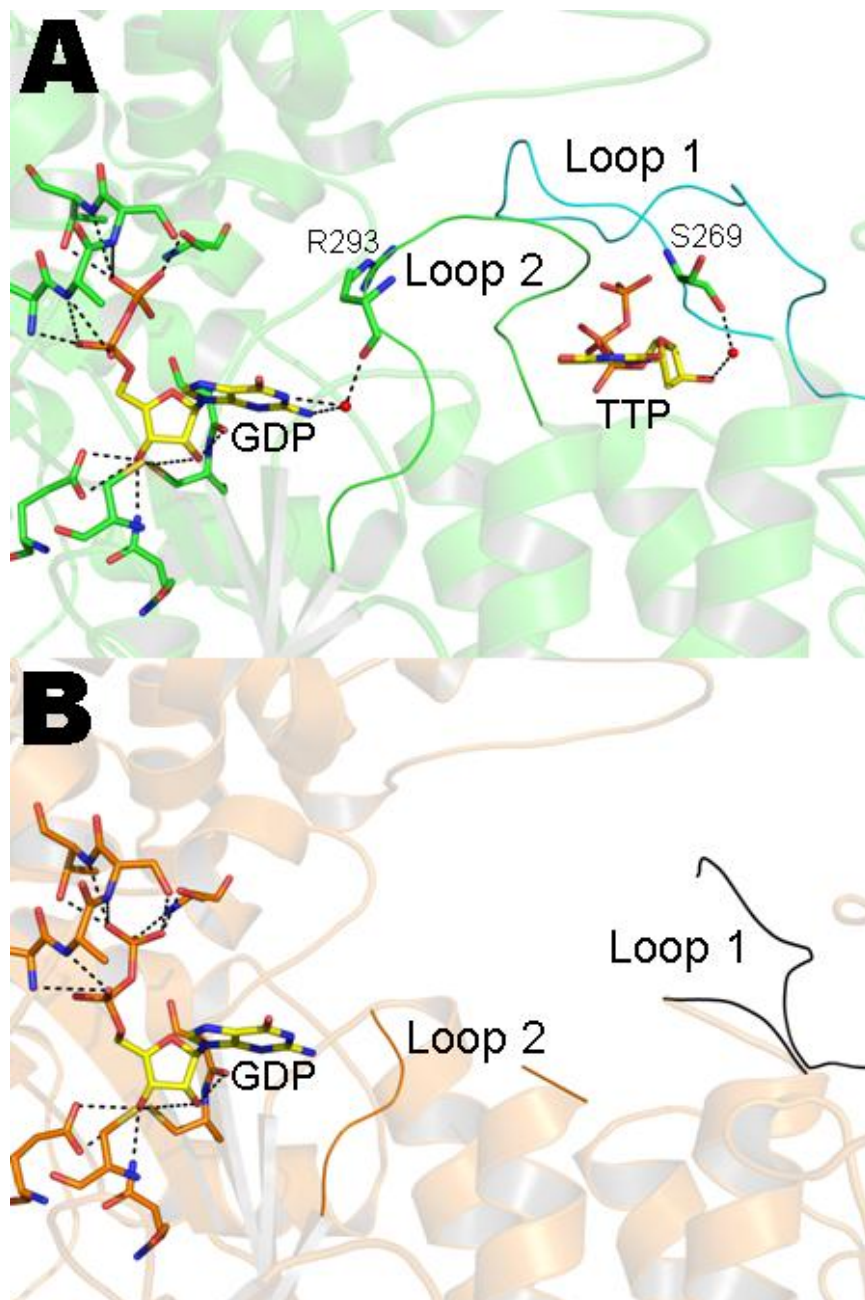
Figure 3.3: The C- and S-sites of WT and S269P Rnr1p complexed with TTP and GDP.
(A) WT Rnr1p complexed with TTP and GDP. Amino acids in the C-site plus residues S269 are shown as sticks with green carbons, blue nitrogens, and red oxygens. Loop 1 is shown in cyan and Loop 2 is shown in green. TTP and GDP are shown in stick form with yellow carbons, blue nitrogens, red oxygens, and orange phosphorous atoms. **(B)** Rnr1p-S269P complexed with TTP and GDP. Amino acids in the C-site are shown as sticks with orange carbons, blue nitrogens, and red oxygens. Loop 1 is shown in black and Loop 2 is shown in orange. GDP is shown in stick form with yellow carbons, blue nitrogens, red oxygens, and orange phosphorous atoms.

104

(**Figure 3.2** and **Figure 3.3**). This region of disorder covers residues 287 through 294 and residues 287 through 293 of Loop 2 in the dGTP●ADP and TTP●GDP structures, respectively. Although specificity cross-talk via Loop 2 is destroyed by the S269P mutation, substrates still bind to the C-site, apparently via a hydrogen bonding network with the phosphate and sugar moieties of the ADP and GDP, which appears to be conserved in the Rnr1p-S269P mutant protein (**Figure 3.2** and **Figure 3.3**). Furthermore, the average B-factors for the atoms of both the ADP (Rnr1p-S269P 74.8 $\mathring{A}^2$; WT Rnr1 40.2 $\mathring{A}^2$) and GDP (Rnr1p-S269P 53.6 $\mathring{A}^2$; WT Rnr1 45.5 $\mathring{A}^2$) bound at the 105atalytic-site are higher in the Rnr1p-S269P mutant X-ray structure than in the wild-type, suggesting that the substrate may not be bound as tightly to the C-site in the Rnr1p-S269P mutant as compared to the wild-type. This is consistent with the observed decrease in activity (**Figure 3.1A** and **3.1B**).

The S610F point mutation is also deleterious to the activity of the enzyme, reducing the specific activity to 4.6 percent (CDP reduction) and 0.7 percent (ADP reduction) of the wild-type enzyme (**Figure 3.1A** and **3.1B**). The Rnr1p-S610F mutant was crystallized under identical conditions to that of the wild-type and Rnr1p-S269P mutant as reported in **Section 2.8.5**. Crystals were soaked with the nucleotide combinations dATP●CDP, dATP●UDP, or dGTP●ADP, and X-ray diffraction data were collected to a resolution of 2.8, 2.8, and 2.2 Å, respectively (**Table 3.2**).

Serine 610 interacts with the β-phosphate of the substrate bound in the C-site of the wild-type R1 via hydrogen bonds between the Oγ of S610 and the oxygen group(s) of the β-phosphate (Xu *et al.* 2006). The three crystal structures of the Rnr1p-S610F mutants in complex with effectors and substrates are very similar to the wild-type. Both effector and substrate are bound in the S- and C-sites for all combinations, and have observable electron density in their 2Fo-Fc

maps (**Figure 3.4**). However, in the dATP●CDP structure, the side-chain of R293, which is involved in conferring specificity, is disordered (Xu *et al.* 2006). The average temperature factor for the UDP in the Rnr1p-S610F●dATP●UDP structure is 88 Å^2 while it is 52.1 Å^2 when bound to wild-type, indicative of weaker binding between UDP and the mutant protein. On the other hand, effectors and substrates for both the dGTP●ADP and dATP●CDP combinations have B-factors which are comparable to the wild-type structure (Rnr1p-S610F B-factors ADP=52.2 Å^2; CDP=63.3 Å^2). Although phosphate binding should be somewhat weakened by this mutation, this alone is insufficient to explain the huge loss of activity (**Figure 3.1A** and **3.1B**). Interestingly, the substitution of Rnr1p-S610F by the larger aromatic group causes the phenyl ring to extend into the nucleotide base binding site.

The Rnr1p-S610F●dGTP●ADP ternary complex structure shows the loss of three hydrogen-bonding interactions to the diphosphate of the substrate, including one due to the Ser to Phe mutation resulting in the loss of the hydroxyl donor of the Oγ of S610 (**Table 3.3** and **Figure 3.5**). Mutation of serine 610 to phenylalanine slightly affects the conformation of the adjacent amide of residue 609 such that it cannot hydrogen bond to the oxygen atom of the β-phosphate, and the side chain of S202 in the mutant is also too far away to make a hydrogen bond to O1β of the β-phosphate. The Loop 2 conformation is fairly well conserved between the mutant and wild-type. However, the residue R293 proposed to be involved in substrate recognition (Xu *et al.* 2006), which makes hydrogen bonds and stacking interactions to the adenine base, has an altered conformation in the mutant and is unable to make the same interactions (**Figure 3.5**).
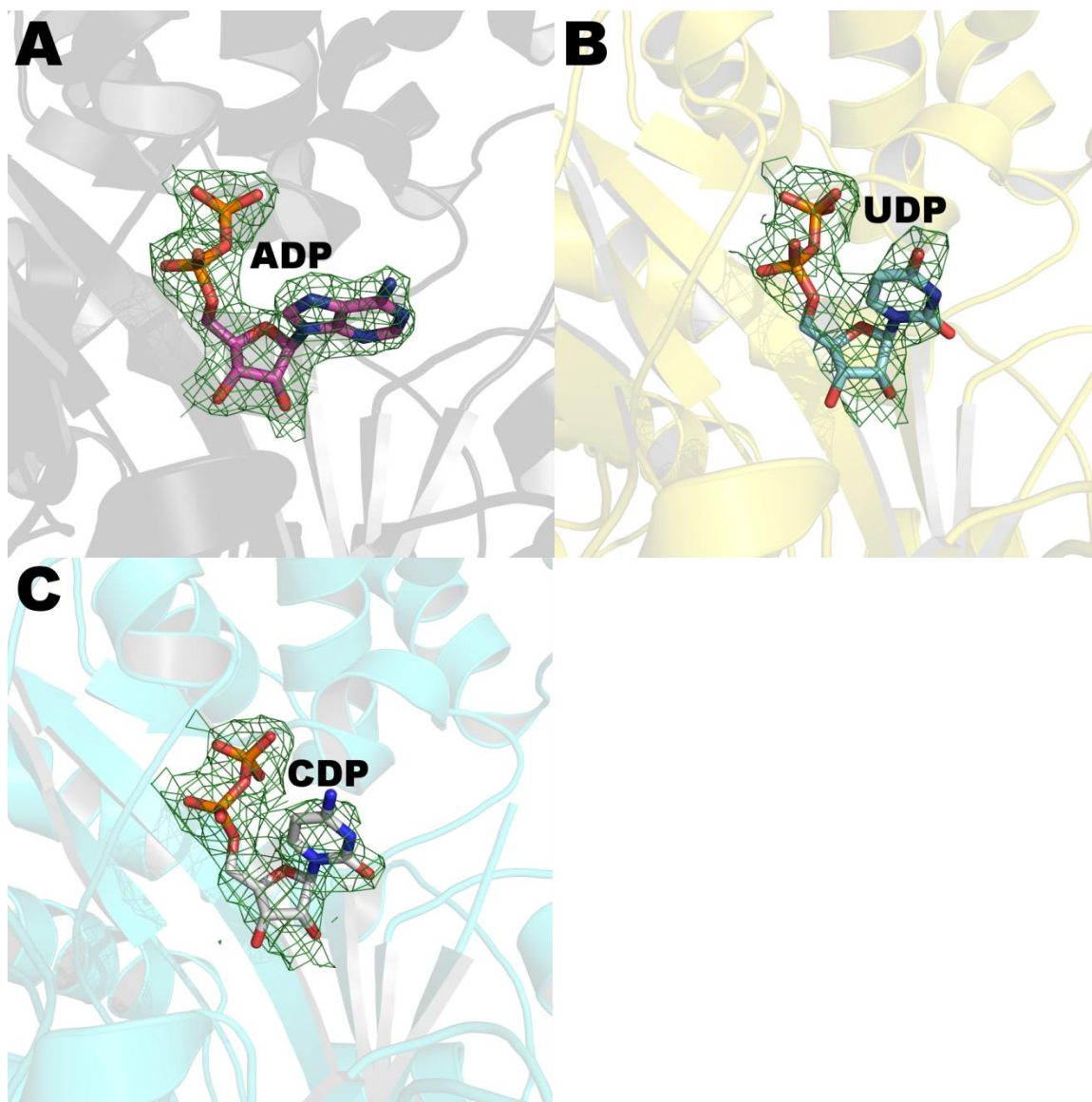
Figure 3.4: $2F_o$-F_c electron density of substrates bound to the C-site of Rnr1p-S610F. $2F_o$-F_c density is shown as green for the Rnr1p-S610F R1 C-site with **(A)** ADP (shown with magenta carbons), **(B)** UDP (shown with cyan carbons), and **(C)** CDP (shown with white carbons) bound. The electron density is contoured at 1σ in A, B, and C.

Table 3.3: Hydrogen bond distances between Rnr1p and ADP bound at the catalytic site in both the wild-type and Rnr1p-S610F mutant.

Wild-type bound to dGTP and ADP			S610F bound to dGTP and ADP		
Hydrogen Bonds to Base and Ribose			Hydrogen Bonds to Base and Ribose		
Ligand	Protein	Distance[*]	Ligand	Protein	Distance[*]
N1	Q288 Nε2	2.92	N1	Q288 Nε1	3.18
	R293 NH2	3.45			
N3	G246 N via water		N3		
	G247 N	3.13		G247 N	3.03
N6	P294 O via water		N6		
2' OH	S217 O	3.01	2' OH	S217 O	2.93
	C218 Sγ	3.41		C218 Sγ	3.43
	G247 O via water			G247 O via water	
	N426 Nδ2 via water				
	L427 N via water			L427 N via water	
3' OH	C218 Sγ	3.31	3' OH	C218 Sγ	3.5
	N426 Nδ2	2.72		N426 Nδ2	2.9
	E430 Oε1	2.54		E430 Oε1	2.6
	E430 Oε2	3.1		E430 Oε2	3.1
Phosphate Hydrogen Bonds			Phosphate Hydrogen Bonds		
O1A	A609 N	2.82	O1A	A609 N	2.8
O2A	T608 N	2.68	O2A	T608 N	2.77
O1B	S202 N	2.91	O1B	S202 N	2.88
	S202 Oγ	3.31			
O2B	S202 Oγ	2.57	O2B	S202 Oγ	2.64
	S610 Oγ	3.32			
O3B	A609 N	3.39	O3B		
	S610 N	3.18		F610 N	3.47
	T611 N	3.08		T611 N	3.04
	T611 Oγ	2.81		T611 Oγ	2.62

*Distances are defined in Angstroms.
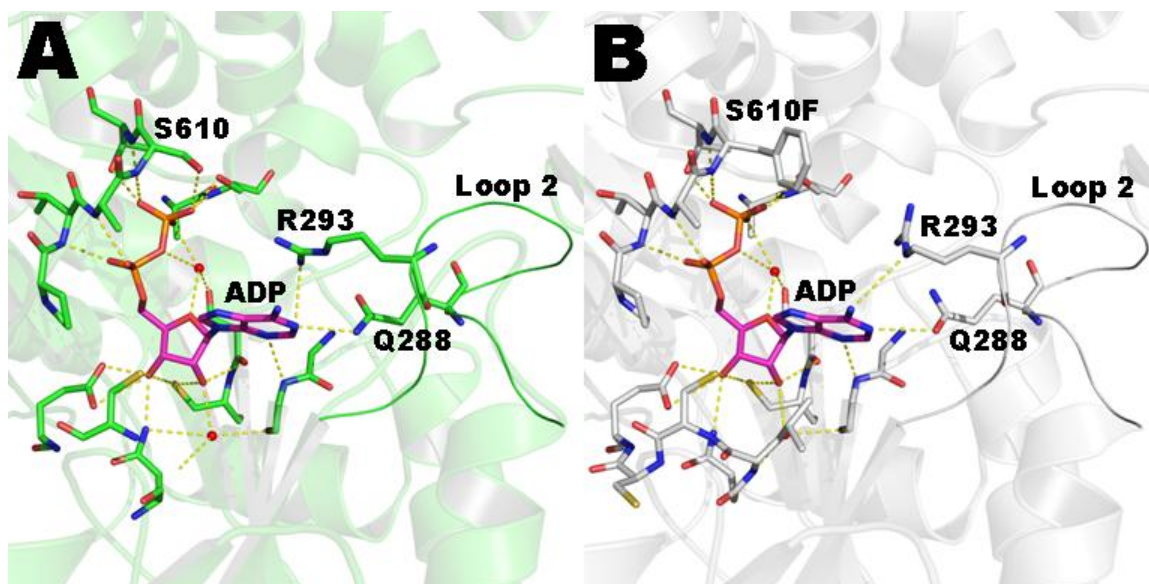
Figure 3.5: Comparison of C-site between wild-type Rnr1p and Rnr1p-S610F bound to dGTP and ADP.

(A) C-site interactions, shown as dashed yellow lines, when ADP is bound to the wild-type Rnr1p. For the protein, carbon atoms are rendered as green, nitrogens are blue, and oxygens are red. For the ADP substrate, carbons are rendered magenta and phosphorous atoms are orange. **(B)** Representation of the C-site of Rnr1p-S610F bound to ADP. Interactions are shown as yellow dashed lines. Protein carbons are colored as white, nitrogens are blue, and oxygens are red. ADP is colored as in (A).

In the Rnr1p-S610F●dATP●CDP ternary complex structure there are subtle structural differences which result in a net loss of one hydrogen bond compared to the wild-type (**Table 3.4**). Compared to the wild-type, one hydrogen bond is gained between the backbone N of F610 and O1 of the β-phosphate in the mutant, while one hydrogen bond is lost due to increased distance between the Oγ of S202 and O3B of the β-phosphate. Additionally, the oxygen atoms of the β-phosphate are rotated by sixty degrees as compared to the wild-type (**Figure 3.6**). An additional hydrogen bond is lost between the ribose ring of the substrate and of Rnr1p. Specifically, the loop region from residue 243 to 247 is slightly shifted, which results in the loss of the hydrogen bond between the backbone N of G247 and the 2' OH (**Figure 3.6** and **Table 3.4**). Loop 2 adopts a similar conformation in the mutant as compared to the wild-type. However, there are small differences that lead to alterations in the side-chain conformations of residue Q288, which is involved in specificity crosstalk (**Figure 3.6**). In addition, the residue R293 is disordered in this structure and no electron density is observed for either its main-chain or side-chain atoms.

The Rnr1p-S610F●dATP●UDP ternary complex, when compared to the wild-type structure, has a net loss of three hydrogen bonds between residues in the catalytic site and the UDP substrate (**Figure 3.7** and **Table 3.5**). The phosphate groups of the substrate lose one hydrogen bond from the T611 amide nitrogen to O1 of the β-phosphate in the mutant as compared to the wild-type. However, there are two new hydrogen bonds observed: one between the T608 N and O2 of the α-phosphate and another between the S202 Oγ and O3 of the β-phosphate.

Table 3.4: Hydrogen bond distances between Rnr1p and CDP bound at the catalytic site in both the wild-type and Rnr1p-S610F mutant.

Wild-type bound to AMPPNP and CDP			S610F bound to dATP and CDP		
Hydrogen Bonds to Base and Ribose			Hydrogen Bonds to Base and Ribose		
Ligand	Protein	Distance*	Ligand	Protein	Distance*
O2	G247 N	3.12	O2	G247 N	3.27
2' OH	S217 O	2.9	2' OH	S217 O	3.22
	G247 N	3.35			
	G247 O via water			G247 O via water	
	L427 N via water			L427 N via water	
				N426 ND2 via water	
3' OH	C218 Sγ	3.29	3' OH	C218 Sγ	2.86
	N426 Nδ2	2.56		N426 Nδ2	2.6
	E430 Oε1	2.96		E430 Oε1	2.92
	E430 Oε2	3.44		E430 Oε2	3.49
Phosphate Hydrogen Bonds			Phosphate Hydrogen Bonds		
O2A	T608	2.59	O2A	T608	2.49
O1A	A609 N	3.17	OA1	A609 N	3.39
O1B	202 Oγ	3.25	O1B	202 Oγ	2.68
	T611 N	3.26		T611 N	2.81
	T611 Oγ	2.6		T611 Oγ	3.03
				F610 N	3.35
O2B	S202 Oγ	3.26	O2B	S202 Oγ	3.07
O3B	S202 N	2.87	O3B	S202 N	3.4
	S202 Oγ	3.09			

*Distances are defined in Anstroms.
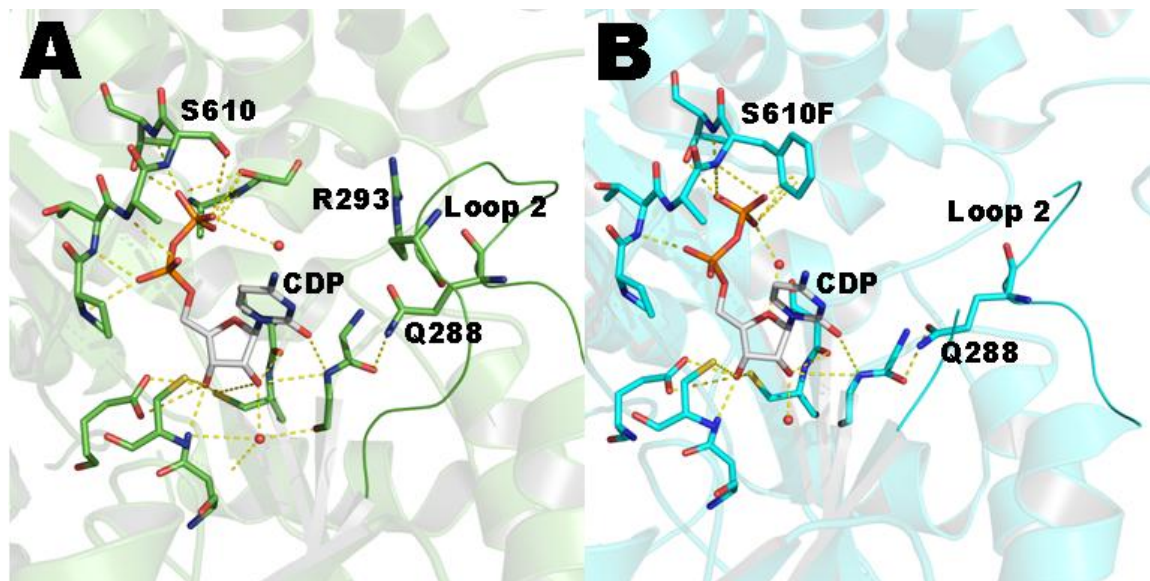
Figure 3.6: Comparison of C-site between wild-type Rnr1p and Rnr1p-S610F bound to dATP and CDP.
(**A**) C-site interactions, shown as dashed yellow lines when CDP is bound to the wild-type Rnr1p. For the protein, carbon atoms are rendered as green, nitrogens are blue, and oxygens are red. For the CDP substrate, carbons are rendered white and phosphorous atoms are orange. (**B**) Representation of the C-site of Rnr1p-S610F bound to CDP. Interactions are shown as yellow dashed lines. Protein carbons are colored as cyan, nitrogens are blue, and oxygens are red. CDP is colored as in (A).
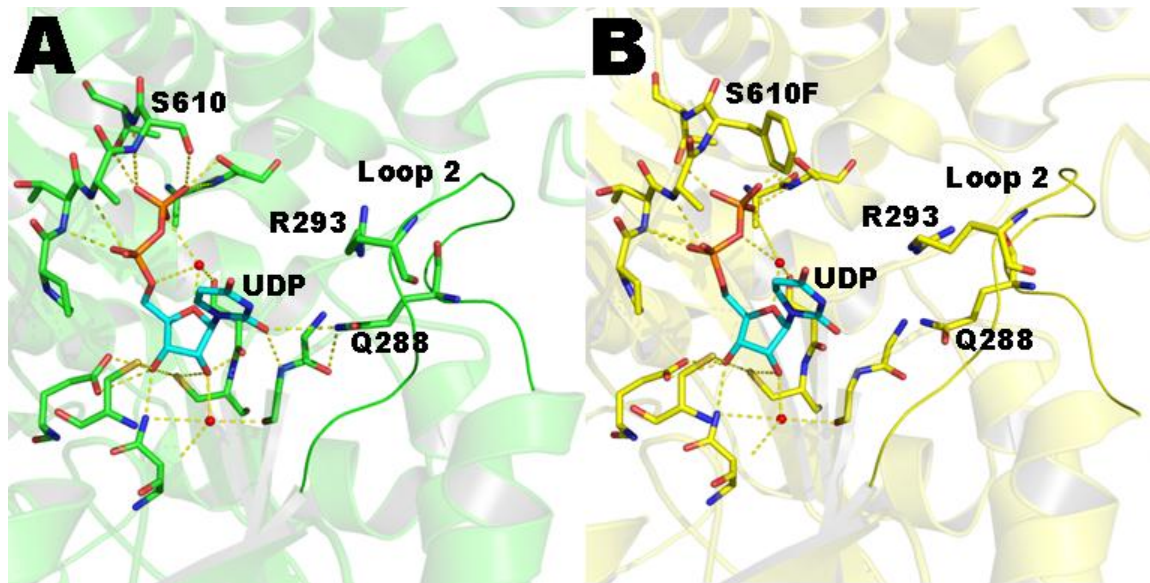
Figure 3.7: Comparison of C-site between wild-type Rnr1p and Rnr1p-S610F bound to dATP and UDP.
(**A**) C-site interactions, shown as dashed yellow lines when UDP is bound to the wild-type Rnr1p. For the protein, carbon atoms are rendered as green, nitrogens are blue, and oxygens are red. For the UDP substrate, carbons are rendered cyan and phosphorous atoms are orange. (**B**) Representation of the C-site of Rnr1p-S610F bound to UDP. Interactions are shown as yellow dashed lines. Protein carbons are colored as yellow, nitrogens are blue, and oxygens are red. CDP is colored as in (A).

Table 3.5: Hydrogen bond distances between Rnr1p and UDP bound at the catalytic site in both the wild-type and Rnr1p-S610F mutant.

Wild-type bound to AMPNP and UDP		
Hydrogen Bonds to Base and Ribose		
Ligand	Protein	Distance
O2	Q288 Nε2	3.46
	G247 N	2.99
N3	Q288 OE1 via water	
2' OH	S217 O	2.73
	G247 O via water	
	N426 Nδ2 via water	
	L427 N via water	
3' OH	C218 Sγ	3.37
	N426 Nδ2	2.53
	E430 Oε1	2.69
	E430 Oε2	2.89
	C428 Sγ	3.5
Phosphate Hydrogen Bonds		
O1A	T608 N	2.75
O2A		
	A609 N	3.18
O1B	T611 Oγ	2.67
	T611 N	3.29
O2B	S202 Oγ	2.41
O3B	S202 N	3.34

S610F bound to dATP and UDP		
Hydrogen Bonds to Base and Ribose		
Ligand	Protein	Distance
O2		
N3		
2' OH	S217 O	3.5
	G247 O via water	
	N426 Nδ2 via water	
	L427 N via water	
3' OH	C218 Sγ	3.04
	N426 Nδ2	2.73
	E430 Oε1	2.81
	E430 Oε2	2.95
Phosphate Hydrogen Bonds		
O1A	T608 N	2.56
O2A	T608 N	3.26
	A609 N	2.73
O1B	T611 Oγ	2.37
O2B	S202 Oγ	2.61
O3B	S202 N	2.8
	S202 Oγ	3.39

The ribose moiety and the uridine base of the substrate also have altered interactions compared to the wild-type. For example, the conserved active site residue C428, which is directly involved in catalysis, is 4.59 Å from the 3' OH, while 3.5 Å in the wild-type (**Figure 3.7** and **Table 3.5**). Residues from the Loop 2 region that make interactions with the uridine base in the wild-type (specifically Q288 Nε2 to O2, G247 N to O2, and Q288 Oε1 to N3) are too far from the base to make those interactions in the S610F mutant (**Figure 3.7** and **Table 3.5**). In addition, the UDP bound at the catalytic site in the mutant has a significantly higher temperature factor (88 Å^2) as compared to the wild-type (52.1 Å^2), which indicates that the Rnr1p-S610F mutant may not bind the UDP as tightly as the wild-type.

Dissociation Constants for Rnr1p-S610F

Since the Rnr1p-S610F mutation caused the loss of a hydrogen bond to the substrate's β-phosphate group, it was originally hypothesized that the binding of substrates to the C-site would be impaired, contributing to at least some of the loss of catalytic activity observed in this mutant. To directly test this hypothesis and elucidate the effects of this mutation on substrate binding to the C-site, the dissociation constant (K_d) of the substrate ADP for both wild-type and Rnr1p-S610F was determined in the presence of saturating concentrations of the effector dGTP using the *in vitro* binding assay described in **Section 2.13** and **Appendix A.3** (**Table 3.6** and **Figure 3.8**). The K_d of the S610F mutant enzyme for ADP was approximately two times weaker than that of the wild-type (76.6 μM vs. 29.4 μM) (**Table 3.6**). According to these dissociation constants, under the conditions of the *in vitro* activity assays the concentration of substrate is high enough that the catalytic sites of the wild-type and S610F mutant would

Table 3.6: Dissociation constants determined for the binding of both wild-type and Rnr1p-S610F to both ADP and dGTP.

Rnr1 Protein	WT	S610F	WT	S610F	WT	S610F
Assayed for binding to	ADP	ADP	dGTP	dGTP	dGTP	dGTP
Rnr2/Rnr4 Present	-	-	-	-	+	+
Dissociation Constant (μM)	29.4 ± 3.0	76.6 ± 15.9	1.75 ± 0.19	1.31 ± 0.13	0.84 ± 0.12	0.98 ± 0.15
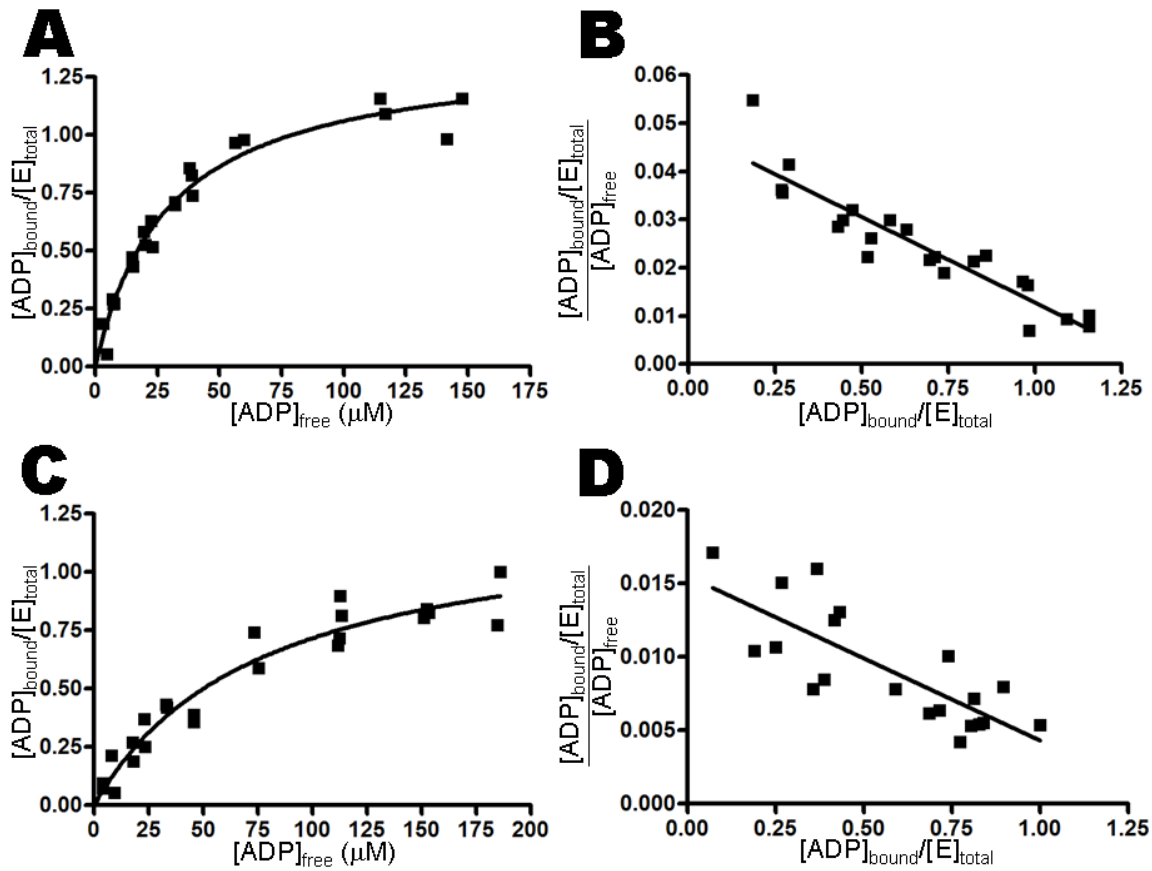
Figure 3.8: Dissociation constants determined for the binding of both wild-type and Rnr1p-S610F to ADP.
(**A**) Wild-type Rnr1p binding to ADP. (**B**) Scatchard plot of the wild-type binding data depicted in A. (**C**) Rnr1p-S610F binding to ADP. (**D**) Scatchard plot of the Rnr1p-S610F binding data depicted in C. Values for the dissociation constants determined in this figure are reported in **Table 3.6**.

Be 97% and 93% occupied by substrates. Therefore, the hypothesis that the loss of the hydrogen bond to the substrate due to the mutation S610F decreases the affinity of the C-site for substrate is disproven. The 2-fold weaker binding of substrates to the mutant over the wild-type does not explain the observed loss of activity recorded by the *in vitro* activity assays (**Figure 3.1**). Therefore, other reason(s) for the loss of activity must come into play, some of which are examined below.

It was also considered that a mutation in the C-site of the enzyme might affect the binding of effector nucleotide triphosphates to the S-site. Therefore, the K_d of the effector dGTP for the S-site was also determined (**Figure 3.9** and **Table 3.6**). However, the S610F mutation in the catalytic site does not affect the binding of the effector dGTP to the S-site. The binding affinity of the mutant was not found to be significantly different from the wild-type enzyme (1.75 μM for the wild-type vs. 1.31 μM for Rnr1p-S610F).

It is believed that the formation of the holo complex ($\alpha_2\beta\beta'$) alters the dissociation constants of the nucleoside-binding sites for their ligands. To ensure that the Rnr1p-S610F mutant was not altering the binding of dGTP to the S-site while complexed with the small subunits, the assay was repeated in the presence of an excess of Rnr2p and Rnr4p. Interestingly, the binding of the small subunits to the large subunit was observed to increase the affinity of the S-site for the effector molecule dGTP (**Figure 3.9B** and **3.9D** and **Table 3.6**). However, the binding constants of both the wild-type and Rnr1p-S610F mutant for dGTP in the presence of Rnr2p and Rnr4p were approximately the same, indicating that the S610F mutation did not interfere with the allosteric decrease in dissociation constant for dGTP upon the binding of Rnr2p and Rnr4p.

Attempts were made to measure the dissociation constant of ADP for both wild
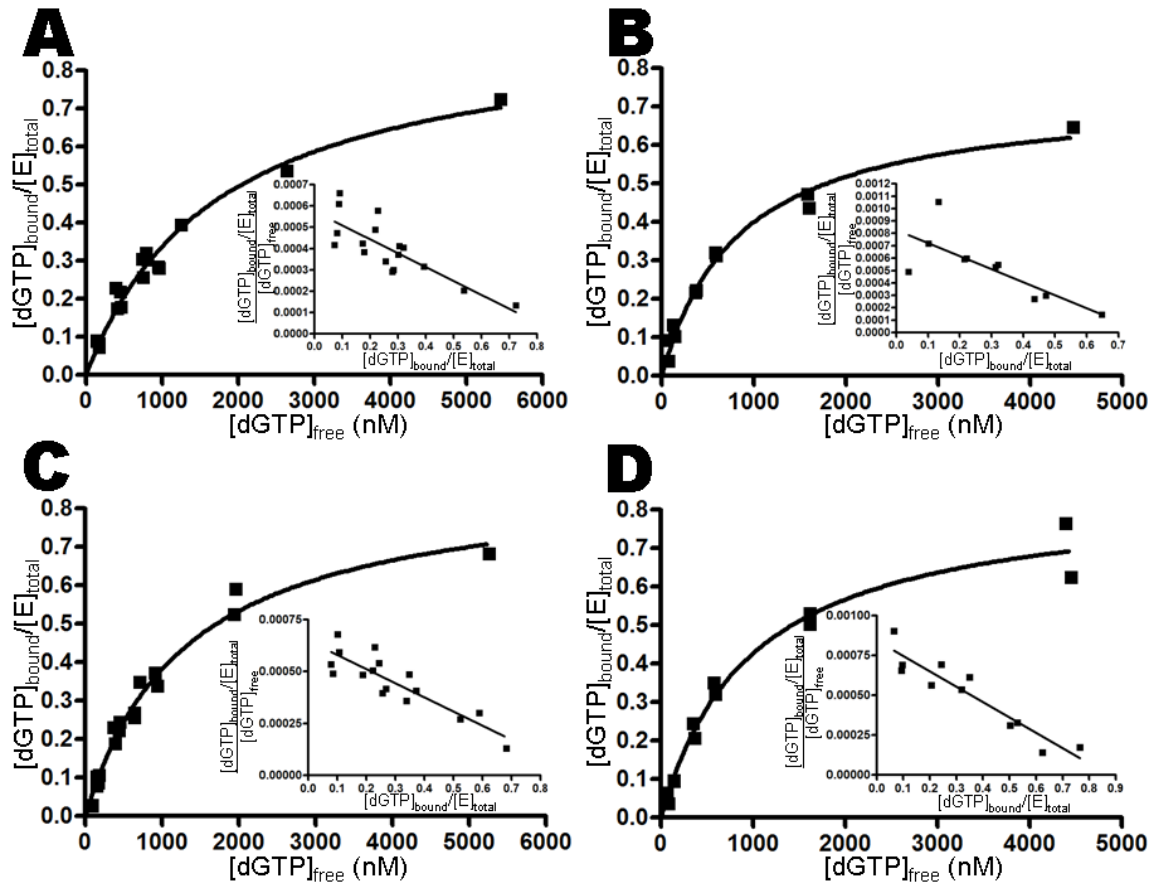
Figure 3.9: Dissociation constants determined for the binding of both wild-type and Rnr1p-S610F to dGTP.

The K_d of dGTP was determined both in the presence and absence of 10-fold molar excess of the small subunit Rnr2p/Rnr4p. **(A)** Wild-type Rnr1p and dGTP, **(B)** Wild-type Rnr1p and dGTP in the presence of Rnr2p/Rnr4p, **(C)** Rnr1p-S610F and dGTP and **(D)** Rnr1p-S610F and dGTP in the presence of Rnr2p/Rnr4p. Scatchard plots of the best fit line to the data are shown as an inset in each panel. Values for the dissociation constants determined in this figure are reported in **Table 3.6**.

type and Rnr1p-S610F in the presence of Rnr2p and Rnr4p. However, free-radicals provided to the large subunits by the small subunits caused catalytic turnovers to occur, making determination of the dissociation constant impossible. To remedy this problem, several experiments were attempted with the addition of the free-radical scavenger hydroxyurea to the binding reaction, which is known to destroy the free-radical from the small subunit. However, even concentrations of up to 50 mM hydroxyurea did not prevent turnovers from occurring, and the concentrations for the total and free ADP present were measured to be identical, indicating that no binding of ADP to the large subunit had taken place.

3.4 DISCUSSION AND IMPLICATIONS

A molecular basis for the *msl* phenotype induced by both $Rnr1^{S269P}$ and $Rnr1^{S610F}$ mutations is provided by the high-resolution structures of the mutants bound to substrates and allosteric effectors. The Rnr1p-S269P mutation causes Loop 1, which is essential for binding allosteric effectors at the S-site, to become disordered (**Figure 3.2** and **3.3**). Loss of the ability to bind effectors in the S-site has the secondary effect of causing amino acids present in Loop 2, which is absolutely essential for specificity cross-talk (Larsson *et al.* 2004; Xu *et al.* 2006), to also become disordered in the X-ray crystal structures. Even though specificity cross-talk is abolished by the Rnr1p-S269P mutation, substrates are still able to bind to the C-site via a conserved network of hydrogen bonds to the ribose and phosphate moieties of the ribonucleotide diphosphates, providing Rnr1p-S269P with the low level of observed activity (**Figure 3.1**). This is in agreement with the previous observation that ribonucleotide reductase possesses low basal activity with the no effectors bound to the S-site (Ge et al. 2003). Consistent with the observation that Loop 1 is disordered in the Rnr1p-S269P mutant, the Robetta Full-Chain Structure Prediction Server (Chivian et al. 2003; Kim et al. 2004; Chivian et al. 2005; Kim et al.

2005) also predicts residues 261-270 to be disordered. Since Loop 2 most likely can not perform its function as the mediator of specificity cross-talk, the Rnr1p-S269P mutant cannot be allosterically activated by effectors binding at the S-site.

The Rnr1p-S610F mutation targets a residue present in the C-site that interacts with the β-phosphate of the substrate, and also causes a drastic reduction in the activity of the enzyme (**Figure 3.1**). In the X-ray crystal structures of this mutant, there are substrate and effector nucleosides bound at both the C-site and S-site. Although phosphate binding is possibly weakened in the Rnr1p-S610F mutant due to the loss of one or two hydrogen bonds, this alone cannot explain the drastic loss of activity. To discern whether the loss of activity was due to the binding of substrate or to a change in the catalytic rate, the dissociation constant of the wild-type and Rnr1p-S610F mutants were determined for the substrate molecule ADP in the presence of the allosteric effector dGTP (**Figure 3.8** and **Table 3.6**). The measured binding constants (29.4 μM in wild-type vs. 76.6 μM in Rnr1p-S610F) indicate that ADP substrate binds approximately two times weaker to the S610F mutant than the wild-type enzyme. However, this small decrease in the affinity of the enzyme is insufficient to explain the extreme loss of activity in the presence of saturating concentrations of substrates. Under the *in vitro* assay conditions the concentration of substrate is 1 mM, and 97% and 93% of the catalytic sites should be occupied with substrate for wild-type and Rnr1p-S610F, respectively. Although the binding of dGTP to the S-site remains unchanged, when comparing the wild-type and Rnr1p-S610F mutant, it is interesting that the affinity of Rnr1p for dGTP increases approximately two-fold in the presence of Rnr2p/Rnr4p (**Figure 3A** and **3C** vs. **Figure 3B** and **3D** and **Table 3.6**).

We propose that the substitution of the larger phenyl group must be altering the rate of reaction by slowing down the rate-limiting step of the reaction (k_{cat}). The laboratory of Dr.

120

Joanne Stubbe has shown, with experiments on *E. coli* NrdA, that the rate limiting step of substrate reduction in Class Ia Rnrs is either a conformational isomerization preceding nucleoside reduction during pre-steady-state conditions, or the reduction of the active site by the C-terminal tail after each catalytic turnover under steady-state conditions (Ge *et al.* 2003) (**Figure 3.10**).

Since the *in vitro* activity assays were performed at concentrations of Rnr1p that correspond to those in (Ge *et al.* 2003), and the concentration of substrate used is in the steady-state region, we believe that the Rnr1p-S610F mutant is slowing down the reduction of the C-site (**Figure 3.10** highlighted in green), rather than the conformational gating step which occurs before catalysis (**Figure 3.10** highlighted in red). This will result in a decrease in the value of k_{cat}, leading to the reduced activities observed in the *in vitro* activity assays (**Figure 3.1**). The bulky phenylalanine residue may restrict the access of the C-terminal tail to the catalytic site to slow down the reduction of the catalytic cysteines. Indeed, analysis of the C-site cavity with the program CAVER (Petrek *et al.* 2006) confirms that the phenylalanine group restricts width of the opening to the C-site. The data heavily favor the hypothesis that the step of the catalytic cycle affected by the Rnr1p-S610F mutation is the re-reduction of the large subunit, but the possibility that the Rnr1p-S610F mutation instead slows the conformational isomerization observed by Dr. Stubbe's pre-steady-state experiments can not be totally
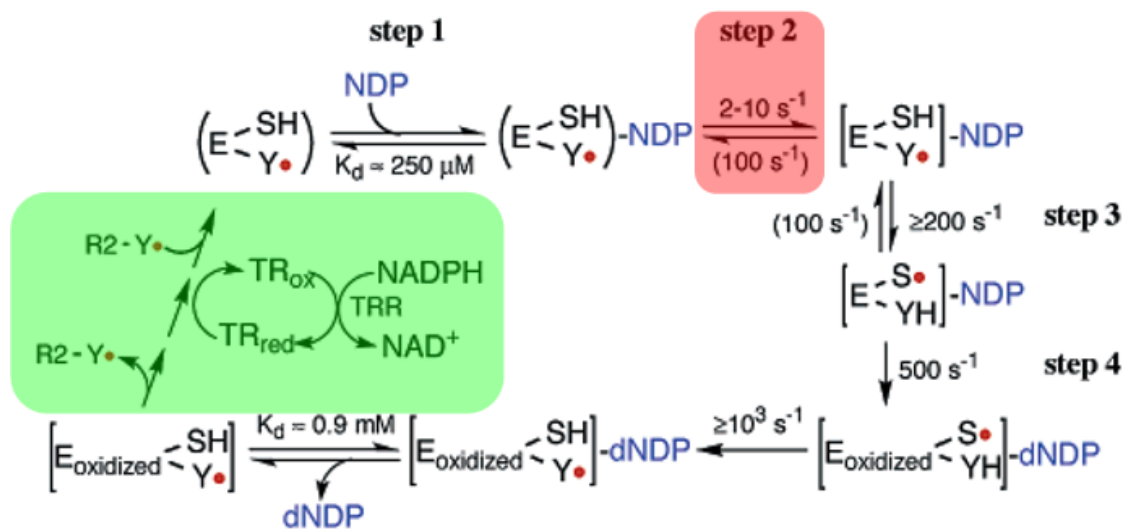
Figure 3.10: Rate-limiting steps of catalysis in Class Ia Rnrs.
Under pre-steady state conditions and low concentrations of the large subunit (0.05-0.4 μM) the rate limiting step is proposed to be a slow structural gating step, highlighted in red, which takes place before catalysis. Under physiological concentrations of the large subunit ($\geq$ 1 μM) and steady state conditions, the re-reduction step of the catalytic cycle, highlighted in green, becomes rate limiting. This figure was adapted with permission from (Ge *et al.* 2003). © 2003 American Chemical Society.

ruled out (**Figure 3.10** highlighted in red). Although the Rnr1p-S269P mutation disrupts substrate binding indirectly, and Rnr1p-S610F alters the value of k_{cat}, the net effect of both mutations is the unbalanced production of deoxynucleotides.

The Rnr1p-S269P and Rnr1p-S610F mutations decrease the ability of the enzyme to reduce ribonucleoside diphosphates to deoxyribonucleoside diphosphates, as indicated by the *in vitro* activity assays. Decreased ribonucleotide reductase activity will eventually lead to depressed and/or imbalanced dNTP pools within the cell, which is known to cause increased mutation rates and genomic instability (Reichard 1988; Desany *et al.* 1998; Chabes *et al.* 2003). In addition to impairing overall Rnr activity, these mutations under-produce dATP relative to the other nucleotides, as indicated by the impaired ability of these alleles to reduce ADP *in vitro*. Three lines of evidence support this hypothesis: (1) preliminary results from Dr. Simon's group where the dNTP pools were measured in *S. cerevisiae* cells harboring these mutations, (2) the mutational spectra that were observed, and (3) the rescue of the *msl* phenotype in $Rnr1^{S610F}$ strains grown on dAMP supplemented media. Interestingly, hydroxyurea, which also impairs overall ribonucleotide reductase activity, leads to a decrease in all four dNTP levels and is not selectively toxic to MMR-deficient strains (Simon et al. 2000). This further suggests that the *msl* phenotype of the $Rnr1^{S269P}$ and $Rnr1^{S610F}$ alleles is due to underproduction of dATP relative to the other three dNTPs. The skewed deoxynucleotide pools produced by these mutant alleles induce genomic instability that requires cells to have a functional mismatch repair system to remain viable.

One plausible explanation for the *msl* phenotype is a mutational catastrophe hypothesis: the mutation rate is so elevated in MMR-deficient cells bearing $Rnr1^{S269P}$ and $Rnr1^{S610F}$ alleles that a deleterious mutation is made to a random essential gene each time replication is attempted.

Another possibility is that only a subset of essential genes that are A or T rich are vulnerable in the low dATP environment. The same essential gene must be disrupted twice, independently, to kill a diploid cell. Therefore MMR-defective diploids should be resistant to the mutational catastrophe mechanism. MMR-defective diploids should be less resistant when only a small subset of the essential gene pool is vulnerable to the low dATP environment. This hypothesis has been put forth as an explanation of the genomic instability and tumor generation in human MMR-deficient cells. Nucleotide sequences of DNA repair and damage response genes such as ATR, RAD50, and MRE11 were found to be altered in MMR-deficient colorectal tumors in humans, leading to reduced expression of the target genes and reduced function (Ham et al. 2006; Miquel et al. 2007). In addition, disruption of the poly-A run in the human TGF-β type II receptor has been linked to its inactivation in human MMR-deficient colon cancer (Markowitz et al. 1995; Wang et al. 1995). Therefore, MMR-deficiency can lead to disruption of other, non-MMR functions. Together, the results of this dissertation research plus that of Dr. Simon's group suggest that a therapeutic strategy targeting either the S-site or the C-site that de-regulates rather than just inhibits Rnr activity may provide an additional avenue for killing MMR-deficient cancer cells.

4. X-RAY CRYSTAL STRUCTURES OF HUMAN RIBONUCLEOTIDE REDUCTASE AND THE OLIGOMERIC REGULATION OF RNR BY dATP

4.1 INTRODUCTION

This chapter will focus mostly on the large subunit of ribonucleotide reductase (Rnr) from *H. sapiens* (hRRM1). First, a brief introduction on ribonucleotide reductase in humans will be presented to the reader in **Section 4.2**. Then, X-ray crystallographic and biophysical data will be presented along with a discussion of the impact of this dissertation on the field of ribonucleotide reductase research in **Section 4.3**. The results of this dissertation work, along with the work of a fellow graduate student in the lab, Sanath Wijerathna, have been combined into a manuscript, which is currently being prepared for submission to the scientific journal *Cell*, entitled "A Structural Basis for Allosteric Regulation of Human Ribonucleotide Reductase 1 by dATP". Experimental methods used to obtain the results in this chapter are described in **Chapter 2** of this dissertation.

4.2 BACKGROUND AND OBJECTIVES

Ribonucleotide reductase plays a crucial role in *de novo* DNA synthesis by reducing ribonucleoside diphosphates to 2'-deoxyribonucleotide diphosphates (Brown *et al.* 1969) and maintaining balanced pools of dNTPs in the cell (Eliasson *et al.* 1994). Ribonucleotide reductase is an $\alpha_n\beta_n$ multi-subunit protein where the minimal active form is $\alpha_2\beta_2$. The α subunit, called RR1, contains two allosteric sites and a catalytic site (Brown *et al.* 1969), while the β subunit, called RR2, houses a free-radical that is transferred some 35 Å to the catalytic site to initiate radical-based chemistry on the substrate (Reece *et al.* 2006) (see **Section 1.2** and **1.3**). In rapidly proliferating cells, Rnr is targeted by anti-cancer drugs, such as gemcitabine (Gandhi *et al.*

1991), that cause dNTP pool imbalances, and the promotion of nucleotide misincorporations leading to radio-sensitization (Flanagan *et al.* 2007).

Rnr from *H. sapiens* is regulated transcriptionally, via cell-cycle dependent degradation of the small subunit, allosterically via the S-site and A-site of the large subunit, and by the oligomeric state of the large subunit (see **Section 1.4**). In mammalian mouse fibroblast cells, the level of RR1 in G_0/G_1 serum-starved cells has previously been measured to be 0.05 μM, while the concentration of RR1 in S-phase cells reaches 0.5 μM (Hakansson *et al.* 2006). On the other hand, RR2 levels go from being undetectable during G_0/G_1 to 1.9 μM during S-phase (Hakansson *et al.* 2006). Consistent with this, dNTP pools also vary with respect to the phases of the cell cycle, reaching their highest concentration during S-phase.

Due to the role Rnr plays in balancing the nucleotide pools within the cell, it is heavily regulated by an intricate allosteric mechanism (Brown *et al.* 1969; Chabes *et al.* 2003). The hRRM1 subunit harbors two allosteric sites: (1) the specificity site (S-site), which determines substrate preference, and (2) the activity site (A-site), which stimulates activity when ATP is bound and inhibits activity when dATP is bound (see **Section 1.4.1**) (Soderman *et al.* 1986). The structural basis for substrate selection has been shown to be a series of conformational changes in the amino acids that compose Loop 2, a regulatory loop located between the S-site and the C-site (Larsson *et al.* 2004; Xu *et al.* 2006). However, the structural basis for enhancement or inhibition of Rnr activity via the binding of ATP or dATP to the A-site is not well understood.

Recent reports in the literature suggest that both dATP and ATP regulate Rnr by changing the oligomeric state of hRRM1 in a concentration-dependent manner (Kashlan *et al.* 2002; Rofougaran *et al.* 2006). Mouse RR1 (mRRM1) has been shown to form dimers (α_2) at 2 μM dATP, tetramers (α_4) at 8 μM, and hexamers (α_6) at a non-physiologic concentration of 10

mM dATP (Kashlan *et al.* 2002). The dATP-induced tetramers were shown to be 66 % less active than the dimers. In addition, the formation of mRRM1 α_2 was shown to be induced by 200 µM ATP, α_4 by 400 µM ATP, and α_6 by 1-2 mM ATP. The ATP-induced α_2 and α_6 oligomers have been shown to be active while the α_4 is less active (Kashlan *et al.* 2002). Another research group in Sweden has also performed similar experiments with mRRM1. They observe oligomerization of monomers into α_6 at 50 µM dATP, and at 1 µM dATP in the presence of 50 µM dGTP (Rofougaran *et al.* 2006). The same study shows that mRRM1 can exist as active α_2 and α_6 at 100 µM ATP, and 50 µM dGTP (Rofougaran *et al.* 2006). Furthermore, the active mouse Rnr is proposed to be the ATP induced $\alpha_6\beta_2$ complex.

However, there are significant differences in the findings of the two groups. For example, Kashlan and co-workers propose that the dATP bound tetramer is the least active oligomeric species of mRRM1 and furthermore they do not obtain mRRM1 hexamers at physiologic levels of dATP (Kashlan *et al.* 2002). In contrast, Rofougaran and co-workers do not observe dATP-induced tetramers, and instead show that the dATP-induced formation of hexamers is the major contributor to low Rnr activity (Rofougaran *et al.* 2006). In another study, the widely used cancer inhibitor gemcitabine was shown to induce the formation of a stable $\alpha_6\beta_6$ RR complex *in vitro* (Wang *et al.* 2007). X-ray crystal structures of RR1 dimers have been solved for prokaryotes (Nordlund *et al.* 1990; Uhlin *et al.* 1994; Sintchak *et al.* 2002; Uppsten *et al.* 2003; Larsson *et al.* 2004) and yeast (Xu *et al.* 2006; Xu *et al.* 2006). In addition, a holocomplex of $\alpha_2\beta_2$ from the bacteria *Salmonella typhimurium* is also available (Uppsten *et al.* 2006). However, no higher order oligomeric structures of tetramers or hexamers are available, so the structural basis of oligomerization is not known.

In the dissertation research presented in this chapter, the X-ray crystal structures of hRRM1, the first mammalian RR1 to have its X-ray crystal structure solved, bound to TTP, TTP●GDP, TTP●ATP, and TTP●dATP are reported. The crystal structures of hRRM1●TTP●ATP and hRRM1●TTP●dATP provide a structural basis for the difference in ATP and dATP binding at the A-site and insight into the oligomeric regulation of Rnr. In addition, size exclusion chromatography data is also presented which shows that hRRM1 is able to form hexamers at concentrations of dATP as low as 5 μM. Finally, the low-resolution X-ray crystal structure of *S. cerevisiae* RR1 (ScRR1) provides the first-ever observed structure of a dATP-induced hexamer. Size exclusion chromatography and structural data are combined together to provide a model for regulation of the large subunit of Rnr by dATP-induced oligomerization.

4.3 RESULTS AND DISCUSSION

4.3.1 hRRM1 Crystal and Tertiary Structural Information

The first mammalian Class Ia RR1 to have its X-ray crystal elucidated is presented here. The X-ray crystal structure of hRRM1●TTP was obtained via co-crystallization, while hRRM1●TTP●GDP, hRRM1●TTP●ATP, and hRRM1●TTP●dATP were obtained by soaking experiments as reported in **Chapter 2** and produced reflection data to resolutions of 2.4 Å, 3.2 Å, 3.1 Å, and 3.15 Å, respectively (**Figure 4.1**, **Table 4.1**, and **Table 4.2**). Two non-isomorphous orthorhombic crystal forms of hRRM1, called form A and form B, were obtained by co-crystallization experiments with TTP. Both forms crystallize as a dimer with two molecules in the asymmetric unit. In form A, electron density is for residues 14-742 in molecule A and residues 1-742 in molecule B. Form B is almost the same as form A, except in molecule B residue 1 is disordered. The root mean square deviation (RMSD) for the Cα carbon atoms

between the two forms are less than 0.5 Å. All structures were crystallized in form A except for the TTP●GDP complex. The electron densities for the first structures of ATP and dATP bound to the activity site of the large subunit of any RR1 are shown in **Figure 4.2A** and **4.2B**.

The hRRM1 enzyme tertiary structure is composed of four domains which stretch from N to C-terminus (**Figure 4.1**). At the N-terminus of the enzyme, residues 1-91 consist of a four-helix ATP-binding cone called the activity site (A-site) (**Figure 4.1** colored in red). The ATP-binding cone is followed by the catalytic 10-stranded α/β barrel which stretches from residues 92 to 638 and 683 to 742. This domain contains both the S-site, where nucleoside triphosphates bind to determine substrate specificity, and the catalytic site (C-site), where ribonucleoside diphosphate substrates are reduced. A three-helix domain consisting of a forty-five amino acid insertion compared to the *E. coli* structure spans residues 639 to 682. This insertion is present in the sequences of all eukaryotic RR1 enzymes, but not in *E. coli* RR1 and a majority of other prokaryotic RR1s and at the time of the publication of this dissertation has no known function. At the C-terminus of hRRM1 is a flexible domain spanning residues 743 to 792, referred to as
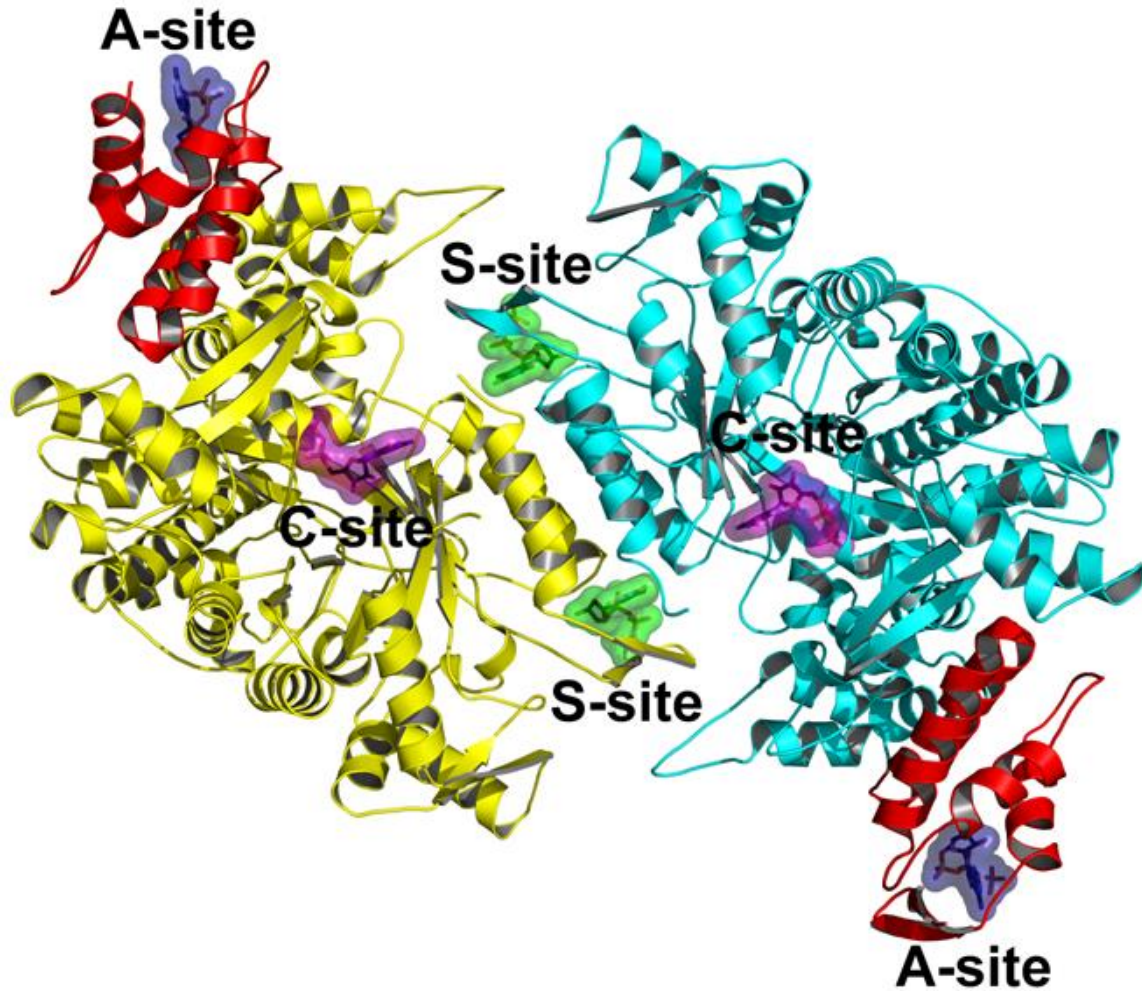
Figure 4.1: The structure of hRRM1 in dimer form.
Ribbon diagram of the dimer of hRRM1. Chain A and Chain B are colored yellow and cyan, respectively. The four-helix ATP-binding cones of both subunits are shown in red. Nucleotide binding sites for TTP (green), GDP (magenta), and ATP/dATP (blue) are represented as transparent surfaces.

Table 4.1: Data collection and refinement statistics for hRRM1●TTP, hRRM1●TTP●dATP, and hRRM1●TTP●ATP.

Name of Data	HuR1 + TTP	HuR1 + TTP + dATP	HuR1 + TTP + ATP
Space Group	$P2_12_12_1$	$P2_12_12_1$	$P2_12_12_1$
Cell Dimensions			
a,b,c	69.0, 114.1, 219.3	68.9, 114.4, 220.0	69.1, 114.4, 222.5
α,β,γ	90,90,90	90,90,90	90,90,90
wavelength	0.9002	0.9002	0.9002
resolution	50.0 - 2.40	50.0 - 3.15	50.0 - 3.10
molecules per asymmetric unit	2	2	2
unique reflections	67702	27445	28874
R_{sym}	9.3 (55.2)	48.2 (14.9)	45.3 (11.5)
I/σ	13.1 (2.3)	10.7 (3.5)	8.5 (2.5)
% completeness	98.7 (98.8)	90.1 (92.6)	89.4 (92.9)
redundancy	3.9 (3.0)	5.5 (4.8)	4.6 (4.9)
Refinement			
resolution	50.0 - 2.40	50.0 - 3.15	50.0 - 3.10
# reflections	62082	26016	27243
R_{work}/R_{free}	18.6/23.7	18.9/26.0	18.9/27.5
# Atoms	11770	11545	11384
protein	11327	11391	11215
ligand/ion	90	110	89
water	353	44	80
Average B-factors			
protein	45.0		
ligand/ion	52.6		
water	43.2		
RMS Deviations			
bond length	0.009	0.011	0.015
bond angle	1.231	1.458	1.672

Table 4.2: Data collection and refinement statistics for hRRM1●TTP●GDP and ScRR1●dATP.

Name of Data	HuR1 + TTP + GDP	ScRR1 + dATP
Space Group	P2$_1$2$_1$2$_1$	P6$_3$
Cell Dimensions		
a,b,c	73.2, 115.8, 221.3	166.5, 166.5, 381.7
α,β,γ	90,90,90	90,90,120
wavelength	0.9002	0.9002
resolution	50.0 - 3.20	50.0-6.60
molecules per asymmetric unit	2	4
unique reflections	31062	9893
R$_{sym}$	49.9 (10.0)	12.2 (47.9)
I/σ	12.8 (3.1)	14.3 (1.6)
% completeness	98.9 (99.2)	88.3 (52.4)
redundancy	4.9 (4.8)	5.3 (1.3)
Refinement		
resolution	50.0 - 3.20	50.0 - 6.60
# reflections	29455	9377
R$_{work}$/R$_{free}$	18.3/25.4	37.5/40.1
# Atoms	11510	23000
protein	11337	23000
ligand/ion	136	0
water	37	0
Average B-factors		
protein		
ligand/ion		
water		
RMS Deviations		
bond length	0.014	0.009
bond angle	1.550	1.157
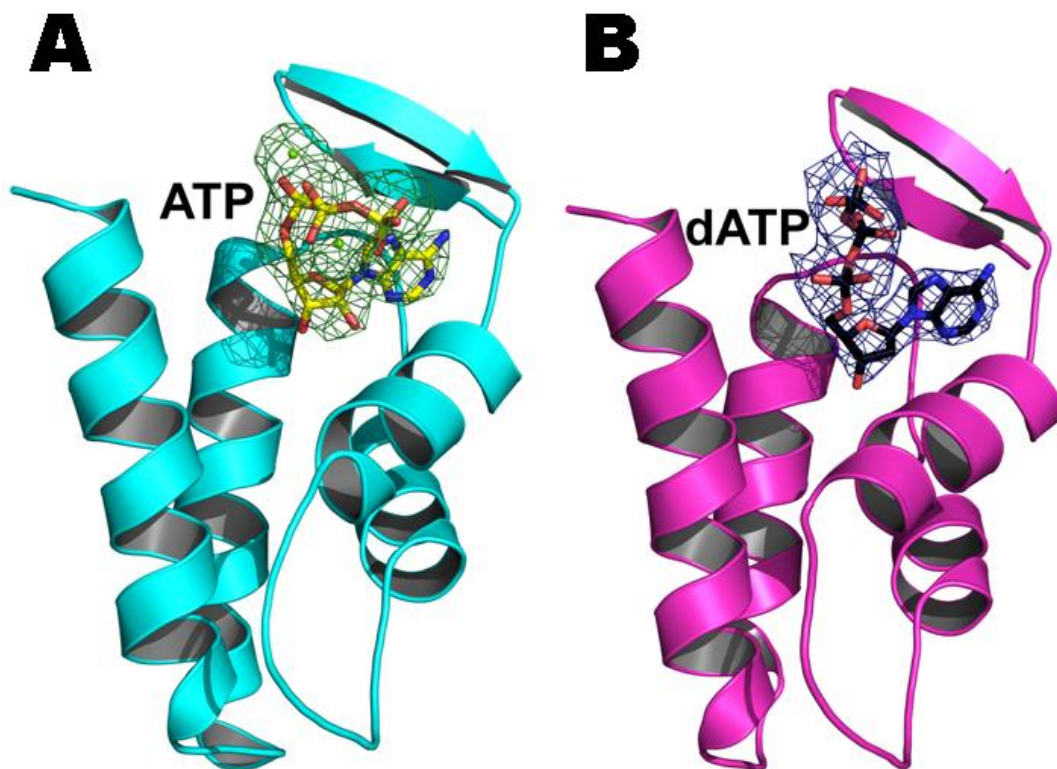
Figure 4.2: The four-helix cone at the N-terminus of hRRM1.
(**A**) The four-helix cone with ATP bound. $2F_o$-F_c electron density for ATP (carbons are colored yellow) contoured at 1σ is shown in green. (**B**) The four-helix cone with dATP bound. $2F_o$-F_c electron density for dATP (carbons are colored black) is shown in blue. Oxygen is colored red, and nitrogen is blue.

the C-terminal domain. The C-terminal domain contains two conserved cysteines (C787 and C790 in hRRM1) which shuttle reducing equivalents to the C-site to reduce its redox pair (C218 and C444 in hRRM1) after each catalytic turnover. Electron density is not observed for the C-terminal tail after residue 742, as the flexibility of this domain required for its function causes it to be inherently disordered.

To assess the degree of similarity of hRRM1 to its class I and class II homologues, the structures of ScRR1, *Eschericia coli* (EcRR1), *Thermotoga maritima* (TmRR1), and *Salmonella typhimurium* (StRR1) were aligned with all four of the hRRM1 complex structures in a pair-wise fashion (**Table 4.3**). In addition, the sequence identity of RR1 was also calculated from each species in pair-wise fashion (**Table 4.3**). hRRM1 and ScRR1 share the most structural homology with an RMSD of 0.8 Å, while EcRR1, TmRR1, and StRR1 have RMSDs with hRRM1 of 1.4 Å, 1.3 Å, and 1.3 Å, respectively (**Table 4.3**). The amount of structural similarity between hRRM1 and its bacterial homologues is quite high considering that the sequence similarities are only 26 to 27 percent.

4.3.2 The Specificity Site of hRRM1

In all of the hRRM1 co-crystal structures, the effector molecule TTP is bound to the S-site which is present at the end of a four-helix bundle. Each monomer of hRRM1 contains two helices of the four-helix bundle, which forms at the dimer interface (**Figure 4.1**, **Figure 4.3A** and **4.3B**). The S-site binds deoxynucleoside triphosphate effectors primarily through three loops at the dimer interface: (1) Loop 1 that spans residues 255-271, (2) Loop 2 which spans residues 286-295, and (3) Loop 3 which spans residues 223-228. Loop 1 and Loop 3 interact with the effector only, while Loop 2 interacts with

Table 4.3: Sequence identity and pairwise root mean square deviation of Cα atoms of RR1.

	hRRM1●TTP	hRRM1●TTP●GDP	hRRM1●TTP●ATP	hRRM1●TTP●dATP	ScRR1	EcRR1●AMPPNP	TmRR1	StRR1
hRRM1●TTP		100	100	100	66	27	26	26
hRRM1●TTP●GDP	0.338		100	100	66	27	26	26
hRRM1●TTP●ATP	0.409	0.481		100	66	27	26	26
hRRM1●TTP●dATP	0.29	0.385	0.37		66	27	26	26
ScRR1	0.752	0.819	0.911	0.85		27	24	25
EcRR1●AMPPNP	1.474	1.342	1.357	1.382	1.732		24	24
TmRR1	1.294	1.216	1.221	1.276	1.394	3.369		25
StRR1	1.347	1.339	1.374	1.35	1.614	1.423	1.599	

Pairwise root mean square deviation (RMSD) of Cα atoms for the structures of hRRM1, ScRR1, TmRR1, EcRR1, and StRR1 calculated using the molecular graphics program PyMOL are shown in the lower quadrant. The sequence identity is shown in the upper quadrant based on BLAST (Altschul *et al.* 1997).
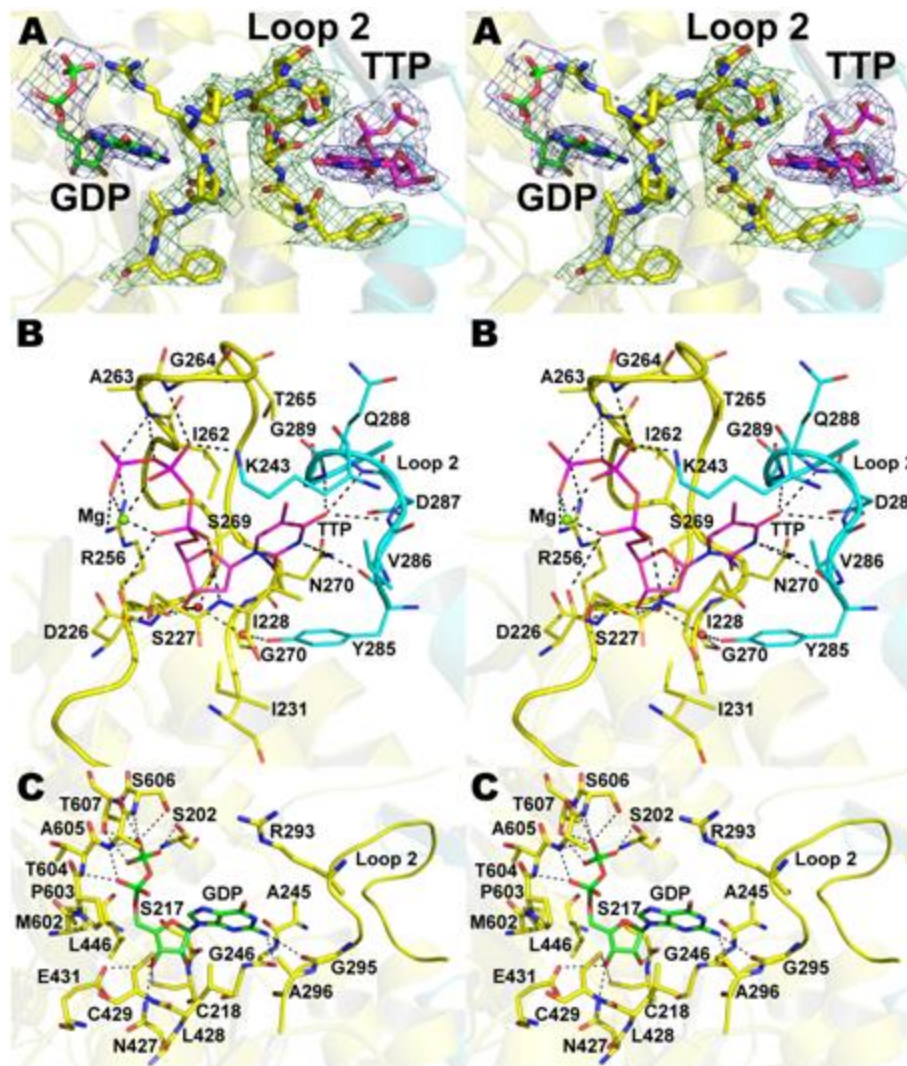
Figure 4.3: Stereo views of effector and substrate binding to hRRM1.
(**A**) View of the C-site and S-site lying between Loop 2. The $2F_o$-F_c electron density map contoured at 1σ for TTP (carbons colored magenta) and GDP (carbons colored green) is drawn as a dark blue mesh. Loop 2 residues from chain A are drawn as sticks (carbon colored yellow), and the 2Fo-Fc electron density map is colored green. The Arg 293 is partially ordered. All the oxygen atoms are colored red and nitrogen atoms colored blue in (A-C). (**B**) Interactions between hRRM1 and the effector nucleotide TTP in the hRRM1●TTP structure. The carbon atoms of Chain A and Chain B are shown in yellow and cyan, respectively. The TTP carbons and phosphorous atoms are shown as magenta, and hydrogen bonds are shown as dashed black lines. (**C**) The GDP substrate bound at the catalytic site of hRRM1. Chain A of the hRRM1●TTP●GDP structure is shown in yellow; interacting residues are shown as sticks. The carbon and phosphorous atoms of the GDP substrate are drawn in green, oxygen red and nitrogen blue. Hydrogen bonds between substrate and enzyme are shown as dashed black lines.

Table 4.4: Summary of S-site interactions with TTP from hRRM1●TTP, ScRR1●TTP●GDP, and EcRR1●TTP.

hRRM1●TTP Interactions	
Hydrogen bonds	
hRRM1●TTP Interactions	Atom(s) from Rnr1
O4	D287 N, Q288 N, G289 N
N3	N270 Nδ2, Y285 O
O2	N270 N
3'-OH	D226 Oδ2, H2O
Alpha Phosphate	D226 O, I228 N, Mg
Beta Phosphate	K243 NZ, A263 N, G264 N, Mg
Gamma Phosphate	R256 NH1, R256 NH2, A263 N, Mg
Van der Waals	
TTP	Atom(s) from Rnr1
Thymine Base	D287, Q288, G289, Y285, V286, K243, I228, I262, T265, N270, S269,
Ribose	S269, I262, I228, I231, D226, S227, R256, S269
ScRR1●TTP Interactions	
Hydrogen bonds	
Atom from TTP	Atom(s) from Rnr1
N3	N270 Oδ1
O2	N270 N
O4	G289 N, Q288 N, D287 N
Alpha Phosphate	D226 O, I228 N, Mg
Beta Phosphate	R256 NH2, Mg
Gamma Phosphate	R256 NH2, A263 O, A263 N, Mg
Van der Waals	
TTP	Atom(s) from Rnr1
Thymine Base	I228, K243, I262, S269, N270, G271, Y285, V286, D287, Q288, G289
Ribose	D226, S227, I228, I231, K243, I255, R256, I262, S269, Y285
EcRR1●TTP Interactions	
Hydrogen bonds	
Atom from TTP	Atom(s) from Rnr1
O2	H275 Nδ1
O4	S249 O
3'-OH	D232 Oδ1
Alpha Phosphate	L234 N, Mg
Beta Phosphate	R262 NH2, Mg
Gamma Phosphate	R262 NH2, R262 NH1, R269 N, Mg
Van der Waals	
TTP	Atom(s) from Rnr1
Thymine Base	L234, S249, I268, H275, T276, F281, C292
Ribose	D232, S233, L234, I237, I261, R262, I268, H275, F281

ligands bound in both the S-site and C-site and undergoes unique conformational changes to mediate substrate selection (Larsson *et al.* 2001; Xu *et al.* 2006). Comparison of the TTP●GDP complexes of hRRM1 with eukaryotic ScRR1, and prokaryotic EcRR1 and TmRR1, shows that the TTP binds very similarly with the exception of EcRR1 where the effector is substantially shifted by a distance of 5 Å (**Figure 4.4**).

4.3.3 The Catalytic Site of hRRM1

The hRRM1●TTP●GDP ternary complex was obtained by soaking co-crystals of hRRM1●TTP as described in Materials and Methods in **Section 2.8.6**. Even at a resolution of 3.2 Å the $2F_o$-F_c electron density clearly shows a GDP molecule bound in the C-site (**Figure 4.3A**). The ribose ring of the substrate adopts a puckered 3'-*endo* conformation as previously observed in both the TmRR1 and ScRR1 substrate-effector complex structures (Larsson *et al.* 2004; Xu *et al.* 2006) (**Figure 4.3C**). Although the C-site interactions to the GDP's ribose in hRRM1 and ScRR1 are fairly well conserved, there are differences in these interactions when comparing hRRM1 with TmRR1 (**Figure 4.5A** and **4.5B**). For instance, the sulfur of the catalytic Cys 218 in hRRM1 and ScRR1 is within hydrogen bonding distance of the 2' and 3' hydroxyls of the ribose, while they are more than 4 Å apart in TmRR1. The 2' hydroxyl of the substrate forms a hydrogen bond to the main-chain carboxyl group of S217 in hRRM1●TTP●GDP, similar to its interactions in the ScRR1●TTP●GDP structure (**Figure 4.3C** and **Figure 4.5A**). In addition, the 3' hydroxyl of the substrate is held in place in the hRRM1 structure by the two catalytic residues N427 and E431 (**Figure 4.3C**), residues which are conserved across all Class I RR1s. This places the catalytic cysteine residues, C218 and C429, within 3.9 Å and 3.5 Å of the 3' hydroxyl in hRRM1, respectively. The redox cysteine
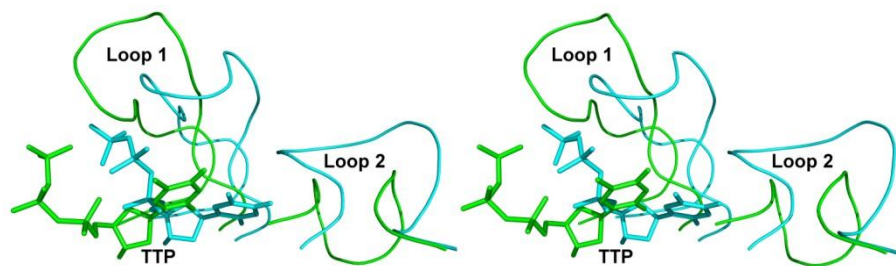
Figure 4.4: Stereo view of the effector TTP bound to the S-site of RR1.
hRRM1●TTP●GDP (cyan) and EcRR1●TTP●GDP (green) were aligned using the molecular graphics program PyMOL to superimpose the Cα-carbons of the proteins. The TTP from the EcRR1 structure is shifted left approximately 5 Å compared to hRRM1.
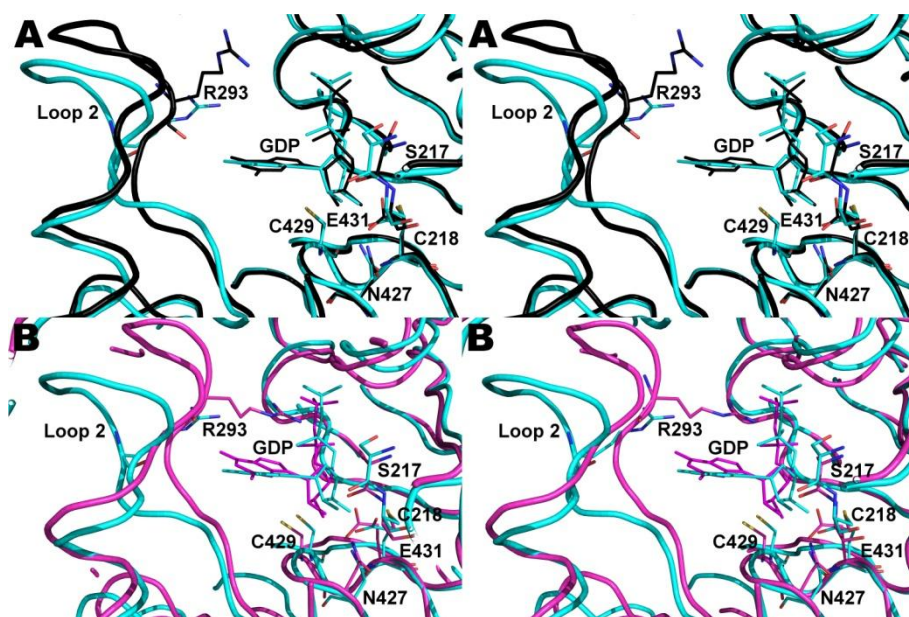
Figure 4.5: Stereo view of the catalytic site of RR1 bound to the substrate GDP.
hRRM1●TTP●GDP (cyan), ScR1●TTP●GDP (black), and TmR1●TTP●GDP (magenta) were aligned in the molecular graphics program PyMOL via the Cα-carbons of the protein. **(A)** The residues C218, S217, R293, N427, C429, and E431 from hRRM1●TTP●GDP and their equivalents in ScR1●TTP●GDP are shown as sticks. **(B)** hRRM1●TTP●GDP and TmR1●TTP●GDP shown in the same orientation as (A).

C444, which forms a disulfide bond with C218 after each catalytic cycle, is 7.6 and 8.7 Å distant from the 3' and 2' hydroxyls, respectively and not represented in **Figure 4.3C**.   One additional hydrogen bond is made by the N2 atom of the nitrogenous base with the main-chain carboxyl of G246 which is not shown in **Figure 4.3C**.

The selection of substrates is mediated by unique conformational changes adopted by amino acids in Loop 2 (residues 286-295) which mediate specificity cross-talk between the S- and C-sites (Larsson *et al.* 2004; Xu *et al.* 2006). Due to the inherent flexibility of Loop 2, some of the side-chains are not fully ordered in the hRRM1 structures. For example, the electron density for the R293 side-chain in the hRRM1●TTP●GDP structure is discontinuous until the σ level is decreased to 0.7 or below (**Figure 4.3A**). Interestingly, Loop 2 in the hRRM1 and ScRR1 structures is further from the substrate compared to its position in TmRR1, in which it folds towards the catalytic site (**Figure 4.5B** and **4.6**). This is partially due to steric constraints imposed by Phe 240 in TmRR1, a single residue insertion compared to hRRM1 and ScRR1, which forces loop 2 to impinge on the C-site and move closer to the substrate (**Figure 4.6**).

As TmRR1, ScRR1, and hRRM1 all utilize CDP, UDP, GDP and ADP as substrates, it is reasonable to expect conserved interactions between their respective substrates and the C-site in all three species. However, this is not the case for the three structures with GDP bound (**Figure 4.5**). For example, Arg 293 (Arg 207 in TmRR1) from loop 2 stretches towards GDP in TmRR1 making a cation-π interaction with the adenine base, while in hRRM1 and ScRR1 it only makes van der Waals contacts with the base (**Figure 4.5** and **Table 4.5**). On the other hand, it has been previously observed that solvent mediates several second sphere interactions between the C-site and substrate that
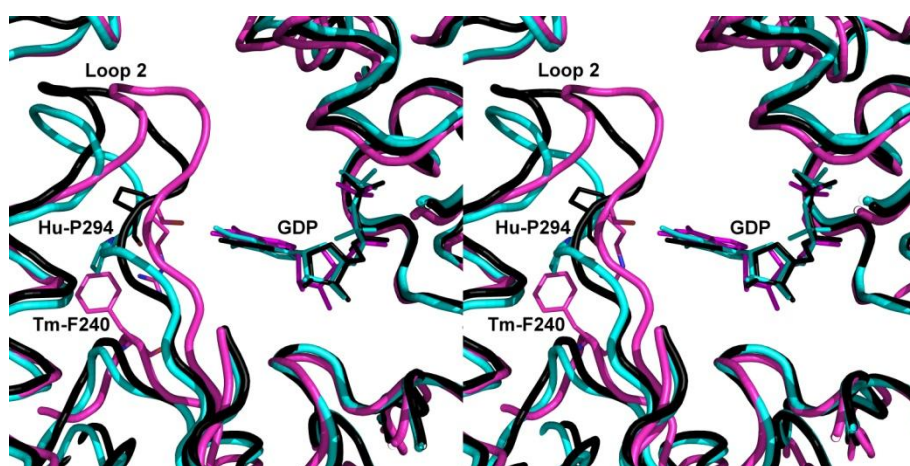
Figure 4.6: Stereo view of the catalytic site of RR1 bound to the substrate GDP.
The Cα-carbons of hRRM1●TTP●GDP (cyan), ScR1●TTP●GDP (black), and TmR1●TTP●GDP (magenta) were aligned in the molecular graphics program PyMOL. Phe 240 from TmRR1 and Pro 294 from hRRM1 and ScRR1 are shown in stick representation.

Table 4.5: Summary of C-site interactions with GDP from hRRM1●TTP●GDP, ScRR1●TTP●GDP, and EcRR1●TTP●GDP.

hRRM1●GDP Interactions	
Hydrogen bonds	
Atom from GDP	Atom(s) from Rnr1
N2	G246 O, G295 O
2'-OH	S217 O
3'-OH	C218 Sγ, N427 Nδ2, C429 Sγ, E431 Oε1
Alpha Phosphate	T604 N, A605 N
Beta Phosphate	S202 Oγ, S202 N, A605 N, S606 Oγ, S606 N, T607 Oγ1, T607 N
Van der Waals	
GDP	Atom(s) from Rnr1
Guanosine Base	A245, G246, G247, R293, G295, A296, L428, C429
Ribose	S217, C218, G247, N427, L428, C429, E431, L446, M602, P603
ScRR1●GDP Interactions	
Hydrogen bonds	
Atom from GDP	Atom(s) from Rnr1
N2	G246 O
N3	G247 N
2'-OH	G247 N, S217 O
3'-OH	C218 Sγ, E430 Oε1, E430 Oε2, N426 Nδ2, C428 Sγ,
Alpha Phosphate	A609 N
Beta Phosphate	T611 Oγ1, S202 N
Van der Waals	
GDP	Atom(s) from Rnr1
Guanosine Base	G247, L427, G246, R293, A296, C428
Ribose	S217, G247, C218, N426, L427, C428, L445, E430, M606, P607
EcRR1●GDP Interactions	
Hydrogen bonds	
Atom from GDP	Atom(s) from Rnr1
N2	T209 Oγ1
2'-OH	C225 Sγ, N437 ND2
3'-OH	N437 Nδ2, C439 Sγ, E441 Oε1, E441 Oε2
Alpha Phosphate	P621 O
Beta Phosphate	T209 Oγ1, E623 N, T624 Oγ1, T624 N, S625 Oγ, S625 N
Van der Waals	
GDP	Atom(s) from Rnr1
Guanosine	T209, P210, S224, R251, A252, G253, L438
Ribose	S224, C225, N437, C439, E441, L464, P621

may compensate for the lack of conservation of interactions between the species (Larsson *et al.* 2004; Xu *et al.* 2006; Xu *et al.* 2008).

In the structures of hRRM1, ScRR1, and TmRR1, the phosphates of the GDP substrate bind almost identically, where they interact with two loop regions (**Figure 4.3C**). The α-phosphate forms hydrogen bonds to the main-chain nitrogen atoms of T604 and A605, while the β-phosphate forms multiple hydrogen bonds to the side-chain Oγ and the main-chain nitrogen of residues S202, S606, and T607 (**Figure 4.3C**).

4.3.4 Allosteric Regulation at the Activity Site

The molecular basis by which ATP binding at the A-site stimulates RR1 activity while dATP binding inhibits activity currently remains unknown. Furthermore, compared to ATP, dATP is required to have higher affinity for the A-site to maintain allosteric regulation. This is because, under physiological conditions, the higher concentrations of ATP (1-5 mM) compared to dATP (1-20 μM), would cause the A-site to always be saturated with ATP. Therefore, compared to ATP, dATP binds the A-site with an approximately 13-fold lower K_d for EcRR1 and 40-fold for mRRM1(Ormo *et al.* 1990; Kashlan *et al.* 2002). These questions have remained unanswered because, until now, only the X-ray crystal structure of the ATP-analog adenosine 5'-(β,γ-imido) triphosphate (AMPPNP) bound at the A-site of EcRR1 was available (Eriksson *et al.* 1997).

Here, the first X-ray crystal structures of ATP and dATP bound at the A-site of any RR1 are presented (**Figure 4.2** and **Figure 4.7**). In both these structures, TTP is also bound at the S-site. To maintain previously established naming conventions with the ScRR1 and EcRR1 structures, the four helices of the ATP-binding cone have been named
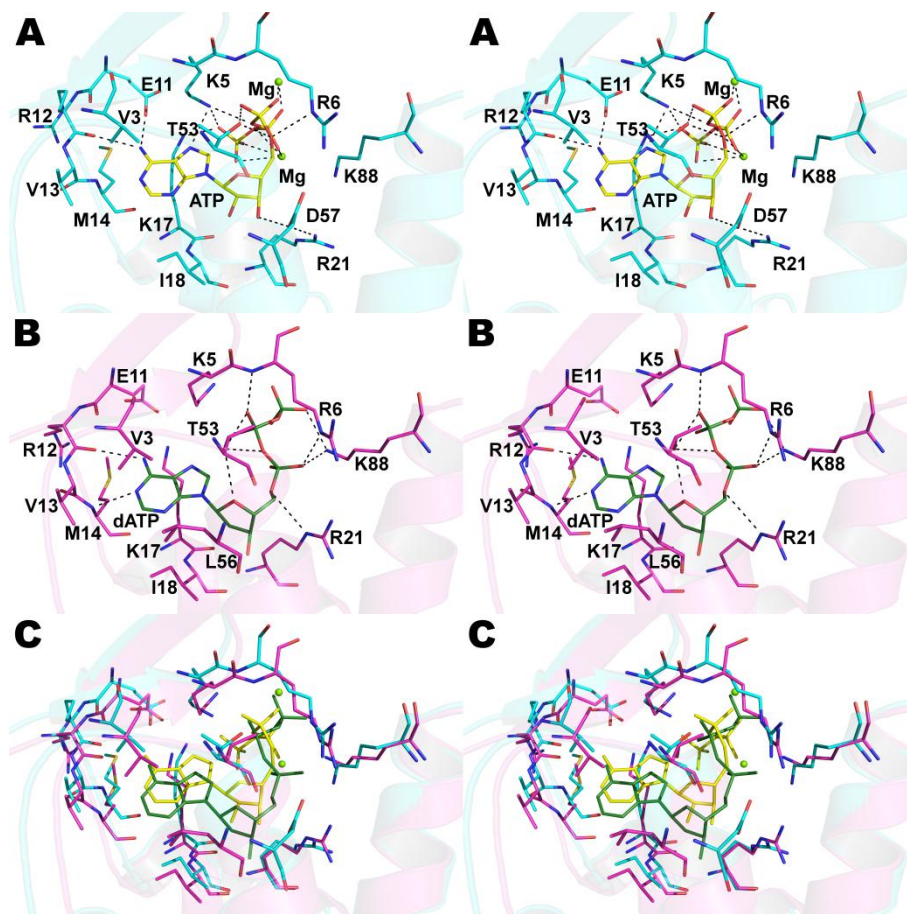
Figure 4.7: Stereo views of ATP and dATP binding at the A-site of hRRM1
(**A**) ATP binding. The protein is represented as ribbons, where carbons are cyan, oxygen red, and nitrogen blue (A-C), interacting residues are drawn as sticks, and ATP is represented as sticks with yellow carbons and phosphorous atoms. Hydrogen bonds and electrostatic interactions are shown as black dashed lines. Magnesium ions are represented as a lime-green spheres. (**B**) dATP binding. The protein is represented as ribbons with carbons colored magenta, and interacting residues drawn as sticks. dATP is represented as sticks, where its carbon and phosphorous atoms are colored green, and hydrogen bonds and electrostatic interactions are shown as dashed black lines. (**C**) Comparison of ATP and dATP binding by superimposing (A) and (B). The same coloring scheme as in (A-B) is kept, except that the ATP nucleotide is shown only in yellow and dATP is shown only in green. Magnesium atoms are represented as lime-green spheres.

146

H1-H4; H1 spans amino acids 15-26, H2 spans 36-46, H3 spans 53-70, and H4 spans 74-90 (**Figure 4.8**). The initial N-terminal fourteen amino acid residues form a β-hairpin which combines together with residues 48-51 to form the previously named "β-cap", which covers the end of the binding cavity made by the four-helix bundle formed by H1-H4 (Uhlin *et al.* 1994).

ATP or dATP binding causes helix H1 and the three β-strand cap to shift compared to the TTP-bound form to accommodate binding (**Figure 4.8**). Hence, some induced fit is observed due to effector binding at the A-site. What is striking about the ATP versus the dATP mode of binding is that dATP binds more deeply inside the four-helical bundle and its ribose adopts a half-chair conformation with the 2'-carbon out of plane, while ATP binds less deeply and its ribose adopts a 2'-endo conformation (**Figure 4.7** and **4.8**). In fact, the distance between the 3' hydroxyl of ATP and dATP when the structures are superimposed is 2.4 Å (**Figure 4.7**), and atomic depth calculations using the program DPX (Pintar *et al.* 2003) give dATP an average depth of 1.53 Å while ATP has a shallower average depth of 1.33 Å. Furthermore, calculations using the program Areaimol in the software suite CCP4 (1994) show that dATP buries 310 $Å^2$ of surface area when binding to the A-site, while the binding of ATP buries only 297 $Å^2$. The deeper binding of dATP, which buries more surface area of the four-helical cone than ATP, likely contributes to its higher affinity. In fact, the binding energy of protein-ligand interactions can be expressed as a change in solvent-accessible surface areas between the bound and unbound states (Murphy *et al.* 1993) supports this finding.

Interestingly, it is the chemical difference (the 2' hydroxyl) between ATP and dATP that causes the difference in binding at the A-site. The hydroxyl at the 2' position
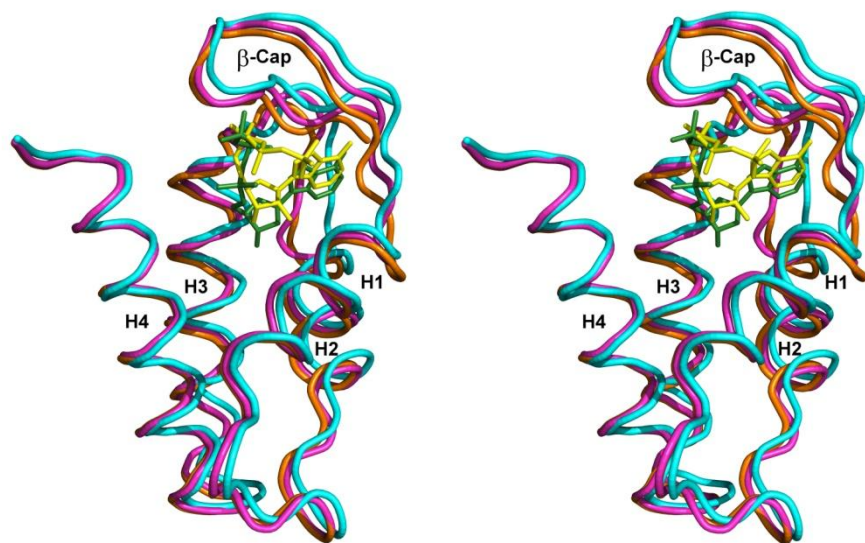
Figure 4.8:   Stereo view of the superimposition of hRRM1●TTP●ATP and hRRM1●TTP●dATP.
The ATP-binding cones of hRRM1●TTP●ATP (cyan) and hRRM1●TTP●dATP (magenta) were aligned to that of hRRM1●TTP (orange).   The proteins are represented as ribbons and the nucleotides are represented as sticks with ATP in yellow and dATP in green.

of ATP sterically precludes the ribose from binding deeper inside the four-helix bundle, while dATP, which lacks the 2' hydroxyl, is able to bind deeper in the pocket. In particular, Ile 18 would clash with the 2' hydroxyl of an ATP binding at the dATP position, acting as a steric gate (**Figure 4.7**). The 2' carbon of dATP makes several interactions with hydrocarbon atoms (**Figure 4.7B** and **Table 4.6**). However, the 3' hydroxyl of dATP makes no hydrogen bonds with hRRM1. In contrast, the 3' hydroxyl of ATP makes a hydrogen bond to the side-chain of Asp 57. The mutation of Asp 57 to Asn abolishes hRRM1's ability to discriminate between ATP and dATP bound to the A-site (Reichard *et al.* 2000). Binding of dATP to D57N mutants does not inhibit the activity of the enzyme as it does in the wild-type enzyme. In the ATP-bound structure, Asp 57 forms a salt-bridge with Arg 21, a residue that interacts with both the phosphate and ribose moieties (**Figure 4.7A**). The mutation of Asp 57 to Asn is likely to abolish this salt-bridge and change the electrostatic environment of the A-site, which may in part explain the previous observation.

The phosphate groups of dATP and ATP adopt different conformations when bound at the A-site (**Figure 4.7** and **4.8**). When ATP is bound in the A-site, its phosphate groups are positioned near the entrance to the binding pocket and held in place by a ring of positively charged residues (Arg 6, Lys 5, Lys 17, Arg 21, and Lys 88) (**Figure 4.7A**). Two magnesium ions are also observed interacting with the negatively charged phosphate groups in the ATP-bound structure, which appear to be absent in the dATP bound form (**Figure 4.7A** and **4.7B**). In contrast to the phosphate groups of ATP in the hRRM1●TTP●ATP structure, the phosphate groups of dATP in the

Table 4.6:   Summary of A-site interactions with ATP, dATP, and AMPPNP from hRRM1●TTP●ATP, hRRM1●TTP●dATP, and EcRR1●AMPPNP.

hRRM1●ATP Interactions	
Hydrogen bonds	
Atom from ATP	Atom(s) from Rnr1
N6	E11 Oε2, R12 O
N7	K5 NZ
3'-OH	D57 Oδ1
Alpha Phosphate	Mg4, R6 N, R6 Nε, T53 Oγ1
Beta Phosphate	Mg3, Mg4
Gamma Phosphate	Mg3, K5 NZ, K17 NZ
Van der Waals	
ATP	Atom(s) from Rnr1
Adenine Base	V3, K5, E11, R12, V13, M14, K17, I18, T53, L56
Ribose	R6, K17, I18, R21, T53, D57, K88
hRRM1●dATP Interactions	
Hydrogen bonds	
Atom from dATP	Atom(s) from Rnr1
N1	M14 N
N6	R12 O
4'-O	T53 Oγ
Alpha Phosphate	R6 Nε, R21 Nε, T53 Oγ1, K88 NZ
Beta Phosphate	R6 N, T53 Oγ1
Gamma Phosphate	K88 NZ
Van der Waals	
dATP	Atom(s) from Rnr1
Adenine Base	V3, K5, E11, R12, V13, M14, K17, I18, T53, L56
Ribose	K17, I18, R21, T53, L56
EcRR1●AMPPNP Interactions	
Hydrogen bonds	
Atom from AMPPNP	Atom(s) from RNR1
N1	N18 N
N6	E15 Oε2, K21 NZ
2'-OH	I22 N
3'-OH	H59 Nε2
4'-O	T55 Oγ1
Alpha Phosphate	K9 NZ, T55 Oγ1
Beta Phosphate	K9 NZ, K91 NZ
Gamma Phosphate	K21 NZ
Van der Waals	
AMPPNP	Atom(s) from Rnr1
Adenine Base	E15, R16, I17, N18, K21, I22
Ribose	K21, I22, V25, T55, H59, I62, F87

hRRM1●TTP●dATP structure are extended rather than folded back to place the γ-phosphate close to the adenine ring. The residue Lys 17 no longer interacts with the γ-phosphate as in the ATP-bound structure due to the extended phosphate conformation (**Figure 4.7A** and **4.7B**).

The adenine ring in dATP binds deeper in the pocket than it does in ATP. As a consequence of this, dATP is not within hydrogen-bonding distance of the side-chain atoms of the surface residues Lys 5 and Glu 11, unlike the ATP-bound form. In addition, the amide nitrogen of Met 14 hydrogen bonds with the adenine base of dATP, an interaction not observed in the ATP-bound structure (**Figure 4.7A** and **4.7B**). Moreover, both the bases form hydrophobic interactions with residues Val 3, Ile 18, and Leu 56 which pack against both faces of the adenine ring. For clarity, Leu 56 is not shown in **Figure 4.7**.

Although no major changes in the secondary or tertiary structure of hRRM1 were observed in the hRRM1●TTP●dATP X-ray crystal structure due to dATP binding at the A-site, confirmation that this was also the case in solution was sought. Circular dichroism experiments were performed on hRRM1 both in the absence of dATP or in the presence of 100 μM dATP (**Figure 4.9**). No major changes in the secondary structure of hRRM1 are observable due to the occupation of the A-site by dATP. However, circular dichroism method does have a limitation in its sensitivity to secondary structural changes. Small or subtle changes in the secondary structure may not be detectable by this method.

The only other RR1 structure of an effector-bound A-site currently available is EcRR1 bound to the ATP analogue AMPPNP (Eriksson *et al.* 1997) (**Figure 4.10**). The adenine base of AMPPNP in *E. coli* occupies a different position from that of ATP in
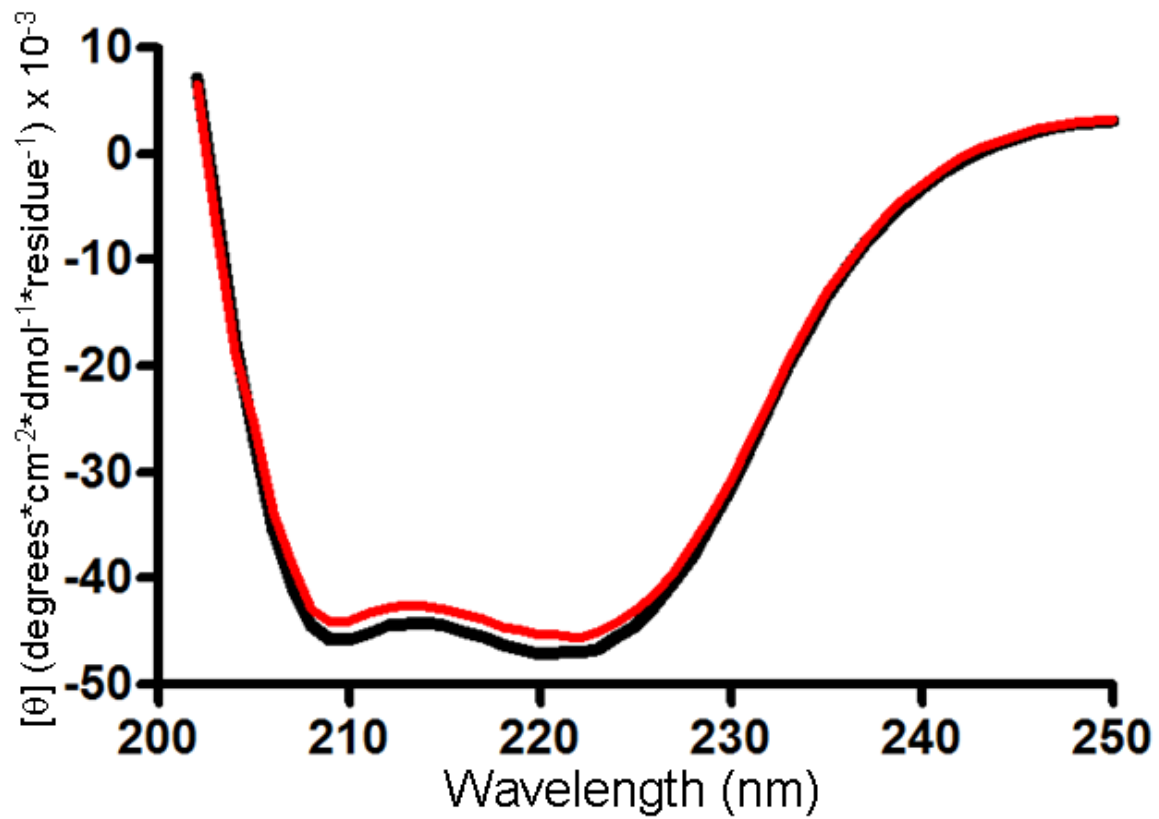
Figure 4.9: Circular dichroism spectra of hRRM1.
Circular dichroism spectra of hRRM1 both in the absence (black) and presence of 100 μM dATP (red).
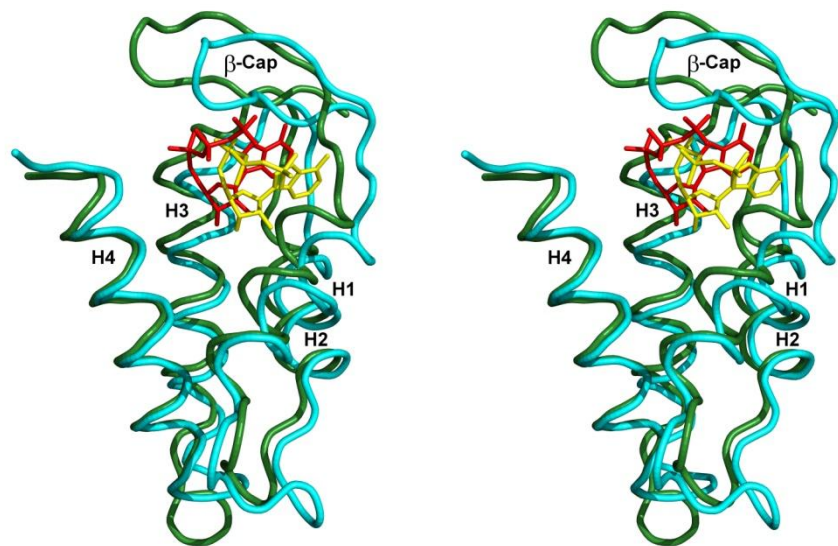
Figure 4.10: Stereo view of the ATP-binding cones of hRRM1 and EcRR1.
The ATP-binding cones of hRRM1•TTP•ATP (cyan) and EcRR1•TTP•AMPPNP (green) were aligned via the Cα carbon atoms in chain B. The proteins are represented as ribbons. AMPPNP (red) and ATP (yellow) are represented as sticks.

hRRM1 (**Figure 4.10**). This difference in binding can be attributed to: (1) the conformational difference of the β-cap, (2) the displacement of the *E. coli* β-cap toward solvent by at least 6 Å, and (3) the N-terminal portion of helix H1 in EcRR1 protruding toward the ribose, unlike its position in the hRRM1 structure. The phosphate group of AMPPNP in *E.coli* adopts a conformation comparable to that of ATP in the hRRM1 structure, folding back over the adenine base and interacting with Lys 21 (**Figure 4.7A** and **Figure 4.10**). The ribose moieties of AMPPNP and ATP in EcRR1 and hRRM1 adopt a 2'-endo conformation. There are also differences in the contacts and hydrogen bonds made by the adenine base of ATP when bound to EcRR1 versus hRRM1 (**Table 4.6**). This is due to the base being shifted more towards the surface in EcRR1 than it is in hRRM1, and the conformational difference in the β-cap between the two RR1s (**Figure 4.10**).

4.3.5 dATP-induced Oligomerization

Size exclusion chromatography (SEC) experiments to observe the formation of higher order oligomers were originally performed on Rnr1p from *S. cerevisiae* by fellow graduate student Sanath Wijerathna. See **Appendix A.4** for details on analysis of SEC data. To confirm that hRRM1 formed higher order oligomers in a dATP concentration-dependent manner, hRRM1 was also examined using SEC. The results show that at 1 μM or less dATP, hRRM1 forms a mixture of dimer and monomers (**Table 4.10**). These results can easily be explained. The binding of dATP to the S-site causes the formation of dimers and the monomer fraction consists of hRRM1 subunits which have not yet bound a dATP at their S-site. At a concentration of 5 μM dATP, in addition to the observed monomers and dimers, a peak is observed on the SEC chromatogram which corresponds to a molecular weight of 491 kDa.

Table 4.7: dATP-induced oligomerization visualized by SEC.

[dATP] (uM)	V_e	log Mol. Wt.	Mol. Wt. (kDa)	Oligomer
1	1.42	5.28	192	Dimer
	1.57	4.98	95.3	Monomer
5	1.22	5.69	492	Hexamer
	1.41	5.30	202	Dimer
	1.58	4.96	90.9	Monomer
10	1.22	5.69	492	Hexamer
	1.38	5.37	232	Dimer
20	1.21	5.71	516	Hexamer
	1.37	5.39	243	Dimer
50	1.2	5.73	540	Hexamer
	1.38	5.37	232	Dimer
100	1.2	5.73	540	Hexamer
	1.39	5.35	222	Dimer

The increased concentration of dATP has begun to occupy the A-site, and larger order oligomers have started to appear due to its occupation. The theoretical molecular weight of a hexamer is 540 kDa, so this peak is 50 kDa less than expected if it is indeed a hexamer. As the concentration of dATP is further increased, the observed peak at 491 kDa shifts upwards in molecular weight, eventually obtaining the correct size for a hexamer at 50 μM dATP (**Table 4.10**). These results indicate that as the concentration of dATP is increased, the monomer population is depleted and converted into the dimer and hexamer fractions. Shifting of the observed molecular weight of the hexamer peak indicates that at 5 μM dATP the peak is a mixture of hexamers and some lower oligomeric state, most probably a tetramer. As the concentration of dATP increases and the A-site becomes fully bound to dATP, hexamers become the dominant species.

Indeed, further SEC experiments performed on hRRM1 by Sanath Wijerathna confirm these results (data not shown). Sanath Wijerathna has recently completed a set of SEC

experiments in which the pH of the running buffer has been decreased from pH 8.0 to pH 7.6 to mimic physiological conditions as closely as possible. In addition, he has sampled a significantly larger number of dATP concentrations. His results indicate that the binding of dATP to the A-site initially causes the formation of tetramers. As concentration of dATP is increased and the A-site becomes fully occupied, the formation of hexamers is favored. However, a dynamic equilibrium was observed between all of these species, even at high concentrations of dATP.

These findings deviate from the previously reported studies on mRRM1. In the study reported by (Kashlan *et al.* 2002), only a dATP-induced tetramer was reported at physiological levels of dATP, with hexamer formation only observed at non-physiologic concentrations. This discrepancy may not be due to the light scattering results obtained in this publication, but rather in their interpretation. Since dynamic light scattering gives an average mass, a mixture of monomers, dimers, tetramers and hexamers may have skewed this result. The report by (Rofougaran *et al.* 2006) also observed hexameric species using gas-phase electrophoretic molecular mobility analysis (GEMMA) at similar dATP concentrations to those reported in this dissertation, but they do not observe the presence of tetramers.

4.3.6 *Low Resolution X-ray Crystal Structure of dATP-induced ScRR1 Hexamer*

To obtain a structural basis of these findings, crystallization the hRRM1 α_4 and α_6 were attempted. Although dATP-induced hexamers of hRRM1 crystallized in a hexagonal space group, the crystals only diffracted to a resolution of 15 Å. As ScRR1 also forms inactive hexamers at 20 μM dATP, fellow graduate student Sanath Wijerathna was able to crystallize the dATP-induced ScRR1 α_6 oligomer, producing crystals in the P6$_3$ space group which produced reflection data to a resolution of 6.0 Å. Provided with Sanath's data, a low resolution structure

using molecular replacement was determined, which gave a unique solution with four ScRR1 monomers in the asymmetric unit (**Table 4.2**). Since no structure of a dATP-bound ScRR1 exists, the hRMM1●TTP●dATP structure was used as the search model for molecular replacement. Rigid body refinement of the solution in REFMAC gave an R-free of 40%, which is indicative of a correct structure solution at this resolution.

The structure shows the packing arrangement of ScRR1 hexamers in the crystal can accommodate two possible models, model A and model B (**Figure 4.11A** and **4.11B**)
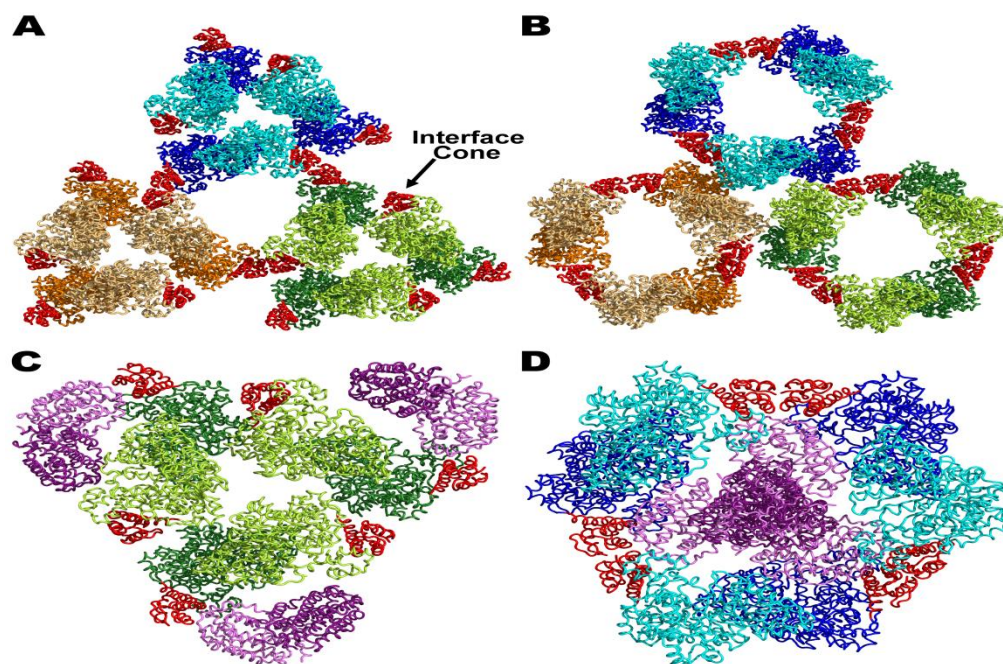
Figure 4.11: RR1 hexameric packing based on the low resolution X-ray crystal structure of the ScRR1 hexamer.
(**A and B**) Ribbon diagrams of the two possible hexamer packing arrangements. Three hexamers are shown in each each packing arrangement colored in shades of green, shades of orange, or shades of blue. The four-helix ATP-binding cone is colored red. (**C**) Model of the RR holo hexamer complex based on (A) with ScRR2 modeled based on the StRR1●StRR2 holo-complex. ScRR1 monomers are colored forest green and limon with the ATP-binding cone in red. ScRR2 subunits are colored dark purple and light-violet. (**D**) Model of the RR holo hexamer complex based on (B) with ScRR2 modeled based on the StRR1●StRR2 holo-complex. ScRR1 monomers are colored blue and cyan with the ATP-binding cone in red. ScRR2 subunits are colored dark purple and light-violet.

. In both models, the ScRR1 α_6 packs as a trimer of dimers, where the three dimers are related to each other by a three-fold axis (**Figure 4.11A** and **4.11B**). However, model A and B have different pore sizes at the center of the hexamer. In model A, three dATP-bound ATP-binding cones form the hexamer interface, leaving the remaining three free to interact with the small subunit (**Figure 4.11A** and **4.11B**). In model B, the dATP-bound ATP-binding cone sits at the interface, promoting RR1 hexamerization, where two dATP-bound four-helical cones from adjacent RR1 dimers contact each other in an antiparallel conformation, and are related by 2-fold symmetry (**Figure 4.11B**). Hence in model B, unlike in model A, all the four-helical ATP-binding cones will form hexamer interfaces.

To examine which packing arrangement supports published data on subunit interactions, modeling studies were performed using the previously determined StRR1●StRR2 $\alpha_2\beta_2$ holo-complex crystal structure. The StRR1●StRR2 holo-complex (PDB ID: 2BQ1) was used to model the holo-complex of ScRR1●ScRR2●ScRR4. The molecular graphics manipulation program PyMOL (DeLano Scientific) was used to superimpose the RR1 subunits of the StRR1●StRR2 holo-complex onto the RR1 subunits of ScRR1●dATP α_6 models A and B. The yeast small subunits, ScRR2 and ScRR4, were then modeled into the same positions as the StRR2 subunits. The models were energy minimized using the program Refmac. **Figure 4.11C** clearly shows that, using model A, up to six of the small subunits can simultaneously bind to the ScRR1●dATP α_6, permitting the formation of $\alpha_6\beta_2$, $\alpha_6\beta_4$, or $\alpha_6\beta_6$ complexes. On the other hand, using the same modeling scheme for model B, only two of the small subunits can fill the central cavity, suggesting that dATP-bound ScRR1 is an $\alpha_6\beta_2$ complex (**Figure 4.11D**).

The existence of a $\alpha_6\beta_2$ RR complex has been proposed based on light scattering, kinetics, and gas phase mass measurements (Kashlan *et al.* 2002; Rofougaran *et al.* 2006). If this were

true, one β_2 will have to provide free-radicals to three RR1 dimers. It has been previously shown that in Class II RRs, one adenosylcobalamin co-factor can serve as the radical generator for multiple large subunits (Licht 1999). If one β_2 can serve as the free-radical generator for multiple large subunits as in the Class II RRs, model B will be viable. Although the existence of model B cannot be completely ruled out, there are reports that support the existence of both $\alpha_6\beta_4$ and $\alpha_6\beta_6$ oligomers in mammalian RR1s (Kashlan *et al.* 2002; Wang *et al.* 2007). Since model A is able to account for all published data regarding active α_6 oligomers, while model B is not, it is proposed that model A is the most likely candidate for the structure of α_6 in solution. The data are also in agreement with a previous report which suggests that dATP significantly enhances subunit interactions (Ingemarson *et al.* 1996). In model A, the dATP-bound ATP-binding cone of the α subunit is free to directly interact with the β subunit (**Figure 4.11C**), promoting subunit interactions.

4.3.7 Conclusions & A Model for dATP-induced Oligomerization

Here, the X-ray crystal structures of hRRM1 bound to TTP only, TTP●GDP, TTP●ATP, TTP●dATP are reported. Although the X-ray crystal structure of the first eukaryotic large subunit for Class Ia Rnr is that of *S. cerevisiae,* hRRM1 is the first X-ray crystal structure of a mammalian Class Ia large subunit. RR1 from *S. cerevisiae* and *H. sapiens* share only 66% sequence identity. Therefore, the crystal structures reported in this dissertation will provide an improved model for the implementation of *in silico* drug design over that of the ScRR1 structure. In addition, the crystal structures of hRRM1●TTP●ATP and hRRM1●TTP●dATP provide a structural basis for the difference in ATP and dATP binding at the A-site and insight into the oligomeric regulation of Rnr.

Based on the structural and functional data presented in this chapter, a model which accounts for the dATP concentration-dependent oligomerization of eukaryotic RR1s is proposed (**Figure 4.12**). Size exclusion chromatography data show that there is dynamic equilibrium between the α, α_2, α_4 and α_6 forms of hRRM1, even at high concentrations of dATP. In the absence of nucleotide effectors, RR1 exists as an inactive monomer (**Figure 4.12**). Binding of ATP, dATP, TTP or dGTP to the S-site causes RR1 to form dimers, which can then combined together with the small subunit to form $\alpha_2\beta_2$ hetero-tetramers (**Figure 4.12**). Partial occupation of the A-site by dATP causes two α_2 subunits to associate into a transient tetramer intermediate (**Figure 4.12**). This is because after the α_2 subunit is formed via the occupation of the S-site by nucleoside triphosphate effectors, higher order oligomerization will occur by the association of sets of RR1 dimers rather than monomers with dimers. Hence, transient tetramers will be formed by the association of two RR1 dimers. As the A-site becomes fully occupied by dATP an additional RR1 dimer will associate with a tetramer to form a hexamer (**Figure 4.12**). Consistent with all currently published data (Kashlan *et al.* 2002; Rofougaran *et al.* 2006; Wang *et al.* 2007), α_6 can associate with β to form $\alpha_6\beta_2$, $\alpha_6\beta_4$ and $\alpha_6\beta_6$ complexes which are in dynamic equilibrium. Finally, when dATP levels become depleted during DNA replication or repair, active ATP-bound Rnr oligomers will be formed to replenish the dNTP supply.
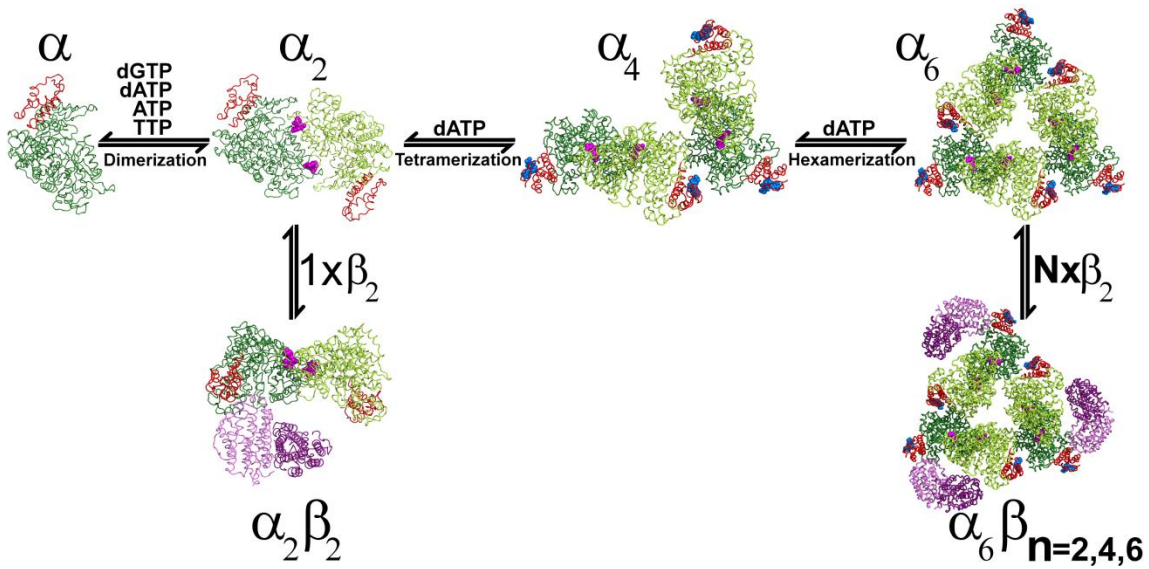
Figure 4.12: Model for dATP-dependent oligomerization of eukaryotic RRs.
Binding of effectors to the S-site causes dimerization. Subsequent binding of dATP to the A-site initially causes the formation of tetramers and then hexamers as the site becomes fully occupied. Effectors bound at the S-site are shown as magenta spheres and dATPs bound at the A-site are shown as marine blue spheres.

5. CONCLUSIONS

5.1 CONCLUSIONS FROM THIS DISSERTATION RESEARCH

The overarching goals of this dissertation research are divided into two parts: (1) the functional and structural characterization of the *S. cerevisiae Rnr1p msl* alleles $Rnr1p^{S269P}$ and $Rnr1p^{S610F}$, and (2) elucidation of the first X-ray crystal structures of hRRM1 and characterization of dATP-dependent oligomerization in eukaryotic Rnrs. Results presented in **Chapter 3** provide both structural and biochemical data to explain molecular mechanisms in Rnr1p causing observed *msl* phenotypes. In **Chapter 4**, the first X-ray crystal structures of the large subunit of Rnr from a mammalian species are presented with each nucleoside-binding site occupied. In addition, size exclusion chromatography data combined a low resolution X-ray crystal structure of a dATP-induced hexamer from *S. cerevisiae* provide a model for oligomeric regulation of the large subunit of Rnr.

5.1.1 Mutant Rnr1p Alleles $Rnr1p^{S269P}$ and $Rnr1p^{S610F}$

A molecular basis for the *msl* phenotype induced by both $Rnr1^{S269P}$ and $Rnr1^{S610F}$ mutations is provided by the X-ray crystal structures of the mutant proteins bound to both substrates and allosteric effectors. The Rnr1p-S269P mutation causes the regulatory loop, known as Loop 1, to become disordered in both of the X-ray crystal structures. Since Loop 1 is involved in the binding of nucleoside triphosphates to the S-site, the mutant protein is no longer able to bind to allosteric effectors. As a secondary effect, residues in a second regulatory loop, known as Loop 2, also become disordered. Loop 2 is required for specificity cross-talk between the S-site and the C-site (Larsson *et al.* 2004; Xu *et al.* 2006). Essentially, the Rnr1p-S269P disables the ability of the enzyme to bind effectors efficiently, which results in the abolishment

of specificity cross-talk. However, electron density for substrates bound to the C-site is observed even in the presence of this mutation, which accounts for the low levels of activity observed in the *in vitro* activity assays.   This is in agreement with the previous observation that ribonucleotide reductase possesses low basal activity with no effectors bound to the S-site (Ge et al. 2003).

The Rnr1p-S610F point mutation occurs in the C-site, and interacts with the β-phosphate of the substrate. In the X-ray crystal structures of this mutant, there are substrate and effector nucleotides bound at both the C-site and the S-site. Since this residue is involved in the binding of a portion of the substrates, it was hypothesized that the observed loss in activity was due to a change in substrate affinity. To test this hypothesis, ultrafiltration nucleotide binding assays were performed to determine the dissociation constant of the wild-type and Rnr1p-S610F mutant for the substrate molecule ADP in the presence of the allosteric effector dGTP.

The affinity of the wild-type enzyme for ADP was measured to be 29.4 μM, while that of the S610F mutant was measured to be 76.6 μM. Under the *in vitro* activity assay conditions, the concentration of substrate is 1 mM, and 97% and 93% of the catalytic sites should be occupied with substrate for wild-type and Rnr1p-S610F, respectively. If depression of catalytic activity was due to the observed change in the dissociation constant, a decrease of about 5% activity would be expected. However, the two-fold drop in affinity is insufficient to explain the extreme loss of activity in the presence of saturating concentrations of substrates, as the activity of the S610F mutant was measured to be 0.7 percent of the wild-type enzyme.

We propose that the substitution of the larger phenyl group must be altering the rate of reaction by slowing down the rate-limiting step of the reaction (k_{cat}). The rate-limiting step of the Class I Rnr catalytic cycle has been previously shown to be either a conformational

isomerization preceding nucleoside reduction during pre-steady-state conditions, or the reduction of the active site by the C-terminal tail after each catalytic turnover under steady-state conditions (Ge *et al.* 2003). Since the *in vitro* activity assays performed in **Chapter 3** contained concentrations of Rnr1p that correspond to those in the steady-state experiments of (Ge *et al.* 2003), and the concentration of substrate used in the assays is in the steady-state region, we believe that the Rnr1p-S610F mutant is slowing down the reduction of the C-site, rather than the conformational gating step which occurs before catalysis. Since phenylalanine is a larger bulkier residue than serine, it may restrict the access of the C-terminal tail to the catalytic site to slow down the reduction of the catalytic cysteines. Although the data heavily favors this hypothesis, the possibility that the Rnr1p-S610F mutation instead slows the conformational isomerization observed under pre-steady-state conditions can not be totally ruled out.

Although the Rnr1p-S269P mutation disrupts specificity cross-talk, and Rnr1p-S610F alters the value of k_{cat}, the net effect of both mutations is the unbalanced production of deoxynucleotides, which has been previously shown to cause increased mutation rates and genomic instability (Reichard 1988; Desany *et al.* 1998; Chabes *et al.* 2003). In the case of both the S269P and the S610F point mutations, the DNA precursor dATP is under-produced with respect to the other dNTPs, as a majority of mutation events were observed to occur at AT base pairs. In addition, providing yeast cells harboring the *msl* alleles with dAMP was able to suppress the *msl* phenotype. The skewed deoxynucleotide pools produced by these mutant alleles induce genomic instability that requires cells to have a functional mismatch repair system to remain viable (**Figure 5.1**). Combined with data from Dr. Simon's study, this dissertation research suggests a new therapeutic approach involving dysregulation or Rnr, leading to skewed

dNTP pools, rather than inhibition of Rnr activity as a treatment strategy for cancers harboring deficient or defective MMR genes.

For example, the substrate analogues discussed in **Section 1.3.3** are all targeted at the over-all inhibition of the catalytic activity of Rnr, and act by destruction of the free-radical or covalent modification of residues in the C-site of the large subunit. The ideal situation is one in which only cancerous cells are targeted by these molecules, however this is not the case. While these drugs are effective at stopping the growth of rapidly growing cancer cells, they are also toxic to other healthy actively propagating cells. Toxicity of these chemotherapeutic agents can result in conditions such as hair loss and anemia in patients receiving treatment regimes.

Consider now that a patient is afflicted with a cancer harboring defective MMR gene(s), and all of the other cells in this individual's body contain a functional MMR system. If the hypothesis from this dissertation research is true, a small molecule could be designed which targets either the S-site or A-site to cause imbalances in the dNTP pools. Cancer cells with defective MMR gene(s) would experience the synthetic lethal phenotype induced by the combination of the skewed nucleotide pools and defective MMR system, while normal cells with functional MMR genes would remain unharmed (**Figure 5.1**). This drug would be a selective killer, targeting only cells with defective MMR systems.

5.1.2 X-ray Crystal Structures of hRRM1 and Oligomeric Regulation by dATP

In **Chapter 4** the first X-ray crystal structures of hRRM1 bound to TTP, TTP●GDP, TTP●ATP, TTP●dATP are reported. Although the X-ray crystal structure of the first eukaryotic large subunit for Class Ia Rnr is that of *S. cerevisiae,* hRRM1 is the first X-ray crystal structure of a mammalian Class Ia large subunit. Even though the large subunit of Rnr from *H. sapiens* shares only 66% and 27% sequence identity with *S. cerevisiae* and *E. coli*, their overall folds are

quite conserved, as illustrated by the overall RMSDs for their Cα carbon atoms. However, there are still subtle differences in the A-site, S-site, and C-site as compared to the previously-determined X-ray crystal structures. Therefore, the crystal structures reported in this dissertation will provide an improved model for the implementation of *in silico* anti-cancer drug design over that of the *S. cerevisiae* structure.

The crystal structures of hRRM1●TTP●ATP and hRRM1●TTP●dATP provide the first structures of any RR1 bound to ATP and dATP at the A-site. Until now, the only available structural model of the A-site bound to a ligand was that of the Class Ia *E. coli* occupied by the ATP analogue AMPPNP (Eriksson *et al.* 1997). The binding ofATP and dATP to the A-site were observed to be different. dATP binds more deeply inside the four-helical bundle and its ribose adopts a half-chair conformation with the 2'-carbon out of plane, while ATP binds less deeply and its ribose adopts a 2'-endo conformation. The distance between the 3' hydroxyl group of the bound ATP and dATP was measured to be 2.4 Å when their structures were superimposed and atomic depth calculations also confirm that dATP is bound deeper in the pocket than ATP. Binding of dATP also buried a larger portion of the A-site's surface area than the binding of ATP. Differential binding of ATP and dATP is hypothesized to be caused by a steric gate involving the residue isoleucine 18. Docking of ATP into the same position as dATP results in the 2' hydroxyl group clashing with the backbone and side-chain residues of this key isoleucine residue.

Although the X-ray crystal structures of hRRM1●TTP●dATP and hRRM1●TTP●ATP provide a molecular mechanism for their altered binding at the A-site, the basis by which ATP binding at the A-site stimulates Rnr activity, while dATP binding inhibits activity currently remains unknown. Interestingly, circular dichroism experiments show no major secondary
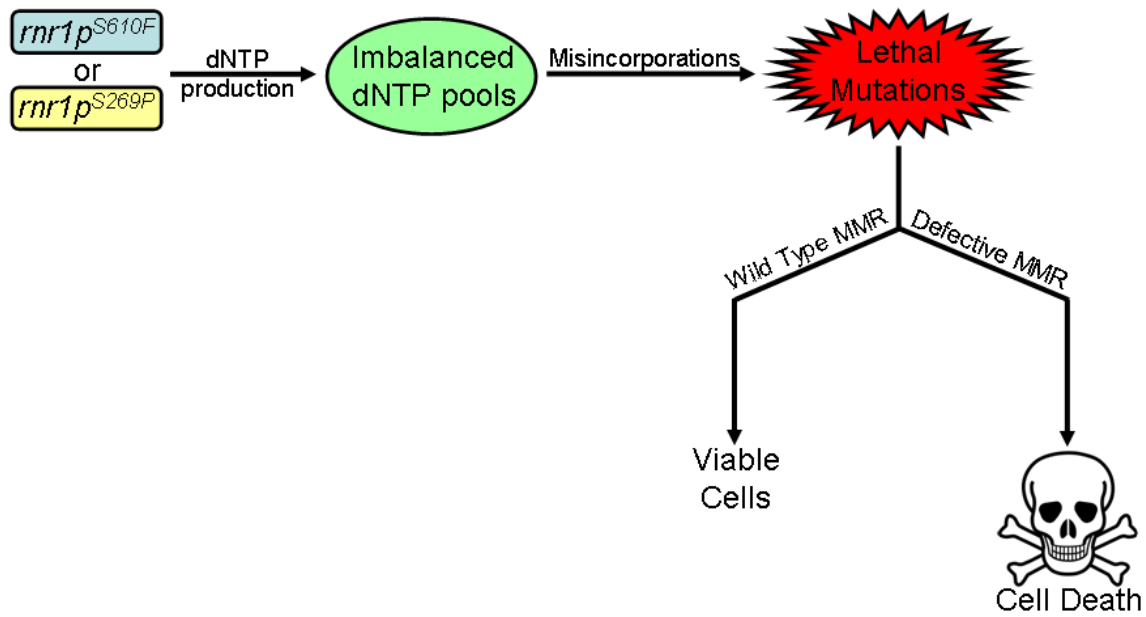
Figure 5.1: Alleles of *Rnr1p* result in *msl* phenotype when combined with defective MMR machinery.

structural re-arrangements due to dATP binding. Therefore, any structural changes that occur in the large subunit due to A-site occupation must be small or subtle. Since the hRRM1●TTP●dATP and hRRM1●TTP●ATP structures presented here are the result of soaking experiments, it was considered that these structures may only provide a snapshot of the initial binding of ligands to this site. To remedy this, co-crystallization experiments with dATP and hRRM1 were attempted. Although dATP-induced hexamers of hRRM1 were crystallized in a hexagonal space group in multiple crystallization conditions, the crystals only diffracted to a resolution of 15 Å at best.

The large subunit of Rnr from *S. cerevisiae* also forms inactive hexamers when bound to dATP, and fellow graduate student Sanath Wijerathna was able to crystallize the dATP-induced hexamer, producing crystals in the $P6_3$ space group which generated reflection data to a resolution of 6.0 Å. Provided with Sanath's data, a low resolution structure using molecular replacement was determined, which gave a unique solution. Rigid body refinement of the solution in REFMAC gave an R-free of 40%, which is indicative of a correct structure solution at this resolution. The electron density shows the packing arrangement of ScRR1 hexamers in the crystal can accommodate two possible models.

Combined together with size exclusion data, a model is proposed which describes the dATP-induced oligomerization of the large subunit of Rnr (**Figure 4.12**). In the absence of nucleotide effectors, RR1 exists as an inactive monomer. Binding of ATP, dATP, TTP or dGTP to the S-site causes RR1 to form dimers, which can then combine together with the small subunit to form $\alpha_2\beta_2$ hetero-tetramers. Partial occupation of the A-site by dATP causes two dimers to associate into a transient tetramer intermediate. As the A-site becomes fully occupied by dATP an additional RR1 dimer will associate with a tetramer to form a hexamer. Consistent with all

currently published data (Kashlan *et al.* 2002; Rofougaran *et al.* 2006; Wang *et al.* 2007), α_6 can associate with β to form $\alpha_6\beta_2$, $\alpha_6\beta_4$ and $\alpha_6\beta_6$ complexes which are in dynamic equilibrium.

5.2 FUTURE DIRECTIONS

As mentioned above, it has been previously shown that in Class Ia Rnrs, the rate-limiting step is either the reduction of the catalytic site after each catalytic turnover or a structural gating step that occurs before free-radical transfer and catalysis (Ge *et al.* 2003). Since the conditions used in the *in vitro* activity assays in this dissertation research match those of the steady-state measurements in (Ge *et al.* 2003), it was hypothesized that the S610F mutation was affecting the reduction of catalytic site after each turnover, resulting in reduction of k_{cat}. However, with the currently available experimental evidence, it is not possible to unequivocally determine which of these two steps becomes affected, and therefore rate-limiting in this mutant. To fully elucidate which of these two mechanisms results in the observed reduction of k_{cat}, kinetics of substrate reduction by Rnr1p-S610F in pre-steady-state conditions are required. Under pre-steady-state conditions, the Class Ia Rnr from *E. coli* shows an initial burst phase with a k_{cat} value of between 8 and 10 s^{-1}, which corresponds to a gating step the precedes radical transfer and catalysis of substrates. However, under steady state conditions where multiple turnovers take place, the k_{cat} is reduced to between 1 and 2 s^{-1}, which is attributed to the reduction of the catalytic site after each catalytic turn over. If pre-steady-state measurements of k_{cat} with Rnr1p-S610F give results with a higher rate constant than k_{obs} measured during steady-state conditions, reduction of the catalytic site is the step affected by the S610F mutation. However, if the k_{cat} measured under pre-steady-state conditions is approximately equal to k_{obs} measured under steady-state conditions, the structural gating step that precedes free-radical transfer is the step affected by the S610F mutation.

At the time of the publishing of this dissertation, no functional stopped flow apparatus which allows the usage of ^{14}C or ^{3}H-labeled substrates was available at either the University of Tennessee or Case Western Reserve University. If such an apparatus becomes available in the future, pre-steady-state kinetics of Rnr1p-S610F as performed in (Ge *et al.* 2003) would allow the determination of which step is affected by this mutation.

Based on the packing arrangement of large subunits in the low resolution X-ray crystal structure of the dATP-induced hexamer of *S. cerevisiae* Rnr1p, two solutions are possible for the packing of the hexamer in solution. It is not possible to distinguish between these two possibilities by analysis of the electron density. However, site-directed mutagenesis of residues that make up the hexamer interfaces of the two models provide a solution to this problem. In fact, we have selected several residues in the interface regions of both packing models for mutagenesis be examining the interfaces. For hexamer packing model A, we observed two ion pair interactions by the residues D182 and R12. We hypothesized that mutation of these charged residues to the opposite charge (D183R and R12E) would be unfavorable, disallowing the formation of hexamers if model A is the correct model. Likewise, we also observed the residues H2, D16, and F15 forming ion pair interactions and a hydrophobic packing interaction for hexamer packing model B. Therefore, the site-directed mutants H2E, F15A, and D16R were designed to break packing model B. Each site-directed mutant should be expressed, purified, and then have size exclusion chromatography performed on the purified protein in the presence of 100 μM dATP. If D182R or R12E mutants no longer form hexamers, packing model A is most likely the correct model, or if H2E, F15A, or D16R mutants no longer form hexamers, packing model B is most likely the correct model. If all of the site-directed mutants are still able to form hexamers, another experimental method will most likely be required to distinguish

between the two. As an alternative, cryo electron microscopy (EM) makes and ideal candidate, as particles are directly visualized during the data collection process. Although this method is known to be unusable on small proteins, the size of the hexamer (540 kDa) is within the experimental range of cryo EM.

Many questions about the regulation of the activity of the large subunit of the enzyme by ATP and dATP remain unknown. Although this dissertation research provides the molecular details of the differences between the binding of ATP and dATP to the A-site, the mechanism by which they alter the overall activity of the enzyme is still a mystery. It is clear that the binding of either ATP or dATP to the A-site is able to induce the formation of hexameric populations of large subunits. ATP-induced hexamers stimulate the activity of the enzyme, while dATP-induced hexamers inactivate the enzyme. The elucidation of the mechanism for activation and deactivation by these allosteric effectors is an important biological question that needs to be answered. One hypothesis is that the ATP-induced hexamers are structurally distinct from dATP-induced hexamers. Crystallization experiments to elucidate the X-ray crystal structure of an ATP-induced hexamer should be undertaken to compare the packing of ATP-induced hexamers to that of the dATP-induced *S. cerevisiae* hexamers presented in this dissertation.

The dATP feedback resistant mutant allele D57N was first discovered in mouse lymphoma cells in 1980 and was cloned in 1988 (Ullman *et al.* 1980; Caras *et al.* 1988). Mutation of Asp 57 to Asn abolishes the large subunit's ability to inhibit the activity of the enzyme by binding dATP to the A-site (Reichard *et al.* 2000; Kashlan *et al.* 2003). Instead, the specific activity of D57N mutant enzyme is activated by the binding of dATP. This mutant provides an interesting method for studying the regulation of the large subunit by ATP and dATP. How does this single mutation abolish inactivation of the enzyme by the binding of

dATP? One hypothesis is that the D57N mutation does not allow for hexamerization to occur due to dATP binding, thereby relieving the inhibitory effect. It was reported by (Kashlan *et al.* 2003) that the D57N mutant only formed tetrameric species in the presence of dATP. However, the same group was also only able to observe tetramers of the wild-type enzyme in the presence of dATP, when there is evidence from multiple laboratories that dATP clearly induces the formation of hexamers. Therefore, the ability of D57N to form hexameric species due to the binding of dATP needs to be re-examined in detail. If it is possible to form dATP-induced hexamers of D57N, they must be distinct from those formed by the wild-type enzyme.

REFERENCES

(1994). "The CCP4 suite: programs for protein crystallography." <u>Acta Crystallogr D Biol Crystallogr</u> **50**(Pt 5): 760-3.

Aberg, A., S. Hahne, M. Karlsson, A. Larsson, M. Ormo, A. Ahgren and B. M. Sjoberg (1989). "Evidence for two different classes of redox-active cysteines in ribonucleotide reductase of Escherichia coli." J Biol Chem **264**(21): 12249-52.

Abuin, A., H. Zhang and A. Bradley (2000). "Genetic analysis of mouse embryonic stem cells bearing Msh3 and Msh2 single and compound mutations." Mol Cell Biol **20**(1): 149-57.

Alani, E. (1996). "The Saccharomyces cerevisiae Msh2 and Msh6 proteins form a complex that specifically binds to duplex oligonucleotides containing mismatched DNA base pairs." Mol Cell Biol **16**(10): 5604-15.

Altschul, S. F., T. L. Madden, A. A. Schaffer, J. Zhang, Z. Zhang, W. Miller and D. J. Lipman (1997). "Gapped BLAST and PSI-BLAST: a new generation of protein database search programs." Nucleic Acids Res **25**(17): 3389-402.

Andersson, K. K. (2008). General Short Overview of RNR and Introduction. Ribonucleotide Reductase. K. K. Andersson. New York, Nova Science Publishers**:** 1-15.

Andersson, M. E., M. Hogbom, A. Rinaldo-Matthis, W. Blodig, Y. Liang, B. O. Persson, B. M. Sjoberg, X. D. Su and P. Nordlund (2004). "Structural and mutational studies of the carboxylate cluster in iron-free ribonucleotide reductase R2." Biochemistry **43**(24): 7966-72.

Aravind, L., Y. I. Wolf and E. V. Koonin (2000). "The ATP-cone: an evolutionarily mobile, ATP-binding regulatory domain." J Mol Microbiol Biotechnol **2**(2): 191-4.

Avval, F. Z. and A. Holmgren (2009). "Molecular mechanisms of thioredoxin and glutaredoxin as hydrogen donors for Mammalian s phase ribonucleotide reductase." J Biol Chem **284**(13): 8233-40.

Ayusawa, D., K. Iwata and T. Seno (1983). "Unusual sensitivity to bleomycin and joint resistance to 9-beta-D-arabinofuranosyladenine and 1-beta-D-arabinofuranosylcytosine of mouse FM3A cell mutants with altered ribonucleotide reductase and thymidylate synthase." Cancer Res **43**(2): 814-8.

Balzarini, J. (2000). "Effect of antimetabolite drugs of nucleotide metabolism on the anti-human immunodeficiency virus activity of nucleoside reverse transcriptase inhibitors." Pharmacol Ther **87**(2-3): 175-87.

Ban, C., M. Junop and W. Yang (1999). "Transformation of MutL by ATP binding and hydrolysis: a switch in DNA mismatch repair." Cell **97**(1): 85-97.

Ban, C. and W. Yang (1998). "Crystal structure and ATPase activity of MutL: implications for DNA repair and mutagenesis." Cell **95**(4): 541-52.

Bard, J., K. Ercolani, K. Svenson, A. Olland and W. Somers (2004). "Automated systems for protein crystallization." Methods **34**(3): 329-47.

Beck, W. S., M. Goulian, A. Larsson and P. Reichard (1966). "Hydrogen donor specificity of cobamide-dependent ribonucleotide reductase and allosteric regulation of substrate specificity." J Biol Chem **241**(9): 2177-9.

Bergfors, T. (1999). Protein Crystallization: Techniques, Strategies, and Tips. La Jolla, California, International University Line.

Bergfors, T. (2003). "Seeds to crystals." J Struct Biol **142**(1): 66-76.

Berglund, O., O. Karlstrom and P. Reichard (1969). "A new ribonucleotide reductase system after infection with phage T4." Proc Natl Acad Sci U S A **62**(3): 829-35.

Birgander, P. L., A. Kasrayan and B. M. Sjoberg (2004). "Mutant R1 proteins from Escherichia coli class Ia ribonucleotide reductase with altered responses to dATP inhibition." J Biol Chem **279**(15): 14496-501.

Blakley, R. L., R. K. Ghambeer, P. F. Nixon and E. Vitols (1965). "The cobamide-dependent ribonucleoside triphosphate reductase of lactobacilli." Biochem Biophys Res Commun **20**(4): 439-45.

Bondar, T., A. Ponomarev and P. Raychaudhuri (2004). "Ddb1 is required for the proteolysis of the Schizosaccharomyces pombe replication inhibitor Spd1 during S phase and after DNA damage." J Biol Chem **279**(11): 9937-43.

Booker, S., S. Licht, J. Broderick and J. Stubbe (1994). "Coenzyme B12-dependent ribonucleotide reductase: evidence for the participation of five cysteine residues in ribonucleotide reduction." Biochemistry **33**(42): 12676-85.

Borovok, I., R. Kreisberg-Zakarin, M. Yanko, R. Schreiber, M. Myslovati, F. Aslund, A. Holmgren, G. Cohen and Y. Aharonowitz (2002). "Streptomyces spp. contain class Ia and class II ribonucleotide reductases: expression analysis of the genes in vegetative growth." Microbiology **148**(Pt 2): 391-404.

Boukovinas, I., C. Papadaki, P. Mendez, M. Taron, D. Mavroudis, A. Koutsopoulos, M. Sanchez-Ronco, J. J. Sanchez, M. Trypaki, E. Staphopoulos, V. Georgoulias, R. Rosell and J. Souglakos (2008). "Tumor BRCA1, RRM1 and RRM2 mRNA expression levels and clinical response to first-line gemcitabine plus docetaxel in non-small-cell lung cancer patients." PLoS ONE **3**(11): e3695.

Bourdon, A., L. Minai, V. Serre, J. P. Jais, E. Sarzi, S. Aubert, D. Chretien, P. de Lonlay, V. Paquis-Flucklinger, H. Arakawa, Y. Nakamura, A. Munnich and A. Rotig (2007). "Mutation of RRM2B, encoding p53-controlled ribonucleotide reductase (p53R2), causes severe mitochondrial DNA depletion." Nat Genet **39**(6): 776-80.

Bradford, M. M. (1976). "A rapid and sensitive method for the quantitation of microgram quantities of protein utilizing the principle of protein-dye binding." Anal Biochem **72**: 248-54.

Branch, P., M. Masson, G. Aquilina, M. Bignami and P. Karran (2000). "Spontaneous development of drug resistance: mismatch repair and p53 defects in resistance to cisplatin in human tumor cells." Oncogene **19**(28): 3138-45.

Bronner, C. E., S. M. Baker, P. T. Morrison, G. Warren, L. G. Smith, M. K. Lescoe, M. Kane, C. Earabino, J. Lipford, A. Lindblom and et al. (1994). "Mutation in the DNA mismatch repair gene homologue hMLH1 is associated with hereditary non-polyposis colon cancer." Nature **368**(6468): 258-61.

Brown, N. C., Z. N. Canellakis, B. Lundin, P. Reichard and L. Thelander (1969). "Ribonucleoside diphosphate reductase. Purification of the two subunits, proteins B1 and B2." Eur J Biochem **9**(4): 561-73.

Brown, N. C., R. Eliasson, P. Reichard and L. Thelander (1969). "Spectrum and iron content of protein B2 from ribonucleoside diphosphate reductase." Eur J Biochem **9**(4): 512-8.

Brown, N. C. and P. Reichard (1969). "Role of effector binding in allosteric control of ribonucleoside diphosphate reductase." J Mol Biol **46**(1): 39-55.

Brunger, A. T. (1992). "The free R value: a novel statistical quantity for assessing the accuracy of crystal structures." Nature **355**(355): 527-474.

Brunger, A. T., P. D. Adams, G. M. Clore, P. Gros, R. W. Grosse-Kunstleve, J.-S. Jiang, J. Kuszewski, N. Nilges, N. S. Pannu, R. J. Read, L. M. Rice, T. Simonson and G. L. Warren (1998). "Crystallography and NMR System (CNS), A new software suite for macromolecular structure determination." Acta Cryst **54**(54): 905-921.

Brunger, A. T., J. Kuriyan and M. Karplus (1987). "Crystallographic R Factor Refinement by Molecular Dynamics." Science **235**(4787): 458-460.

Camier, S., E. Ma, C. Leroy, A. Pruvost, M. Toledano and M. C. Marsolier-Kergoat (2007). "Visualization of ribonucleotide reductase catalytic oxidation establishes thioredoxins as its major reductants in yeast." Free Radic Biol Med **42**(7): 1008-16.

Caras, I. W. and D. W. Martin, Jr. (1988). "Molecular cloning of the cDNA for a mutant mouse ribonucleotide reductase M1 that produces a dominant mutator phenotype in mammalian cells." Mol Cell Biol **8**(7): 2698-704.

Cavaluzzi, M. J. and P. N. Borer (2004). "Revised UV extinction coefficients for nucleoside-5'-monophosphates and unpaired DNA and RNA." Nucleic Acids Res **32**(1): e13.

Chabes, A., V. Domkin, G. Larsson, A. Liu, A. Graslund, S. Wijmenga and L. Thelander (2000). "Yeast ribonucleotide reductase has a heterodimeric iron-radical-containing subunit." Proc Natl Acad Sci U S A **97**(6): 2474-9.

Chabes, A., V. Domkin and L. Thelander (1999). "Yeast Sml1, a protein inhibitor of ribonucleotide reductase." J Biol Chem **274**(51): 36679-83.

Chabes, A., B. Georgieva, V. Domkin, X. Zhao, R. Rothstein and L. Thelander (2003). "Survival of DNA Damage in Yeast Directly Depends on Increased dNTP Levels Allowed by Relaxed Feedback Inhibition of Ribonucleotide Reductase." Cell **112**: 391-401.

Chabes, A., B. Georgieva, V. Domkin, X. Zhao, R. Rothstein and L. Thelander (2003). "Survival of DNA damage in yeast directly depends on increased dNTP levels allowed by relaxed feedback inhibition of ribonucleotide reductase." Cell **112**(3): 391-401.

Chabes, A. and L. Thelander (2000). "Controlled protein degradation regulates ribonucleotide reductase activity in proliferating mammalian cells during the normal cell cycle and in response to DNA damage and replication blocks." J Biol Chem **275**(23): 17747-53.

Chabes, A. and L. Thelander (2003). "DNA building blocks at the foundation of better survival." Cell Cycle **2**(3): 171-3.

Chabes, A. L., S. Bjorklund and L. Thelander (2004). "S Phase-specific transcription of the mouse ribonucleotide reductase R2 gene requires both a proximal repressive E2F-binding site and an upstream promoter activating region." J Biol Chem **279**(11): 10796-807.

Chabes, A. L., C. M. Pfleger, M. W. Kirschner and L. Thelander (2003). "Mouse ribonucleotide reductase R2 protein: a new target for anaphase-promoting complex-Cdh1-mediated proteolysis." Proc Natl Acad Sci U S A **100**(7): 3925-9.

Chan, V. L., S. Guttman and P. Juranka (1981). "Mutator genes of baby hamster kidney cells." Mol Cell Biol **1**(6): 568-71.

Chayen, N. E. (2004). "Turning protein crystallisation from an art into a science." Curr Opin Struct Biol **14**(5): 577-83.

Chayen, N. E. and E. Saridakis (2008). "Protein crystallization: from purified protein to diffraction-quality crystal." Nat Methods **5**(2): 147-53.

Chen, D., A. Abend, J. Stubbe and P. A. Frey (2003). "Epimerization at carbon-5' of (5'R)-[5'-2H]adenosylcobalamin by ribonucleoside triphosphate reductase: cysteine 408-independent cleavage of the Co-C5' bond." Biochemistry **42**(15): 4578-84.

Chivian, D., D. E. Kim, L. Malmstrom, P. Bradley, T. Robertson, P. Murphy, C. E. Strauss, R. Bonneau, C. A. Rohl and D. Baker (2003). "Automated prediction of CASP-5 structures using the Robetta server." Proteins **53 Suppl 6**: 524-33.

Chivian, D., D. E. Kim, L. Malmstrom, J. Schonbrun, C. A. Rohl and D. Baker (2005). "Prediction of CASP6 structures using automated Robetta protocols." Proteins **61 Suppl 7**: 157-66.

Cotruvo, J. A., Jr. and J. Stubbe (2008). "NrdI, a flavodoxin involved in maintenance of the diferric-tyrosyl radical cofactor in Escherichia coli class Ib ribonucleotide reductase." Proc Natl Acad Sci U S A **105**(38): 14383-8.

Crowther, R. A. (1972). A collection of papers on the use of non-crystallographic symmetry. The Molecular Replacement Method. M. G. Rossman. New York, New York, Gordon and Breach.

Danesi, R., G. Altavilla, E. Giovannetti and R. Rosell (2009). "Pharmacogenomics of gemcitabine in non-small-cell lung cancer and other solid tumors." Pharmacogenomics **10**(1): 69-80.

Dao, V. and P. Modrich (1998). "Mismatch-, MutS-, MutL-, and helicase II-dependent unwinding from the single-strand break of an incised heteroduplex." J Biol Chem **273**(15): 9202-7.

Delucas, L. J., D. Hamrick, L. Cosenza, L. Nagy, D. McCombs, T. Bray, A. Chait, B. Stoops, A. Belgovskiy, W. William Wilson, M. Parham and N. Chernov (2005). "Protein crystallization: virtual screening and optimization." Prog Biophys Mol Biol **88**(3): 285-309.

Desany, B. A., A. A. Alcasabas, J. B. Bachant and S. J. Elledge (1998). "Recovery from DNA replicational stress is the essential function of the S-phase checkpoint pathway." Genes Dev **12**(18): 2956-70.

DeWeese, T. L., J. M. Shipman, N. A. Larrier, N. M. Buckley, L. R. Kidd, J. D. Groopman, R. G. Cutler, H. te Riele and W. G. Nelson (1998). "Mouse embryonic stem cells carrying one or two defective Msh2 alleles respond abnormally to oxidative stress inflicted by low-level radiation." Proc Natl Acad Sci U S A **95**(20): 11915-20.

Domkin, V., L. Thelander and A. Chabes (2002). "Yeast DNA damage-inducible Rnr3 has a very low catalytic activity strongly stimulated after the formation of a cross-talking Rnr1/Rnr3 complex." J Biol Chem **277**(21): 18574-8.

Eliasson, R., E. Pontis, X. Sun and P. Reichard (1994). "Allosteric control of the substrate specificity of the anaerobic ribonucleotide reductase from Escherichia coli." J Biol Chem **269**(42): 26052-7.

Elledge, S. J. and R. W. Davis (1987). "Identification and isolation of the gene encoding the small subunit of ribonucleotide reductase from Saccharomyces cerevisiae: DNA damage-inducible gene required for mitotic viability." Mol Cell Biol **7**(8): 2783-93.

Elledge, S. J. and R. W. Davis (1990). "Two genes differentially regulated in the cell cycle and by DNA-damaging agents encode alternative regulatory subunits of ribonucleotide reductase." Genes Dev **4**(5): 740-51.

Emsley, P. and K. Cowtan (2004). "Coot: model-building tools for molecular graphics." Acta Crystallogr D Biol Crystallogr **60**(Pt 12 Pt 1): 2126-32.

Eriksson, M., U. Uhlin, S. Ramaswamy, M. Ekberg, K. Regnstrom, B. M. Sjoberg and H. Eklund (1997). "Binding of allosteric effectors to ribonucleotide reductase protein R1: reduction of active-site cysteines promotes substrate binding." Structure **5**(8): 1077-92.

Eriksson, M., U. Uhlin, S. Ramaswamy, M. Ekberg, K. Regnstrom, B. M. Sjoberg and H. Eklund (1997). "Binding of allosteric effectors to ribonucleotide reductase protein R1: reduction of active-site cysteines promotes substrate binding." Structure **5**(8): 1077-92.

Fersht, A. (1998). Structure and Mechanism in Protein Science: A Guide to Enzyme Catalysis and Protein Folding, W.H. Freeman.

Flanagan, S. A., B. W. Robinson, C. M. Krokosky and D. S. Shewach (2007). "Mismatched nucleotides as the lesions responsible for radiosensitization with gemcitabine: a new paradigm for antimetabolite radiosensitizers." Mol Cancer Ther **6**(6): 1858-68.

Fontecave, M., R. Eliasson and P. Reichard (1989). "Oxygen-sensitive ribonucleoside triphosphate reductase is present in anaerobic Escherichia coli." Proc Natl Acad Sci U S A **86**(7): 2147-51.

Fox, G. C. and K. C. Holmes (1966). "An Alternative Method of Solving the Layer Scaling Equation of Hamilton, Rollet and Sparks." Acta Cryst **20**(20): 886-891.

Fritscher, J., E. Artin, S. Wnuk, G. Bar, J. H. Robblee, S. Kacprzak, M. Kaupp, R. G. Griffin, M. Bennati and J. Stubbe (2005). "Structure of the nitrogen-centered radical formed during inactivation of E. coli ribonucleotide reductase by 2'-azido-2'-deoxyuridine-5'-diphosphate: trapping of the 3'-ketonucleotide." J Am Chem Soc **127**(21): 7729-38.

Fu, Y. and W. Xiao (2006). "Identification and characterization of CRT10 as a novel regulator of Saccharomyces cerevisiae ribonucleotide reductase genes." Nucleic Acids Res **34**(6): 1876-83.

Gallicchio, V. S. (2005). "Ribonucleotide reductase: target therapy for human disease." Expert Opinion on Therapuetic Patents **15**: 659-673.

Gandhi, V., P. Huang, Y. Z. Xu, V. Heinemann and W. Plunkett (1991). "Metabolism and action of 2',2'-difluorodeoxycytidine: self-potentiation of cytotoxicity." Adv Exp Med Biol **309A**: 125-30.

Gasteiger, E., C. Hoogland, A. Gattiker, S. Duvaud, M. R. Wilkins, R. D. Appel and A. Bairoch (2005). Protein Identification and Analysis Tools on the ExPASy Server. The Proteomics Protocols Handbook. J. M. Walker, Humana Press.

Ge, J., D. L. Perlstein, H. H. Nguyen, G. Bar, R. G. Griffin and J. Stubbe (2001). "Why multiple small subunits (Y2 and Y4) for yeast ribonucleotide reductase? Toward understanding the role of Y4." Proc Natl Acad Sci U S A **98**(18): 10067-72.

Ge, J., G. Yu, M. A. Ator and J. Stubbe (2003). "Pre-steady-state and steady-state kinetic analysis of E. coli class I ribonucleotide reductase." Biochemistry **42**(34): 10071-83.

Gerfen, G. J., S. Licht, J. Broderick, B. M. Hoffman and J. Stubbe (1996). "Electron paramagnetic resonance investigations of a kinetically competant intermediate formed in ribonucleotide reduction: Evidence for a thiyl radical-Cob(II)alamin interaction." J Am Chem Soc **118**(118): 8192-8197.

Gewirth, D., Z. Otwinowski and W. Minor (2004). The HKL Manual.

Gon, S., M. J. Faulkner and J. Beckwith (2006). "In vivo requirement for glutaredoxins and thioredoxins in the reduction of the ribonucleotide reductases of Escherichia coli." Antioxid Redox Signal **8**(5-6): 735-42.

Grinberg, I., T. Shteinberg, A. Q. Hassan, Y. Aharonowitz, I. Borovok and G. Cohen (2009). "Functional analysis of the Streptomyces coelicolor NrdR ATP-cone domain: role in nucleotide binding, oligomerization, and DNA interactions." J Bacteriol **191**(4): 1169-79.

Guittet, O., P. Hakansson, N. Voevodskaya, S. Fridd, A. Graslund, H. Arakawa, Y. Nakamura and L. Thelander (2001). "Mammalian p53R2 protein forms an active ribonucleotide reductase in vitro with the R1 protein, which is expressed both in resting cells in response to DNA damage and in proliferating cells." J Biol Chem **276**(44): 40647-51.

Guittet, O., A. Tebbi, M. H. Cottet, F. Vesin and M. Lepoivre (2008). "Upregulation of the p53R2 ribonucleotide reductase subunit by nitric oxide." Nitric Oxide **19**(2): 84-94.

Gupta, V., C. B. Peterson, L. T. Dice, T. Uchiki, J. Racca, J. T. Guo, Y. Xu, R. Hettich, X. Zhao, R. Rothstein and C. G. Dealwis (2004). "Sml1p is a dimer in solution: characterization of denaturation and renaturation of recombinant Sml1p." Biochemistry **43**(26): 8568-78.

Habraken, Y., P. Sung, L. Prakash and S. Prakash (1996). "Binding of insertion/deletion DNA mismatches by the heterodimer of yeast mismatch repair proteins MSH2 and MSH3." Curr Biol **6**(9): 1185-7.

Hakansson, P., L. Dahl, O. Chilkova, V. Domkin and L. Thelander (2006). "The Schizosaccharomyces pombe replication inhibitor Spd1 regulates ribonucleotide reductase activity and dNTPs by binding to the large Cdc22 subunit." J Biol Chem **281**(3): 1778-83.

Hakansson, P., A. Hofer and L. Thelander (2006). "Regulation of mammalian ribonucleotide reduction and dNTP pools after DNA damage and in resting cells." J Biol Chem **281**(12): 7834-41.

Hall, M. C., J. R. Jordan and S. W. Matson (1998). "Evidence for a physical interaction between the Escherichia coli methyl-directed mismatch repair proteins MutL and UvrD." EMBO J **17**(5): 1535-41.

Hall, M. C. and S. W. Matson (1999). "The Escherichia coli MutL protein physically interacts with MutH and stimulates the MutH-associated endonuclease activity." J Biol Chem **274**(3): 1306-12.

Ham, M. F., T. Takakuwa, W. J. Luo, A. Liu, A. Horii and K. Aozasa (2006). "Impairment of double-strand breaks repair and aberrant splicing of ATM and MRE11 in leukemia-lymphoma cell lines with microsatellite instability." Cancer Sci **97**(3): 226-34.

Holbrook, S. R. and S. H. Kim (1984). "Local mobility of nucleic acids as determined from crystallographic data. I. RNA and B form DNA." J Mol Biol **173**(3): 361-88.

Holmgren, A., P. Reichard and L. Thelander (1965). "Enzymatic synthesis of deoxyribonucleotides, 8. The effects of ATP and dATP in the CDP reductase system from E. coli." Proc Natl Acad Sci U S A **54**(3): 830-6.

Hristova, D., C. H. Wu, W. Jiang, C. Krebs and J. Stubbe (2008). "Importance of the maintenance pathway in the regulation of the activity of Escherichia coli ribonucleotide reductase." Biochemistry **47**(13): 3989-99.

Huang, M. and S. J. Elledge (1997). "Identification of RNR4, encoding a second essential small subunit of ribonucleotide reductase in Saccharomyces cerevisiae." Mol Cell Biol **17**(10): 6105-13.

Huang, M., Z. Zhou and S. J. Elledge (1998). "The DNA replication and damage checkpoint pathways induce transcription by inhibition of the Crt1 repressor." Cell **94**(5): 595-605.

Hurd, H. K., C. W. Roberts and J. W. Roberts (1987). "Identification of the gene for the yeast ribonucleotide reductase small subunit and its inducibility by methyl methanesulfonate." Mol Cell Biol **7**(10): 3673-7.

Ingemarson, R. and L. Thelander (1996). "A kinetic study on the influence of nucleoside triphosphate effectors on subunit interaction in mouse ribonucleotide reductase." Biochemistry **35**(26): 8603-9.

Ingram, G. M. and J. H. Kinnaird (1999). "Ribonucleotide reductase: A new target for antiparasite therapies." Parasitol Today **15**(8): 338-42.

Jancarik, J. and S. H. Kim (1991). "Sparse-matrix sampling - a screening method for crystallization of proteins." J. Appl. Cryst. **24**(24): 409-411.

Johansson, E., K. Hjortsberg and L. Thelander (1998). "Two YY-1-binding proximal elements regulate the promoter strength of the TATA-less mouse ribonucleotide reductase R1 gene." J Biol Chem **273**(45): 29816-21.

Johns, D. G. and W. Y. Gao (1998). "Selective depletion of DNA precursors: an evolving strategy for potentiation of dideoxynucleoside activity against human immunodeficiency virus." Biochem Pharmacol **55**(10): 1551-6.

Jordan, A., F. Aslund, E. Pontis, P. Reichard and A. Holmgren (1997). "Characterization of Escherichia coli NrdH. A glutaredoxin-like protein with a thioredoxin-like activity profile." J Biol Chem **272**(29): 18044-50.

Jordan, A. and P. Reichard (1998). "Ribonucleotide reductases." Annu Rev Biochem **67**: 71-98.

Jordan, A., E. Torrents, C. Jeanthon, R. Eliasson, U. Hellman, C. Wernstedt, J. Barbe, I. Gibert and P. Reichard (1997). "B12-dependent ribonucleotide reductases from deeply rooted eubacteria are structurally related to the aerobic enzyme from Escherichia coli." Proc Natl Acad Sci U S A **94**(25): 13487-92.

Kashlan, O. B. and B. S. Cooperman (2003). "Comprehensive model for allosteric regulation of mammalian ribonucleotide reductase: refinements and consequences." Biochemistry **42**(6): 1696-706.

Kashlan, O. B., C. P. Scott, J. D. Lear and B. S. Cooperman (2002). "A comprehensive model for the allosteric regulation of mammalian ribonucleotide reductase. Functional consequences of ATP- and dATP-induced oligomerization of the large subunit." Biochemistry **41**(2): 462-74.

Kashlan, O. B., C. P. Scott, J. D. Lear and B. S. Cooperman (2002). "A Comprehensive Model for the Allosteric Regulation of Mammalian Ribonucleotide Reductase. Functional Consequences of ATP- and dATP-Induced Oligomerization of the Large Subunit." Biochemistry **41**: 462-474.

Kasrayan, A., A. L. Persson, M. Sahlin and B. M. Sjoberg (2002). "The conserved active site asparagine in class I ribonucleotide reductase is essential for catalysis." J Biol Chem **277**(8): 5749-55.

Kauppi, B., B. B. Nielsen, S. Ramaswamy, I. K. Larsen, M. Thelander, L. Thelander and H. Eklund (1996). "The three-dimensional structure of mammalian ribonucleotide reductase protein R2 reveals a more-accessible iron-radical site than Escherichia coli R2." J Mol Biol **262**(5): 706-20.

Kim, D. E., D. Chivian and D. Baker (2004). "Protein structure prediction and analysis using the Robetta server." Nucleic Acids Res **32**(Web Server issue): W526-31.

Kim, D. E., D. Chivian, L. Malmstrom and D. Baker (2005). "Automated prediction of domain boundaries in CASP6 targets using Ginzu and RosettaDOM." Proteins **61 Suppl 7**: 193-200.

Kim, D. H., K. F. Faull, A. J. Norris and C. D. Eckhert (2004). "Borate-nucleotide complex formation depends on charge and phosphorylation state." J Mass Spectrom **39**(7): 743-51.

Kimura, T., S. Takeda, Y. Sagiya, M. Gotoh, Y. Nakamura and H. Arakawa (2003). "Impaired function of p53R2 in Rrm2b-null mice causes severe renal failure through attenuation of dNTP pools." Nat Genet **34**(4): 440-5.

King, D. S. and P. Reichard (1995). "Mass spectrometric determination of the radical scission site in the anaerobic ribonucleotide reductase of Escherichia coli." Biochem Biophys Res Commun **206**(2): 731-5.

Kirkpatrick, S., C. D. Gelatt and M. P. Vecchi (1983). "Optimization by Simulated Annealing." Science **220**: 671-680.

Koc, A., C. K. Mathews, L. J. Wheeler, M. K. Gross and G. F. Merrill (2006). "Thioredoxin is required for deoxyribonucleotide pool maintenance during S phase." J Biol Chem **281**(22): 15058-63.

Kolodner, R. D. and G. T. Marsischky (1999). "Eukaryotic DNA mismatch repair." Curr Opin Genet Dev **9**(1): 89-96.

Kraut, J. (1987). DHFR. Volume 3: Active Sites of Enzymes. New York, John Wiley and Sons**:** 1-71.

Lamers, M. H., A. Perrakis, J. H. Enzlin, H. H. Winterwerp, N. de Wind and T. K. Sixma (2000). "The crystal structure of DNA mismatch repair protein MutS binding to a G x T mismatch." Nature **407**(6805): 711-7.

Larsson, A. and P. Reichard (1966). "Allosteric effects and substrate specificity of the ribonucleoside diphosphate reductase system from Escherichia coli B." Biochim Biophys Acta **113**(2): 407-8.

Larsson, A. and B. M. Sjoberg (1986). "Identification of the stable free radical tyrosine residue in ribonucleotide reductase." EMBO J **5**(8): 2037-40.

Larsson, K. M., J. Andersson, B. M. Sjoberg, P. Nordlund and D. T. Logan (2001). "Structural basis for allosteric substrate specificity regulation in anaerobic ribonucleotide reductases." Structure (Camb) **9**(8): 739-50.

Larsson, K. M., J. Andersson, B. M. Sjoberg, P. Nordlund and D. T. Logan (2001). "Structural basis for allosteric substrate specificity regulation in anaerobic ribonucleotide reductases." Structure **9**(8): 739-50.

Larsson, K. M., A. Jordan, R. Eliasson, P. Reichard, D. T. Logan and P. Nordlund (2004). "Structural mechanism of allosteric substrate specificity regulation in a ribonucleotide reductase." Nat Struct Mol Biol **11**(11): 1142-9.

Lee, Y. D. and S. J. Elledge (2006). "Control of ribonucleotide reductase localization through an anchoring mechanism involving Wtm1." Genes Dev **20**(3): 334-44.

Lee, Y. D., J. Wang, J. Stubbe and S. J. Elledge (2008). "Dif1 is a DNA-damage-regulated facilitator of nuclear import for ribonucleotide reductase." Mol Cell **32**(1): 70-80.

Lembo, D. and W. Brune (2009). "Tinkering with a viral ribonucleotide reductase." Trends Biochem Sci **34**(1): 25-32.

Lenz, R. and B. Giese (1997). "Studies on the Mechanism of Ribonucleotide Reductases." J Am Chem Soc **119**(12): 2784-2794.

Licht, S., G. J. Gerfen and J. Stubbe (1996). "Thiyl radicals in ribonucleotide reductases." Science **271**(5248): 477-81.

Licht, S., C. C. Lawrence and J. Stubbe (1999). "Class II ribonucleotide reductases catalyze carbon-cobalt bond reformation on every turnover." J Am Chem Soc **121**: 7463-7468.

Licht, S. S., S. Booker and J. Stubbe (1999). "Studies on the catalysis of carbon-cobalt bond homolysis by ribonucleoside triphosphate reductase: evidence for concerted carbon-cobalt bond homolysis and thiyl radical formation." Biochemistry **38**(4): 1221-33.

Licht, S. S., Lawrence, C. and Stubbe, J (1999). "Class II Ribonucleotide Reductases Catalyze Carbon−Cobalt Bond Reformation on Every Turnover." JACS **33**: 7463-7468.

Lin, A. N., G. W. Ashley and J. Stubbe (1987). "Location of the redox-active thiols of ribonucleotide reductase: sequence similarity between the Escherichia coli and Lactobacillus leichmannii enzymes." Biochemistry **26**(22): 6905-9.

Liu, X., F. Un and Y. Yen (2008). Biological Role of p53R2 Ribonucleotide Reductase. Ribonucleotide Reductase. J. Andersson. New York, Nova Science Publishers**:** 125-134.

Liu, X., L. Xue and Y. Yen (2008). "Redox property of ribonucleotide reductase small subunit M2 and p53R2." Methods Mol Biol **477**: 195-206.

Liu, X., B. Zhou, L. Xue, J. Shih, K. Tye, C. Qi and Y. Yen (2005). "The ribonucleotide reductase subunit M2B subcellular localization and functional importance for DNA replication in physiological growth of KB cells." Biochem Pharmacol **70**(9): 1288-97.

Logan, D. T., J. Andersson, B. M. Sjoberg and P. Nordlund (1999). "A glycyl radical site in the crystal structure of a class III ribonucleotide reductase." Science **283**(5407): 1499-504.

Luft, J. R., R. J. Collins, N. A. Fehrman, A. M. Lauricella, C. K. Veatch and G. T. DeTitta (2003). "A deliberate approach to screening for initial crystallization conditions of biological macromolecules." J Struct Biol **142**(1): 170-9.

Luft, J. R. and G. T. DeTitta (1999). "A method to produce microseed stock for use in the crystallization of biological macromolecules." Acta Crystallogr D Biol Crystallogr **55**(Pt 5): 988-93.

Manegold, C. (2004). "Gemcitabine (Gemzar) in non-small cell lung cancer." Expert Rev Anticancer Ther **4**(3): 345-60.

Mao, S. S., T. P. Holler, G. X. Yu, J. M. Bollinger, Jr., S. Booker, M. I. Johnston and J. Stubbe (1992). "A model for the role of multiple cysteine residues involved in ribonucleotide reduction: amazing and still confusing." Biochemistry **31**(40): 9733-43.

Markowitz, S., J. Wang, L. Myeroff, R. Parsons, L. Sun, J. Lutterbaugh, R. S. Fan, E. Zborowska, K. W. Kinzler, B. Vogelstein and et al. (1995). "Inactivation of the type II TGF-beta receptor in colon cancer cells with microsatellite instability." Science **268**(5215): 1336-8.

Marsischky, G. T., N. Filosi, M. F. Kane and R. Kolodner (1996). "Redundancy of Saccharomyces cerevisiae MSH3 and MSH6 in MSH2-dependent mismatch repair." Genes Dev **10**(4): 407-20.

Marti, T. M., C. Kunz and O. Fleck (2002). "DNA mismatch repair and mutation avoidance pathways." J Cell Physiol **191**(1): 28-41.

McCoy, A. J., R. W. Grosse-Kunstleve, P. D. Adams, M. D. Winn, L. C. Storoni and R. J. Read (2007). "Phaser crystallographic software." J. Appl. Cryst. **40**(40): 658-674.

Mechanic, L. E., B. A. Frankel and S. W. Matson (2000). "Escherichia coli MutL loads DNA helicase II onto DNA." J Biol Chem **275**(49): 38337-46.

Miquel, C., S. Jacob, S. Grandjouan, A. Aime, J. Viguier, J. C. Sabourin, A. Sarasin, A. Duval and F. Praz (2007). "Frequent alteration of DNA damage signalling and repair pathways in human colorectal cancers with microsatellite instability." Oncogene **26**(40): 5919-26.

Moore, E. C. and P. Reichard (1964). "Enzymatic Synthesis of Deoxyribonucleotides. Vi. The Cytidine Diphosphate Reductase System from Novikoff Hepatoma." J Biol Chem **239**: 3453-6.

Mulliez, E., S. Ollagnier, M. Fontecave, R. Eliasson and P. Reichard (1995). "Formate is the hydrogen donor for the anaerobic ribonucleotide reductase from Escherichia coli." Proc Natl Acad Sci U S A **92**(19): 8759-62.

Murphy, K. P., D. Xie, K. C. Garcia, L. M. Amzel and E. Freire (1993). "Structural energetics of peptide recognition: angiotensin II/antibody binding." Proteins **15**(2): 113-20.

Murshudov, G. N., A. A. Vagin and E. J. Dodson (1997). "Refinement of macromolecular structures by the maximum-likelihood method." Acta Cryst **D53**(D53): 240-255.

Nguyen, H. H., J. Ge, D. L. Perlstein and J. Stubbe (1999). "Purification of ribonucleotide reductase subunits Y1, Y2, Y3, and Y4 from yeast: Y4 plays a key role in diiron cluster assembly." Proc Natl Acad Sci U S A **96**(22): 12339-44.

Nordlund, P. and H. Eklund (1993). "Structure and function of the Escherichia coli ribonucleotide reductase protein R2." J Mol Biol **232**(1): 123-64.

Nordlund, P. and P. Reichard (2006). "Ribonucleotide reductases." Annu Rev Biochem **75**: 681-706.

Nordlund, P., B. M. Sjoberg and H. Eklund (1990). "Three-dimensional structure of the free radical protein of ribonucleotide reductase." Nature **345**(6276): 593-8.

Obmolova, G., C. Ban, P. Hsieh and W. Yang (2000). "Crystal structures of mismatch repair protein MutS and its complex with a substrate DNA." Nature **407**(6805): 703-10.

Ollagnier, S., E. Mulliez, J. Gaillard, R. Eliasson, M. Fontecave and P. Reichard (1996). "The anaerobic Escherichia coli ribonucleotide reductase. Subunit structure and iron sulfur center." J Biol Chem **271**(16): 9410-6.

Ormo, M. and B. M. Sjoberg (1990). "An ultrafiltration assay for nucleotide binding to ribonucleotide reductase." Anal Biochem **189**(1): 138-41.

Otwinowski, Z. and W. Minor (1997). "Processing of X-ray Diffraction Data Collected in Oscillation Mode." Methods in Enzymology **276**: 307-326.

Pace, C. N., F. Vajdos, L. Fee, G. Grimsley and T. Gray (1995). "How to measure and predict the molar absorption coefficient of a protein." Protein Sci **4**(11): 2411-23.

Page, R. and R. C. Stevens (2004). "Crystallization data mining in structural genomics: using positive and negative results to optimize protein crystallization screens." Methods **34**(3): 373-89.

Panagou, D., M. D. Orr, J. R. Dunstone and R. L. Blakley (1972). "A monomeric, allosteric enzyme with a single polypeptide chain. Ribonucleotide reductase of Lactobacillus leichmannii." Biochemistry **11**(12): 2378-88.

Pannu, N. S. and R. J. Read (1996). "Improved structure refinement through maximum likelihood." Acta Cryst **A52**(A52): 659-668.

Papadopoulos, N., N. C. Nicolaides, Y. F. Wei, S. M. Ruben, K. C. Carter, C. A. Rosen, W. A. Haseltine, R. D. Fleischmann, C. M. Fraser, M. D. Adams and et al. (1994). "Mutation of a mutL homolog in hereditary colon cancer." Science **263**(5153): 1625-9.

Pavlov, Y. I., I. M. Mian and T. A. Kunkel (2003). "Evidence for preferential mismatch repair of lagging strand DNA replication errors in yeast." Curr Biol **13**(9): 744-8.

Pemberton, L. F. and G. Blobel (1997). "Characterization of the Wtm proteins, a novel family of Saccharomyces cerevisiae transcriptional modulators with roles in meiotic regulation and silencing." Mol Cell Biol **17**(8): 4830-41.

Pereira, S., N. M. Cerqueira, P. A. Fernandes and M. J. Ramos (2006). "Computational studies on class I ribonucleotide reductase: understanding the mechanisms of action and inhibition of a cornerstone enzyme for the treatment of cancer." Eur Biophys J **35**(2): 125-35.

Pereira, S., P. A. Fernandes and M. J. Ramos (2004). "Mechanism for ribonucleotide reductase inactivation by the anticancer drug gemcitabine." J Comput Chem **25**(10): 1286-94.

Pereira, S., P. A. Fernandes and M. J. Ramos (2004). "Theoretical study of ribonucleotide reductase mechanism-based inhibition by 2'-azido-2'-deoxyribonucleoside 5'-diphosphates." J Comput Chem **25**(2): 227-37.

Petersson, L., A. Graslund, A. Ehrenberg, B. M. Sjoberg and P. Reichard (1980). "The iron center in ribonucleotide reductase from Escherichia coli." J Biol Chem **255**(14): 6706-12.

Petrek, M., M. Otyepka, P. Banas, P. Kosinova, J. Koca and J. Damborsky (2006). "CAVER: A New Tool to Explore Routes from Protein Clefts, Pockets, and Cavities." BMC Bioinformatics **7**: 316.

Pintar, A., O. Carugo and S. Pongor (2003). "Atom depth as a descriptor of the protein interior." Biophys J **84**(4): 2553-61.

Pontarin, G., A. Fijolek, P. Pizzo, P. Ferraro, C. Rampazzo, T. Pozzan, L. Thelander, P. A. Reichard and V. Bianchi (2008). "Ribonucleotide reduction is a cytosolic process in mammalian cells independently of DNA damage." Proc Natl Acad Sci U S A **105**(46): 17801-6.

Powell, D. R., U. Desai, M. J. Sparks, G. Hansen, J. Gay, J. Schrick, Z. Z. Shi, J. Hicks and P. Vogel (2005). "Rapid development of glomerular injury and renal failure in mice lacking p53R2." Pediatr Nephrol **20**(3): 432-40.

Prolla, T. A., D. M. Christie and R. M. Liskay (1994). "Dual requirement in yeast DNA mismatch repair for MLH1 and PMS1, two homologs of the bacterial mutL gene." Mol Cell Biol **14**(1): 407-15.

Radivoyevitch, T. (2008). "Equilibrium model selection: dTTP induced R1 dimerization." BMC Syst Biol **2**: 15.

Randi, M. L., E. Ruzzon, F. Tezza, G. Luzzatto and F. Fabris (2005). "Toxicity and side effects of hydroxyurea used for primary thrombocythemia." Platelets **16**(3-4): 181-4.

Reece, S. Y., J. M. Hodgkiss, J. Stubbe and D. G. Nocera (2006). "Proton-coupled electron transfer: the mechanistic underpinning for radical transport and catalysis in biology." Philos Trans R Soc Lond B Biol Sci **361**(1472): 1351-64.

Reichard, P. (1988). "Interactions between deoxyribonucleotide and DNA synthesis." Annu Rev Biochem **57**: 349-74.

Reichard, P., R. Eliasson, R. Ingemarson and L. Thelander (2000). "Cross-talk between the allosteric effector-binding sites in mouse ribonucleotide reductase." J Biol Chem **275**(42): 33021-6.

Rhodes, G. (2000). Crystallography Made Crystal Clear. San Diego, CA, Elsevier.

Riera, J., F. T. Robb, R. Weiss and M. Fontecave (1997). "Ribonucleotide reductase in the archaeon Pyrococcus furiosus: a critical enzyme in the evolution of DNA genomes?" Proc Natl Acad Sci U S A **94**(2): 475-8.

Roca, I., E. Torrents, M. Sahlin, I. Gibert and B. M. Sjoberg (2008). "NrdI essentiality for class Ib ribonucleotide reduction in Streptococcus pyogenes." J Bacteriol **190**(14): 4849-58.

Rofougaran, R., M. Crona, M. Vodnala, B. M. Sjoberg and A. Hofer (2008). "Oligomerization status directs overall activity regulation of the Escherichia coli class Ia ribonucleotide reductase." J Biol Chem **283**(51): 35310-8.

Rofougaran, R., M. Vodnala and A. Hofer (2006). "Enzymatically active mammalian ribonucleotide reductase exists primarily as an alpha6beta2 octamer." J Biol Chem **281**(38): 27705-11.

Roguska, M. A. and L. J. Gudas (1984). "Mutator phenotype in a mutant of S49 mouse T-lymphoma cells with abnormal sensitivity to thymidine." J Biol Chem **259**(6): 3782-90.

Romanelli, F., C. Pomeroy and K. M. Smith (1999). "Hydroxyurea to inhibit human immunodeficiency virus-1 replication." Pharmacotherapy **19**(2): 196-204.

Roshick, C., E. R. Iliffe-Lee and G. McClarty (2000). "Cloning and characterization of ribonucleotide reductase from Chlamydia trachomatis." J Biol Chem **275**(48): 38111-9.

Rossmann, M. G. (1972). The Molecular Replacement Method. London, England, Gordon and Breach.

Rossmann, M. G. and D. M. Blow (1962). "The detection of subunits within the crystallographic asymmetric unit." Acta Cryst **15**(15): 24.

Saban, N. and M. Bujak (2009). "Hydroxyurea and hydroxamic acid derivatives as antitumor drugs." Cancer Chemother Pharmacol.

Sali, A., B. Veerapandian, J. B. Cooper, D. S. Moss, T. Hofmann and T. L. Blundell (1992). "Domain flexibility in aspartic proteinases." Proteins **12**(2): 158-70.

Schomaker, V. and K. N. Trueblood (1968). "On the Rigid-Body Motion of Molecules in Crystals." Acta Cryst **24B**: 63-76.

Schomaker, V. and K. N. Trueblood (1998). "Correlation of Internal Torsional Motion with Overall Molecular Motion in Crystals." Acta Cryst **B54**: 507-514.

Seyedsayamdost, M. R., J. Xie, C. T. Chan, P. G. Schultz and J. Stubbe (2007). "Site-specific insertion of 3-aminotyrosine into subunit alpha2 of E. coli ribonucleotide reductase: direct evidence for involvement of Y730 and Y731 in radical propagation." J Am Chem Soc **129**(48): 15060-71.

Shao, J., B. Zhou, B. Chu and Y. Yen (2006). "Ribonucleotide reductase inhibitors and future drug design." Curr Cancer Drug Targets **6**(5): 409-31.

Shao, J., B. Zhou, L. Zhu, W. Qiu, Y. C. Yuan, B. Xi and Y. Yen (2004). "In vitro characterization of enzymatic properties and inhibition of the p53R2 subunit of human ribonucleotide reductase." Cancer Res **64**(1): 1-6.

Silva, D. J., J. Stubbe, V. Samano and M. J. Robins (1998). "Gemcitabine 5'-triphosphate is a stoichiometric mechanism-based inhibitor of Lactobacillus leichmannii ribonucleoside triphosphate reductase: evidence for thiyl radical-mediated nucleotide radical formation." Biochemistry **37**(16): 5528-35.

Simon, J. A., P. Szankasi, D. K. Nguyen, C. Ludlow, H. M. Dunstan, C. J. Roberts, E. L. Jensen, L. H. Hartwell and S. H. Friend (2000). "Differential toxicities of anticancer agents

among DNA repair and checkpoint mutants of Saccharomyces cerevisiae." <u>Cancer Res</u> **60**(2): 328-33.

Sintchak, M. D., G. Arjara, B. A. Kellogg, J. Stubbe and C. L. Drennan (2002). "The crystal structure of class II ribonucleotide reductase reveals how an allosterically regulated monomer mimics a dimer." <u>Nat Struct Biol</u> **9**(4): 293-300.

Soderman, K. and P. Reichard (1986). "A nitrocellulose filter binding assay for ribonucleotide reductase." <u>Anal Biochem</u> **152**(1): 89-93.

Sofia, H. J., G. Chen, B. G. Hetzler, J. F. Reyes-Spindola and N. E. Miller (2001). "Radical SAM, a novel protein superfamily linking unresolved steps in familiar biosynthetic pathways with radical mechanisms: functional characterization using new analysis and information visualization methods." <u>Nucleic Acids Res</u> **29**(5): 1097-106.

Sommerhalter, M., W. C. Voegtli, D. L. Perlstein, J. Ge, J. Stubbe and A. C. Rosenzweig (2004). "Structures of the yeast ribonucleotide reductase Rnr2 and Rnr4 homodimers." <u>Biochemistry</u> **43**(24): 7736-42.

Stearns, B., K. A. Losee and J. Bernstein (1963). "Hydroxyurea. A New Type of Potential Antitumor Agent." <u>J Med Chem</u> **6**: 201.

Strouse, J. J., S. Lanzkron, M. C. Beach, C. Haywood, H. Park, C. Witkop, R. F. Wilson, E. B. Bass and J. B. Segal (2008). "Hydroxyurea for sickle cell disease: a systematic review for efficacy and toxicity in children." <u>Pediatrics</u> **122**(6): 1332-42.

Stubbe, J., J. Ge and C. S. Yee (2001). "The evolution of ribonucleotide reduction revisited." <u>Trends Biochem Sci</u> **26**(2): 93-9.

Sun, X., R. Eliasson, E. Pontis, J. Andersson, G. Buist, B. M. Sjoberg and P. Reichard (1995). "Generation of the glycyl radical of the anaerobic Escherichia coli ribonucleotide reductase requires a specific activating enzyme." <u>J Biol Chem</u> **270**(6): 2443-6.

Sun, X., S. Ollagnier, P. P. Schmidt, M. Atta, E. Mulliez, L. Lepape, R. Eliasson, A. Graslund, M. Fontecave, P. Reichard and B. M. Sjoberg (1996). "The free radical of the anaerobic ribonucleotide reductase from Escherichia coli is at glycine 681." <u>J Biol Chem</u> **271**(12): 6827-31.

Surtees, J. A., J. L. Argueso and E. Alani (2004). "Mismatch repair proteins: key regulators of genetic recombination." <u>Cytogenet Genome Res</u> **107**(3-4): 146-59.

Taira, K., N. Boku, A. Fukutomi, Y. Onozawa, S. Hironaka, T. Yoshino, H. Yasui, K. Yamazaki, K. Taku, T. Hashimoto and T. Nishimura (2008). "Results of a retrospective analysis of gemcitabine as a second-line treatment after chemoradiotherapy and maintenance chemotherapy using 5-fluorouracil in patients with locally advanced pancreatic cancer." <u>J Gastroenterol</u> **43**(11): 875-80.

Tamarit, J., C. Gerez, C. Meier, E. Mulliez, A. Trautwein and M. Fontecave (2000). "The activating component of the anaerobic ribonucleotide reductase from Escherichia coli. An iron-sulfur center with only three cysteines." <u>J Biol Chem</u> **275**(21): 15669-75.

Tanaka, H., H. Arakawa, T. Yamaguchi, K. Shiraishi, S. Fukuda, K. Matsui, Y. Takei and Y. Nakamura (2000). "A ribonucleotide reductase gene involved in a p53-dependent cell-cycle checkpoint for DNA damage." <u>Nature</u> **404**(6773): 42-9.

Tauer, A. and S. A. Benner (1997). "The B12-dependent ribonucleotide reductase from the archaebacterium Thermoplasma acidophila: an evolutionary solution to the ribonucleotide reductase conundrum." <u>Proc Natl Acad Sci U S A</u> **94**(1): 53-8.

Thelander, L. (1974). "Reaction mechanism of ribonucleoside diphosphate reductase from Escherichia coli. Oxidation-reduction-active disulfides in the B1 subunit." J Biol Chem **249**(15): 4858-62.

Thelander, L. and B. Larsson (1976). "Active site of ribonucleoside diphosphate reductase from Escherichia coli. Inactivation of the enzyme by 2'-substituted ribonucleoside diphosphates." J Biol Chem **251**(5): 1398-405.

Thurman, W. G., C. Bloedow, C. D. Howe, W. C. Levin, P. Davis, M. Lane, M. P. Sullivan and K. M. Griffith (1963). "A phase I study of hydroxyurea." Cancer Chemother Rep **29**: 103-7.

Torrents, E., G. Buist, A. Liu, R. Eliasson, J. Kok, I. Gibert, A. Graslund and P. Reichard (2000). "The anaerobic (class III) ribonucleotide reductase from Lactococcus lactis. Catalytic properties and allosteric regulation of the pure enzyme system." J Biol Chem **275**(4): 2463-71.

Torrents, E., R. Eliasson, H. Wolpher, A. Graslund and P. Reichard (2001). "The anaerobic ribonucleotide reductase from Lactococcus lactis. Interactions between the two proteins NrdD and NrdG." J Biol Chem **276**(36): 33488-94.

Torrents, E., M. Sahlin, D. Biglino, A. Graslund and B. M. Sjoberg (2005). "Efficient growth inhibition of Bacillus anthracis by knocking out the ribonucleotide reductase tyrosyl radical." Proc Natl Acad Sci U S A **102**(50): 17946-51.

Torrents, E., M. Sahlin and B. M. Sjoberg (2008). The Ribonucleotide Reductase Family - Genetics and Genomics. Ribonucleotide Reductase. K. K. Andersson. New York, Nova Science Publishers**:** 17-77.

Torrents, E., M. Westman, M. Sahlin and B. M. Sjoberg (2006). "Ribonucleotide reductase modularity: Atypical duplication of the ATP-cone domain in Pseudomonas aeruginosa." J Biol Chem **281**(35): 25287-96.

Tripathy, D. (2002). "Gemcitabine in breast cancer: future directions." Clin Breast Cancer **3 Suppl 1**: 45-8.

Tronrud, D. E. (2004). "Introduction to macromolecular refinement." Acta Crystallogr D Biol Crystallogr **60**(Pt 12 Pt 1): 2156-68.

Trueblood, K. N., H. B. Burgi, H. Burzlaff, J. D. Dunitz, C. M. CGramaccioli, H. H. Shulz, U. Shmueli and S. C. Abrahams (1996). "Atomic Displacement Parameter Nomenclature. Report of a Subcommittee on Atomic Displacement Parameter Nomenclature." Acta Cryst **A52**: 770-781.

Tsai, P. K. and H. P. Hogenkamp (1980). "The purification and characterization of an adenosylcobalamin-dependent ribonucleoside diphosphate reductase from Corynebacterium nephridii." J Biol Chem **255**(4): 1273-8.

Uchiki, T., L. T. Dice, R. L. Hettich and C. Dealwis (2004). "Identification of phosphorylation sites on the yeast ribonucleotide reductase inhibitor Sml1." J Biol Chem **279**(12): 11293-303.

Uchiki, T., R. Hettich, V. Gupta and C. Dealwis (2002). "Characterization of monomeric and dimeric forms of recombinant Sml1p-histag protein by electrospray mass spectrometry." Anal Biochem **301**(1): 35-48.

Uhlin, U. and H. Eklund (1994). "Structure of ribonucleotide reductase protein R1." Nature **370**(6490): 533-9.

Ullman, B., S. M. Clift, L. J. Gudas, B. B. Levinson, M. A. Wormsted and D. W. Martin, Jr. (1980). "Alterations in deoxyribonucleotide metabolism in cultured cells with ribonucleotide reductase activities refractory to feedback inhibition by 2'-deoxyadenosine triphosphate." J Biol Chem **255**(17): 8308-14.

Uppsten, M., J. Davis, H. Rubin and U. Uhlin (2004). "Crystal structure of the biologically active form of class Ib ribonucleotide reductase small subunit from Mycobacterium tuberculosis." FEBS Lett **569**(1-3): 117-22.

Uppsten, M., M. Farnegardh, V. Domkin and U. Uhlin (2006). "The first holocomplex structure of ribonucleotide reductase gives new insight into its mechanism of action." J Mol Biol **359**(2): 365-77.

Uppsten, M., M. Farnegardh, A. Jordan, R. Eliasson, H. Eklund and U. Uhlin (2003). "Structure of the large subunit of class Ib ribonucleotide reductase from Salmonella typhimurium and its complexes with allosteric effectors." J Mol Biol **330**(1): 87-97.

Vaish, M. (2007). "Mismatch repair deficiencies transforming stem cells into cancer stem cells and therapeutic implications." Mol Cancer **6**: 26.

Vaish, M., A. Mandhani, R. D. Mittal and B. Mittal (2005). "Microsatellite instability as prognostic marker in bladder tumors: a clinical significance." BMC Urol **5**: 2.

van der Donk, W. A., G. Yu, L. Perez, R. J. Sanchez, J. Stubbe, V. Samano and M. J. Robins (1998). "Detection of a new substrate-derived radical during inactivation of ribonucleotide reductase from Escherichia coli by gemcitabine 5'-diphosphate." Biochemistry **37**(18): 6419-26.

van der Donk, W. A., G. Yu, D. J. Silva, J. Stubbe, J. R. McCarthy, E. T. Jarvi, D. P. Matthews, R. J. Resvick and E. Wagner (1996). "Inactivation of ribonucleotide reductase by (E)-2'-fluoromethylene-2'-deoxycytidine 5'-diphosphate: a paradigm for nucleotide mechanism-based inhibitors." Biochemistry **35**(25): 8381-91.

Voegtli, W. C., J. Ge, D. L. Perlstein, J. Stubbe and A. C. Rosenzweig (2001). "Structure of the yeast ribonucleotide reductase Y2Y4 heterodimer." Proc Natl Acad Sci U S A **98**(18): 10073-8.

Wang, J., G. J. Lohman and J. Stubbe (2007). "Enhanced subunit interactions with gemcitabine-5'-diphosphate inhibit ribonucleotide reductases." Proc Natl Acad Sci U S A **104**(36): 14324-9.

Wang, J., L. Sun, L. Myeroff, X. Wang, L. E. Gentry, J. Yang, J. Liang, E. Zborowska, S. Markowitz, J. K. Willson and et al. (1995). "Demonstration that mutation of the type II transforming growth factor beta receptor inactivates its tumor suppressor activity in replication error-positive colon carcinoma cells." J Biol Chem **270**(37): 22044-9.

Wang, P. J., A. Chabes, R. Casagrande, X. C. Tian, L. Thelander and T. C. Huffaker (1997). "Rnr4p, a novel ribonucleotide reductase small-subunit protein." Mol Cell Biol **17**(10): 6114-21.

Weber, P. C. (1997). "Overview of Protein Crystallization Methods." Methods in Enzymology **276**: 13-22.

Weinberg, G., B. Ullman and D. W. Martin, Jr. (1981). "Mutator phenotypes in mammalian cell mutants with distinct biochemical defects and abnormal deoxyribonucleoside triphosphate pools." Proc Natl Acad Sci U S A **78**(4): 2447-51.

Welsh, K. M., A. L. Lu, S. Clark and P. Modrich (1987). "Isolation and characterization of the Escherichia coli mutH gene product." J Biol Chem **262**(32): 15624-9.

Whiteside, D., R. McLeod, G. Graham, J. L. Steckley, K. Booth, M. J. Somerville and S. E. Andrew (2002). "A homozygous germ-line mutation in the human MSH2 gene predisposes to hematological malignancy and multiple cafe-au-lait spots." Cancer Res **62**(2): 359-62.

Wilson, M. A. and A. T. Brunger (2000). "The 1.0 A crystal structure of Ca(2+)-bound calmodulin: an analysis of disorder and implications for functionally relevant plasticity." J Mol Biol **301**(5): 1237-56.

Winn, M. D., M. N. Isupov and G. N. Murshudov (2001). "Use of TLS parameters to model anisotropic displacements in macromolecular refinement." Acta Crystallogr D Biol Crystallogr **57**(Pt 1): 122-33.

Winn, M. D., G. N. Murshudov and M. Z. Papiz (2003). "Macromolecular TLS refinement in REFMAC at moderate resolutions." Methods Enzymol **374**: 300-21.

Woo, G. H., K. Katayama, E. J. Bak, M. Ueno, H. Yamauchi, K. Uetsuka, H. Nakayama and K. Doi (2004). "Effects of prenatal hydroxyurea-treatment on mouse offspring." Exp Toxicol Pathol **56**(1-2): 1-7.

Wu, C. H., W. Jiang, C. Krebs and J. Stubbe (2007). "YfaE, a ferredoxin involved in diferric-tyrosyl radical maintenance in Escherichia coli ribonucleotide reductase." Biochemistry **46**(41): 11577-88.

Wu, X. and M. Huang (2008). "Dif1 controls subcellular localization of ribonucleotide reductase by mediating nuclear import of the R2 subunit." Mol Cell Biol **28**(23): 7156-67.

Xu, H., C. Faber, T. Uchiki, J. W. Fairman, J. Racca and C. Dealwis (2006). "Structures of eukaryotic ribonucleotide reductase I provide insights into dNTP regulation." Proc Natl Acad Sci U S A **103**(11): 4022-7.

Xu, H., C. Faber, T. Uchiki, J. Racca and C. Dealwis (2006). "Structures of eukaryotic ribonucleotide reductase I define gemcitabine diphosphate binding and subunit assembly." Proc Natl Acad Sci U S A **103**(11): 4028-33.

Xu, H., J. W. Fairman, S. R. Wijerathna, N. R. Kreischer, J. LaMacchia, E. Helmbrecht, B. S. Cooperman and C. Dealwis (2008). "The structural basis for peptidomimetic inhibition of eukaryotic ribonucleotide reductase: a conformationally flexible pharmacophore." J Med Chem **51**(15): 4653-9.

Xue, L., B. Zhou, X. Liu, W. Qiu, Z. Jin and Y. Yen (2003). "Wild-type p53 regulates human ribonucleotide reductase by protein-protein interaction with p53R2 as well as hRRM2 subunits." Cancer Res **63**(5): 980-6.

Yamaguchi, T., K. Matsuda, Y. Sagiya, M. Iwadate, M. A. Fujino, Y. Nakamura and H. Arakawa (2001). "p53R2-dependent pathway for DNA synthesis in a p53-regulated cell cycle checkpoint." Cancer Res **61**(22): 8256-62.

Yang, F. D., R. A. Spanevello, I. Celiker, R. Hirschmann, H. Rubin and B. S. Cooperman (1990). "The carboxyl terminus heptapeptide of the R2 subunit of mammalian ribonucleotide reductase inhibits enzyme activity and can be used to purify the R1 subunit." FEBS Lett **272**(1-2): 61-4.

Yao, R., Z. Zhang, X. An, B. Bucci, D. L. Perlstein, J. Stubbe and M. Huang (2003). "Subcellular localization of yeast ribonucleotide reductase regulated by the DNA replication and damage checkpoint pathways." Proc Natl Acad Sci U S A **100**(11): 6628-33.

Young, P., J. Andersson, M. Sahlin and B. M. Sjoberg (1996). "Bacteriophage T4 anaerobic ribonucleotide reductase contains a stable glycyl radical at position 580." J Biol Chem **271**(34): 20770-5.

Young, P., M. Ohman and B. M. Sjoberg (1994). "Bacteriophage T4 gene 55.9 encodes an activity required for anaerobic ribonucleotide reduction." J Biol Chem **269**(45): 27815-8.

Zaim, J., E. Speina and A. M. Kierzek (2005). "Identification of new genes regulated by the Crt1 transcription factor, an effector of the DNA damage checkpoint pathway in Saccharomyces cerevisiae." J Biol Chem **280**(1): 28-37.

Zhang, Z., X. An, K. Yang, D. L. Perlstein, L. Hicks, N. Kelleher, J. Stubbe and M. Huang (2006). "Nuclear localization of the Saccharomyces cerevisiae ribonucleotide reductase small subunit requires a karyopherin and a WD40 repeat protein." Proc Natl Acad Sci U S A **103**(5): 1422-7.

Zhang, Z., K. Yang, C. C. Chen, J. Feser and M. Huang (2007). "Role of the C terminus of the ribonucleotide reductase large subunit in enzyme regeneration and its inhibition by Sml1." Proc Natl Acad Sci U S A **104**(7): 2217-22.

Zhao, X., E. G. Muller and R. Rothstein (1998). "A suppressor of two essential checkpoint genes identifies a novel protein that negatively affects dNTP pools." Mol Cell **2**(3): 329-40.

Zhao, X. and R. Rothstein (2002). "The Dun1 checkpoint kinase phosphorylates and regulates the ribonucleotide reductase inhibitor Sml1." Proc Natl Acad Sci U S A **99**(6): 3746-51.

Zipse, H., E. Artin, S. Wnuk, G. J. Lohman, D. Martino, R. G. Griffin, S. Kacprzak, B. M. Hoffman, M. Bennati, J. Stubbe and N. Lees (2009). "Structure of the nucleotide radical formed during reaction of CDP/TTP with the E441Q-alpha2beta2 of *E. coli* ribonucleotide reductase." J Am Chem Soc **131**(1): 200-211.

APPENDICES

A.1 PREPARATION OF RADIOLABELED NUCLEOTIDE STOCKS FOR ACTIVITY AND BINDING ASSAYS

This section describes the preparation of ^{14}C-CDP, ^{14}C-ADP, or 8-^{3}H-dGTP stocks in detail along with sample calculations and measurements. A few assumptions must be made when creating or using radio-labeled substrates. First, it must be assumed that the behavior and physical properties of the radio-labeled compounds are exactly identical to the behavior of an unlabeled compound (ie: the extinction coefficients of the radio-labeled and unlabeled molecules are identical). Second, the enzyme under investigation must act identically with the radio-labeled molecule as with the unlabeled molecule. Kinetic isotope effects can occur if the radio-label is in a position known to be involved in catalysis and is of greater mass than the unlabeled substrate (Fersht 1998). Therefore, the position of the radio-label must be carefully chosen such that it does not alter either kinetic or binding values as compared to the unlabeled compound. Third, the stocks created via this protocol are composed of mostly unlabeled molecules that are in far greater excess to the radio-labeled compounds (≤0.01%).

The first consideration when undertaking the creation of these stocks of radio-labeled compounds is the specific activity. Specific activity, in this case, refers to the amount of radioactivity present per number of total molecules and, in this dissertation, will be expressed in the units of disintegrations per minute per nanomole of compound (DPM/nmol). The specific activity determines the sensitivity of any experiment performed using a particular radio-labeled stock. The higher the specific activity, the more resolution you will have when it comes to interpreting your results. For example, a stock with a specific activity of 1000 DPM/nmol has a resolution of 1 picomole, while a stock with a specific activity of 50000 DPM/nmol has a resolution of 20 femtomoles. While the increased sensitivity of a 50000 DPM/nmol stock is far

superior to that of the 1000 DPM/nmol stock, creating an equal volume of stock that is 50000 DPM/nmol vs. 1000 DPM/nmol requires the use of 50 times more radio-labeled compound. One must consider the prohibitively high cost of creating stocks with a large specific activity as well as possible health and environmental impact of the radioactive compounds.

Radioactive material is usually provided from the manufacturer in the form of curies per microliter (Ci/µL). It is ideal to use the units DPM when creating the stocks of radio-labeled materials and the units of curies can be converted to DPM and vice-versa via the following formula:

$$1 \text{ Ci} = 2.22 \text{ x } 10^{12} \text{ DPM} \hspace{3cm} \textbf{(Equation A.1)}$$

Note that the value of DPM is used and not that of counts per minute (CPM). Liquid scintillation counters (LSCs) have an inherit fault in that they are only able to count a certain percentage of the radiation emitting events that occur, which is referred to as the counting efficiency (ie: if a sample put through a LSC has a CPM value of 500, but its real DPM value is 1000, the counting efficiency is 50%). Modern LSCs are able to account for the counting efficiency for each sample, they can correct the CPM value to give the actual DPM events that are occurring.

The example to be considered in this section is the creation of a stock of 8-^{3}H-dGTP which was prepared in January of 2009. 8-^{3}H-dGTP was obtained from Amersham Biosciences (Item # TRK335) in aqueous form in a 50% ethanol solution. The concentration of radioactivity provided was 1 µCi/µL (2.22 x 10^6 DPM/µL). This stock was used for determining sub micromolar binding constants, and therefore needed to have an extremely high specific activity (around 200000 DPM/nmol) to obtain the necessary sensitivity. Therefore, 100 µL of the 1

µCi/µL stock was taken from the manufacturer's vial and placed into a sterile 1.5 mL centrifuge tube which has previously had small holes drilled through the top of it. Liquid was removed from the sample via a speed-vac until it reached complete dryness. Unlabeled dGTP was obtained from Roche Biochemicals at a concentration of 100 mM in dH_2O solution. Ten µL of the 100 mM dGTP solution was then added to 190 µL of 50 mM HEPES pH 7.0 so that the final concentration should have been approximately 5 mM. All 200 µL of the 5 mM dGTP solution was then added to the centrifuge tube containing the dried ^{3}H-dGTP sample and mixed up and down 40-50 times with a micropipetter. Five µL was then removed for analysis: 2 µL for liquid scintillation analysis and 3 µL for spectrophotometry (**Table A.1**). Spectrophotometric analysis of the ^{3}H-dGTP was accomplished by diluting 1 µL of the stock into 999 µL of HEPES pH 7.0 and recording the absorbance at a wavelength of 253 nm in a quartz cuvette with a path-length of 1 cm. The extinction coefficient for dGTP at the wavelength of 253 nm is known (ε_{253}=13700 M^{-1}/cm) and the concentration of dGTP in the solution can be calculated using the Beer-Lambert Law as follows:

Table A.1: Spectrophotometric and liquid scintillation analysis of ^{3}H-dGTP.

Spectrophotometric Analysis [*]			Liquid Scintillation Analysis [$]			
	A_{253}	Concentration (mM)		CPM/µL	DPM/µL	Efficiency
Reading 1	0.0720	5.26	Reading 1	414980	1101565	37.67%
Reading 2	0.0710	5.18	Reading 2	403700	1081093	37.34%
Reading 3	0.0715	5.22				
Average		5.22	Average	409340	1091329	37.51%

[*] For the spectrophotometric readings, 1 µL of ^{3}H-dGTP stock was diluted 1:1000 and then had its absorbance at a wavelength of λ=253 nm recorded while in a 1 cm path-length quartz cuvette.
[$] For liquid scintillation counting, 1 µL of ^{3}H-dGTP stock was added to 5 mL of Scintiverse Scintanalyzed (Item # SX-18-4) liquid scintillation cocktail from Fisher Scientific.

$$C = \left[\frac{A_\lambda}{\varepsilon_\lambda l} \right] \times 1000 \qquad\qquad \textbf{(Equation A.2)}$$

where C is the concentration in mol per liter, A_λ is the absorbance of the sample at a wavelength λ, l is the path-length of the cuvette in centimeters, and ε_λ is the extinction coefficient of the compound of interest at a wavelength λ in M^{-1}/cm. The average of three independent readings is used for the final calculation of the concentration (**Table A.1**). To determine the amount of radiation present per unit volume of the stock solution, 1 μL aliquots are added to 5 mL of liquid scintillation cocktail and then counted in a Beckman LS 6500 liquid scintillation counter (**Table A.1**). The average of two independent measurements is used.

To obtain the the specific activity, the measurement of DPM/μL was dividied by the concentration of the dGTP, determined spectrophotomectrically by converting its units to nanomoles/μL. The average measurement of dGTP concentration from **Table A.1** was 5.2 millimoles/L, which is equivalent to 5.2 nanomoles/μL. Dividing 1091329 DPM/μL by the concentration of 5.2 nanomoles/μL yields a specific activity of 209870 DPM/nanomole dGTP.

A.2 QUANTITATIVE ASSAY FOR DETERMINATION OF THE SPECIFIC ACTIVITY OF RNR1

The exact details on performing the assay up until data analysis takes place can be found in **Section 2.12** of this dissertation. In this section there will be a detailed example of how the specific activity (nanomoles per minute per milligram of Rnr1) is calculated from several sets of DPM data. Data from two duplicate experiments for the conversion of CDP to dCDP is shown in **Table A.2** in the column labeled DPM. The DPM value

Table A.2: Data analysis of in vitro activity assay data for Rnr1.

	Time (min)	DPM	Nanomoles dCDP	Activity* (nmol/min)	Specific Activity (nmol/min/mg Rnr1)
Reaction 1	0	746.8	1.259		
	4	1613.2	2.719	0.3593	71.86
	8	2479.51	4.180		
	12	3300.33	5.563		
Reaction 2	0	747.4	1.260		
	4	1691.4	2.851	0.4074	81.48
	8	2614.03	4.406		
	12	3662.18	6.173		

* Activity was determined by plotting time in minutes on the X-axis and nanomoles of dCDP on the Y-axis and fitting a straight line to the data as in **Figure A.1**.

was determined for each reaction quenched at a particular timepoint, which is listed in the column to the left of the DPM column labeled time (**Table A.2**). The DPM data must first be converted into nanomoles of dCDP produced at each timepoint by dividing the the DPM value at each time point by the specific activity of the radio-labeled CDP stock used for that experiment, which happens to be 1863 DPM/nanomole in this case. The original 50 μL aliquot collected and quenched during the experiment had 950 μL of alkaline phosphatase solution added to it, bringing the total volume to 1 mL. Out of that 1 mL, only 950 μL was taken to add to the borate affinity resin. The borate resin has 950 μL of sample added plus the 8 mL of dH$_2$O it was washed with, bringing the total volume to 8.95 mL. Out of that 8.95 mL, only 3.0 mL was counted in the liquid scintillation counter. Therefore, the amount of dCDP is calculated by multiplying it by a series of dilution ratios as follows:

$$\text{nmol dCDP} = \frac{\left[DPM \times \left(\frac{8.95}{3} \right) \times \left(\frac{1}{0.95} \right) \right]}{\left[\frac{1863 DPM}{nmol} \right]} \qquad \textbf{(Equation A.3)}$$

Plugging the values from the DPM column in **Table A.2** into **Equation A.3** provides the results in the 'Nanomoles dCDP' column in **Table A.2**. The data from 'Nanomoles dCDP' is then plotted versus time and a linear regression is performed to fit a straight line to the data in the scientific graphing program Prism (Graphpad Software) (**Figure A.1**). The rate of the reaction in nanomoles dCDP produced per minute is the slope of the straight line fit to the data, 0.3593 and 0.4074 nanomoles dCDP/min for
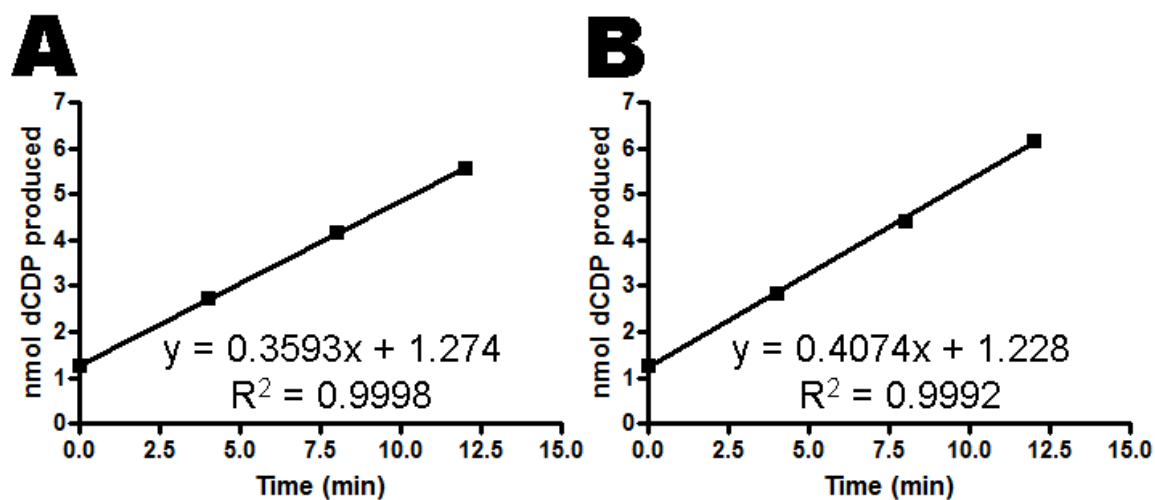
Figure A.1: Linear regression analysis of Rnr1 *in vitro* activity data.
(A) Data from Reaction 1 in **Table A.2**. **(B)** Data from Reaction 2 in **Table A.2**. Linear regressions were fit to the data in the scientific graphing program Prism.

Reaction 1 and Reaction 2 respectively. Notice that the graph does not intercept the Y-axis at 0 at the 0 time point. This is because when the CDP substrate was first added to the reaction mixture and mixed them together, the reaction is already proceeding. By the time the '0 minute time point' is taken, the reaction has already been proceeding for up to 30 seconds during the mixing process. It is also known that the reaction is performed in the steady state because the data adheres to a straight line. If the conditions within the reaction were not in the steady state, the data points would produce a curve rather than a straight line. In addition, the concentrations of substrates used in these *in vitro* reactions are several hundred-fold higher than the previously determined K_m values for the Rnr1 subunit (Ge *et al.* 2003).

The activities determined in **Figure A.1** are then divided by the total mass of Rnr1 present in the reaction to calculate the specific activity with the unit nanomoles dCDP per minute per milligram of Rnr1. Calculation of the specific activity provides a method to normalize activity measurements from reaction to reaction since the mass of Rnr1 present from reaction to reaction can vary. The reaction volume removed at each time point was 50 μL, therefore the activity must be divided by the total milligrams of Rnr1 present in that 50 μL aliquot. For the reactions in this example, the concentration of Rnr1 was 1 μM which equates to 0.005 mg of RNR1 ([1 μmol / L] x [1 L / 1×10^6 μL] x [50 μL] x [1 mole / 1×10^6 μmole] x [1×10^5 grams / 1 mole] x [1000 grams / 1 gram]). Division of the activities for Reaction 1 and Reaction 2 by 0.005 mg Rnr1 gives specific activities of 71.86 and 81.48 nanomoles dCDP per minute per milligram Rnr1, respectively. The specific activity for all of the duplicate reactions are then averaged together to give the final specific activity of 76.67.

If the value of k_{cat} in the units of sec^{-1} is desired, specific activity with the units nmol/min/mg Rnr1 can be converted to k_{cat} using the following equation:

$$k_{cat} = SA \text{ x } (1.666 \text{ x } 10^{-8}) \text{ x } (MW)$$ **(Equation A.4)**

Where k_{cat} is the number of turnovers of substrate to product that occurs in 1 second from one molecule of Rnr1, *SA* is the specific activity of the Rnr1 protein in the units nmol/min/mg Rnr1, and *MW* is the molecular weight of Rnr1 being used (ie: *MW* for *S. cerevisiae* Rnr1 is 100000 while *H. sapiens* is 90000).

A.3 QUANTITATIVE ASSAY FOR DETERMINATION OF THE DISSOCIATION CONSTANTS OF RNR1

The method for determining the dissociation constants (K_d) of *S. cerevisiae* Rnr1 for both effectors and substrates is based upon the method of (Ormo *et al.* 1990). In this section the experimental setup will be described in detail and then a detailed example of obtaining a K_d from some sample data will be considered. The dissociation constant or K_d is an equilibrium constant which describes the propensity of a protein-ligand complex to break apart into a separate ligand and protein. It is defined mathematically as follows:

$$K_d = \frac{[L]_{free}[P]_{free}}{[L \bullet P]}$$ **(Equation A.5)**

Where $[L]_{free}$ is the concentration of unbound ligand, $[P]_{free}$ is the concentration of unbound protein, and $[L \bullet P]$ is the concentration of protein-ligand complex. In the ultrafiltration method described here, it is possible to measure the total amount of protein present ($[P]_{total}$, which is equal to $[P]_{free} + [P]_{bound}$), the amount of unbound ligand ($[L]_{free}$) and the total amount of ligand

present ($[L]_{total}$, which is equal to $[L]_{bound} + [L]_{free}$). With these measurements, one has all the information needed to determine the K_d value for any protein-ligand interaction.

First, the concentration of protein to use in the experiment must be considered. This concentration should be at or below the K_d to be determined, as using protein concentrations higher than the K_d to be determined can result in false determination of its value using this method. Second, both the specific activity (DPM/nmol) and concentration range of the ligand to be used for the binding assay must be considered. The specific activity should be high enough to give the resolution needed for the lowest concentration of ligand used. For the example in this section, the specific activity was 209000 DPM/nmol. The concentration range used for the experiments should contain at least data points below the K_d, just above the K_d, and at several times the K_d. If no previous information about the K_d of the protein-ligand interaction is available, it may be necessary to perform a set of screening experiments over a large concentration range before undertaking a detailed K_d determination.

For the experiments in this example, the protein concentration used was 0.5 µM Rnr1 monomer. The ligand in this example is the effector molecule dGTP, which binds to the S-site of Rnr1 with a ratio of one dGTP to one RNR1. There was some previous knowledge of the K_d value for this interaction from studies on the *E. coli* Rnr1 enzyme and therefore the K_d was predicted to be in the range of 0.5-2 µM. The selected concentrations of protein and substrate were mixed together at a volume of 150 µL in the top reservoir of an Amicon Ultrafree-MC 30,000 molecular weight cut-off polysulfone PTTK membrane ultrafiltration device from Millipore (**Figure A.2**). The composition of the membrane is critical; it can not non-specifically bind the ligand molecule or false binding constants will be obtained. Attempts to perform this assay with Microcon devices with membranes composed of cellulose resulted in failure due to

non-specific binding of nucleotides to the membrane material. The mixture was allowed to

equilibrate for 5 minutes at room temperature and then a 30 µL aliquot was removed for liquid

scintillation analysis. This aliquot was used to determine the total amount of dGTP present (ie:

the dGTP bound to Rnr1 plus the dGTP which is free in solution). Each ultrafiltration device

was then added to a bench-top microcentrifuge and underwent centrifugation at 5000 x g for

between 2 and 5 minutes. The amount of centrifugation time depended on the viscosity of the

solution in the upper chamber of the device. Solutions which contained higher concentrations of

protein required longer centrifugation times approaching 4 to 5 minutes, while lower

concentrations of protein only required 2 to 3 minutes of centrifugation. The end goal of

centrifugation was to obtain between 50 and 70 µL of flow-through in the bottom chamber of the

ultrafiltration device (**Figure A.2**). Thirty µL of the flow-through was then aliquoted for liquid

scintillation counting. This aliquot was then used to calculate the concentration of unbound

dGTP present. Sample data for a previously performed binding assay for dGTP binding to the *S.*

cerevisiae Rnr1 mutant S610F in the presence of the small subunits Rnr2 and Rnr4 is found in

Table A.3. The DPM counts for the total concentration of dGTP and the free concentration of

dGTP are the left two columns. To calculate the concentration of dGTP present in solution from

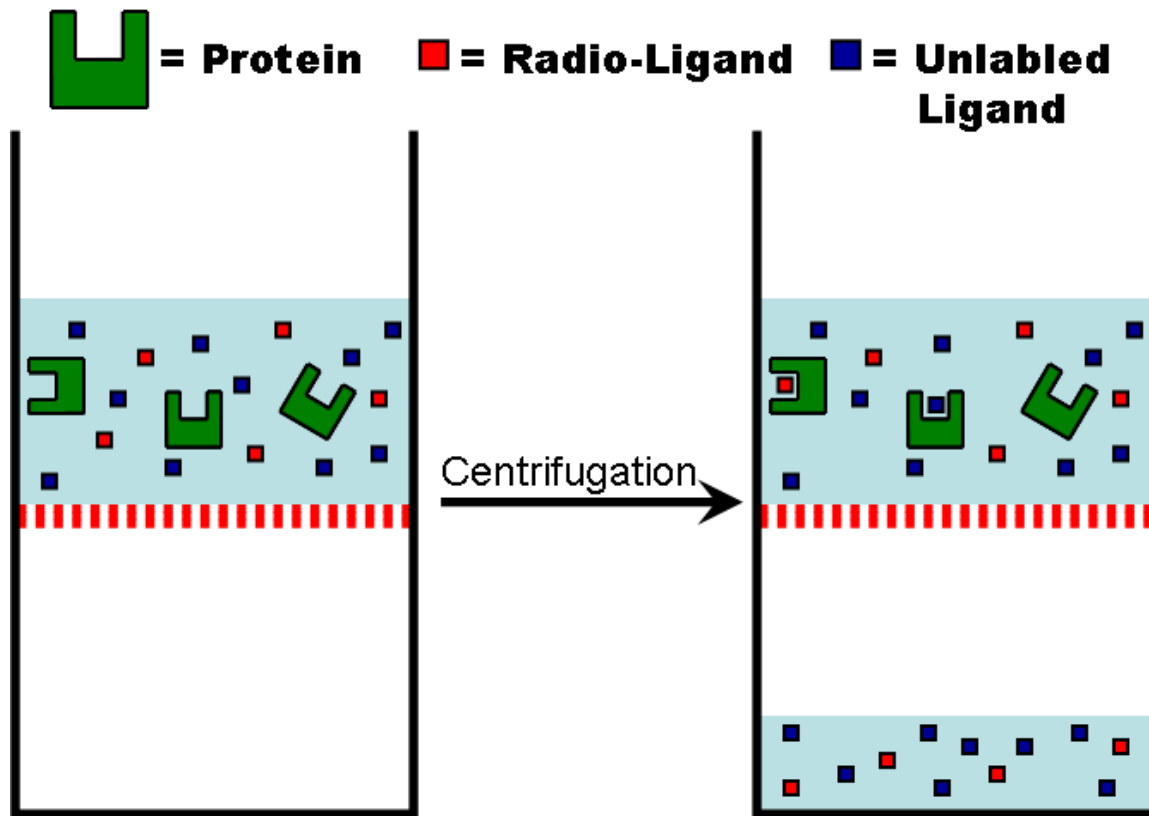the DPM counts, the following formula is used:

Figure A.2: Diagram of the ultrafiltration apparatus.
Protein and radio-labeled ligand are mixed in the upper chamber of an ultrafiltration concentration device. The dashed red lines represent a semi-permeable membrane with a molecular weight cut-off of 30 kDa. A sample is taken from the top reservoir for calculation of the total ligand concentration and then exposed to centrifugal force. After centrifugation, a sample is taken from the flow-through for calculation of free ligand concentration.

Table A.3: Binding data for dGTP binding to the *S. cerevisiae* Rnr1 mutant S610F.

DPM_{total}	DPM_{free}	$[dGTP]_{total}$ (nM)	$[dGTP]_{free}$ (nM)	$[dGTP]_{bound}$ (nM)	$[dGTP]_{bound}/[Rnr1]_{total}$	Corrected $[dGTP]_{free}$
645.06	600.45	102.5	95.4	7.1	0.0354	84.74
654.71	573.27	104.0	91.1	12.9	0.0647	71.65
1189.96	896.01	189.0	142.3	46.7	0.0934	142.31
1178.77	876.55	187.2	139.2	48.0	0.0960	139.22
2980.33	2213.87	473.4	351.6	121.7	0.2435	351.63
2943.98	2296.68	467.6	364.8	102.8	0.2056	364.78
4709.19	3605.99	748.0	572.7	175.2	0.3504	572.73
4761.45	3754.6	756.3	596.3	159.9	0.3198	596.34
11791.72	8630.93	1872.9	1370.8	502.0	0.5020	1621.85
11866.75	8531.67	1884.8	1355.1	529.7	0.5297	1619.93
30003.6	26074.2	4765.4	4141.3	624.1	0.6241	4453.38
30078.18	25260.64	4777.3	4012.1	765.2	0.7652	4394.69

$$C = \frac{\left(\dfrac{DPM}{SA}\right)}{V}$$

(Equation A.6)

where C is the concentration of dGTP with the units nmol/L (nM), *DPM* is the radioactive count from the liquid scintillation counter, *SA* is the specific activity of the dGTP stock used with the units DPM/nanomole, and *V* is the volume of the aliquot that was removed from the ultrafiltration device for scintillation counting with the unit liters.

For this sample experiment, the specific activity *SA* of the dGTP stock used was 209870 DPM/nmol and the volume *V* of the aliquots removed for scintillation counting were 3×10^{-5} liters in volume. Concentrations of $[dGTP]_{total}$ and $[dGTP]_{free}$ calculated from **Equation A.6** and the DPM data are shown in **Table A.3**. The concentration of dGTP which is bound to the Rnr1 protein ($[dGTP]_{bound}$) is then calculated by subtracting $[dGTP]_{free}$ from $[dGTP]_{total}$. Fractional occupation ($[dGTP]_{bound}/[Rnr1]_{total}$) is then calculated by dividing $[dGTP]_{bound}$ by the total concentration of Rnr1 ($[Rnr1]_{total,}$) present in the binding assay mixture. If the concentrations of Rnr1 used in each experiment were not identical, the $[dGTP]_{free}$ value was corrected to account for this, which is shown in **Table A.3** in the right-most column.

The fractional occupation and $[dGTP]_{free}$ values calculated in **Table A.3** can then be used to analyze the data graphically in a scientific graphing program, such as Prism (Graphpad Software), to obtain the k_d and the number of binding sites (B_{max}) (**Figure A.3**). There are two way to fit the data to obtain the binding information. The classical
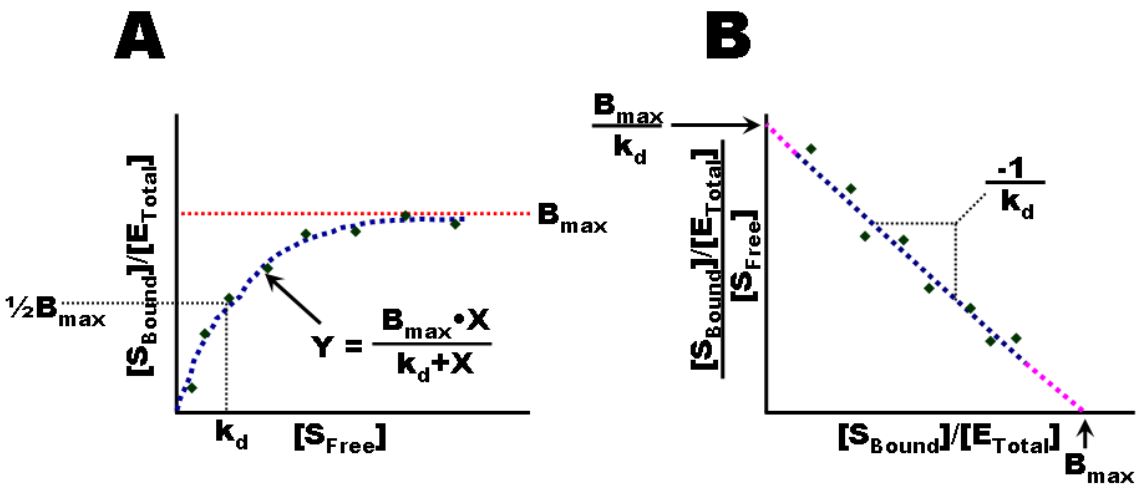
Figure A.3: Non-linear and linear analysis of binding data.
(**A**) Binding data is plotted with $[S_{free}]$ on the X-axis and $[S_{bound}]/[E_{total}]$ on the Y-axis. A non-linear equation in the form $Y = (B_{max}*X)/(k_d+X)$ is fitted to the data. (**B**) Scatchard plot of the same data from **A**. The Y-axis from **A** is used for the X-axis and the Y-axis is the X-axis divided by $[S_{free}]$. The number of binding sites (B_{max}) and k_d are obtainable from both data analysis methods.

method is to perform a Scatchard plot by transforming the data into a form to which a linear equation can be fit (**Figure A.3B**). In a Scatchard plot the fractional occupation is plotted on the X-axis and the fractional occupation divided by concentration of free ligand is plotted on the Y-axis. However, according to the Prism user manual "the Scatchard transformation distorts the experimental error, so the data on the Scatchard plot do not obey the assumptions of linear regression. Use nonlinear regression to obtain the most accurate values of k_d and B_{max}". Therefore the nonlinear regression method was used to fit a hyperbolic isotherm with to the binding data as shown in **Figure A.3A**. In this analysis method, $[dGTP]_{free}$ is plotted on the X-axis and the fractional occupation is plotted on the Y-axis. The hyperbolic function used to fit the experimental data is as follows:

$$Y = \frac{B_{max} X}{k_d + X}$$
(**Equation A.7**)

Where Y is the fractional occupation, X is $[dGTP]_{free}$, K_d is the dissociation constant, and B_{max} is the number of binding sites. The hyperbolic binding curve fit to the sample data is shown in **Figure A.4A**. The k_d for this data was determined to be 980 nM with an error of 146.1 nM (0.98 μM ± 0.15) with a B_{max} of 0.8449, indicating one binding site (which is what was expected). Although the Scatchard plot may not be the best method to use for the fitting of data, it is still a very straight forward method to present the data. The Scatchard plot in **Figure A.4B** was created with a straight line drawn through 2 points: one at X=B_{max},Y=0 and the other at X=0,Y=B_{max}/k_d.
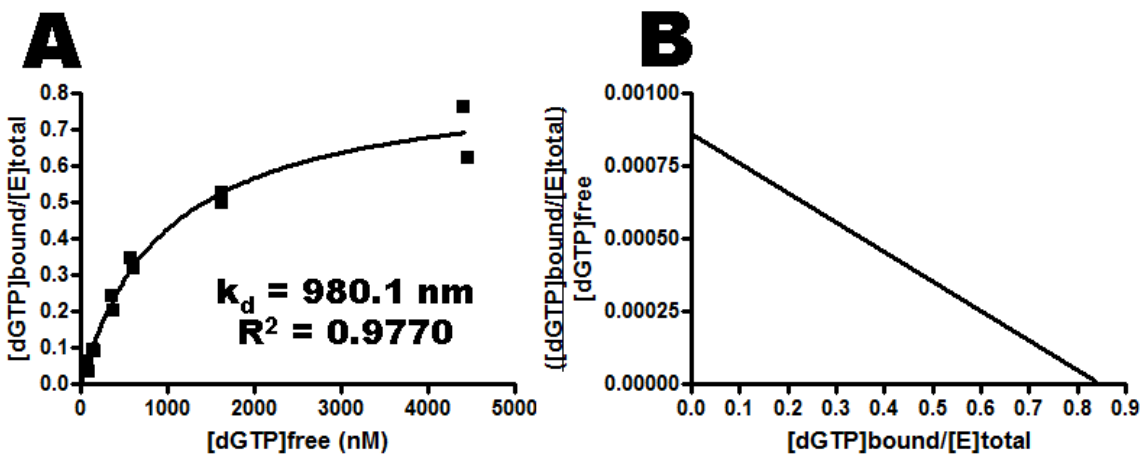
Figure A.4: Sample data represented in non-linear and Scatchard forms.

A.4 SIZE EXCLUSION CHROMATOGRAPHY

Molecular weights for Rnr complexes by size exclusion chromatography (SEC) performed in **Section 4.3.5** were obtained by using the elution volume (V_e) of each each oligomeric species to calculate the K_{av} values for each oligomeric species:

$$K_{av} = \frac{V_e - V_o}{V_T - V_o}$$
(Equation A.8)

Where V_o is the void volume of the column, determined by blue dextran, V_T is the total volume of the size exclusion column, and V_e is the elution volume of a protein. Proteins with known molecular weights were applied to the column, their elution volumes were observed, and their K_{av} values were calculated using **Equation A.8** (**Table A.4**). The log of the molecular weights of the known proteins were then plotted against their values of K_{av} to form a standard curve (**Figure A.5**). Standard proteins chosen for calibration of the Superdex 200 PC 3.2/30 size exclusion column used in **Section 4.3.5** were thyroglobulin (670 kDa), gamma-globulin (158 kDa), ovalbumin (44 kDa), and myoglobin (17 kDa). K_{av} values for proteins with unknown size can then have their molecular weight estimated by extrapolation using the standard cuve.

Table A.4: Size exclusion data for proteins with known molecular weights.

Sample	M_r (Da)	log (M_r)	V_e (mL)	K_{av}
Blue Dextran	2000000	6.301	1.03	N/A
Thyroglobulin	670000	5.826	1.16	0.094
Gamma Globulin	158000	5.199	1.48	0.325
Ovalbumin	44000	4.643	1.75	0.521
Myoglobin	17000	4.230	1.93	0.651

$$y = -0.3504x + 2.141$$
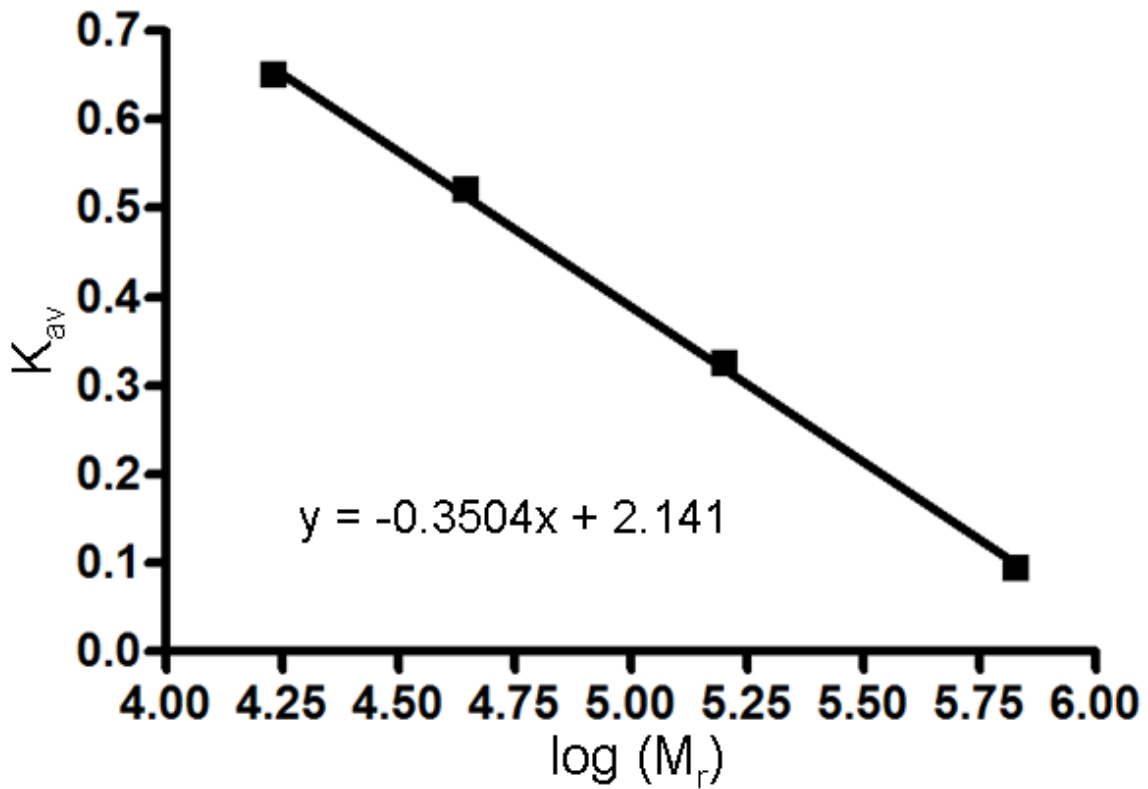
Figure A.5: Standard curve for size exclusion chromatography.

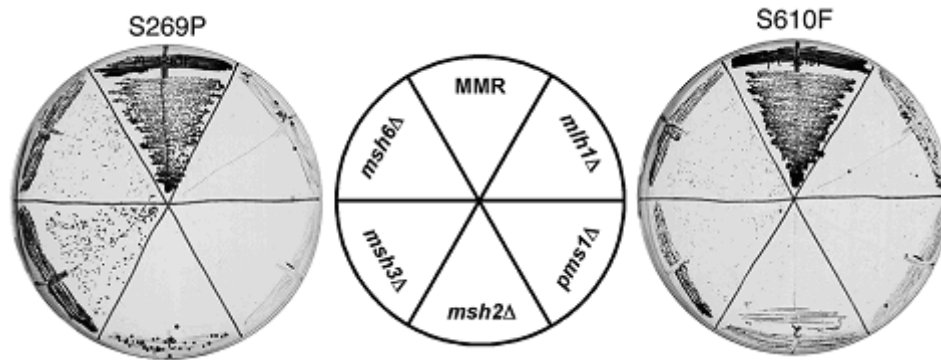**Figure A.6: *Rnr1 msl* alleles S269P and S610F in MMR+ (*MLH1*) and *mlh1Δ, pms1Δ, msh2Δ, msh3Δ,* and *msh6Δ* strains.**

A weak *msl* phenotype is observed for *Rnr1*^{S269P} in *msh6Δ* and *msh3Δ* strains and a strong *msl* phenotype is observed for *msh2Δ*, *pms1Δ*, and *mlh1Δ* strains. On the other hand, the *Rnr1*^{S610F} allele displayed a strong *msl* phenotype when combined with the deletion of any of the MMR genes. This figure was kindly provided by our collaborator Dr. Julian Simon at the Fred Hutchinson Cancer Research Center in Seattle, Washington.

VITA

James Fairman was born in Indiana, Pennsylvania on November 23rd, 1980 and was raised in a small rural town called Creekside, Pennsylvania until the age of 16. In 1997, his family relocated to the town of Elizabethton, Tennessee and he eventually graduated from Elizabethton High School in 1999. He then began attending Eastern Tennessee State University in the fall of 1999, where he studied novel β-lactamase genes in the bacterium *Moraxella catarrhalis* under the supervision of Dr. Foster Levy. He graduated from Eastern Tennessee State University in May of 2003 with honors, obtaining a B.S. in Biology with a concentration in Biochemistry.

James was accepted to the Biochemistry, Cellular, and Molecular Biology (BCMB) program at the University of Tennessee -- Knoxville in the Spring of 2003 and began attending classes soon afterwards in the Fall of 2003. He joined the laboratory of Dr. Chris Dealwis in June of 2004 where he applied the technique X-ray crystallography to the protein ribonucleotide reductase. He graduated with his doctorate in August of 2009, and pursued a post-doctoral research position in the laboratory of Dr. Susan Buchanan at the National Institutes of Health in Bethesda, Maryland.